Dissertations

Fall 12-1-2015

Hybrid Aryl-Ether-Ketone and Hyperbranched Epoxy Networks

John Misasi
University of Southern Mississippi

The University of Southern Mississippi

HYBRID ARYL-ETHER-KETONE AND HYPERBRANCHED EPOXY NETWORKS

by

John Michael Misasi

Abstract of a Dissertation
Submitted to the Graduate School
of The University of Southern Mississippi
in Partial Fulfillment of the Requirements
for the Degree of Doctor of Philosophy

December 2015

ABSTRACT

HYBRID ARYL-ETHER-KETONE AND HYPERBRANCHED EPOXY NETWORKS

by John Michael Misasi

December 2015

In this dissertation, relationships between chemical structures, cure kinetics and network architectures are correlated to bulk mechanical properties for novel, hybrid epoxy-amine networks. The work is split into two primary sections: the first is the synthesis and characterization of multifunctional glassy networks based on aryl-ether-ketone diamine curatives, while the second is based on the synthesis and characterization of hyperbranched epoxy polymers and their resulting networks.

Three aryl-ether-ketone (AEK) diamines of increasing molecular weights were synthesized and used to cure 4,4'-tetraglycidylether of diaminodiphenylmethane (TGDDM); the resulting networks were compared to 4,4'-diaminodiphenyl sulfone cured TGDDM. Architectural differences were created by varying cure profiles, and characteristics such as sub-T_g motions and free volume were altered to study bulk properties such as thermal stability, glass transition, mechanical properties, and moisture resistance. Additional analysis coupled molecular dynamics simulations and free volume data to relate AEK molecular-level characteristics to bulk properties. Simulation showed that enhanced chain packing and conformational freedom provided networks with similar hole free volume characteristics but created increased fractional free volume with increase in M_c. Activation energies of the two sub-T_g relaxations correlated with the free volume findings. Conformational freedom was also related to mechanical properties, which was related to enhanced secondary interactions.

ii

Additionally, AEK diamines were copolymerized with DDS to form blended, hybrid networks with TGDDM. Blended networks offered further insight into the effects of chemical composition and M_c effects by varying AEK concentration. It was found that low concentrations of AEK-diamines could significantly alter DDS-cured networks.

The second section of this work involved the blending of an epoxide-functional hyperbranched polymer (HBE) into a glassy epoxy network. It was found that the network-level incorporation and high concentration of secondary interactions allowed simultaneous improvements in modulus and toughness. Further thermal and mechanical improvements were found by incorporation of POSS-units onto the hyperbranched polymer. The bulk property improvements were found to correlate with the multiscale dispersion of POSS. Finally, POSS-HBE carbon-fiber composites were fabricated and tested. Composite properties were related to those of the matrix material.

HYBRID ARYL-ETHER-KETONE AND HYPERBRANCHED EPOXY NETWORKS

by

John Michael Misasi

A Dissertation
Submitted to the Graduate School
and the School of Polymers and High Performance Materials
at The University of Southern Mississippi
in Partial Fulfillment of the Requirements
for the Degree of Doctor of Philosophy

Approved:

_____
Dr. Jeffrey S. Wiggins, Committee Chair
Associate Professor, School of Polymers and High Performance Materials

_____
Dr. James W. Rawlins, Committee Member
Associate Professor, School of Polymers and High Performance Materials

_____
Dr. Derek L. Patton, Committee Member
Associate Professor, School of Polymers and High Performance Materials

_____
Dr. Sarah E. Morgan, Committee Member
Professor, School of Polymers and High Performance Materials

_____
Dr. Robson F. Storey, Committee Member
Distinguished Professor, School of Polymers and High Performance Materials

_____
Dr. Karen S. Coats
Dean of the Graduate School

December 2015

DEDICATION

Above all else, this dissertation is dedicated to my family. I dedicate this to my parents, who's austere devotion compelled me to become the ambitious man I am today. I also dedicate this to my sister, who was always there for me when coping with *austere devotion* became difficult.

"Fate gives all of us three teachers, three friends, three enemies, and three great loves in our lives. But these twelve are always disguised, and we can never know which one is which until we've loved them, left them, or fought them."

- Gregory David Roberts[193]

I would also like to dedicate this work to those of the twelve who have come, who have gone, and those who I've yet to meet.

ACKNOWLEDGMENTS

First and foremost I would like to thank my advisor, Dr. Jeffrey Wiggins. In what some may say is an unorthodox form of student development, Dr. Wiggins has provided me with a complete scientific toolset to tackle the career challenges that lie ahead. He allowed me to choose my own scientific path, struggle through my own technical problems, and even allowed me to fail, never meddling or influencing my process. Although frustrating at times, his "hands-off" approach has made me a better scientist, engineer, teacher, and leader. "Doc" is more than just an advisor, I have personally learned as much from him outside the professional setting as I have in it. His advice and support through some of my most important life decisions was invaluable; I cannot fully express the gratitude I feel.

I sincerely thank my committee Dr. James Rawlins, Dr. Robson Storey, Dr. Derek Patton, and Dr. Sarah Morgan. I would like to offer an extended thanks to Dr. Morgan who has undoubtedly helped improve my writing and communication skills.

I would also like to acknowledge those who have contributed to make this research possible, including Jessica Douglas and her help with TEM and SEM, and Ramesh Ramakrishnan and his assistance with PALS. I thank everyone from CSIRO, including Dr. Russell Varley, Buu Dao, and Wendy Tian for helping me "kick-off" my research efforts. Importantly, I would like to thank Dr. Qifeng Jin for his initiation of the hyperbranched epoxy work. Without his help, half of my dissertation would be empty white pages.

There will forever be a special place in my heart for the WRG administrative staff, Ms. Charlie and Ms. Stephanie. These two women are the backbone of WRG,

without them we are but a pile of silly putty. I thank them for feeding me, caffeinating me, keeping parking services at-bay, and for being the voice of reason (whether I wanted it or not).

Finally I would like to recognize the entire WRG family, all of which have had a significant impact on my tenure as a graduate student. In particular I would like to thank our collaborators, Steve Christensen and Dr. Rob Maskell and past graduate students Dr. Sam Tucker, Dr. Matthew Jackson, Dr. Stephen Heinz, and Dr. Xiaole Cheng. A special thanks to Jarred Tramell. I am grateful for his work ethic and perseverance, both have helped me to expedite my graduate research. More importantly however, I thank him for his eagerness to learn and his patience during my long-winded pontifications. Lastly, I cannot think of a better group of friends to have as lab mates. Kyler Knowles, Brian Greenhoe, Jeremy Moskowitz, Andrew Frazee, and Andrew Janise, thank you for listening to the scientific rants and discussions, and for pressuring me into a life outside of the lab.

TABLE OF CONTENTS

LIST OF TABLES

LIST OF ILLUSTRATIONS

Figure

xiii

xviii

CHAPTER I

INTRODUCTION

Motivation and Scope

Over the last 75 years continued proliferation of polymer matrix composites in the aerospace industry has advanced materials and manufacturing technologies to produce aircraft with higher strength-to-weight ratio, reduced fuel consumption, and increased service life.[1] Since the overwhelming majority of aerospace composites are composed of thermoset epoxy matrices reinforced with carbon fiber, a renewed interest in polymer matrix materials has evolved. Glassy network epoxies offer advantages over other polymer matrices due to their combination of properties, processability, and cost. High performance epoxies are characterized by high modulus, high strength, fatigue life, and solvent resistance. However, high modulus matrices used in aerospace are inherently brittle and fail before ultimate fiber potential is realized. In an effort to gain performance, brittle networks often employ a discreet second phase which increases "toughness" but compromises other properties and complicates manufacturing processes. Improving glassy network mechanical deformation capability, or toughness, while maintaining or advancing other key thermal and mechanical properties will enhance ultimate composite performance and lead to additional weight reductions in aerostructures.

It is clear that macroscopic behaviors such as a polymer's response to deformation are linked to molecular-level phenomena.[2,3] Recent advancements in computational tools have provided researchers new methods for studying and predicting these structure-property-relationships on various time and length scales and with a high degree of certainty. Previously, new matrix chemistries required multi-month or year-long

processes to develop, synthesis, and validate performance, but with molecular dynamics (MD) simulations numerous formulations can be explored with predicted performance in days. Particularly beneficial are the visualization tools employed in MD simulation which provide the researcher a pathway to "witness" molecular-level conformational and torsional rearrangements during simulated thermal and mechanical experimentation. Our collaborators at Boeing Research and Technology have recently introduced the physics-based "Onset theory" to reduce their dependence on empirical testing for prediction of composite performance in aerospace structures.[4] Onset theory uses both matrix critical and fiber critical strain invariants to describe the initiation of composite failure. The matrix invariants are associated with dilatational and distortional strain values, which can be readily studied with MD techniques.

The advancement of these techniques has manifested in a promising new approach to develop next-generation aerospace composite matrix chemistry formulations, but the relationship between simulated and experimental approaches to optimize monomer chemical structure, network architecture, and macroscale performance is still in its early stages of development. Further understanding of structure-property-relationships will increase the efficiency and efficacy of simulations through educated monomer selection. This multi-scale examination of glassy polymer network architecture contained in this body of work aims to present finding regarding the effects of hybrid network chemical composition and network architecture on the distortional deformation capability and key engineering properties of glassy epoxy networks.

Background

Glassy Epoxy Networks

Network Formation. Epoxy networks are formed through step-growth crosslinking reactions when glycidyl-rings of di- or multifunctional epoxies are opened from attack via strong nucleophiles such as primary-amines. In the first steps of network formation, a primary amine reacts with a glycidyl-ring to create a hydroxypropylether linkage and a secondary amine; this stage of the reaction is sometimes referred to as the "B-stage". During the second steps of the reaction, secondary amines react with other epoxides to from crosslinks (or junctions), forming another hydroxypropylether and a tertiary amine. Depending on conditions, such as when epoxides are in stoichiometric excess or at elevated temperatures, further reaction can occur between hydroxyl- and glycidyl-groups.[5] This forms an ether linkage and is referred to as etherification.

During the consumption of functional groups through crosslinking reactions, the physical state of the system evolves from liquid, to gel, to solid. First, liquid monomers react until the network becomes infinite in both molecular weight and viscosity; this threshold is known as gelation.[6] Throughout gelation the reaction between amines and epoxides continues and the amount of intractable gel increases without a decrease in reaction rate. At some point during the polymerization, reactive groups no longer possess the mobility nor collision frequency to further react due to the systems glass transition (T_g) exceeding that of the surrounding environment or cure temperature. This state-change is referred to as vitrification. In the vitreous state crosslinking reactions and group conversion are slowed appreciably to a "diffusion-controlled" regime and further reaction minimally affects crosslink density or network architecture.[7]

Network Properties. The physical and thermal properties of cured epoxy-amine networks are dependent on a multitude of factors. Notably, cured matrices are affected by stoichiometry, monomer functionality, and chemical composition. Networks formulated with a 1:1 ratio of oxirane to active amino-hydrogen are considered "stoichiometric". In theory, step-growth polymerizations produce 100% functional group conversion only when 1:1 stoichiometry is employed, but etherification and other side-reactions during epoxy-amine crosslinking allow for deviation from principle.[6] Additionally, off-stoichiometric networks produce higher concentrations of dangling ends and increased molecular weight between crosslinks.[8] Due to decreased crosslink density, these un-tethered segments have improved chain packing and decrease free volume which has implications on T_g and modulus. Finally, although not purposefully formulated, properties similar to those of off-stoichiometric networks can occur from early onset vitrification; this is common to high functionality networks.[9]

The average functionality of the epoxy-amine mixture is an important factor in determining the final properties of the cured network. Structural epoxy-amine matrices in aerospace formulations are composed mainly of multifunctional epoxies (f >2) such as tetraglycidyl-4,4'-diaminodiphenylmethane (TGDDM) and tetrafunctional diamines such as 4,4'-diaminodiphenylsulfone (44DDS). High functionality formulations such as these have short times to vitrification and increased crosslink densities. Theoretically, increased crosslink density results in higher modulus[10], T_g[11], reduced free volumes, and less fluid ingress.[12] However, as will be discussed throughout this work, experimental crosslink density can deviate from calculated values due to vitrification and network architecture.

The result is an increase in network-level heterogeneity which can cultivate a unique set of physical properties.

Chemical composition refers to the chemical make-up of a polymer, and with all else equal, it is one of the most important characteristics of an epoxy amine network. First, chemical attributes of epoxy and amine monomers effect the reactivity of the system. The aromatic diamines used to cure epoxies are strong nucleophiles and their reaction temperatures (or cure protocol) are governed by the basicity of the amine.[13,14] Bascisity, or pKa, is controlled by monomer chemical features such as aromatic ring substitution (*ortho/para* or *meta*), electron donating/withdrawing nature of the linkage, and structure rigidity. Physical and thermal properties are also influenced by chemical composition. In general, aromatic networks show higher rigidity and thermal stability than those composed of aliphatic segments. The linking groups between aromatic rings effect the remaining flexibility of the system with common linkages being isopropyl, methylene, sulfone, ether, and ketone groups. Hydroxyls generated during polymerization or included from network-modifiers contribute to network properties through hydrogen bonding and can effect modulus, density, and fluid ingress.[15,16]

Dilatational and Distortional Polymer Deformations

Polymer deformations have been scrutinized for several decades, but it is generally accepted that deformations of condensed-phase matter can be broken into two components, volumetric (dilatational) and deviatoric (distortional). These two mechanisms correspond to plastic and elastic processes that occur under load, and at some amount of deformation one mechanism becomes critical to produce permanent deformation.

Onset Theory. Onset theory is a physics-based polymeric failure criteria for carbon-fiber reinforced polymer-matrix composites and it has been shown to accurately predict ultimate composite capability and failure mechanisms.[4,17] Onset theory uses two strain invariants to predict the onset of critical failure events, the first invariant of the volumetric strain tensor, J_1, and the von Mises strain, ε_{vm}. The volumetric strain is composed of three invariants, but as 98% of the total volume change during deformation is accounted for in J_1, dilation is estimated with this value alone. Both J_1 and ε_{vm} are calculated from the three principle strains of the x, y and z axis of deformation (ε_1, ε_2, ε_3).

$$J_1 = \varepsilon_1 + \varepsilon_2 + \varepsilon_3$$

$$\varepsilon_{vm} = \sqrt{\frac{1}{2}[(\varepsilon_1 - \varepsilon_2)^2 + (\varepsilon_2 - \varepsilon_3)^2 + (\varepsilon_1 - \varepsilon_3)^2]}$$

A materials dilatational response to an applied strain is measured by J_1, while its distortional response is given by ε_{vm}. Materials such as glassy polymer networks dilate when an applied load causes deformation resulting in volume expansion without a change in shape (Figure 1); this is the dominant failure mechanism in currently employed composite matrices and brittle glassy polymers such as polystyrene.[18] Dilation of epoxy networks follows Lennard-Jones fracture behavior in which the Pauli Exclusion Principle repels atoms at a distance less than their van der Waals (vdW) radius and electrostatic differences attract atoms at a distance greater than their vdW radius.[19] Dilation occurs when the cohesive forces of the polymer are exceeded by outside forces resulting in cavitation. Continuance of the induced stress causes subsequent nanoscopic cavities to form, beginning the crack propagation process and ultimately, brittle failure.[20]

A distortional response to deformation theoretically avoids volume expansion through a change in shape (Figure 2). Although intermolecular forces may be overcome during a distortional event, the net frictional forces do not change and the ultimate strength of the material remains intact.[21] It is the molecular-level rearrangement followed by the recovery of intermolecular forces that limits cavitation and prevents crack propagation. Shape-change as a result of strain is the dominant energy dissipation mechanism of rubbers, polycarbonate, and polysulfone. It is logical to assume that enhancing the inherent, cavitation-limiting nature of distortion would improve the bulk mechanical properties of polymer networks and carbon-fiber composites.
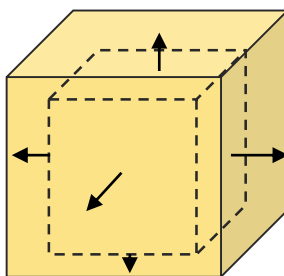
Figure 1. Representation of a dilatational deformation response.
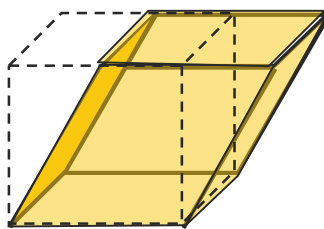
Figure 2. Representation of a distortional deformation response.

Attributes Related to High Distortion

Attributes that effect composite strain-capability span the continuum scale. However, in terms of thermosetting glassy matrices, strain capability is driven by dilation

and distortion. The volume expansion of a dilatational response is controlled by bond

lengths, bond angles, and atomic composition; these factors are not easily manipulated.

On the other hand, distortional deformations are controlled by network architecture and

molecular motions. These factors are more easily influenced and can be designed into the

network. Using ε_{vm} and J_1 as design parameters, Onset theory and multiscale modeling

have helped to predict what chemical and architectural features provide networks with the

improved strain-capability.

Table 1

Simulated strain components of DGEBA networks cured with various diamines
normalized to baseline curative

Model Amine Curative (Normalized)	ε_{vm}	J_1
Para-substituted aromatic sulfone diamine (benchmark)	1.000	1.000
Meta-substituted aromatic sulfone diamine	0.926	1.191
Meta-substituted aromatic ether diamine	1.013	1.306
Para-substituted aromatic ether sulfone diamine	1.035	0.987
Para-substituted aromatic diamine	0.868	1.204
Cycloaliphatic diamine	1.286	0.809

Reproduced from reference with permission.[22]

Improving the distortional capability of composite matrices involves enhancing

molecular-level rearrangements upon deformation. These rearrangements are dependent

on the polymer backbone's ability to undergo rotations through dihedral angles.[20,21,23]

Molecular modeling has enhanced our understanding of the chemical moieties which

improve dihedral angle rotations, and Table 1 shows normalized simulation data to

illustrate the effect of chemical composition on distortional capability by changing the structure of the diamine curative. When used to cure DGEBA, diamines with methylenes, ethers, thioethers, sulfones, and ketones are favorable distortional curatives. Additionally, simulations have provided insights into how crosslink density and molecular weight between crosslinks can affect distortion.[24] It was revealed that distortional capability decreases as the concentration of "favorable" groups between network junctions increases. Architectural effects such as this are dependent on many factors though, including network functionality, flexibility between junction points, and secondary interactions.

Molecular cohesion is dictated by a balance between intermolecular interactions and repulsions. Attractive interactions such as those making up van der Waals forces (Debye, Keesom, and London dispersion forces) describe the instantaneous attractions between neighboring particles, and transpire due to interactions of uncharged atoms or molecules.[25] Pauli repulsions develop from the overlapping of adjacent electron clouds and are the primary repulsive forces between atoms and molecules. The balance of attractive and repulsive forces determines the energy barriers required for bond rotations and conformational rearrangements, and it is determined by the concentration and strength of secondary interactions. Network-level cohesion is therefore tailored by chemical moieties that induce attractive interactions such as those in hydrogen-bonding [16,26] and π-π stacking. Understanding the effects of secondary interactions on engineering properties is key to this dissertation.

Secondary Relaxations

In terms of thermal transitions, or *relaxations*, the glass transition in commonly referred to as the primary thermal relaxation and typically designated the α-transition. Relaxations which occur in the glassy-state are referred to as secondary (or sub-T_g) relaxations and are typically given β, γ, and δ designations. Secondary transitions observed using dynamic mechanical analysis (DMA) have been shown to correspond to engineering properties of glassy networks.[27–29] An example of both primary and secondary relaxations measured by DMA is shown in Figure 3. Unlike the glass transition, secondary relaxations in epoxy networks are associated with short-range molecular motions such as those of methyl rotations[30,31], phenyl-ring flips[32–34], and hydroxypropylether crank-shaft motions.[35,36]
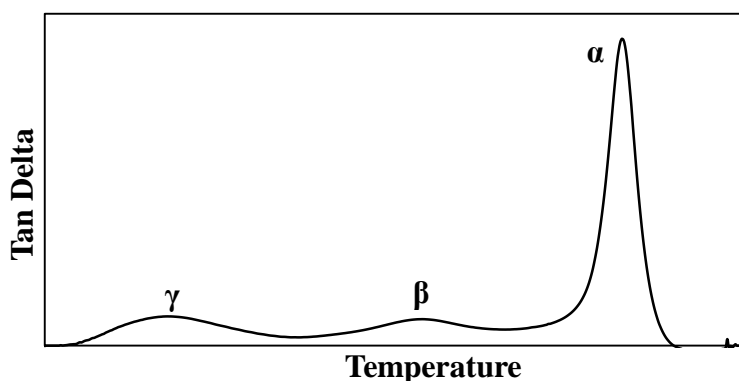
Figure 3. Example of the thermal relaxations observed using the thermomechanical tan delta as a function of temperature from DMA.

Sub-T_g relaxations are described as either simple or cooperative. Simple motions exemplify fast methyl rotations, ring flips, and crank-shaft motions, and are hypothesized to occur without requiring long-range structural rearrangement.[37] Cooperative motions

refer to an assemblage of motion from neighboring groups or segments. Cooperativity is controlled by symmetry, backbone rigidity, and steric hindrance, but its specific motions are still not fully understood.[38] In DMA, simple motions are typically designated to the γ-relaxation while cooperative, or complex, relaxations are attributed to the β-transition.

Secondary relaxations are of particular interest in glassy-network research since application of such materials occurs at temperatures well into the glassy-state. Compared to the glass transition, these simpler motions control polymer network dynamics and have been directly correlated to engineering properties such as distortion and fluid resistance. However, the architectural heterogeneity and complex structures of highly crosslinked polymers makes determination of the structure-property-relationships responsible for secondary relaxations challenging. Sub-Tg molecular motions have been shown to be affected by chemical composition[28,29,35,38], crosslink density[29,39–41], and free volume[42–47]. This work presents the effects of certain network-level attributes on sub-T_g relaxations by varying crosslink molecular weight, and cure conversion, and by modifying the concentration of different chemical moieties.

Aryl-ether-ketone Network Segments

One interesting means to producing distortional networks is by incorporation of aryletherketone segments. Consistent to their namesake, aryletherketones (AEKs) are a family of aromatic materials which contain phenylenes linked by both ketone and ether functionalities. Preliminary molecular modeling results in collaboration with Boeing revealed that DGEBA epoxy networks formed with various AEK curatives had some of the highest von Mises strain values simulated to date. The observed property improvements were attributed to the ketone's dihedral angle and the flexibility of the

ether linkages. From these promising results it was determined that experimental investigation was necessary to further understand and substantiate the simulation properties.
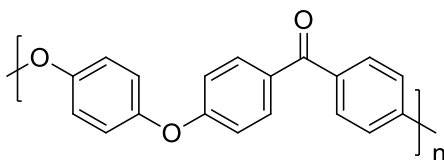
Figure 4. PEEK repeat unit.

Poly(aryletherketone)s (PAEK) represent a family of linear semi-crystalline polymers with high thermal and mechanical properties controlled by the sequence of phenylene, ketone and ether moieties along the polymer backbones. Common PAEK polymers include polyetherketones (PEK), polyetheretherketones (PEEK, Figure 4), and polyetherketoneketones (PEKK). PAEKs are synthesized through electrophilic aromatic substitution reactions, nickel-catalyzed coupling reactions, and nucleophilic aromatic substitution reactions (NAS).[48–52] High reaction temperatures are required to prevent premature crystallization during polymerization and promote high molecular weight. A broad selection of dihalobenzoid and bisphenol monomers are available to tailor reaction conditions and final polymer properties.[6]

PAEKs have an excellent combination of thermomechanical engineering properties with T_gs typically in the range of 140-170 °C, melt-temperatures between 330-370 °C and continuous service temperatures up to 250 °C.[53] Tensile strengths at break reside around 80-95 MPa with ultimate elongations between 50-60% percent. In addition, PAEKs have the lowest smoke and fume densities compared to other engineering polymers, combined with extremely low heat release rates.[54] Their high-degree of crystallinity (~35%) provides excellent fluid resistance, distortional deformation and

impact strength. This combination of properties makes PAEKs excellent candidates for use as continuous fiber thermoplastic composite matrices.

Few reports exist on the incorporation of AEK segments into epoxy networks. Furthermore, the published studies involve the modification of difunctional epoxies, but to this author's knowledge, none exist on more pertinent multifunctional networks. Hwang *et al.* showed the synthesis and network modification of a diglycidyl ether ether ketone compound.[55] The novel AEK monomer was blended with cyclo-aliphatic epoxies and cured by an anhydride to observe the effects on thermal resistance and degradation. It was found that the blended networks had improved thermal properties, but no further investigation was provided. Varma and coworker synthesized a variety of aromatic diamines to study the structure-property relationships of changing the linkages between phenylenes; included in this study was an aryl-ether-ketone diamine.[56] It was found that AEK-cured DGEBA had improved thermal and mechanical properties. Additionally, it contained the highest modulus of the networks studied. However, the cure protocol employed (100 °C, 4hrs, 150 °C, 2 hrs) is believed to have produce severely under-cured networks and the true thermomechanical response was not believed to be conveyed. Furthermore, little information on AEK solubility in the epoxy prepolymer exists, as both literature accounts report the use of solvent to reduce viscosity and adequately mix the blends. The few reports that exist for AEK-networks suggest promising material attributes, but further exploration into processability, network formation, and thermomechanical stability is required to employ these as composite matrix materials.
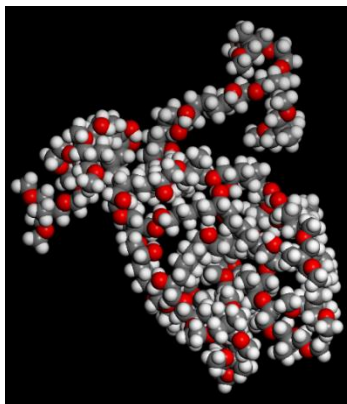
Figure 5. Space-filling model representative of the compact, globular nature of hyperbranched polymers.

Hyperbranched Polymer Modified Epoxy Networks

      Another potential route to developing networks with distortional capability is through the use of hyperbranched polymers. Represented in Figure 5, hyperbranched polymers were first theorized by Flory[57] in 1952 and then later realized in 1988 by Kim and Webster who synthesized hyperbranched poly(phenylene)s from the Suzuki-coupling of AB_2 monomers.[58] Hyperbranched polymers are part of a class of highly branched polymer architectures similar to the perfectly structured dendrimer. These highly branched materials have complex and imperfect structures with degrees of branching greater than one, but have desirable properties are similar to those of their perfect relatives. These properties include compact structure, low degree of entanglement, tunable flexibility, numerous chain-ends and functionality, and Newtonian behavior.[59,60] However, unlike dendrimers hyperbranched polymers are industrially-viable materials due to their ease of preparation via various synthetic pathways, which are commonly one- or pseudo-one pot bulk polymerizations.[61–63]
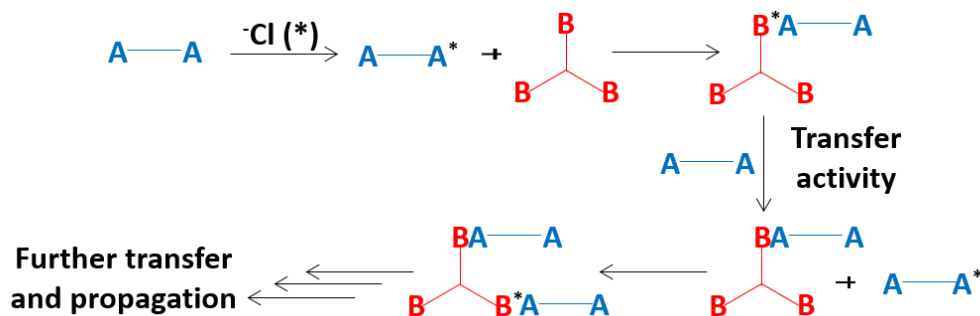
Figure 6. *Proton-transfer polymerization scheme for A_2 and B_3 monomers.*

Although their preparation is far less challenging than that of dendrimers, the reported epoxy-miscible hyperbranched polymers required multiple synthetic steps.[64–66] As one goal of this work is to study industrially relevant materials, a single-pot, bulk polymerization was desired. Frechet *et al* developed one such technique using the so-called proton-transfer polymerization, which is displayed in Figure 6.[63,67] The method involves the transfer of a proton from a nucleophile during each propagation step, creating activated and deactivated sites; the catalytic concentration of activated sites provides a degree of control over the step-growth polymerization and allows use of multiple monomer types such as AB_{n+1} and A_2+B_3. In the case of diepoxide monomers, the activated nucleophile can attack and ring-open the epoxide to generate a secondary hydroxy-anion. Through the thermodynamically driven proton-transfer, the anion is converted to a hydroxyl and deactivated, allowing for further propagation from a newly produced nucleophile. Using the proton-transfer technique, epoxide-functional and network-miscible hyperbranched polymers can be synthesized using the correct stoichiometric ratio of diepoxide A_2 monomers and trihydroxy B_3 monomers.

The highly branched backbone structure, functionality, and low viscosity-to-molecular weight ratios have led to the use of hyperbranched polymers as novel epoxy

tougheners. Compared to traditional tougheners like rubbers and high performance thermoplastics, the unique architectures of hyperbranched polymers provide improved toughness without reducing processability.[68] Furthermore, due to their easily tailored structure hyperbranched polymers can be tuned to influence thermal and mechanical properties of the cured epoxy networks, and many different chemistries have been explored.[69–71] Commercially available hyperbranched aliphatic polyesters such as Boltron[TM] have been the overwhelming focus of study due to their differing molecular weights and functionalities.[60] In multiple reports, hydroxyl-functional hyperbranched-esters have been shown to increase fracture toughness by over 100%.[72–74] Conversely, the hydroxyl-functionalized hyperbranched-esters tend to phase-separate upon curing, leading to the reduction of other critical properties such as glass transition and modulus.[74–76]

One method to provide enhancement in both thermomechanical and fracture resistance (aka distortion) properties is through use of fully miscible hyperbranched materials, but most available hyperbranched polymers are plagued by reaction–induced phase-separation. Mezzenga and coworkers found that improved miscibility after cure was obtained by using low molecular weight, epoxide-functionalized hyperbranched polyesters, although the cured network's T_g and modulus were both reduced.[77] Tang *et al.* found that hyperbranched polyurethanes could be incorporated into an anhydride-cured epoxy network as a homogenous additive with no phase separation. Impact strength of the hyperbranched-modified networks was improved but T_g and modulus were negatively affected; and, due to the network-level urethane incorporation, they described the fracture improvement mechanism as "*in-situ* toughening".[64] Miao and coworkers synthesized

novel epoxide-functional hyperbranched polymers based on poly(ethersulfone) that were soluble in an aliphatic amine-cured epoxy network and showed improved thermal, mechanical, and fracture-resistance properties.[65,66] However, it is this authors belief that the improvement in thermal and mechanical properties (ie. T_g and modulus), can be solely attributed to the increase in aromaticity over the flexible aliphatic-cured network, and not to the hyperbranched polymer itself. To date, *in situ* toughness and distortional improvement of fully aromatic epoxy-amine networks has not been realized from hyperbranched polymers and remains a significant challenge.

POSS-Epoxy Nanocomposites

Another way to manipulate the distortional properties of composite matrices is through the use of the hybrid, inorganic-organic nanoparticle polyhedral oligomeric silsesquioxane (POSS). POSS, who's most basic structure is shown in Figure 7, is a silicon-oxide cage with organic functional groups at each silicon vertex. Previous molecular modeling work from the Wiggins Research Group and The Boeing Company has shown that incorporation of POSS into epoxy networks as pendant-moieties provides additional molecular motions and relaxations that can improve von Mises strain. The improved distortional-capability comes with the caveat that POSS molecules are distributed on the nano-scale throughout the network, but molecular dispersion of POSS is still a substantial challenge.

Synthesis and dispersion difficulties of POSS-epoxy networks arise from the large surface areas and strong intermolecular interactions of nanoparticles.[78] One promising method to break the intermolecular attractions is to react POSS into the network. The most common approach is through the use of multifunctional POSS units.[79–84] The

commercially available octepoxide-POSS produces readily miscible POSS-epoxy blends which when reacted, create POSS-junction points with network-level incorporation. However, systems reported with this type of architecture were stiff and brittle due to increased crosslink density brought about from the increased POSS functionality. Furthermore, the distortional mechanisms observed in modeling could not be realized with this type of architecture.
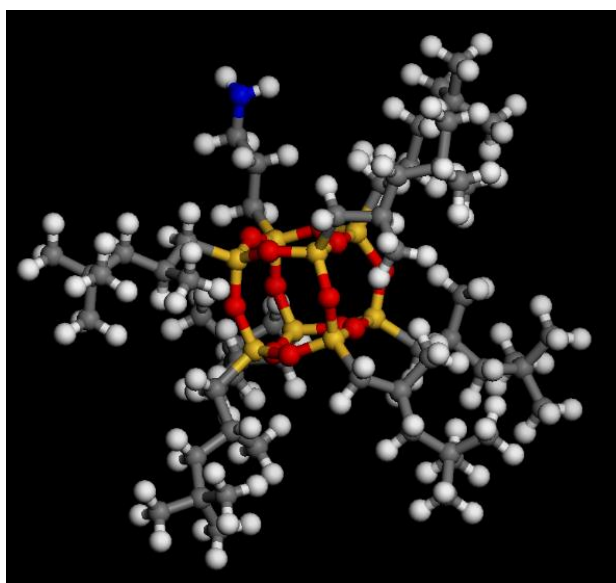
Figure 7. 3D-model of amino-isooctyl-POSS structure as example of the tailorablility of organic R-functionality.

To achieve the observed strain-capability pendant-POSS must be dispersed throughout the network. Pendant POSS-epoxy networks are formed through the use of monofunctional POSS, which has one reactive functional group and seven nonreactive substituents. Contrary to octafunctional POSS, monofunctional cages have the propensity to aggregate and form various size-scale, phase-separated crystallites.[81,85,86] Even when reacted into the network pendant POSS moieties can aggregate due to their lower

crosslink density.[87] Several groups have shown that pre-reacting the POSS-moiety before curing into the network provides improved nanoparticle stabilization and dispersion. Zucchi *et al* showed improved dispersion of POSS by pre-reacting epoxide-functional POSS with the primary amine curative in the melt.[88] Liu and coworkers used a similar procedure and found that high mass fractions (~50%) of POSS could be dispersed showed through pre-reaction. Zucchi and Liu's methods likely produced large fractions of oligomers which could be detrimental to the cured network properties. Frank of the Wiggins Research Group found that mono-amine functional POSS could be pre-reacted with DGEBA in THF to provide mainly DGEBA-POSS-DGEBA trimer which allowed for good molecular-level dispersion.[87] However, in the previous work some aggregation occurs and complete molecular-level dispersion of pendant-POSS has not been achieved.

Although the dispersion of POSS nanoparticles has proven challenging, the nanoparticles have still found use as epoxy-network thermal and mechanical modifiers.[78] Due to POSS's hybrid inorganic-organic structure, there exists an added layer of complexity when understanding the nanocomposite structure-property-relationships, and engineering properties depend largely on POSS concentration, dispersion state, and matrix interaction. POSS can plasticize or fortify a network by either creating of filling free volume, thus influencing modulus and T_g.[82,85,89] However, higher POSS concentrations have been shown to increase POSS-POSS and POSS-network physical interactions and therefore can affect volume in unpredictable ways.[83,87,89,90] The strong property dependence on concentration and secondary interactions makes for challenging prediction of POSS-epoxy structure-property-relationships. Furthering the

comprehension of POSS nanocomposite relationships will help determine the applicability of POSS as a distortional modifier.

Research Overview

This work focuses on the structure-property-relationships of multifunctional epoxy-amine networks in an effort to improve the distortional properties of carbon-fiber composites used in aerospace applications. It is the purpose of this dissertation to investigate molecular-level characteristics that permit concomitant improvements in strength, strain-capability and use-temperature modulus in epoxy-amine networks. The foremost characteristics studied include, but are not limited to, chemical composition, network architecture, and secondary interactions. Two different approaches were investigated: the first method comprised study of novel aryl-ether-ketone diamine-curatives, and the second approach entailed network blending and modification with an epoxide functional hyperbranched polymer.

The specific findings of this research are presented in seven subsequent chapters and include the following objectives:

1. Synthesize and characterize network-precursors and modifiers employed throughout this dissertation.

2. Investigate molecular architecture, thermal, and mechanical properties of multifunctional epoxy networks cured with three aryl-ether-ketone diamines with varied molecular weights.

3. Simulate and characterize physical attributes of aryl-ether-ketone networks to understand molecular mechanisms involved in deformation.

4. Copolymerize aryl-ether-ketone amines at low concentrations with 4,4'-diaminodiphenylsulfone in multifunctional networks to further study effects of conversion, crosslink density, and molecular weight on mechanical properties.

5. Examine thermal and mechanical property effects on aromatic epoxy network modification through use of an aliphatic hyperbranched epoxy polymer.

6. Determine the morphological and physical characteristics of an aromatic epoxy nanocomposite modified by POSS-functionalized hyperbranched epoxy polymer.

7. Manufacture, fabricate, and test POSS-hyperbranched epoxy nanocomposite matrix materials in carbon-fiber reinforced composites for distortional capability.

CHAPTER II

EXPERIMENTAL

Materials

The chemicals used herein were purchased from either Sigma Aldrich or Fischer

Scientific chemical companies and were used as received unless otherwise stated.

Macrocyclic Oligomer Synthesis and Polymerizations

The following materials were used throughout the synthesis and polymerization of

macrocylic oligomers: 4,4'-difluorobenzophenone (97%), 1,2-dihydroxybenzene

(catechol, 98%), potassium carbonate (K_2CO_3, anhydrous), cesium fluoride (CsF,

anhydrous, 99%), dichloromethane (DCM, 99%), dimethylacetamide (99%), toluene

(anhydrous, 99.8%), methanol (MeOH, 98%), and tetrahydrofuran (THF, 98%). Catechol

was recrystallized in toluene before use. Representative structures for cyclic oligomers

and respective polymers studied herein are below:
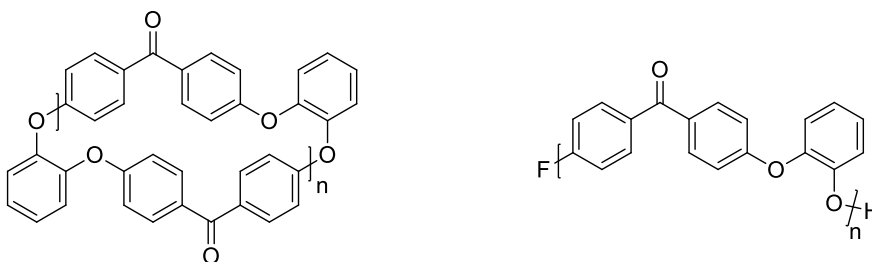
Figure 8. Representative oPEEK chemical structures: (left) cyclic oligomer, (right) single polymer repeat unit and end group.

Synthesis of Aryletherketone Epoxy and Amine Monomers

Along with several materials from the previous section, the following chemicals

were used throughout the preparation of aryletherketone epoxy and amine monomers: 1-

chloro-2,3-epoxypropane (epichlorohydrin, 99%), 1,4-dihydroxybenzene (hydroquinone,

99%), HCl solution (1 M), benzyltrimethylammonium chloride (BTMAC, 97%), *N*-Methyl-2-pyrrolidone (NMP, 97%), 4-aminophenol (99%), 1,3-phenylenebis((4-fluorophenyl)methanone) (97%), aluminum trichloride (AlCl$_3$, anhydrous, 99%), dichloromethane (DCM), diphenylether (99%), 4-fluorobenzoyl chloride (4FBC), sodium hydroxide (NaOH, anhydrous, 97%), and sodium carbonate (NaCO$_3$, anhydrous, 99.5%). The prepared epoxy monomer and amine curatives are presented below in their 2D structures:
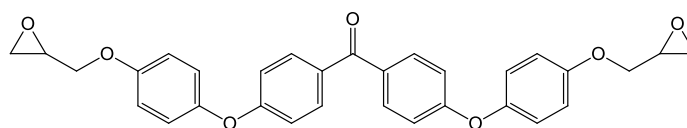
Figure 9. AEK epoxy, DGEEK, chemical structure without chain extension.
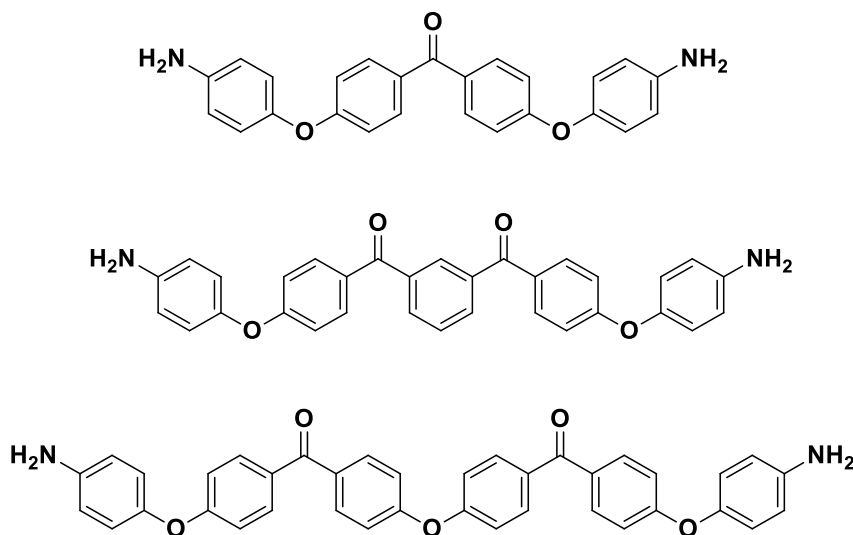
Figure 10. AEK amine-curative chemical structures; (top) 4RA, (middle) 5RA, (bottom) 6RA.

Hyperbranched Epoxy Polymerization and POSS-Functionalization

The materials used in preparation of hyperbranched, epoxide-functional polymers are listed herein: 1, 2, 7, 8-diepoxyoctane (DEO, 97%), 1,1,1-tris(hydroxymethyl)ethane

(THME, 99%), tetrabutylammonium chloride (TBAC, 97%), and MgSO$_4$ (99%) were stored in a desiccation chamber until use. Functionalization of the polymer required the following material: aminopropyl iso-octyl (POSS, 97%), polyoligomericsilsesquioxane which was provided by Hybrid Plastics, Inc. and stored in a freezer at 0 °C. Below are representative structures of the hyperbranched epoxy and POSS:
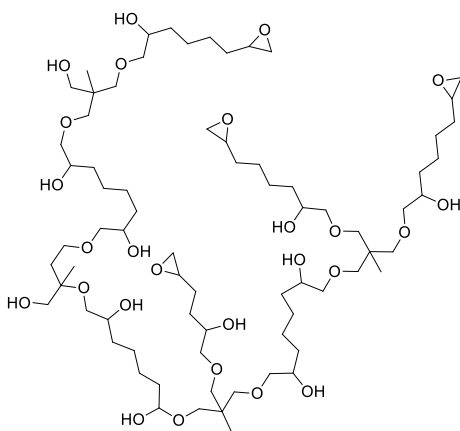
Figure 11. Representative epoxide-functional hyperbranched polymer structure.
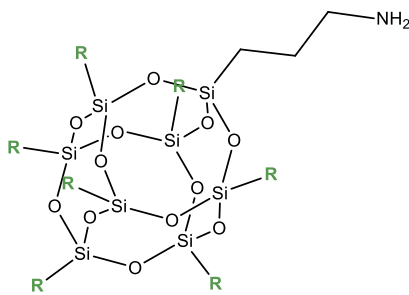
Figure 12. Primary-amine functional POSS; R-group = iso-octyl

Epoxy Network Synthesis

Diglycidyl ether of bisphenol-A (DGEBA, EPON825, EEW=177.5, Momentive), N,N,N',N'-tetraglycidyl-4,4'-diaminodiphenylmethane (TGDDM, MY721, EEW=113, Huntsman), 3,3'-diaminodiphenylsulfone (33DDS, Royce Chemical Corp., 99%, 4 μm

particle size), and 4,4'-diaminodiphenylsulfone (44DDS, Royce Chemical Corp., 99%, 4 μm particle size) were used as epoxies and hardeners during network preparation. Their chemical structures are shown below in non-chain-extended forms.
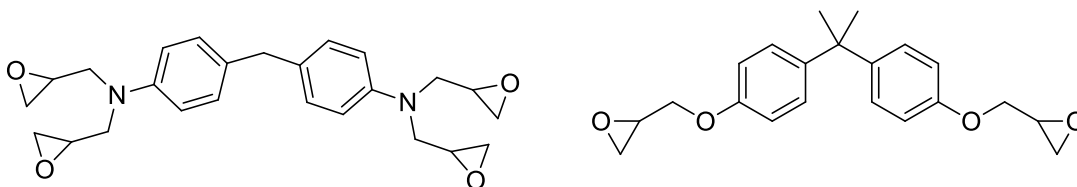
Figure 13. Monomeric epoxies used during studies; (left) TGDDM, (right) DGEBA
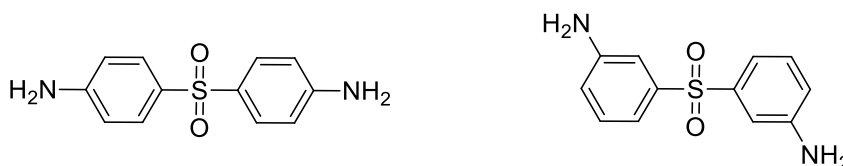
Figure 14. DDS curative structures; (left) 44DDS, (right) 33DDS.

Sample Preparation

Epoxy Cured by Aryletherketone Amines

Epoxy networks were formulated using aryletherketone amines with varying molecular weights. The epoxies were based on TGDDM and were cured in a 1:1 stoichiometric ratio of oxirane to active amino hydrogen. The amine curatives all have elevated melt temperatures and were not easily solubilized into the epoxy due to their high solids content and large particle sizes. Therefore 30-40 gram formulations were pre-mixed at room temperature using a high shear Braebender Plasticorder twin screw mixer. After mixing, liquid nitrogen was used to bring the formulations below T_g and were then scraped from the mixer. The amine particle size was reduced from 1 mm to less than 10 μm.

The premixed blends were then spread over a large surface area of Teflon, heated to 80-90 °C and degassed in a vacuum oven. After degassing and cooling to room temperature the mixtures were hand-pressed into specified molds and either cured in an oven or compression fixture, or frozen for later study. Uncured resin was utilized for DSC cure studies. DMA and compression samples were cured using two different cure prescriptions (Industrial Cure or Post Cure), while PALS samples were driven to high conversion using only the Post Cure. During the Industrial Cure, samples are ramped at 1 °C/min from 120-180 °C and isothermed at 180 °C for 3 hours, and the Post Cure adds an additional step which ramps at 1 °C/min from 180-225 °C and isotherms for 2 hours more at 225 °C. All AEK-cured samples are listed in Table 2. It should also be noted that, to obtain high quality test specimens of 6RA formulations, compression molding at 220 °C and 1000 psi was required, but no mechanical test specimens were produced.

Epoxy Cured by Hybrid-Amines

TGDDM-epoxy networks were also formed by use of dual amine-curatives of DDS and either 4RA or 5RA. The network formulations can be found in Table 3. Mixing and casting of samples was performed using the procedures described for other AEK-epoxy networks.

Table 2

AEK-Amine Curative Formulations and Cure Prescriptions (Chapter IV and V)

Sample Name	Curative Name	Amine (grams)	TGDDM (grams)	Molding Method	Cure Prescription
Neat-IC	DDS	18.5	31.5	Oven	3 hr, 180 °C
Neat-PC	DDS	18.5	31.5	Oven	3 hr, 180 °C,
					2 hr, 225 °C
4RA-IC	4RA	24.4	26.0	Oven	3 hr, 180 °C
4RA-PC	4RA	24.4	26.0	Oven	3 hr, 180 °C,
					2 hr, 225 °C
5RA-IC	5RA	27.3	23.0	Oven	3 hr, 180 °C
5RA-PC	5RA	27.3	23.0	Oven	3 hr, 180 °C,
					2 hr, 225 °C
6RA-IC	6RA	29.4	21.0	Compression	1.5 hr, 220 °C
6RA-PC	6RA	29.4	21.0	Oven	1.5 hr, 220 °C,
					2 hr, 25 °C

Table 3

Hybrid, dual-curative epoxy network formulations using DDS and AEKs (Chapter VI)

Sample Name	DDS mol%	AEK mol%	DDS Mass grams	AEK Mass grams	TGDDM Mass grams
5-4RA	95	5	17.6	1.5	31.6
10-4RA	90	10	16.4	2.9	31.0
25-4RA	75	25	13.2	7.1	30.0
5-5RA	95	5	17.9	1.9	32.0
10-5RA	90	10	15.9	3.6	30.0
25-5RA	75	25	12.6	8.4	28.5

HBE-DGEBA Blends Cured with 33DDS

Hyperbranched-modified networks were formulated using weight ratios of 0:100, 5:95, 10:90, 15:85, and 20:80 of HBE and DGEBA respectively. All blends were cured using 33DDS in a 1:1 stoichiometric equivalence of active amino-hydrogen to oxirane units. In a typical reaction, using 10 wt% as an example, 5.0 grams (1.2 mmol) of HBE and 32.9 grams (93.3 mmol) DGEBA were mechanically stirred and degassed under vacuum at 90 °C for 1 hour. The epoxy blend was then mixed with 12.9 grams (51.9 mmol) of 33DDS and heated at 5 °C every 5 minutes until 110° C where it was then held until the formulation was fully degassed and the hardener had completely dissolved. Immediately after dissolution the mixtures were poured into preheated silicone molds (110 °C) and cured in an oven heated from 110 °C at 1 °C/min to 180 °C and held isothermally for 3 hours. Table 4 contains representative HBE formulations.

Table 4

HBE-modified network formulations (Chapter VII)

Sample Name	HBE wt%	DGEBA wt%	33DDS wt%	Total Mass grams
Neat	0	73	27	20.00
5HBE	5	68	26	20.15
10HBE	10	65	25	20.30
15HBE	15	60.5	24.5	20.46
20HBE	20	57	23	20.61

POSS-HBE-DGEBA Blends Cured with 33DDS

POSS-HBE epoxy networks were formulated using DGEBA, 33DDS, and POSS-HBE product mixture, and all blends were cured using a 1:1 stoichiometric equivalence of active amino-hydrogen to oxirane units. Table 5 illustrates representative formulations. A typical reaction with 10 wt% HBE and 1 wt% POSS pre-reaction product is as follows: 31.03 g of DGEBA and 7.49 g of POSS-HBE mixture were combined to a 1-neck, round-bottom flask, heated to 80 °C and stirred. The epoxy/POSS mixture was degassed for 1 hour, after which 12.11 g of 33DDS was slowly added while stirring. The formulation was then heated at 5 °C every 5 minutes until 110 °C where it was held until the formulation was fully degassed and the hardener had completely dissolved. Immediately after dissolution the mixtures were poured into preheated silicone molds and cured in an oven heated from 110 °C at 1 °C/min to 180 °C and held isothermally for 3 hours. Cured samples containing 1 wt% POSS were optically transparent, while 5 wt% epoxies were partially translucent.

Table 5

POSS-HBE modified network formulations (Chapter VIII)

Sample Name	HBE wt%	POSS wt%	DGEBA wt%	33DDS wt%
Neat	0	0	73	27
10H	10	0	65	25
1P-10H	10	1	64	25
5P-10H	10	5	61	24

POSS-HBE-Epoxy Formulation and B-Staging

To manufacture 80-100 feet of 6 inch wide aerospace-grade prepreg, approximately 500 g of matrix prepolymer formulation is required. The following is a general procedure used for all formulations. First, dissolution of the curative and the mixing of the components was performed within a 4-neck, 500 mL glass reactor equipped with an overhead mechanical stirrer, thermometer, and vacuum port. All components, including 33DDS, DGEBA, and HBE modifiers, were hand mixed before applying heat. The mixture was then stirred at 150 RPM and heated to 80 °C before starting the vacuum, which was applied slowly to mitigate "bumping". After full vacuum was achieved, the resin was heated at a rate of 5 °C/5 minutes until complete dissolution of the amine, which was at approximately 115 °C. After dissolution, the mixture was held at 115 °C until the viscosity was between 200-350 poise (verified by Brookfield viscometer), which occurred after 40-50 minutes. The formulations were then quenched to room temperature by pouring onto release film, vacuum sealed into a secondary plastic bag, and frozen for later filming. Table 6 shows the final formulation information.

Table 6

Formulations used during prepregging and composites testing (Chapter IX)

Sample Name	DGEBA wt%	HBE wt%	POSS wt%	33DDS wt%	Total Mass grams	η^1 Pa*s
Neat	73	0	0	27	775	315
10H	65	10	0	25	754	499
1P-10H	64	10	1	25	534	270

[1]: η, apparent viscosity from Brookfield viscometer

Filming and Prepregging of HBE Formulations

Top and bottom films of DGEBA/33DDS, DGEBA-HBE/33DDS, and DGEBA-POSS-HBE/33DDS were produced on a knife-and-plate coater to produce 37-39 grams per square meter (GSM) films for later prepregging. Resin was sealed into a vacuum bag and heated in an 80 °C water bath. The warmed pre-polymer formulation was then poured onto the coater plate which was also heated at 80 °C and had a coater knife height and width of 0.015" and 7" respectively. The bottom release paper was pulled under the coater knife/prepolymer and was met after by the top release paper just before the first nip-roller. The film was pulled along the line without pressure from the nip rollers until the chiller plate (0 °C), where it was quenched before placing onto "take-up" rolls.

Fabrication and Manufacture of HBE Composite Specimens

Composite test specimens were fabricated according to both Boeing and ASTM standard procedures. Lay-up of the composite panels was performed by hand using the prepregs described above. A 30" x 50" aluminum tool was coated with Frekote® 700-NC and allowed to dry overnight. Next, cork strips were adhered to and spaced around the

tool to create twelve 6" x 12" pockets for each panel. Then a 6" x 12" sheet of FEP

release film was placed into the pocket and held in place by high-temperature tape. The

prepreg was thawed overnight at room temperature and then cut using a razor and plastic

template into 6" x 12" sheets. The panels were debulked under vacuum for 15 minutes by

use of thick, reusable nylon bagging film after every four plies. After lay-up and

debulking were complete, polished aluminum caul plates were placed on the ply stack

and the tool was sealed with high-temperature bagging film and tape. One final debulking

step was performed on the panels after transferring them to the autoclave. Table 7

describes each panel which were fabricated from the three materials manufactured.

Curing of the panels was done within an autoclave using the following cure

prescription: ramp temperature at 1.1 °C/min from 25 °C – 180 °C and hold at 180 °C for

6 hours. The vessel was pressurized at 90 psi with nitrogen and the panels were further

devolatilized under vacuum at a constant 29 inHg throughout the cure. The panels were

then cooled at () °C/min until room temperature and held on the tool overnight. After

removing the panels from the tool, they were cut using a silicon-carbide precision saw.

The saw's backstop was set to the correct coupon width and the specimens were cut using

a feed rate of 5 mm/min and a saw speed of 5000 RPMs. Table 8 describes the final

coupon dimensions and trim angles.

After the coupons were cut, they were prepared for testing by first degreasing

with acetone and isopropanol. Interlaminar fracture toughness samples, or G_{1C}, were

prepared using ASTM D5528 by bonding steel piano-hinges to the pre-cracked end of the

coupons. The substrate area was roughed using 80-grit sand paper and then thoroughly

cleaned with acetone and isopropanol. The hinges were then bonded on at room

temperature and left to cure for 5-days before testing. Off-axis, 10° coupons were tested without tabbing due to their increased ply-count and thickness.

Table 7

Laminate lay-up sequences and information (Chapter IX)

Materials	Layup	Sequence	Top Surface
DGEBA/33DDS	Uni-10°	$[0]_{24}$	Caul
DGEBA/33DDS	Uni-G_{1C}	$[0]_{26}$, Mid-Plane FEP	Caul
10%HBE	Uni-10°	$[0]_{24}$	Caul
10%HBE	Uni-G_{1C}	$[0]_{26}$, Mid-Plane FEP	Caul
1%POSS-10%HBE	Uni-10°	$[0]_{24}$	Caul
1%POSS-10%HBE	Uni-G_{1C}	$[0]_{26}$, Mid-Plane FEP	Caul

Table 8

Composite Test Specimen Trim Data (Chapter IX)

Sample Name	Layup Identifier	Length mm	Width mm	Thickness mm	Trim Notes
DGEBA/33DDS	Uni-10°	254	18.91	3.49	Cut on 10°
DGEBA/33DDS	Uni-G_{1C}	254	25.35	3.65	Cut on 0°, FEP
10%HBE	Uni-10°	254	18.94	3.54	Cut on 10°
10%HBE	Uni-G_{1C}	254	25.43	3.72	Cut on 0°, FEP
1%POSS-10%HBE	Uni-10°	254	19.08	3.48	Cut on 10°
1%POSS-10%HBE	Uni-G_{1C}	254	25.41	3.65	Cut on 0°, FEP

Characterization

Proton Nuclear Resonance Spectroscopy (^{1}H-NMR)

Unless noted otherwise, proton spectra of all synthesized products were obtained using a Varian Mercury spectrometer at 300 MHz. d_6-DMSO, $CDCl_3$ and trimethylsilane were used as solvents and reference respectively.

Size Exclusion Chromatography (SEC)

Molecular weights (M_n and M_w) of the AEK monomers, oligomers, and polymers, as well as the HBE and POSS-modified HBE were characterized by SEC using a TOSOH Bioscience EcoSEC HLC-8329 gel permeation chromatography system. THF and polystyrene were used as the eluent and standard respectively. The eluents were monitored using a UV and refractive index detector.

Static Light Scattering (SLS)

Hydrodynamic radius was calculated from static light scattering using an incident light of 633 nm from a Spectra Physics Model 127 HeNe laser operating at 40 mW and a Brookhaven Instruments BI200SM goniometer with an avalanche photodiode detector and TurboCorr correlator.

Epoxide Equivalent Weight Titrations (EEW)

Epoxide equivalent weight (EEW) of HBE was measured by manual titration of samples per ASTMD1652-11.[91] The hyperbranched resin was dissolved in THF and titrated directly with hydrogen bromide in glacial acetic acid. The initially clear solution remained green during titration and had an end-point of a faint green-to-blue transition.

Attenuated Total Reflectance Infrared Spectroscopy (ATR-IR)

Mid-IR spectra were recorded for AEK amine curatives and cured HBE-modified networks using a Thermo Scientific Nicolet 6700 FT-IR in the range 750-4000 cm^{-1}. An IR light source was used in conjunction with a KBr beam splitter and a DTGS KBr detector. To ensure proper measurement of HBE-network hydroxyl-moieties, cured samples were dried at 100 °C for 2 hours and then placed on the surface of a diamond crystal and held by an ATR accessory while acquiring 64 scans at 4 cm^{-1}.

Differential Scanning Calorimetry (DSC)

DSC was performed on cured and uncured epoxy samples using a TA Instruments Q2000 DSC. Samples were prepared by sealing 5-10 mg of material in a hermetic aluminum pan. Testing of uncured epoxy material was conducted using nonisothermal protocol. The temperature was ramped from 40 °C to 350 °C at rates of 1, 5, 10, and 20 °C/min. The total heat of the cure reaction (H_T) was calculated from the area under the exotherm curve in the DSC scan. Isoconversional analysis using Flynn-Wall-Ozawa methods was applied to the exotherm data to determine activation energy as a function of conversion. Cured samples were tested from 40 °C to 250 °C to 40 °C twice at a heating rate of 10 °C/min. Residual cure reaction heat, H_C, was measured by integration of the exothermic peak after an Industrial Cure profile. Degree of cure, DOC, was then calculated using the following relationship,

$$DOC = \frac{H_C}{H_T} * 100$$

where H_C and H_T are from the cured and uncured DSC specimens, respectively.

Dynamic Mechanical Analysis (DMA)

Dynamic mechanical properties were measured using a TA Instruments Q800 DMA equipped with tension clamps. Samples were processed with the following approximate dimensions: length = 14.00-20.00 mm, width = 5.00-5.20 mm, thickness = 1.20-1.40 mm. Depending on the specific formulation, specimens were tested using a temperature ramp from either -110 °C–275 °C (DGEBA-based) or -120 °C–350 °C (TGDDM-based) at a heating rate of 3°C/min, a strain amplitude of 0.05%, and a loading frequency of 1 Hz. Storage modulus and loss tangent (tan δ) were recorded as a function of temperature. Crosslink density was calculated from the rubbery storage modulus, E_R, using the classical theory of rubbery elasticity[92],

$$\nu_e = \frac{E_r}{3RT}$$

where, R is the universal gas constant (8.314 J*mol/K) and T is the temperature at which the rubbery modulus was taken (T_g+30 °C). Using the crosslink density, molecular weight between crosslinks, M_c, were calculated with the following equation,

$$M_c = \frac{\rho}{\nu_e}$$

where ρ is the cured network physical density at room temperature, and ν_e is the rubbery crosslink density.

The time-dependency of tan δ was determined to calculate activation energies for each of its thermally-activated transitions, γ, β, and α. Using a heating rate of 3 °C/min, a temperature range between -120 – 325 °C, and strain amplitude of 0.05%, four different specimens at four specific frequencies (0.1, 1, 10, 100 Hz) were separately analyzed. Peak analysis was performed with Origin 8.0 plotting software.

Positron Annihilation Lifetime Spectroscopy (PALS)

Average free volume hole size and the relative intensity of ortho-positronium (o-Ps) was determined with positron annihilation lifetime spectroscopy (PALS) on a fast-fast coincidence system based on a system described by Jamieson *et. al* [1] with an average resolution FWHM of 290 ps. Sample disks were prepared by the Industrial cure protocol and were approximately 1 cm in diameter and 1 mm in thickness. A foil wrapped Na-22 source was sandwiched between two sample disks, wrapped in PTFE tape and placed between two photomultiplier assemblies, equipped with BF_3 scintillation crystals and aligned coincident to the sample stack. Spectra were collected under a 200 mTorr vacuum, in the temperature range from -40 to 120 °C, at 10 °C intervals, and with 1 h and 10^6 counts at each interval. The cycle was repeated twice to get three spectra at each temperature interval. Spectra were analyzed for three lifetimes and intensities using PATFIT-88 software.{Merging Citations} Assuming spherical holes, the average radius of free volume elements was calculated using[3],

$$\tau_{o-Ps} = 0.5 \left[1 - \frac{R}{R_0} + \frac{1}{2\pi} \sin\left(\frac{2\pi R}{R_0}\right) \right]$$

where τ_{o-Ps} is the lifetime of the long lived o-Ps, R is the radius of the cavity, and R_0 is a constant 1.66 Å. The volume of the spherical hole is calculated as: $<v_h> = \frac{4}{3}\pi R^3$.

Solvent Ingress

Solvent ingress studies of AEK amine-cured networks were conducted using water and MEK. Epoxy samples having mass of approximately 150 mg and thickness of 1.5 mm were conditioned in a vacuum oven for 12 hours at 100 °C prior to measuring initial weights. Dry epoxy specimens were submerged in 15-18 mL of solvent in 20 mL scintillation vials which were then sealed and stored in an incubator at 25 °C. To measure

fluid ingress, samples were periodically removed from solution, patted dry using a

KimWipe®, and weighed to the nearest 0.1 mg. Percent change in mass for each sample

was calculated as follows:

$$\% \; Change \; in \; Mass = \frac{m_w - m_i}{m_i} * 100,$$

where, m_w is the "wet" sample mass and m_i is the initial sample mass.

Network Density

Ambient condition densities for epoxy/amine networks samples were determined

using a XS104 Mettler Toledo microbalance with a density determination feature based

on Archimedes' principle. The measurements were conducted at 21 °C in air and

deionized water with an accuracy of ± 0.002 cm^3/g.

Uniaxial Compression Testing

Uniaxial compression testing was completed according to ASTM D695 using an

MTS Systems Corporation Model 810 servo-hydraulic universal test frame equipped with

a 15 kN load cell. Compression specimens were machined into 20 mm x 10 mm cylinders

with care taken to produce parallel top and bottom faces. The specimens were tested at 25

°C using a displacement controlled test rate of 1.27 mm/min with sampling rate of 10 Hz

until a strain value of 30% was reached. A minimum of five specimens were tested and

averaged to determine compressive yield stress, yield strain, and Young's modulus.

Fracture Toughness Determination

Fracture toughness testing was carried out by employing the single-edge-notch

beam (SENB) method according to ASTM D 5045-99 using an MTS Insight instrument.

A standard-sized notch was milled into the specimen and then a crack was introduced at

the notch-tip by tapping a razor blade with a 2 lb rubber mallet [22]. The tests were

operated with a load cell of 2.5 kN and cross-head speed of 1.30 mm*min-1. For each

test, a minimum of three specimens were used to determine the fracture toughness at

crack initiation, in terms of the critical stress intensity factor, K_{IC}. According to the

standard used, K_{1C} was calculated using,

$$K_{1C} = \frac{6P}{BW} * a^{\frac{1}{2}} * Y$$

where,

$$Y = \frac{1.99 - \frac{a}{W}(1 - \frac{a}{W})(2.15 - 3.93\frac{a}{W} + 2.7(\frac{a}{W})^2)}{(1 + 2\frac{a}{W})(1 - \frac{a}{W})^{3/2}}$$

and P is the applied load, B and W are the specimen thickness and width, and a is the sum

of the lengths of the notch and crack.

Scanning Electron Microscopy (SEM)

The fracture surface morphology of the epoxy samples was examined using an

FEI Quanta 200 SEM. A small section was cut from the fracture surface of a SENB

sample using a mill and then sputter-coated with gold. SEM images were obtained from

the sputtered surfaces under high vacuum by use of conventional secondary electron

imaging conditions with an accelerating voltage of 15 kV. Energy dispersive x-ray

analysis (EDX) was performed to determine the elemental composition of both the bulk

and other microstructural features.

Transmission Electron Microscopy (TEM)

The morphology and particle dispersion of epoxy matrices modified with POSS

and HBE were investigated using a Zeiss 900 transmission electron micro-scope (Carl

Zeiss, Inc., Thornwood,NY) at an accelerating voltage of 50 kV. Samples were cut into

thin (100–150 nm), trapezoidal sections with a Porter-Blum MT-2B ultramicrotome (Ivan

Sorvall, Inc.), using a diamond knife (Micro Star Technologies, Inc.) at room temperature. Sections were collected on a Formvar-coated, 300 mesh copper TEM grid (Electron Microscopy Sciences) and imaged without staining.

Atomic Force Microscopy (AFM)

Quantitative nano-mechanical mapping (QNM) studies were conducted on a Bruker Dimension Icon 3000 scanning probe microscope in tapping mode in a temperature (23 °C) and humidity (50%) controlled room with a standard Veeco RTESP silicon probe (cantilever length, 125 μm; nominal force constant, 40 N/m; and resonance frequency, 350 kHz). Height, phase, and DMT-modulus were collected simultaneously. The DMT-modulus measured in QNM is not an absolute measurement but is based on calibration of the instrument and is therefore used as a means of comparison between the different samples. The image size ranged from 500×500 nm^2 to 5×5 μm^2, while the resolution was held constant at 512×512 data points. One cryo-fractured surface from each formulation was studied and at least three macroscopically separated segments of the surface were analyzed (representative images are shown). All standard image processing techniques were performed using Nanoscope version 5.30 r2 image analysis software.

Laminate Fiber/Resin Ratio

To calculate fiber volume fraction, sample faces orthogonal to the fiber direction were polished using a Buehler EcoMet 300 polisher using the following sequence of steps (see attached spreadsheet). Olympus Stream Essentials software was used in conjunction with an Olympus GX51 Optical Microscope at 100X magnification. Images were separated into the fiber and matrix constituents using a software function based on

Red/Green/Blue (RGB) color intensities. The user manually refines the RGB ranges to ensure complete selection of the chosen constituent (fiber or matrix) across the entire image. Points determined to be the particle and all pixels sharing that RGB intensity are also selected.

Mechanical Testing: POSS-HBE/Carbon Fiber Composites

A number of composite mechanical properties were investigated to evaluate the distortional properties of POSS-HBE composites. Intralaminar distortional properties were tested using 10° off-axis tension specimens while interlaminar (G_{1C}) properties were studied using dual cantilever beam (DCB) specimens. Specimen properties were measured using the linear variable differential transformer of the MTS as well as using digital image correlation.

10° Off-Axis Tension Properties. Stress, strain, and modulus values of the materials under evaluation were obtained using an MTS Landmark universal test frame with a 100 kN load cell. The specimens were loaded under tension at 25 °C using a displacement controlled test rate of 1.27 mm/min with sampling rate of 10 Hz until failure. Care was taken to ensure that no single fiber was between both clamps to prevent failure from occurring at the clamp. Five specimens were tested and averaged to determine failure stress, failure strain, and Young's modulus.

G_{1C} Fracture Toughness. Mode 1 fracture toughness properties were obtained using an MTS Insight 10 equipped with a 500 N load cell according to ASTM D5528-01. Test specimen tabs were gripped in tension and the coupon-end held in a jig. The specimen was pulled at 1.27 mm/min until failure; r-curves were not obtained, only ultimate G_{1C}.

Digital Image Correlation (DIC). Full field strain analysis using digital image correlation was conducted on DCB and 10°-tension specimens using a GOM Optical Measuring Techniques ARAMIS 3D Deformation Analysis System (Trilion Quality Systems). DIC requires specimens to have a non-uniform surface pattern, which is tracked by the ARAMIS software between digital image sets taken during a deformation process. Previous work in the Wiggins Research Group has involved speckle patterns on the glassy polymer network cylinder surfaces created with white and black aerosol paints. A solid white basecoat was first applied and followed by a misted black paint. In the case of high fiber volume carbon fiber laminates, a machined surface of the coupon specimens provides a sufficiently smooth black surface, which can be speckled with a high contrast, stochastic pattern. White aerosol paint was misted onto the specimens in a controlled airflow environment, which created white speckles in the size range of 2-5 pixels.[93] Prior to testing, the capture volume was calibrated using a 25 mm x 20 mm calibration panel provided from the software manufacturer. The calibration procedures performed obtained a resolution deviation of less than 0.03 pixels. Digital gray scale images were captured using two 2M digital CCD cameras equipped with 50mm lenses at a frame (capture) rate of 1 fps, creating a set of two images upon each capture. Images were taken from the start of the mechanical test until specimen failure, and stored for post-test processing and analysis.

A benefit to DIC, as compared to traditional mechanical testing methods, is the ability to perform complex post-test analysis from the images obtained during the test. Before processing and computation of strain, digital images were taken through a series of steps to increase accuracy and decrease computation time. The first step was to define

areas for image processing and strain analysis, effectively reducing image sizes. Due to sample geometry, up to 50% of the captured image area was composed of either sample testing apparatus or background and was excluded from the defined area for processing and strain computation. Facets, defined by pixel size and step length, were generated in grid patterns across the optimized areas of the digital images. Facet size is the true dimension of the defined area in pixels. Step length is the distance between adjacent facet centers, wherein smaller steps have been shown to increased spatial resolution.[94] Upon facet definition, a start point was defined for the initial image set, which was taken at zero deformation. The start point serves as a reference for the software to recreate the initial facet field on subsequent image sets for computation of three-dimensional strains.[95] It is important to note that the start point is not a reference point from which deformation is measured, but rather a reference for creation of the facet field in sequential image sets. During computer computation, the gray scale speckle pattern is tracked within each facet of each image set, as well as from image set to image set. A three-dimensional displacement gradient tensor field is calculated based on the change in facet coordinates with respect to the facet center. Using this displacement field, strain tensors are calculated to create strain distribution profiles capable of displaying major and minor strain as well as X, Y, and Z direction displacements of the specimen during the deformation event.[94,96,97]

Molecular Dynamics Simulations

The computations from this work were performed on an in-house, 96-core, Linux cluster using Materials 7.0 software from Accelrys Inc. (now Biovia). The proprietary COMPASSII forcefield was used in the calculation of all energies and forces. Atom

based cutoffs were used with the "Medium" quality setting. The quality of the simulation is determined by cutoff distance, spline width, buffer width, and relative dielectric. The cutoff distance determines the distance non-bond forces (van der Waals and Coulombic) will be included in the energy summation. The spline width defines the size of the region which non-bond forces are splined from their full value to zero. Buffer width is the distance beyond cutoff at which non-bond interactions are zero. Finally, dielectric constant is adjusted to the permittivity of free space. The "Medium" quality summation sets the cutoff distance to 9.50 Å, the spline width to 1.00 Å, the buffer width to 0.50 Å, and the relative dielectric to 1.00.

Polymer-Network Build Procedure

The most challenging aspect to authentic simulation of polymer network properties is the accurate representation of the crosslinked network. The networks analyzed herein were built using a scripted build-process similar to the crosslinking method of Strachan and coworker.[98] The procedure creates bonds between "reactive" atoms through close-contacts. If no bonds are formed the close-contact distance is increased, and when a set concentration of the reactive atoms have been converted, the network is said to be cured. The general aspects of the employed script's crosslinking simulation procedure are described in the following steps:

1. Modified TGDDM and AEK monomers were created by using the Sketch modulus in Materials Studio Visualizer. Epoxy rings were opened, protons removed and methylenes added to amines, and hydrogens were adjusted. The "reactive" atoms were defined as hydrogens attached to the ultimate carbons on

the adjusted monomers (Figure 15) and were named as R1 (epoxy) and R2 (amine). The geometries of both optimized through energy minimizations.

2. The adjusted monomers were placed into a cubic simulation box with periodic boundary conditions defined by the Amorphous Cell module. 10 amorphous cells were built to a density of 0.01 g/mL using atom based summations at a temperature of 650 K. The cells contained 35-50 of each monomer type which corresponded to approximately 4000 atoms; the stoichiometric ratio was kept at a 1:1 oxiranes to amino-hydrogens ratio. Of the 10 amorphous cell obtained, the three lowest energy cells were chosen for further analysis.
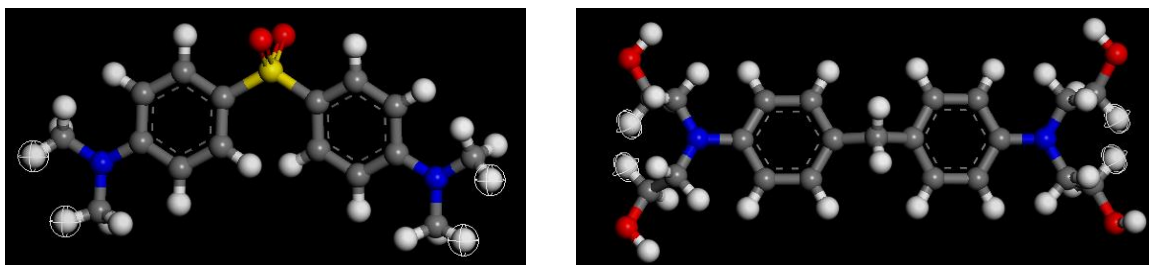
Figure 15. Adjusted DDS and TGDDM monomers showing reactive sites (white cages).

3. A one-time equilibration of the initial, "unreacted" monomer mixture was performed before the crosslinking steps. This equilibration involved sequential NVT and NPT dynamics which were performed at 725 K for 5000 and 2500 ps using the Andersen and Parrinello thermostat and barostats, respectively.

4. Crosslinks were created by forming covalent bonds with labeled groups starting at a close-contact radius of 3.3 Å. If no two proximal groups "reacted" then the contact radius was increased by 0.01 Å. When a favorable distance was reached, reaction occurred to form a bond. Subsequently, the atom labels were changed to

prevent further reaction. This process was repeated until the desired functional group conversion was reached.

5. After obtained the correct conversion, the network structure, or bond angles and lengths, were geometry optimized using a maximum of 500,000 iterations.

6. The final crosslinked network equilibrated through an annealing process to obtain a cell with the correct density and to remove residual stress. The process used NVT and NPT simulations to simultaneously increase temperature from 298 K to 650 K and to increase pressure from atmospheric pressure to 0.1 GPa; the simulation was then run in reverse back to room temperature and atmospheric pressure. After annealing property simulations were performed.

Uniaxial Compression Simulations

Mechanical behavior of the crosslink networks was simulated using a strain controlled approach. A strain controlled simulation process works by reducing the cell size in a specific strain direction. Using a Poisson's ratio determined from a previous set of simulations, the two non-principle axes' sizes are adjusted appropriately. A typical Poisson's ratio for this class of material is 0.35. Unlike experimental compression tests, the simulations cannot be performed in a continuous manner and must instead be performed using a series of discrete intervals. To balance simulation time and data resolution, a strain increment of 0.1% was used. The strain was incremented every seven picoseconds, which results in an effective strain rate of 1.4×10^8 s^{-1}. This process was repeated for all three principle directions (x, y, and z) of the material and averaged. Anisotropy of the polymers is assumed.

CHAPTER III

SYNTHESIS OF ARYL-ETHER-KETONE AND HYPERBRANCHED MONOMERS,

OLIGOMERS, AND POLYMERS

Objective

The objective of this chapter is to describe the synthesis and characterization of

materials employed throughout this work. It is the author's intent to describe the synthetic

parameters, protocols, and purifications used herein so future researchers can easily

follow and replicate these materials. The first section of the chapter is a description of the

synthetic protocols employed during preparation of each material discussed within this

dissertation. Discussion begins with the synthesis and polymerization of aryl-ether-ketone

macrocyclic oligomeric precursors for thermoplastic composites. As the core of the

research presented here is related to epoxy-amine networks, the next section shifts to

describe the results of the synthesis and characterization of aryl-ether-ketone (AEK)

epoxy and amine monomers used in Chapters IV, V, and VI. Finally, the results of the

preparation of hyperbranched epoxy polymer, HBE (Chapter VII, VIII, and IX) and its

subsequent functionalization with the hybrid organic-inorganic cage structure, POSS

(Chapters VIII and IX) is described.

Synthetic Procedures

Synthesis of oPEEK Macrocyclic Oligomers

Macrocyclic oligomers were synthesized via the pseudo-high dilution technique in a 500 mL 3-neck round-bottom flask after distilling 300 mL of DMAc and 50 mL of toluene at 145 °C under nitrogen for five hours to remove water. After cooling the solvent mixture, 115 mL of solution was removed and used to dissolve 4.47 g of 4,4'-difluorobenzophenone (20.5 mmol) and 2.26 g of catechol (20.5 mmol). Potassium carbonate (2.48 g, 18 mmol) was then added to the flask which was returned to the oil bath and reheated to 145 °C with rapid stirring (500-800 RPM). After dissolution the concentrated reagent solution was filtered using a clean fritted filter under vacuum and was sealed into a 200 mL jar blanketed with nitrogen. Once the reaction vessel had come to temperature the reagent solution was added drop-wise using an HPLC pump at a rate of 0.3 mL/min for approximately 5 hours. After the reagents were added, the pump was cleaned with 10 mL of dry DMAc and the reaction temperature was increased to 155 °C. The reaction proceeded for 15 more hours, and after completion was cooled to 50-60 °C. Using a 1 L vacuum-fitted flask and a 600 mL fritted-filter, the potassium salts and insoluble by-products were filtered from the product-mixture. The products were concentrated to ~1/5 the original volume under vacuum using a rotary-evaporator at 20-25 inHg and 45 °C. The product mixture was then slowly precipitated into 1 L of DI water mixed with 20 mL of concentrated HCl by drop-wise addition with a pipette. The cream-colored product was then filtered and washed with water another 3-5 times, or until the pH was neutral. The product was dried *in vacuo* overnight to remove residual water and further purified through methanol-washes. A final vacuum drying step

provided a cream-colored powder. Yield: 70-85 % (4.14-5.03 g); mp: 230 °C, 265 °C;

^{1}H-NMR (400 MHz, CDCl$_3$), ppm: δ = 6.85 (4H, m, aromatic) 7.20 (4H, m, aromatic)

7.65 (4H, m, aromatic); m/z (MALDI-TOF, dithranol) (100% [M + H]$^+$) 577 (dimer), 871

(trimer), 1159 (tetramer), 1448 (pentamer), 1735 (heptamer), 2023 (hexamer), 2311

(octamer), 2600 (nonamer), 2888 (decamer).
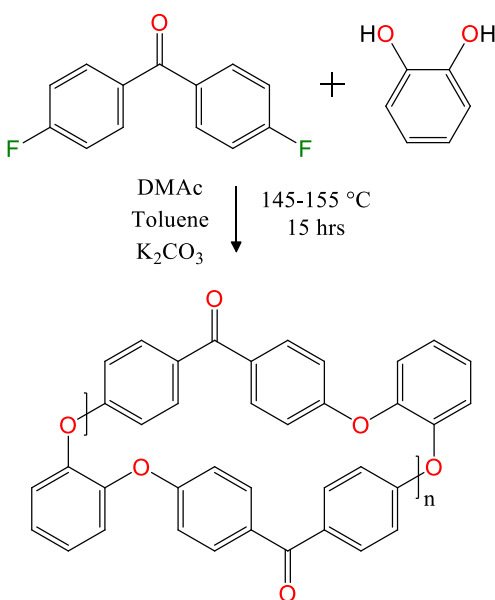
Figure 16. Synthesis of oPEEK macrocyclic oligomers through pseudo-high dilution.

Polymerization of oPEEK Macrocyclic Oligomers

The melt polymerization of oPEEK MCOs was performed using CsF as an

initiator within a DSC and under an inert environment of nitrogen. The MCO/initiator

blends were prepared using the following methods: First a scintillation vial was filled

with nitrogen, sealed, and tared on an analytical balance. The vial was then quickly

placed into a portable, nitrogen-filled glove-box and a small quantity (1-10 mg) of CsF

was sealed into it. The vial was then removed from the glove-box, weighed, and the

previous steps completed until the desired amount of CsF was achieved. After obtaining

the correct CsF concentration, it was dissolved with approximately 1 mL of dry methanol while in the glove box. The quantity oPEEK MCOs was then calculated based on the CsF mass and were weighed separately. The MCOs were then placed into the glove-box, dissolved into dry dichloromethane (~10 mL), and combined with the CsF initiator solution. The solution was then concentrated and dried using rotary-evaporation at 25 inHg and 45 °C for 6 hours. The final mixture was stored in the glove-box until use. Polymerization of the mixtures was performed using 4-8 mg of material that was sealed into a hermetic DSC pan; immediately before the polymerization, a hole was placed in the lid to allow nitrogen to flow through the sample pan. The DSC was then ramped from 30-120 °C at 10 °C/min and held for 5 min to allow the removal of residual volatiles. After the isotherm, the polymerization was ramped at 10 °C/min from 120 °C to the desired polymerization temperature and held for a given period of time. After the polymerization the DSC was cooled at 10 °C/min to 30 °C and then rescanned at 10 °C/min to observe thermal transitions. T_g: 129-132 °C; ^{1}H-NMR (400 MHz, CDCl$_3$), ppm: δ = 6.85 (4H, d, aromatic) 7.25 (4H, m, aromatic) 7.75 (4H, d, aromatic).

Synthesis of 4-{4-[4-(4-hydroxyphenoxy)benzoyl]phenoxy}phenol (4RB)

Charged to a dry, 2 L 4-neck flask fitted with a Dean-Stark trap, condenser, and addition funnel was DMAc (500 mL), toluene (200 mL), 87.9 g (0.79 mol) of hydroquinone, and potassium carbonate (120 g, 0.87 mol). The reaction contents were refluxed at 145 °C for six hours under a nitrogen environment. After distillation 4,4'-difluorobenzophenone (6.5 g, 0.03 mol) in 50 mL of DMAc was added to the vessel via addition funnel. The contents were allowed to equilibrate for 30 minutes and then toluene was removed with the Dean-Stark trap and the reaction temperature was increased to 155

°C; the reaction was allowed to proceed for a further 24 hours. After completion, the flask was cooled to room temperature, salts were filtered, and the product solution was concentrated to approximately 150-200 mL through rotary-evaporation. The rough product was precipitated and neutralized by fast addition to 2 L of DI H_2O and 20 mL of concentrated HCl (1 N). After precipitation the product was filtered and the soluble portion extracted with acetone. Evaporation of the acetone lead to a metallic-brown solid that was washed and recrystallized in hot MeOH to remove excess DMAc. The final product was a cream-colored powder. Yield: 85-95% (10.1-11.2 g); mp: 178 °C; ^{1}H-NMR (300 MHz, CDCl3), ppm: δ = 7.05-7.06 (4H, d, CH, aromatic).
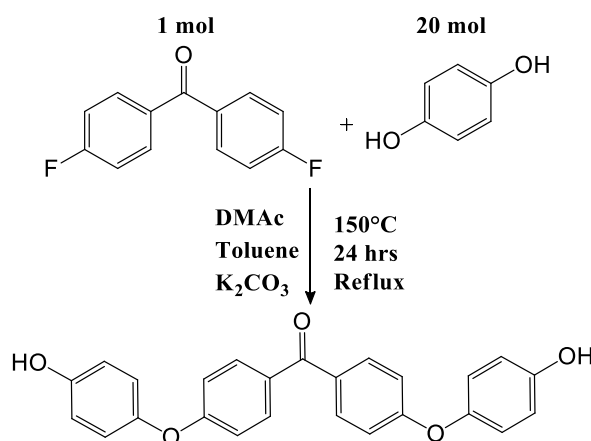
Figure 17. Synthetic scheme of 4RB bisphenol.

Two-step synthesis of 2-[4-(4-{4-[4-(oxiran-2-ylmethoxy) phenoxy] benzoyl} phenoxy) phenoxymethyl] oxirane (DGEEK)

Glycidation of 4RB bisphenol, shown as Figure 18, was performed using a modified method developed in our labs. Immediately after removing from the freezer, 50 mL (0.637 mol) of epichlorohydrin (ECH) was added to a 150 mL 1-neck flask containing 4.60 g (0.012 mol) of 4RKB and a magnetic stirbar. Next 0.132 g of a 30%

solution of the quaternary ammonium catalyst benzyltrimethylammonium chloride in

methanol (BTMAC) was added. The flask was then heated to 70 °C and stirred at 400

RPM; the reaction was allowed to proceed for 25 hours. After cooling, the excess

epichlorohydrin was evaporated at 80 °C under reduced pressure for 2 hours. When the

intermediate product appeared dry, solvent and an alkali solution (Table 12) were added

to the flask which was then heated to 120 °C and stirred at 600 RPM. The biphasic

mixture was allowed to reflux for three hours. While the mixture was still warm the

organic layer was transferred to a separatory funnel and washed with DI H_2O until the pH

was neutral. As the organic mixture cooled the product began to precipitate and the

precipitant and toluene was transferred to a filter and vacuum dried in air overnight. The

product was a cream colored solid. Yield: 96% (5.75 g).
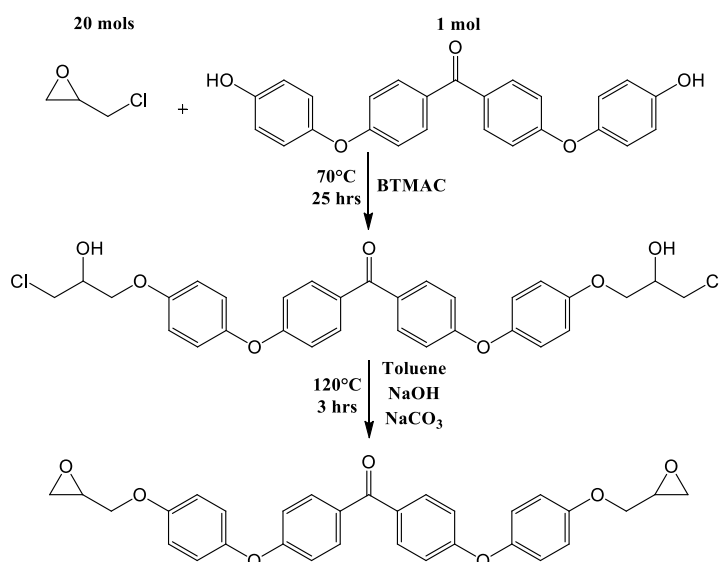
Figure 18. Preparation of DGEEK monomer; structure shown without chain extension.
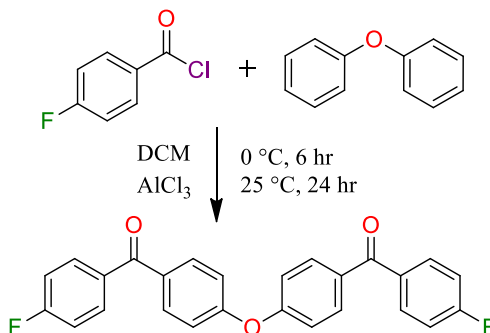
Figure 19. Synthesis of pre6RA through Friedel-Crafts acylation.

Synthesis of oxybis(4,1-phenylene))bis((4-fluorophenyl)methanone (pre6RA)

The precursor material to 6RA was synthesized (Figure 19) using Friedel-Crafts acylation with AlCl$_3$. First, 150 mL of DCM was dried over MgSO$_4$ for 24 hours and then filtered into a 2-neck, 250 mL round-bottom flask equipped with a magnetic stir-bar and nitrogen inlet/outlet. Concurrently, diphenylether was melted in an oven at 40 °C. The flask was placed in an ice-bath after 7.58 g (0.04 mol) of diphenylether and 14.47 g (0.09 mol) 4-fluorobenzoyl chloride were added and was then purged with nitrogen. Next, 14.03 g (0.11 mol) AlCl$_3$ was weighed in an inert environment and quickly added to the reaction vessel to prevent moisture absorption; reaction time was started after promoter addition. The vessel was kept at 0 °C for 6 hours and was then allowed to come to room temperature as the ice melted. After 24 hours, the reaction was quenched and precipitated with 25 mL of concentrated HCl. The solids formed were washed with 100 mL of DI-water 5 times over a fritted filter to remove AlCl$_3$. Finally, the product was washed with acetone and dried under vacuum for 24 hours at 100 °C to leave a white powder. Yield: 82%; mp: 178 °C; ^{1}H-NMR (300 MHz, CDCl$_3$), ppm: δ = 7.05-7.06 (4H, d, CH, aromatic) 7.08-7.12 (4H, d, CH, aromatic) 7.73-7.75 (4H, dd, CH, aromatic) 7.76-7.78 (4H, dd, CH, aromatic).

Synthesis of bis[4-(4-aminophenoxy)phenyl]methanone (4RA) and oxybis(4,1-phenylene))bis((4-(4-aminophenoxy)phenyl)methanone (6RA)

       4RA and 6RA were prepared using the same procedures; the following is an example for 4RA: Synthesis was performed in a 3-neck, 1 L flask under a nitrogen environment. NMP (300 mL) and toluene (150 mL) were added to the reaction vessel and rapid stirring (700 RPM) was initiated, after which 25.4 g K_2CO_3 (0.20 mol) and 20.05 g of 4-aminophenol (0.19 mol) were slowly added to the vessel. When complete the temperature was increased to reflux where trace amounts of water were removed by azeotropic distillation with toluene using a Dean-Stark trap. After 5 hours of distillation, the flask was cooled to room temperature and 20.0 g of DFBP (0.09 mol) in 25 mL of NMP was added via syringe. The temperature was then increased to remove toluene and the reaction was allowed to proceed for 24 hours at 165 °C. After being cooled to room temperature, the solution was precipitated into a 5% NaOH solution, washed twice with 5% NaOH, and then further washed with DI water until neutral. The precipitate was dried overnight on the filter blanketed with N_2 and then dissolved into acetone to remove the residual salt by-products. Acetone was removed via reduced pressure and after, the product was dried *in vacuo* at 100 °C for 12 hours to leave a cream/tan powder.

4RA - Yield: 30.9 g (85%); mp: 152 °C; ^{1}H-NMR (300 MHz, DMSO-d_6), ppm: δ = 5.09 (4H, s, NH$_2$) 6.59-6.62 (4H, d, CH, aromatic) 6.81-6.84 (4H, d, CH, aromatic) 6.91-6.95 (4H, d, CH, aromatic) 7.67-7.70 (4H, d, CH, aromatic).

6RA – Yield: ; mp: 190-210 °C; ^{1}H-NMR (300 MHz, DMSO-d_6), ppm: δ = 5.09 (4H, s, NH$_2$) 6.59-6.62 (4H, d, CH, aromatic) 6.81-6.84 (4H, d, CH, aromatic) 6.91-6.95 (4H, d, CH, aromatic) 7.25-7.35 (4H, d, aromatic), 7.60-7.80 (8H, m, aromatic).

Synthesis of 1,3-phenylenebis((4-(4-aminophenoxy)phenyl)methanone)(5RA)

5RA was synthesized in a 3-neck, 1 L round-bottom flask equipped with a nitrogen inlet/outlet, Dean-Stark trap, and condenser. 500 mL of NMP and 200 mL toluene were added to the flask and magnetic stirring was started. 62.01 g (0.45 mol) of K_2CO_3 and 45.29 g (0.42 mol) of 4-aminphenol were then added and stirring was increased (750 RPM). The reaction vessel was brought to reflux and water was removed from the system by azeotropic distillation with toluene. After 5 hours, the mixture was brought to 100 °C and 1,3-phenylenebis((4-fluorophenyl)methanone) (66.05 g, 0.20 mol) was added. The reaction temperature was increased to 165 °C, toluene was removed via the Dean-Stark trap, and the reaction proceeded for 24 hours. After completion, the mixture was cooled to room temperature and precipitated into a 5% NaOH solution, washed with 5% NaOH twice, and DI water five times on a fritted filter. The precipitate was dried overnight on filter which was blanketed with N_2, and then dissolved into acetone to remove the residual salt. After removing the acetone via reduced pressure the product was dried *in vacuo* at 120 °C for 12 hours to produce a yellow/orange glass. Yield: 81.27 g (79%); T_g (DSC): 75 °C ^{1}H-NMR (300 MHz, DMSO-d_6), ppm: δ = 5.10 (4H, s, NH) 6.59-6.63 (4H, d, CH, aromatic) 6.82-6.85 (4H, d, CH, aromatic) 6.94-6.98 (4H, d, CH, aromatic) 7.67-7.72 (1H, t, CH, aromatic) 7.75-7.79 (4H, d, CH, aromatic) 7.88 (1H, d, CH, aromatic) 7.95-7.97 (2H, d, CH, aromatic).
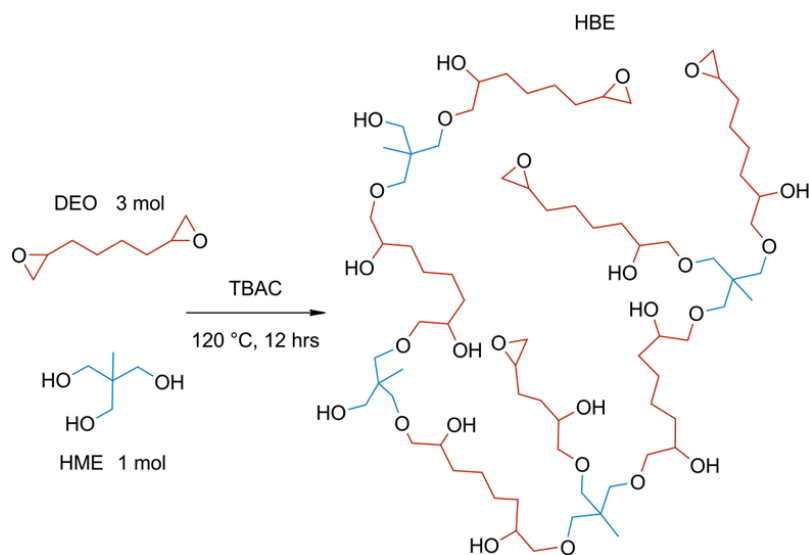
Figure 20. Synthesis and approximate final structure of HBE.

Synthesis of hyperbranched epoxy (HBE)

HBE was synthesized using a modified procedure described by Frechet *et al.*[63]
Typical polymerizations were performed as follows: 1,2,7,8-diepoxyoctane (10.92 g, 76.8
mmol), 1,1,1-Tris(hydroxymethyl)propane (3.08 g, 25.6 mmol) and tetrabutylammonium
chloride (1.07 g, 3.84 mmol), were combined under stirring and heated from room
temperature to 120 °C. After reaching the reaction temperature, the polymerization
proceeded for 12 hours, after which the product was cooled to 50 °C and dissolved in
THF (50 mL). Upon further cooling to room temperature, the product was precipitated
into DI-water (1000 mL), extracted using a separatory funnel, and then dried over $MgSO_4$
in THF. After solvent removal via reduced pressure, the final product was a yellow
viscous liquid. Yield: 12.5 g (90%); ^{1}H-NMR (300 MHz, $CDCl_3$), ppm: δ = 0.85-0.92 (d,
CH_3), 1.42-1.53 (m, branch-CH_2), 2.47 (s, epoxide-CH_2), 2.75 (s, epoxide-CH_2), 2.91 (s,
epoxide-CH), 3.28-3.54 (m, branch-CH/CH_2); T_g (DSC) = -29 °C.
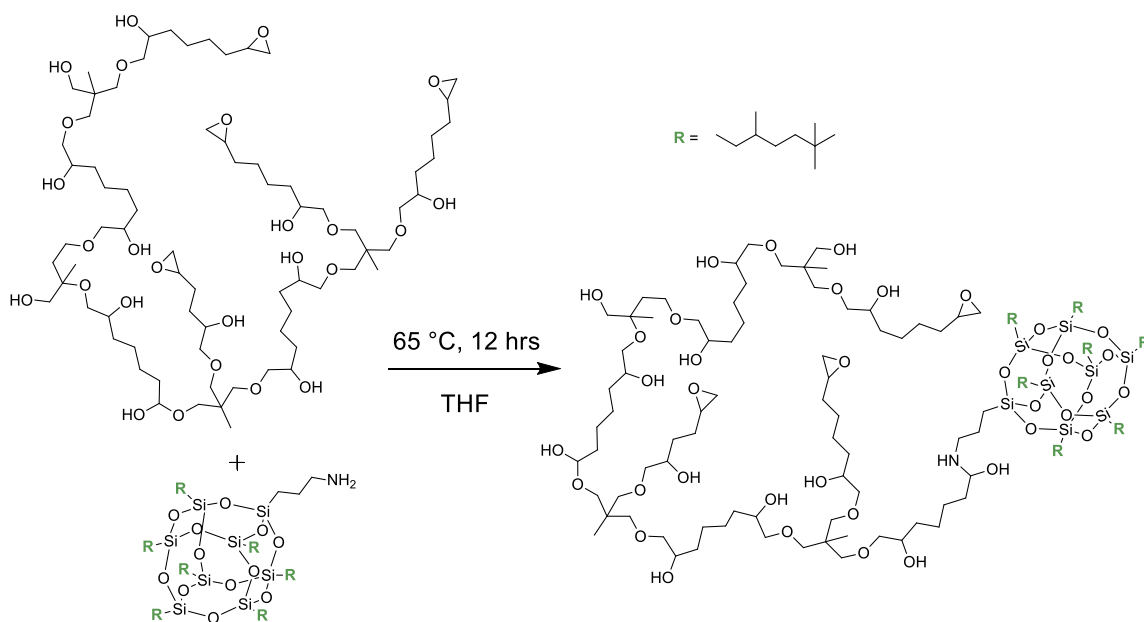
Figure 21. Synthetic scheme of POSS-HBE pre-reaction.

POSS-HBE Pre-Reaction

POSS-modified HBEs were prepared before addition to the epoxy-amine network by reaction of amino-functional-POSS with the epoxide-groups of HBE. To achieve the target POSS concentrations within the final epoxy networks, two different POSS-HBE pre-reactions were performed. An example pre-reaction procedure for 1 wt% POSS is found in Figure 21 and is as follows: Combined in a 100 mL 3-neck round-bottom flask containing a nitrogen inlet, magnetic stirring, and a condenser, was POSS (0.46 g, 0.36 mmol), HBE (4.59 g, 1.12 mmol) and THF (50 mL). Once homogeneous, the solution was heated to 65 °C at which the reaction was continued for 12 hours. After completion, the product was cooled to room temperature while continuing to stir. Once cooled, THF was removed under reduced pressure by rotary evaporation at 40 °C. The product, a viscous cream-colored liquid mixture of POSS-modified HBE, was dried *in vacuo* for 24 hours at room temperature.

Results and Discussion

Macrocyclic Oligomers

oPEEK macrocyclic oligomers were synthesized using the pseudo-high dilution methods developed by Brunelle[99]. A concentrated reagent solution containing catechol and difluorobenzophenone was added drop-wise to a suspension of DMAc, toluene, and potassium carbonate over a period of 5 hours. It was found that to better control the removal of water, and therefore reduce side-reactions, this solution should contain the same concentration of DMAc and toluene as the reaction vessel. Likewise, using the same solvent concentration allowed for better temperature control during the addition stage of synthesis. Removal of water is of the utmost importance when performing high temperature nucleophilic aromatic substitutions with ketone-bearing reagents. It has been shown separately by both Hay and Gibson that use of DMAc can produce an enamine aldol-condensation side-product from the reaction between the equilibrium products of K_2CO_3 and water.[100] After the strong base KOH is formed, hydrolysis of DMAc can occur to produce a carbanion which may react with the ketone. To prevent these side reactions, anhydrous, vacuum dried K_2CO_3 was added to DMAc and toluene after they were dried through azeotropic distillation for at least 5 hours; no aldol-condensation side-products were observed during these syntheses.
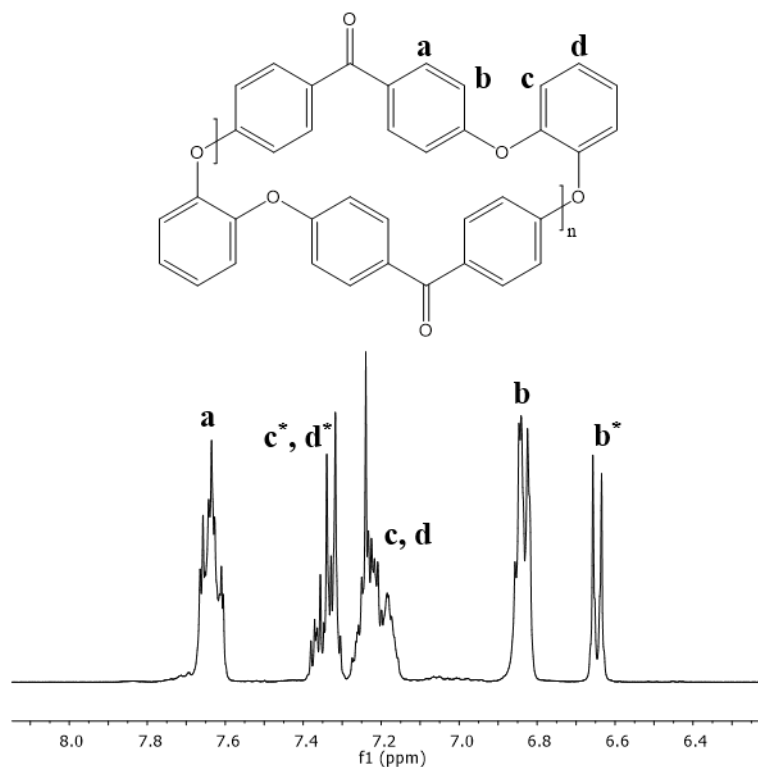
Figure 22. ^{1}H-NMR of oPEEK cyclic oligomers; * indicates cyclic-dimer-specific chemical shifts.

Other reaction parameters were also found to affect the purity of the cyclic product mixture. Due to the easily oxidized catechol, recrystallization before synthesis was found to be an important factor in the formation of cyclic species. Catechol must have a high degree of purity to prevent linear oligomers from forming due to the chain-stopping ability of quinone-like oxidation products. It was therfore hypothesized that air within the reactor would increase oxidation, and nitrogen was both bubbled through and over the reaction solution throughout the entirety of the reactions.

Characterization of MCOs was performed with NMR, GPC, MALDI-TOF, and DSC. The NMR spectrum shown in Figure 22 is characteristic of oPEEK cyclics. Importantly, the spectrum does not show signs of chemical end-groups, signifying a high degree of cyclization. ^{1}H-NMR was the first technique to reveal that the product was a mixture of MCO rings-sizes from the broad, multiplet peaks. This was expected due to the step-growth nature of the reaction. Additionally, the work of Ben-Haida[52] revealed cyclic dimer produces unique chemical shift patterns due to its extremely rigid structure; this was confirmed herein and effects of the cyclic dimer are discussed in subsequent sections.
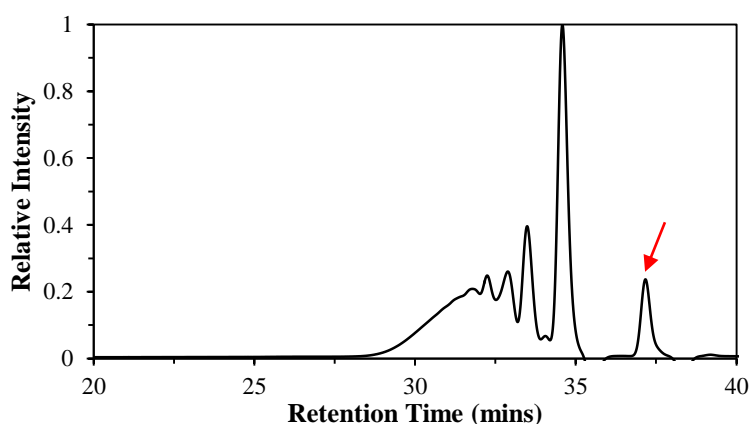
Figure 23. Representative GPC chromatogram of oPEEK MCOs, clearly separated into ring-sizes n=2-5; arrow points at THF solvent peak.

Characterization with GPC and MALDI-TOF (Figure 23 and 24) showed that the MCOs indeed contained many different ring sizes. GPC was able to separate cyclic oligomers between n=2-6 repeat units, but higher molecular weight oligomers appeared as a broad shoulder between 25 and 32 minutes. The chromatograms also provided relative concentrations of each ring-size formed. It was determined that a typical mixture

was composed of 21% dimer, 19% trimer, 15% tetramer, 10% pentamer, 5% hexamer, and 30% higher molecular weight analogues.

MALDI-TOF confirmed the cyclics found with GPC and revealed higher molecular weight oligomers. It was determined that MCOs between n=2-14 existed in the mixture with no observable linear species. Cyclic oligomers above n=6 existed in relatively low concentration, and, interestingly, n=11-14 oPEEK oligomers have not been previously reported.[52] Furthermore, MALDI validated the cyclic dimers's high concentration and that concentration decreases with an increase in repeat-units. This unexpected finding is mainly attributed to the reagent addition rate. Due to the low concentration of end-groups, the cyclic linking reactions are kinetically favored and occur quickly when the reagents are added to the reactor. The slow addition rate forces end-group concentration to remain low during addition, and therefore cyclization can occur with lower molecular weight oligomers.[99] This combination of reagent addition rate and reactor concentration provided the conditions for the favorable formation of cyclic dimer.
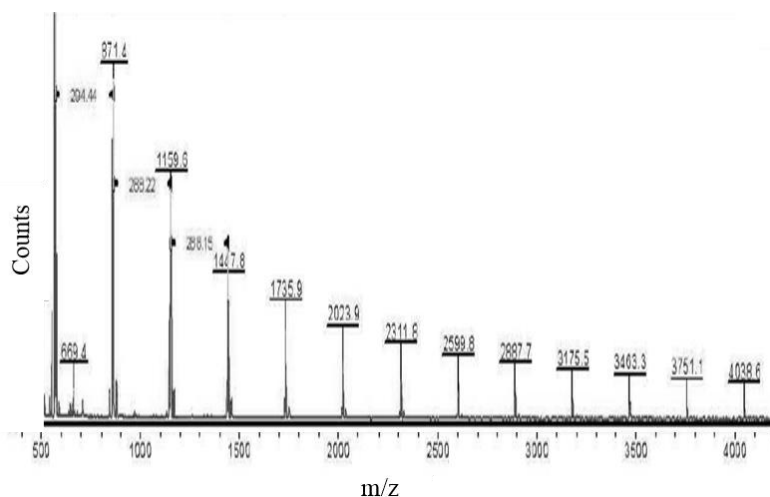
Figure 24. MALDI-TOF spectrum of oPEEK MCOs.

DSC characterization of the MCO mixture was performed to gain a better understanding of the processing parameters that would be required in the polymerization of the oPEEK cyclics. Table 9 describes the general DSC observations. The first DSC scan reveals three discrete thermal transitions for oPEEK cyclic oligomers. The first, at 125 °C, is the T_g of the high molecular weight cyclic materials with repeat structures greater than n=8. The next peaks reveal two different MCO crystalline melt temperatures. The first peak was found to be of the mixture of MCOs, and the second, higher temperature was believed to occur due to the cyclic dimer. Upon scanning a second time, the T_g becomes more distinct and the melt transition merges to a single, lower intensity peak. The convergence of the melt peaks suggests two phenomena: first, the MCOs were able to melt-blend and form a single crystalline form, and second, due to the lower intensity, some spontaneous polymerization may occur due to impurities within the mixture.

Table 9

oPEEK MCO thermal transitions obtained by DSC

Sample	T_g (°C)	Tm_1 (°C)	Tm_2 (°C)
Scan 1	~128	239.78	267.69
Scan 2	~125	251.53	-
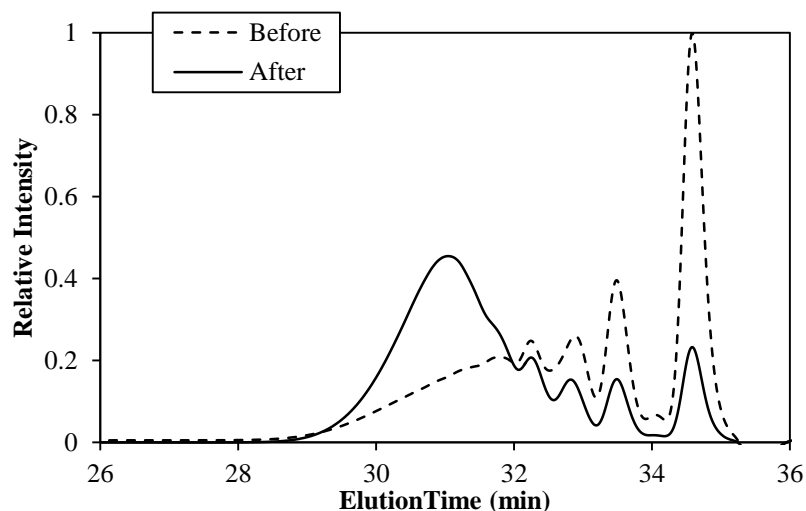
Figure 25. GPC chromatograms of MCOs before (dashed) and after (solid) removal of cyclic dimer.

After learning of the high concentration of cyclic dimer, curiosity arose as to what the MCO mixture's properties would be with the dimer removed. To separate the dimer from the mixture, a simple procedure was developed using the differing solubilities of the dimer material vs. the MCO mixture. The blend was first dissolved into THF at a concentration of 0.04 g/mL which created a cloudy solution with visible particles. The solution was then filtered to obtain a homogenous blend and precipitated into excess methanol. After drying, it was found that the procedure yielded ~20% of the original material. Upon GPC characterization of the newly separated blend, it was found that the majority of the cyclic dimer (over 75%) had been removed (Figure 25). Other cyclic species, including the trimer and tetramer, were also reduced to lower concentrations and the new mixture contained approximately 5% dimer, 5% trimer, 4 % tetramer, 4% pentamer, 2% hexamer, and 80% higher molecular weight analogues. Though not shown, the separated cyclic dimer was further characterized through mass spectroscopy to confirm the species true molecular weight. DSC analysis of the dimer, Figure 26

showed a single melt temperature at 312 °C further indicating the purity of the separation.

Thermal analysis was also performed on the reduced-dimer mixture which revealed a

single broad melt peak of ~240 °C. The importance of cyclic dimer removal was further

revealed during the polymerization of the cyclic oligomers and is discussed below.
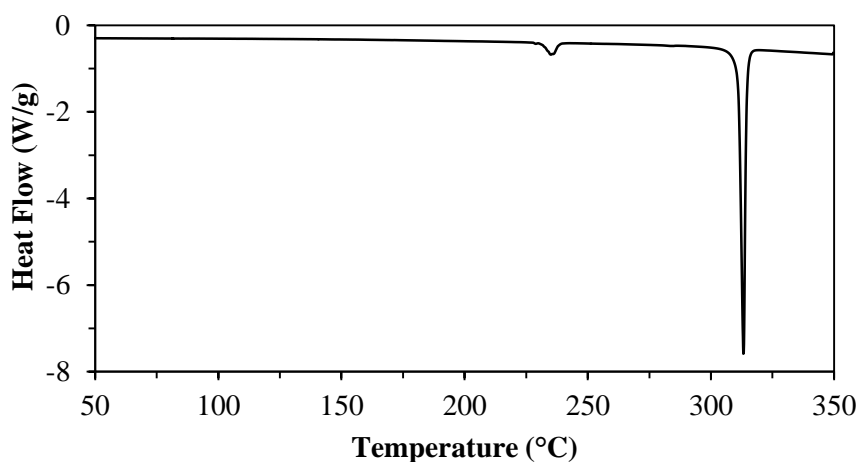
Figure 26. DSC melt temperature of oPEEK dimer after separation of MCO mixture.

Polymerization of oPEEK MCOs

Entropically-driven ring-opening polymerization of oPEEK macrocyclic

oligomers was performed within a DSC to study the effects of reaction parameters on

oPEEKs physical properties. Reaction time, temperature and catalyst level were varied to

study their effects on molecular weight, solubility (crosslinking), and T_g. Previous work

with oPEEK MCOs was shown to result in an amorphous thermoplastic polymer with

good solubility and toughness; the results herein are scrutinized and compared to the

literature.[52]

Table 10

*Parameters for selected oPEEK MCO ring-opening polymerizations; dash indicates insolubility; * indicates partial solubility*

[CsF] (mol%)	Time (min)	Temperature (°C)	Tg (°C)	M_n (g/mol)	Conversion (%)
5.0%	20	325	138.72	-	100
5.0%	20	300	135.54	-	100
2.5%	20	325	138.94	-	100
2.5%	20	300	131.93	-	100
2.5%	20	280	132.13	-	100
2.5%	10	280	130.97	-	100
2.5%	5	280	129.4	124450[*]	50
1.0%	20	300	129.65	-	100
1.0%	5	300	130.04	29128	40
1.0%	20	280	130.37	36727	46
1.0%	30	280	132.35	41500	51
1.0%	40	280	129.98	47275	53
1.0%	50	280	130.04	50854	54

Table 10 is representative, but by no means exhaustive, of the polymerization parameters studied during the DSC trials. Initial polymerizations were carried out using the highest initiator concentration of 5 mol%. It was found that, for all times (5-40 mins) and temperatures (250-325 °C) employed, melt polymerizations containing 5% CsF

produced fully crosslinked glasses and were completely insoluble. These densely

crosslinked materials were found to have the highest T_gs, resulting from the constraints

placed on the polymer after network formation. The first partially soluble polymer was

obtained after decreasing the initiator concentration to 2.5 mol% with five minutes of

polymerization at 280 °C. The partially crosslinked material was found to contain only

25% sol fraction, which was extracted using DMAc. The resulting oPEEK-sol was found

to have a T_g of 129 °C and molecular weight of 124,500 g/mol (the highest of all

materials studied). Of the soluble fraction, only approximately 50% of the material had

been converted to polymer, while the remaining proportion was unpolymerized cyclic

oligomers. Formation crosslinked glasses was unexpected as Ben-Haida and coworkers

showed that oPEEK could be synthesized using similar parameters (4% CsF at 320 °C for

10 minutes) to obtained fully soluble, high molecular weight polymer. One possibility for

the discrepancy is attributed to residual potassium salts left within the MCO starting

materials after purification. Potassium salts have been previously shown to be good

initiators for entropy-driven ring-opening polymerizations, even at low

concentrations.[101–103] Although the MCO mixture was neutralized with HCl, low

concentrations of potassium fluoride and carbonate may have been left behind, increasing

the effective concentration of reactive chain ends and the probability of crosslinking.
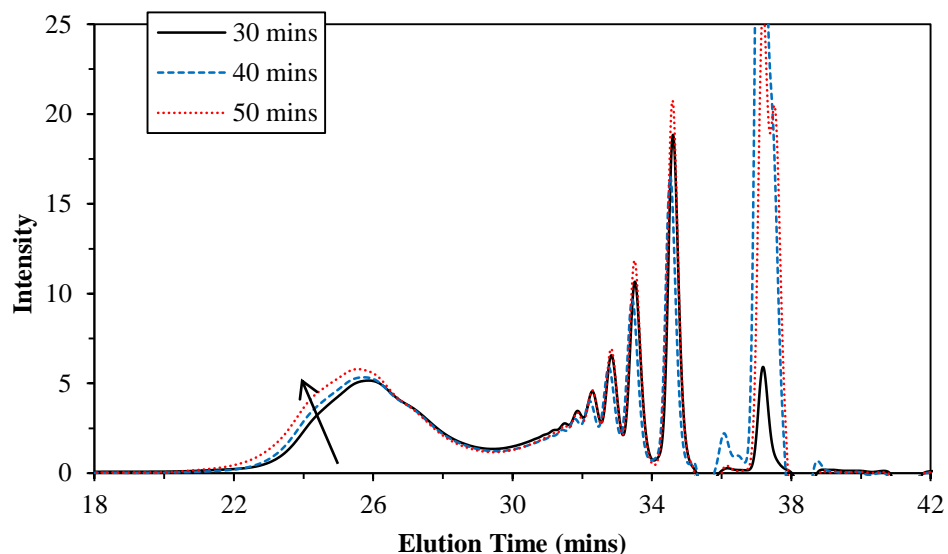
Figure 27. GPC chromatograms of oPEEK synthesized using 1 mol% CsF at 280 °C for various times; arrow indicates increase in reaction time and molecular weight.

When the initiator concentration was decreased to 1 mol%, linear oPEEK was

obtained. Polymerization times were varied between 10 and 60 minutes. Using GPC it

was shown that below 20 minutes the reaction produced very little polymer and

conversion was effectively naught, but between 20 and 50 minutes polymers with

molecular weights between 29,000 and 51,000 g/mol were achieved (Figure 27). After 50

minutes the polymerizations began to gel due to crosslinking. Furthermore, gelation

produced incomplete polymerizations with conversions around 50%. The relatively low

molecular weights are attributed to the viscosity increases that occur during step-growth

polymerization.[6] It is hypothesized that the obtained molecular weights are near the

entanglement molecular weight of amorphous oPEEK, and once reached, reaction is

hindered due to the rapid increase in viscosity from entanglement formation. At 280 °C

and under no shear, the increase in viscosity from crossing over the entanglement

molecular weight threshold outweighs the low viscosity of the MCO mixture, causing the

oligomer mobility to significantly decrease and limit further conversion of precursor. Due to the lack of MCO mobility, the active chain ends are proposed to react with close-proximity sites such as those of the phenyl-rings *ortho/para* to the ketone. These reactions are believed to result in the described crosslinking that occurs at high CsF concentration, elevated temperatures, and longer reaction times.[104] Low conversions are also ascribed to increased viscosity, but also to the high concentration of cyclic dimer. The high melting temperature dimer was believed to be only partially soluble in the melt at 280 °C and thus had low mobility and reactivity, resulting in its remainder after the polymerization.
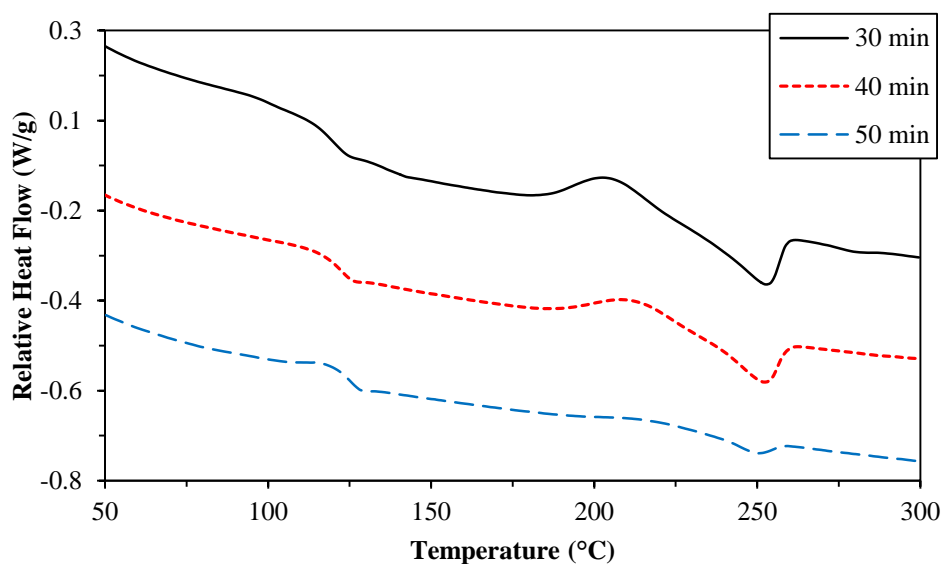
Figure 28. DSC thermograms showing T_g and residual cyclic oligomer melt temperatures of oPEEK after 30, 40, and 50 minutes of polymerization with 1 mol% CsF at 280 °C.

DSC was used to characterize the thermal properties of oPEEK (Figure 28). It was found that the polymerization parameters described above afforded polymer with T_gs between 129 –132 °C. However, Ben-Haida reported oPEEK T_gs around 145 °C. Although their parameters were similar to the ones herein, they achieved molecular

weights twice as high, and therefore an increased T_g is reasonable. The melting of the

residual MCO mixture was observed above 250 °C. It was shown that the intensity of the

MCO melt peak, and therefore MCO concentration, decreased as the polymerization time

was increased, further supporting the gel fraction conversion reported in Table 10.
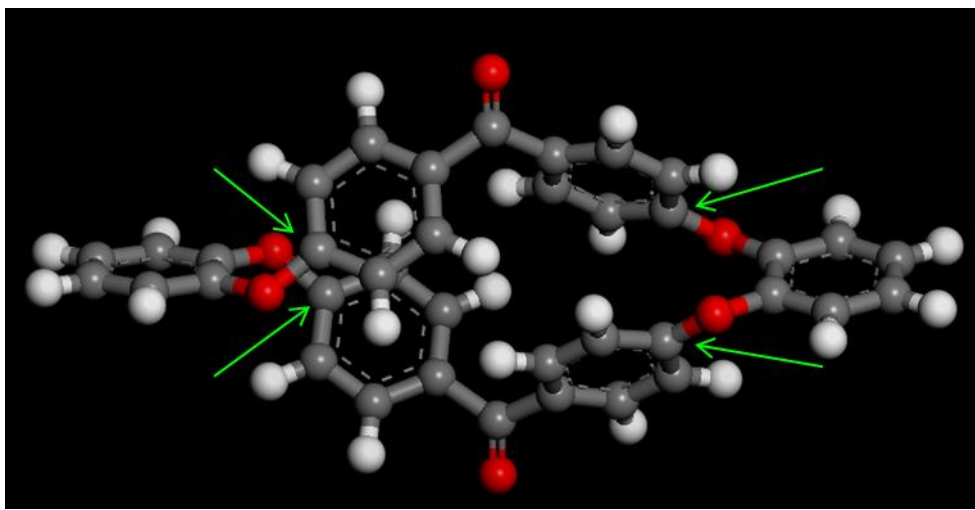
Figure 29. Geometry optimized 3D structure of the cyclic dimer of oPEEK showing
compact and "self-stacked" confirmation; green arrows point to primary sites of reaction
during ring-opening polymerization.

It was hypothesized that the low conversions and molecular weights of previously

described oPEEK were directly related to the high concentration of cyclic dimer within

the system. Along with its high melt point, the dimer cyclic oligomer is believed to be

much less reactive than the larger macrocycles. This poor reactivity is attributed to the

dimer's melt conformation. Using molecular dynamics simulation, Figure 29 shows that

between 250 °C and 300 °C the dimer takes a very compact conformation that has been

referred to in the literature as "self-stacking".[105,106] This dense structure is created

through the *ortho*-substitution of the catechol residues and, from both the polymerization

data and the thermodynamic theory behind entropy-driven ring opening, appears to be both enthalpically and entropically more stable than the other cyclic oligomers. Furthermore, as presented by the green arrows in Figure 29, the primary reaction sites for nucleophilic attack are severely sterically hindered from its odd conformation. This steric effect may contribute to the cyclic dimer's overall lower reactivity and thermodynamic stability.
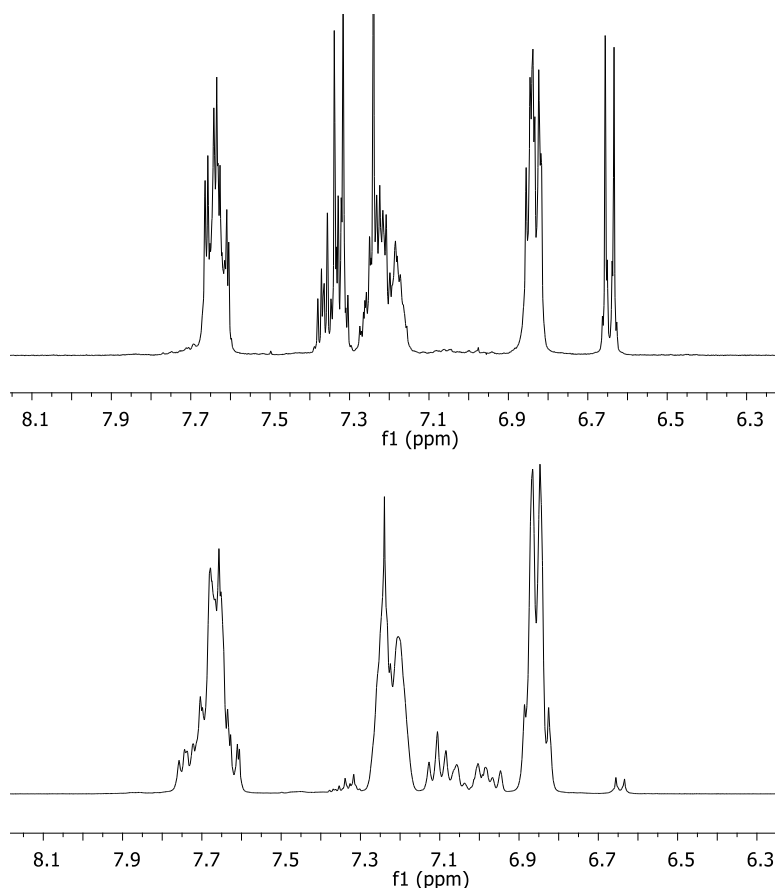
Figure 30. ¹H-NMR spectra of oPEEK polymerized using 1 mol% CsF at 280 °C for 50 minutes; top spectrum, before removal of dimer; bottom spectrum, after removal of dimer.

To circumvent the complications arising from dimer reactivity, the material was extracted before polymerization, as described in *Macrocyclic Oligomers* above. After

dimer removal, polymerizations were carried out using the previously reported parameters of 1% CsF, 280 °C, and 50 minutes as the initiator concentration, temperature, and time, respectively. These parameters were found to produce a partially soluble material with gel and sol fractions of approximately 70 and 30%, respectively. Figure 30 shows representative ^{1}H-NMR spectra of the obtained oPEEK materials before and after the extraction of cyclic dimer. It is shown that both the doublet between 6.6 and 6.7 ppm and the multiplet between 7.3 and 7.4 ppm decrease with the removal of dimer, but more importantly, the multiplets between 6.9 and 7.15 ppm increase after polymerization. These peaks represent the protons nearest a fluoro-end-group and their increase in intensity is attributed to the higher concentration of chain ends within the system from the increase in MCO conversion.
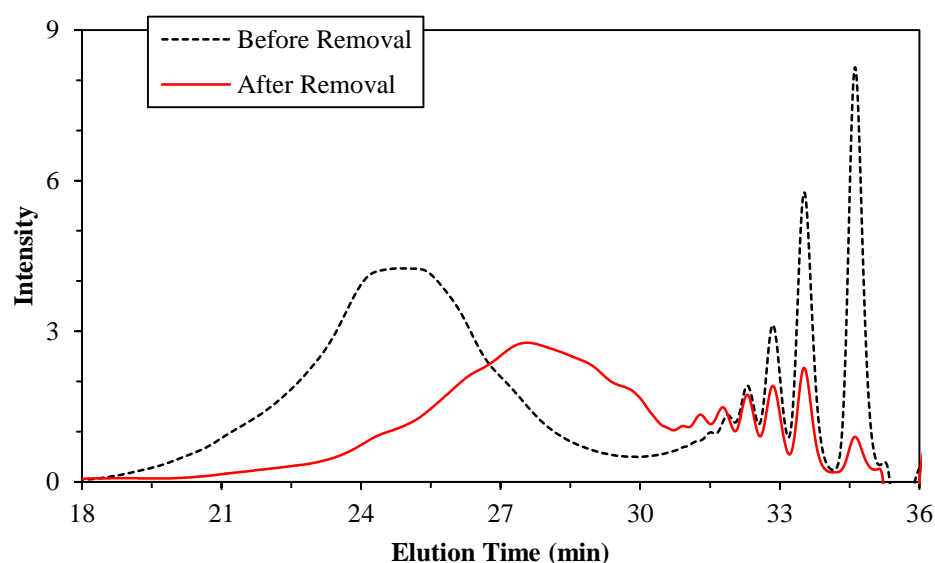
Figure 31. GPC chromatograms of oPEEK sol-fractions before and after cyclic dimer removal; polymers obtained using 1% CsF, 280 °C, and 50 minutes.

Although it was apparent that MCO conversion was increased upon dimer removal, it was found that the sol-fraction's molecular weight was still lower than

literature values. The GPC traces in Figure 31 display oPEEK material before and after

removal of dimer and indicate that the soluble oPEEK has a molecular weight of 19,000

g/mol; before dimer removal the polymer is 50,000 g/mol and, furthermore, literature

shows a molecular weight of 83,000 g/mol.[106] This decrease is ascribed to the large

amount of crosslinking which occurred from the un-optimized polymerization

parameters, and it is hypothesized that higher molecular weight can be obtained with

dimer-free MCOs. Moreover, the chromatograms reveal that the overall concentration of

cyclic oligomers has decreased compared to the neat MCO mixture, further evidencing

that removal of dimer helps to increase conversion. Finally, the T_g of the dimer-free

polymerized oPEEK was found to be within the same range as previously discussed, 129-

132 °C.

Synthesis of oPEEK MCOs and polymers provided a strong foundation in the

synthetic techniques required for preparation of aryl-ether-ketone structures. It became

obvious a more fruitful research direction was the preparation of AEK-based distortional

networks, and thus they are the primary topic of this work.

Aryletherketone Epoxy Monomer

The epoxy monomer prepared was synthesized by a two-step, single-pot

glycidation reaction of an aryletherketone bisphenol precursor; the precursor was

synthesized according to Figure 17 while the glycidation proceeded via Figure 18. A

similar procedure was previously reported by Hwang *et al* but their methods afforded

monomer of low purity and were further questioned by the lack of characterization

provided.[55] They employed a two-step procedure to obtain the precursor bisphenol

through deprotection of the phenyl-methoxy with HBr and acetic acid. Although this

deprotection is reported to have good yields, the extra work-up steps required to purify

the product before glycidation were not commercially-viable and would further reduce

final product yields. Therefore the synthesis of precursor 4RB was performed via a route

which required no deprotection and less purification steps. The reaction proceeded via

nucleophilic aromatic substitution reaction between 20 mole percent excess of the

diphenoxide potassium salt of hydroquinone and difluorobenzophenone (DFBP) under

continuous azeotropic removal of water. It must reiterated that, in any aryletherketone

synthesis or polymerization, removal of water before addition of DFBP is vital to reduce

aldol-condensation side-reactions, and therefore sieve-dried solvents, vacuum dried

K_2CO_3, and azeotropic water removal is required.[107] The relatively moisture and air free

environment allowed for a rough product yield of ~93%.
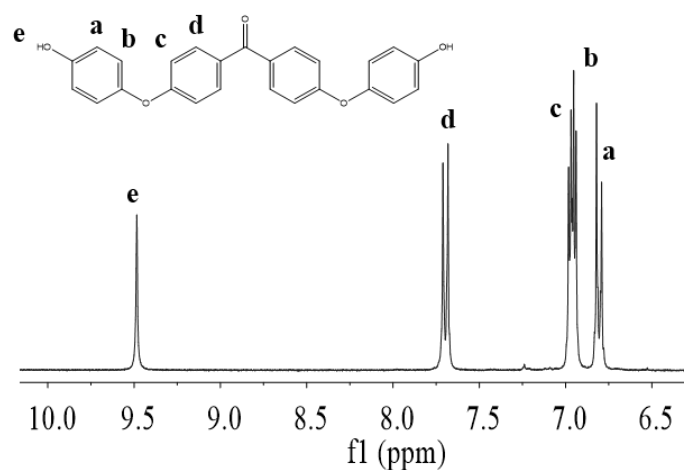
Figure 32. ^{1}H-NMR of 4RB in d_6-DMSO.
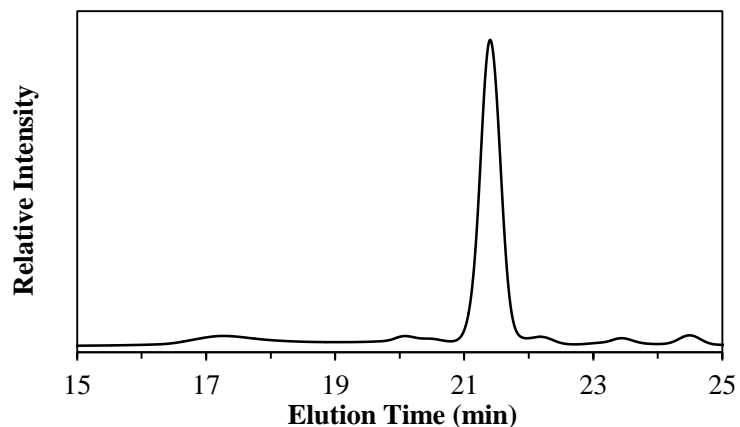
Figure 33. GPC chromatogram of 4RB; performed using THF as eluent.
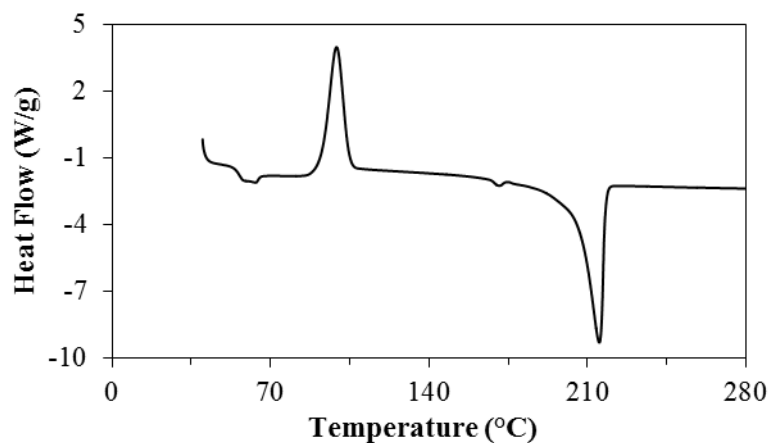
Figure 34. DSC thermogram of 4RB; cold-crystallization and melting transition.

Although HQ is in large excess, a small amount of chain extension occurred and it was noticed that the initial product had only partial solubility in organic solvents. Upon characterization, higher molecular weight species were observed and were designated as hydroquinone-functional oligomers of PEEK. Due to its increased solubility, the desired bisphenol product was easily acetone-extracted from the high molecular weight analogues and obtained in 88% yield. 4RB was soluble in a range of organic solvents including acetone, THF, DMAc, and DMSO. ^{1}H-NMR agreed well with the expected

structures and integration of the peaks revealed a product with high purity (Figure 32).

Analysis by GPC (Figure 33) revealed that the majority-material was the desire product,

but also indicated a small amount of higher molecular weight species by the main peak at

22 minutes and the minor peak at 17.5 minutes. The DSC thermal characterization

confirms the product purity with the sharp melt peak at 218 °C corresponding to the main

product (Figure 34).
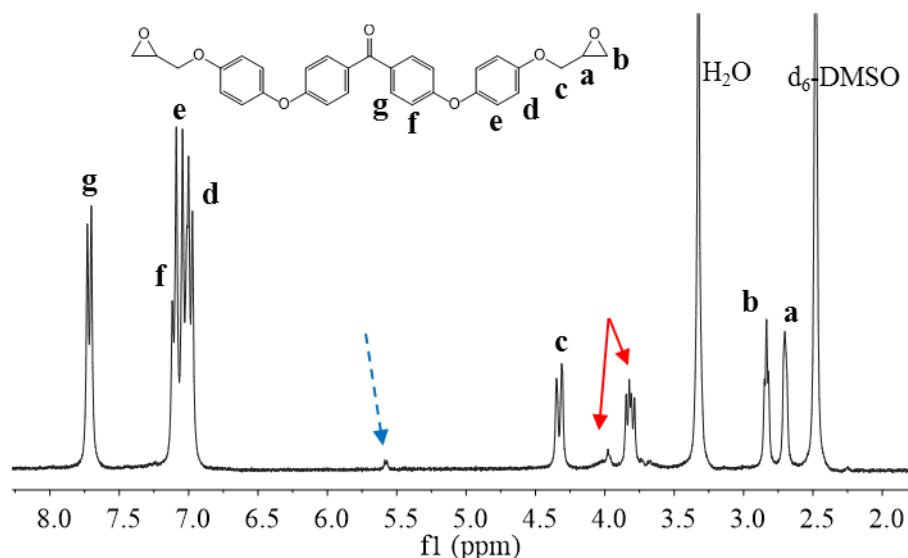
Figure 35. ¹H-NMR of successful DGEEK in d_6-DMSO; (dashed arrow) hydroxyl proton; (solid arrows) chlorohydrin protons.

After the successful characterization of 4RB, synthesis of the diglycidyl analogue

was attempted. Glycidation of the 4-ring bisphenol was performed using multiple

synthetic parameters. Aerospace-grade epoxy network mechanical properties perform

best when chain extension of the epoxy-component is low and the monomeric content is

high. Consequently, industrially-relevant glycidation reactions aim to limit chain

extension and are typically performed in two steps (Figure 18).[108,109] The first step is a

nucleophilic substitution, or "coupling", of epichlorohydrin (ECH) with a bisphenol, and

it is typically performed with a tertiary amine catalyst in large excess of ECH (>20x molar excess) to limit additional reaction and oligomerization. The second step, which closes and forms the epoxide ring, is completed by a similar substitution mechanism, but is performed with an alkali solution typically composed of NaOH. To further limit chain extension, the basic solution must be added in correct concentration, but is not a frequently reported value and is commonly accomplished by "rule of thumb" assessments.[110]
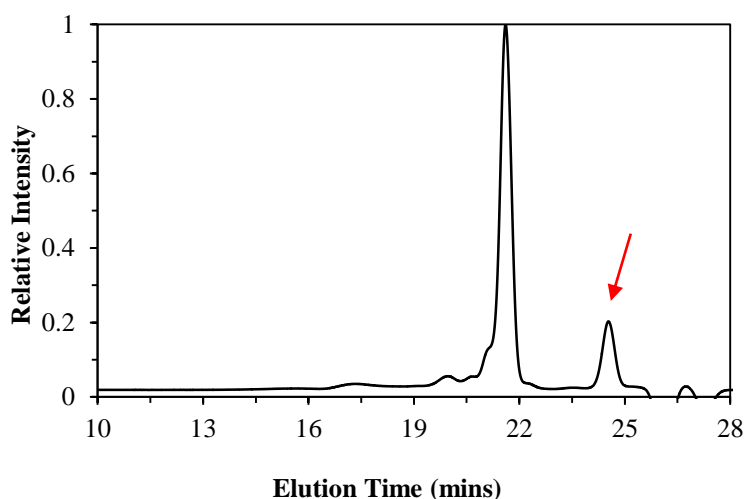
Figure 36. GPC chromatogram of successful DGEEK; arrow indicates residual ECH from synthesis.

The initial synthetic parameters for glycidation of 4RB were chosen from previously-synthesized epoxies in our lab and the reaction scale was kept to approximately five-grams of product. Using a 20x molar excess of ECH, dissolution and coupling to the bisphenol was completed, and through ^{1}H-NMR was found to provide a high yield of the dichlorohydrin-intermediate. After removal of the excess ECH, toluene and a 20% solution of NaOH and $NaCO_3$ were added to the reaction vessel to dissolve

and assist the ring closing step respectively. After three hours of reaction at reflux, a

diglycidyl ether of ether ether ketone (DGEEK) was formed. The ^{1}H-NMR of Figure 35.

reveals the characteristic aliphatic protons of the glycidyl-group at 2.7, 2.8, and 4.7-4.8

respectively. The peaks indicated by the solid red arrows are of chlorohydrin groups and

demonstrate incomplete closing of the epoxide-ring, and or minor chain extension.

Furthermore, the peak at 5.6 (dashed blue arrow) indicates hydroxyl moieties, which can

be from unreacted bisphenol, or from the chain-extension; due to the presence of the

chlorohydrin peaks, it is assumed that the no residual bisphenol is within the system and

instead, ring-closing is incomplete. Upon further NMR analysis it was estimated that

DGEEK contained a hydrolysable chlorine content of ~0.5%, slightly higher than the

industrially applicable 0.2%.[108,109]
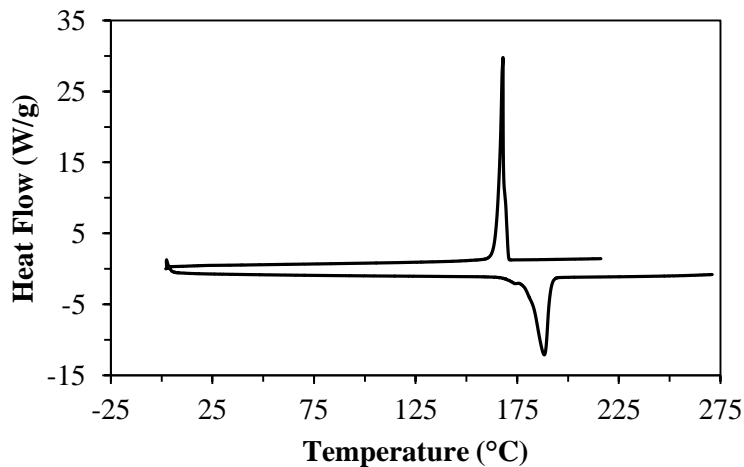
Figure 37. DSC thermogram showing DGEEK melt and crystallization temperatures.

The solubility of DGEEK was poor, and it was found to be insoluble in MeOH,

DCM, and THF. The product mixture was partially soluble in DMF, and to perform GPC

analysis the DGEEK product required dissolution in DMF doped with LiBr. Figure 36

shows a GPC trace of the product mixture and shows distribution products. DGEEK

monomer is found at 21 mins while dimeric-DGEEK is believed to be at 20 mins. Other

oligomers were not clearly separated but from GPC it is obvious that some degree of

chain extension had occurred (broad peak 16-19 mins). DSC melt temperature

characterization (Figure 37) showed single, relatively broad melt and crystallization

peaks indicating that the DGEEK oligomers form similar crystal structures, and melting

occurred between 174–195 °C.   Values from characterization and other product

observations are organized in Table 11 below.

Table 11

Observations and chemical characteristics of DGEEK product

Visual Appearance	Monomer MW (g/mol)	Dimer MW (g/mol)	HCC (%)	T_m (°C)
Cream Powder	510.5	965.3	0.54	185.8

After the successful preparation of two separate DGEEK materials, all subsequent

syntheses were futile. Four different syntheses were performed using the same

chemicals, the same parameters, and the same equipment, but each produced completely

insoluble DGEEK product. Using a 50 v/v% mixture of $CDCl_3$ and trifluoroacetic acid,

^{1}H-NMR was used to characterize the insoluble materials. The spectra, represented by

Figure 38 revealed the product was a mixture of oligomers with various degrees of chain

extension. Oligomerization occurs due to reaction of one ring-opened –OH with another

monomer's –Cl end-group to create hydroxypropylether groups, which are clearly visible by the proton spectrum.
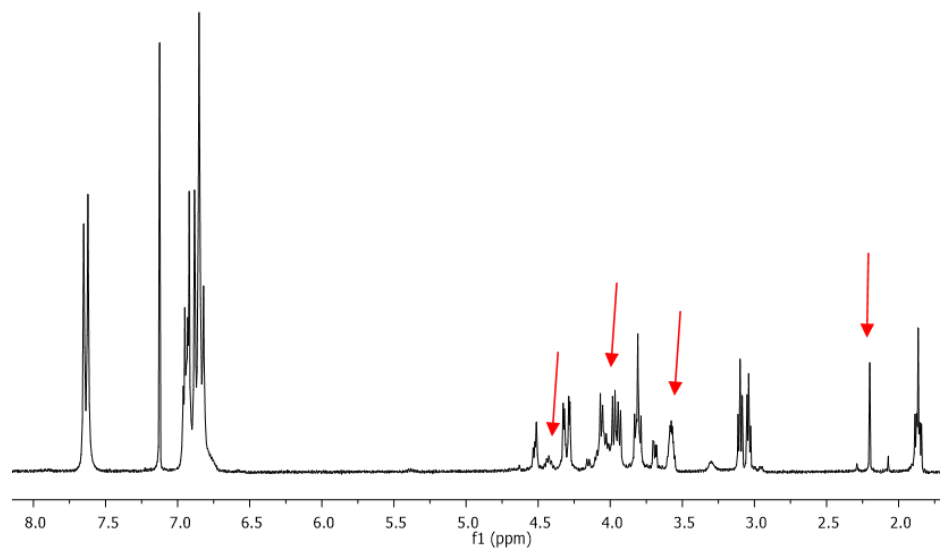
Figure 38. Representative ^{1}H-NMR spectrum of insoluble DGEEK product-mixture dissolved in 50 v/v% CDCl$_3$/TFA; Arrows indicate ring-opened, hydroxypropylether protons.

Further characterization of the insoluble material was performed using GPC. At small concentrations (< 0.1 mg/mL) small quantities of the DGEEK material would go into the DMF/LiBr solution. The GPC trace in Figure 39 represents the soluble portion of the unsuccessful syntheses. Although the low concentration makes accurate determination of molecular weights difficult, it is clear from the GPC results that multiple products exist, many of which are high molecular weight oligomers (broad peak shoulder). It has been shown that dimeric PEEK oligomers have low solubility in all organic solvents, and above trimer, linear PEEK oligomers become insoluble without strong acid.[100] Therefore, although the oligomers contain flexible aliphatic linkages, it is hypothesized that unsuccessful DGEEK attempts created oligomers above dimer and trimer molecular weights.
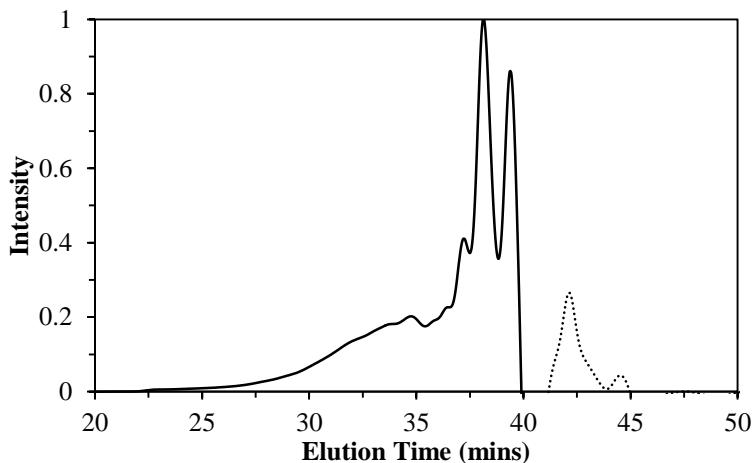
Figure 39. Representative GPC chromatogram of unsuccessful syntheses of DGEEK revealing multiple oligomer products; dashed line shows residual solvent peak.

After multiple attempts and failures to replicate the successful DGEEK synthesis a systematic study of reaction parameters was performed and is summarized in Table 12. The first step of glycidation, the coupling reaction, was found to provide the correct intermediate product and was not further assessed. However, there was evidence to support the hypothesis that the second, ring-closing reaction was the culprit step, and was the focus of the parameter study. Unfortunately, all new parameters tested resulted in similar insoluble materials and no causation for the oligomerization was discovered. Many speculations have been developed as to which factors play the biggest role in the chain extension observed. Literature of glycidation reactions are vague, mainly coming from patent data, but it has been shown that the alkali solution can have major effects on the final diglycidyl-based epoxy.[110] Nonetheless, as to why the first two synthesis were performed successfully using the same synthetic procedure remains unresolved.

Table 12

Parameters investigated during study of the second step of glycidation of 4RB

Base(s)	Base Solution Conc. (w/w%)	Base Solution Volume (mL)	Solvent	Solvent Volume (mL)	Temp. (°C)	Time (hrs)
NaOH/NaCO$_3$	20	50	DCM	50	55	3
NaOH/NaCO$_3$	20	50	Toluene	50	120	3
NaOH/NaCO$_3$	10	50	Toluene	50	120	3
NaOH/NaCO$_3$	10	25	Toluene	50	120	3
NaOH/NaCO$_3$	20	100	Toluene	50	120	3
NaOH/NaCO$_3$	5	50	Toluene	50	120	3
NaOH/NaCO$_3$	5	25	Toluene	50	120	3
NaOH/NaCO$_3$	20	50	DMAc	50	25	3
NaOH/NaCO$_3$	20	25	DMAc	50	25	3
NaOH/NaCO$_4$	10	25	DMAc	50	25	3
NaOH/NaCO$_5$	5	25	DMAc	50	25	3
NaOH	20	50	DMAc	50	25	3
NaOH	20	5	DMAc	50	25	3
NaOH	10	5	DMAc	50	25	3
NaOH	5	5	DMAc	50	25	3

Aryletherketone Amine Monomers

The synthesis of aryletherketone amine monomers was found to be more
straightforward compared to the epoxy analogue. Use of the mono-functional 4-

aminphenol allowed for high-yielding reactions with high purity products. It was found that, like other based-catalyzed aromatic substitutions described herein, environmental moisture content was required to be kept at a minimum. Side-reactions were prevented through drying and distilling of solvents and potassium carbonate before addition of the reagents. The facile purification of AEK-diamines was attributed to their higher crystallinity which allowed for faster precipitation and separation. Further observations of specific curatives and their reactions are discussed below.
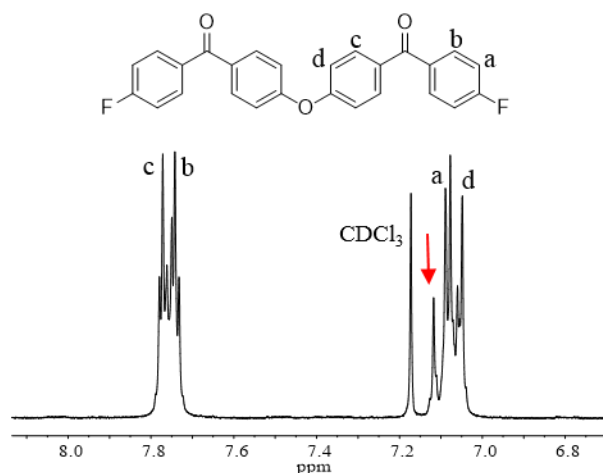
Figure 40. Labeled ^{1}H-NMR spectrum of pre6RA. Arrow depicts *ortho*-substitution.

Preparation of the 6-ring aryletherketone precursor was accomplished through Friedel-Crafts acylation of diphenylether with a 2.01 molar excess of 4-fluorylbenzoyl chloride. After completion, the reaction was quenched with excess 1 N HCl solution and then precipitated into an excess of water. The main product was easily purified as it was completely insoluble in acetone. This reaction provided a white, crystalline product of high purity and excellent yield. Diphenylether is an *ortho/para* director and it was hypothesized that the employed reaction conditions would afford a mixture of isomers.

This mixture was desirable as it was further hypothesized that the isomer content would lower the crystallinity and depress the melting temperature of the final 6RA curative. As shown by NMR in Figure 40, the major product of pre6RA synthesis was that of the *para-para* substitution, with a limited fraction of the product having *ortho*-substitution (indicated by arrow in Figure 40). The product mixture was soluble in halogenated solvents, partially soluble in DMSO, and insoluble in acetone.

Displayed by Figure 41, three specific molecular weight, amine-functional aryletherketone monomers were synthesized by nucleophilic aromatic substitution of various difluoro-aryl-ketone compounds and 4-aminophenol. Nucleophilic aromatic substitutions are known for their high yields, but to ensure complete reaction of the difluoro-compounds, a slight molar excess of 4-aminophenol was employed; it was found that any residual 4-aminphenol was easily removed with base and water washes. Although synthesis of the 4RB bisphenol was performed in DMAc, the initial curative preparation reactions afforded low yields in DMAc. After preparation attempts in DMF, DMAc and DMSO, it was ultimately found that NMP provided the best yields and easiest work-up. It is hypothesized that NMP's higher boiling point also leads to it having a higher stability against water-hydrolysis and therefore less aldol-condensation side-reactions. Although they were not specifically extracted and characterized, enamine side-products are likely to be water soluble and are removed from the product mixture during the initial precipitation and wash steps. This is what most likely led the lower observed yields with DMAc.
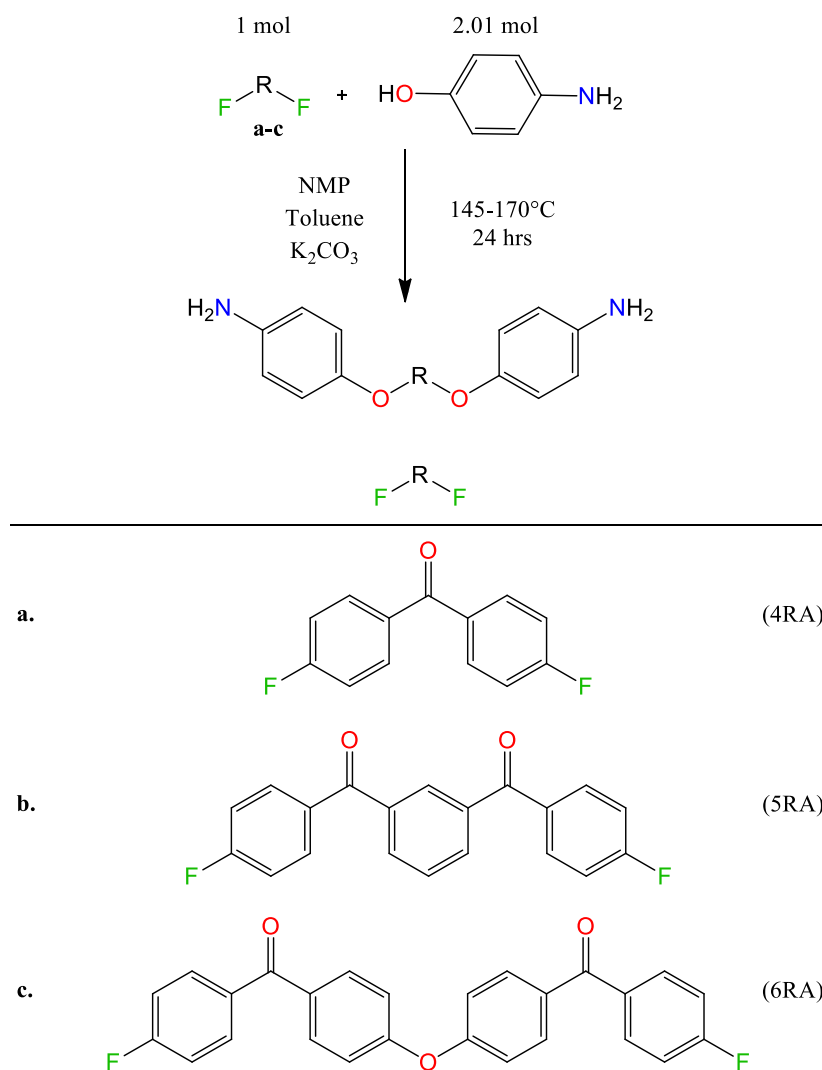
Figure 41. Top: Generalized synthetic pathway for aryletherketone curative monomer synthesis. Bottom: Difluoro-compounds utilized as ketone segments, name of the curative-product in italics.
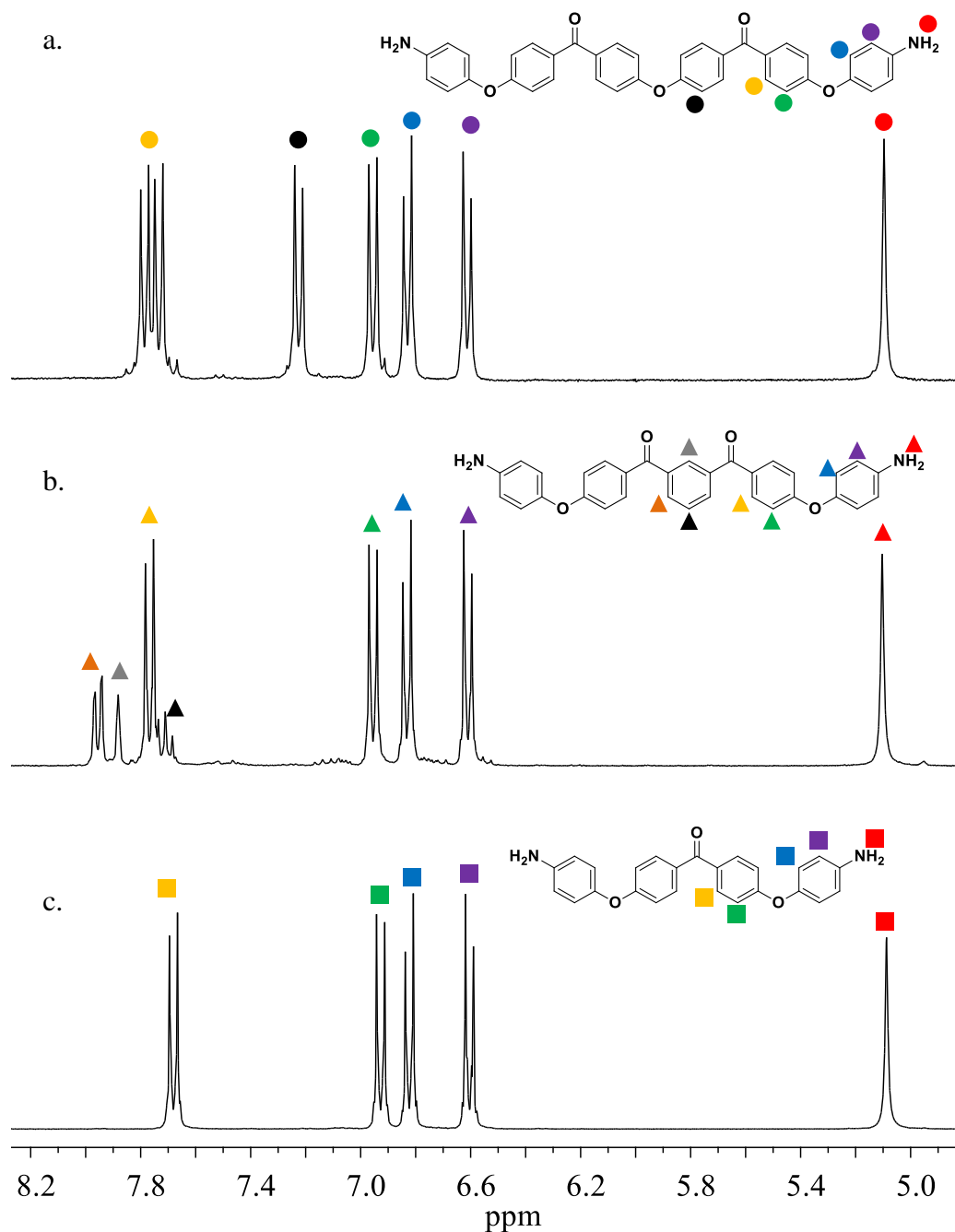
Figure 42. 300 MHz ^{1}H-NMR spectra of aryletherketone amine curatives in d$_6$-DMSO; 6RA (a), 5RA (b), 4RA (c).

The 4-ring and 6-ring curative analogues, 4RA and 6RA, were easily precipitated

and purified. It was found that precipitations and washes with a 5 wt% NaOH solution

removed unconsumed 4-aminophenol and residual potash, and two or three further water-washes neutralized the products. The materials were dried on a filter under nitrogen overnight which yielded a crystalline material, and were then crushed into a fine powder with mortar and pestle. The powdered materials were then vacuum dried at ~120 °C to remove water and any lingering NMP/toluene. ^{1}H-NMR spectra of 4RA and 6RA (Figure 42) reveal relatively pure products. The 4-ring curative shows no residual starting materials and is of very high purity (from peak integration) while the 6-ring spectrum displays a small quantity of isomer content obtained during precursor synthesis, shown by the shoulder-peaks around 6.8 and 7.6 ppm.

Table 13

Physical and chemical characteristics of AEK curatives; DDS included for comparison

Curative Name	Molecular Weight (g/mol)	Melt Temp. (°C)	pKa (Simulated)	Aryl-Ether Ratio	Aryl-Ketone Ratio
DDS	248.3	175	1.6-2.4	-	-
4RA	396.4	152	3.9-4.5	2	4
5RA	500.5	(75)[*]	3.9-4.5	2.5	2.5
6RA	592.2	192	3.9-4.5	2	3

[*]: 5RA was glassy solid until T_g, and showed no melting point

The purification of the 5-ring curative, 5RA, was not as straightforward. The reaction conditions found to work for 4RA and 6RA were also employed for the 5-ring curative synthesis. Likewise, the initial precipitation and washes with basic solution and water provided an easy method to remove residual 4-aminophenol. After washing and

drying on a fritted filter, the rough product became a glassy solid. This "tough" material was removed from the filter only through dissolution into acetone, and then required further vacuum drying. Upon characterization of the dried product, the material appeared to have lower purity according to the ^{1}H-NMR spectrum. Additional washes with ethanol allowed for an increase in the product purity but some residual side-product still existed in the curative, as can be seen by the low intensity, broad peaks around 6.5-7.3 ppm in Figure 42. Further DSC characterization revealed a very broad glass transition temperature but no melt temperature. It is believed that the slightly persistent side-products of the 5RA synthesis are mono-substituted materials which contain both primary amine and fluorine functionalities. This product mixture is hypothesized because of the electron donating capability of the meta-substituted phenyl-ring of the di-fluorinated precursor. These electronics are believed to lead to lower reactivity when compared to the 4- and 6-ring precursor, which could potentially change reaction kinetics. However, peak integration revealed these side-products were below 1% of the total product, and therefore were not believed to affect the final network properties.

Synthesis and Characterization of Hyperbranched Epoxy Polymers

The aliphatic hyperbranched epoxy modifier synthesized herein was prepared according to Frechet *et al*. in a true one-pot procedure using an A2+B3 proton-transfer polymerization technique. In the proton-transfer reactions herein, a chloride anion generates a transient reactive site on the epoxide monomer through alkoxide transformation of the triol. Since this transfer step is faster than propagation, the polymerization is "group-controlled" and propagates through the thermodynamically favored addition of epoxide moieties. Recent epoxide-functional hyperbranched polymer

syntheses describe their preparations as "one-pot" but require work-up and purification steps between reagent additions to achieve the desired epoxide functionality.[65,66] In this work, by varying stoichiometry, epoxide functionality was achieved in a single-step without supplementary reagent additions or purification steps. As confirmed by ^{1}H-NMR, a molar ratio of 3A2:B3 provided HBEs with the high epoxide content and highly branched molecular architectures (Figure 43). The cutout reveals the concentration of di- and tri-substituted hydroxymethyl ethane units within HBE. The higher integral area, and therefore concentration, of tri-substitution (51% tri-) demonstrates the HBEs highly branched structure.
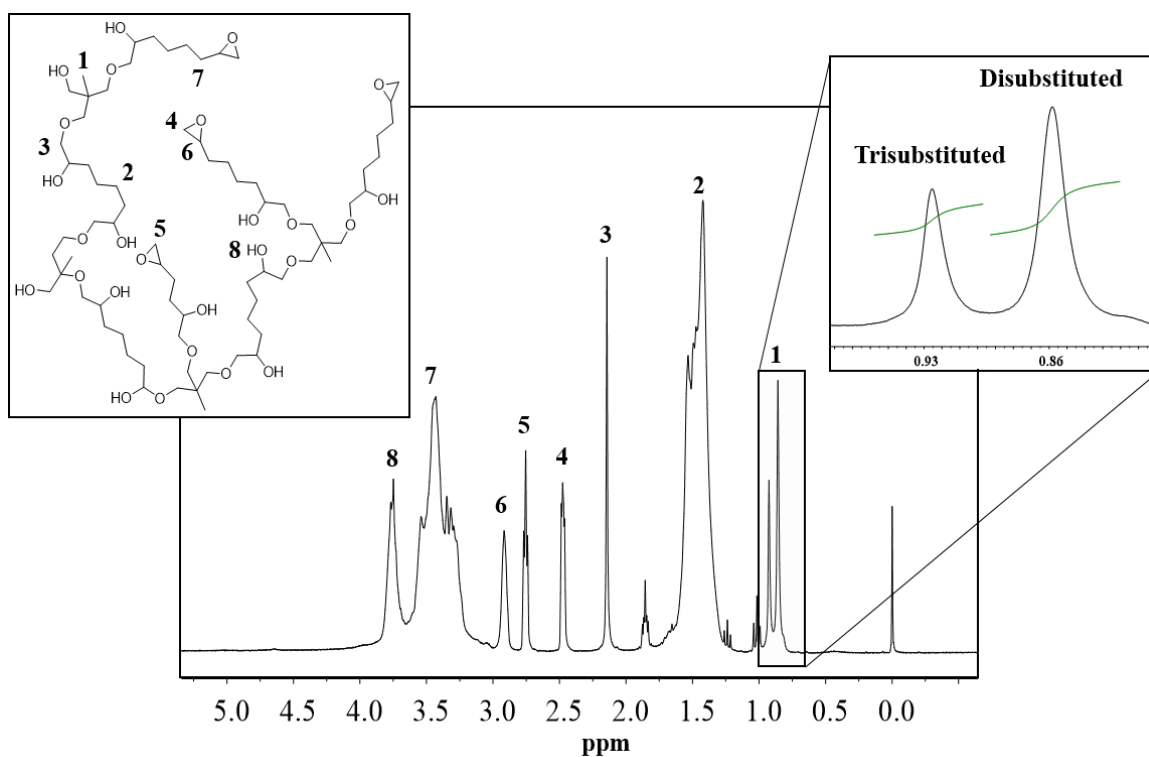
Figure 43. ^{1}H-NMR of HBE in CDCl$_3$; cutout reveals the relative concentrations of di- and tri-substituted tripropylether linkages.

Table 14

HBE physical properties

M_n (g/mol)	R_H (nm)	EEW (g/eq)	HEW (g/eq)	T_g (°C)	*η (Pa∗s)
4110	2.5	409	315	-29	4

Previous studies have demonstrated that hyperbranched polymers larger than 5000-7000 g/mol which contain low epoxide-functionality generally phase separate upon curing.[73,74,111] It has also been shown that pseudo-generation number can effect phase separation, where an increase in generation number is an increase in both molecular weight and branching.[60] Cicala *et al.* reported that an increase in pseudo-generation number led to the formation of particulate morphology, but lower generations contained small and indistinguishable phases.[112] This phase separation can have detrimental effects on the network's physical properties (i.e. T_g and modulus); and, therefore, the HBE used in this work was polymerized to a target average molecular weight below 5000 g/mol, and contained a moderate to high epoxide-functionality (Table 14). The target molecular weight was found after a performing a polymerization kinetics study (not shown), and it was observed that the desired molecular weight was consistently obtained after 12 hours of reaction. As can be seen in the GPC elution diagram (Figure 44), the step-growth polymerization lends itself to a broad distribution of molecular weights with a PDI >2 and, from the peak between 21 and 22 minutes, regularly contains some low molecular weight precursors (~200 g/mol). It should be noted that the molecular weight of HBE was further confirmed by static light scattering and it was also found that the hyperbranched material had a hydrodynamic radius of approximately 2.5 nm.
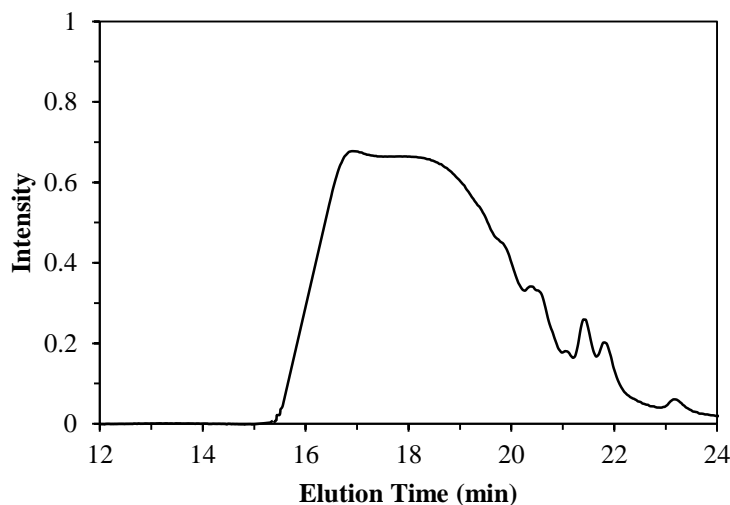
Figure 44. GPC chromatogram of HBE performed with THF as eluent.

Quantitative epoxide content determination of HBE was achieved through epoxide equivalent weight (EEW) titrations with hydrogen bromide. Through EEW calculations it was confirmed that HBE contained a high epoxide functionality, *f,* which was determined by the ratio of M_n to EEW. After the 12 hour reaction, it was found that the HBE polymers contained approximately 10 epoxide groups per molecule. Furthermore, hydroxyl-content was measured through acid neutralization with KOH.[113] Assuming a negligent acid-value after synthesis, HBE had an HEW of 315 and was approximately 5 mol% hydroxyl-moieties; hydroxyl-content is purported to play a significant role in the unique properties observed in *Chapter VII.* The hyperbranched polymer's dynamic viscosity was also determined and is shown in Figure 45 as a temperature sweep. The HBE's low shear viscosity further indicates its highly branched structure and its mixture of molecular weights, and even below room temperature, the polymer's viscosity is lower than that of standard DGEBA epoxy.
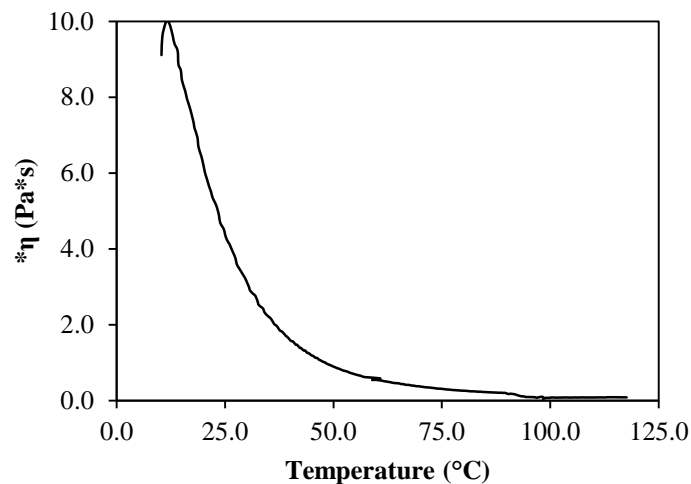
Figure 45. Dynamic viscosity vs. temperature plot of HBE from parallel plate rheometer.

POSS-HBE Preparation

Pre-reactions of POSS and HBE were performed to help improve POSS dispersion in the final cured network and involved the nucleophilic ring-opening of an HBE epoxide by the primary amine of amino isooctyl-POSS. Pre-reactions were performed in solution to decrease the probability of unwanted side-reactions such as the coupling of multiple POSS to the same HBE, or reaction of two HBE to a single POSS. To obtain the correct concentrations of POSS and HBE in the final networks, two separate pre-reactions were performed. Both used a final network equivalent of 10 wt% HBE, but each pre-reaction required a specific POSS concentration. For instance, 1P-10H pre-reaction ratio of HBE-epoxides to POSS-amino-hydrogens is approximately 15:1, whereas in 5P-10H pre-reactions the ratio is reduced to approximately 3:1. However, epoxides were kept in excess to reduce the occurrence of gelation.

The product mixtures were verified by SEC and ^{1}H-NMR (Figures 46 and 47) and were found to contain the anticipated POSS-HBE, HBE, and unreacted POSS products. The peaks at approximately 17.7 mins reveal that the molecular weight of POSS-HBE is approximately 5330 g/mol and indicated that the majority of the modified HBE molecules had a single POSS unit attached. The broad molecular weight distribution suggests some higher molecular weight adducts. These materials are possibly formed from reaction of one HBE with multiple POSS units (6000–9000 g/mol) or two HBE molecules with one POSS (~10,000 g/mol), but higher molecular weight analogues (>10,000 g/mol) were not observed. Similar to the synthesis of HBE, two low molecular weight peaks are observed between 21-22 minutes and suggest a small quantity low molecular weight, branched HBE oligomers remaining from HBE synthesis.
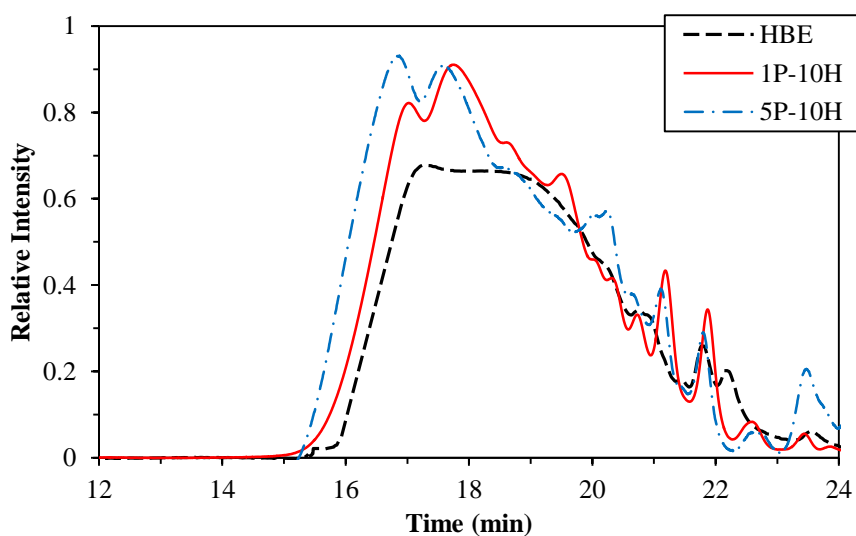
Figure 46. GPC chromatograms of POSS-HBE pre-reaction product mixtures.

SEC and ^{1}H-NMR confirmed that 5P-10H pre-reaction mixtures contained unreacted POSS from the low molecular weight shoulder on the SEC trace between 20-

21 minutes and the primary amine protons observed between 4.3 and 4.5 ppm. Unreacted

POSS is attributed to the relatively low temperature and time used during pre-reactions

(60 °C and 12 hours), which were chosen due to the primary-amine ability to react with

multiple HBEs. The chosen reaction parameters were found to provide good POSS-HBE

yield without obtaining higher molecular weight analogues such as from HBE-POSS-

HBE coupling and prevented gelation.
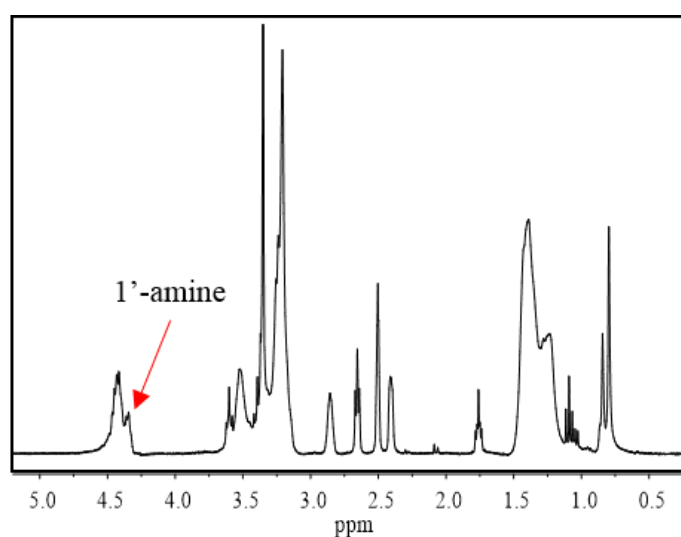
Figure 47. Representative ^{1}H-NMR of 5P-10H product mixture; arrow indicates the
partial reaction of primary amine.

The dynamic viscosity was measured as a function of temperature and shown in

Figure 48. The log-normal plot of the three modifiers demonstrates the expected increase

in viscosity upon incorporation of POSS nanoparticles. The neat HBE shows a clear

viscosity decrease with temperature starting from around 10 Pa*s. Addition of POSS

increases the viscosity at 10 °C an order of magnitude from 10 to 100 Pa*s. The lower

POSS concentration specimen shows a trend similar to that of neat HBE where an

increase in temperature decreases the complex viscosity, but the 5 wt% POSS

concentration shows a viscosity plateau beginning at approximately 70 °C. This linear

region is attributed to an increase in POSS aggregation upon increasing the mobility from

elevated temperatures.
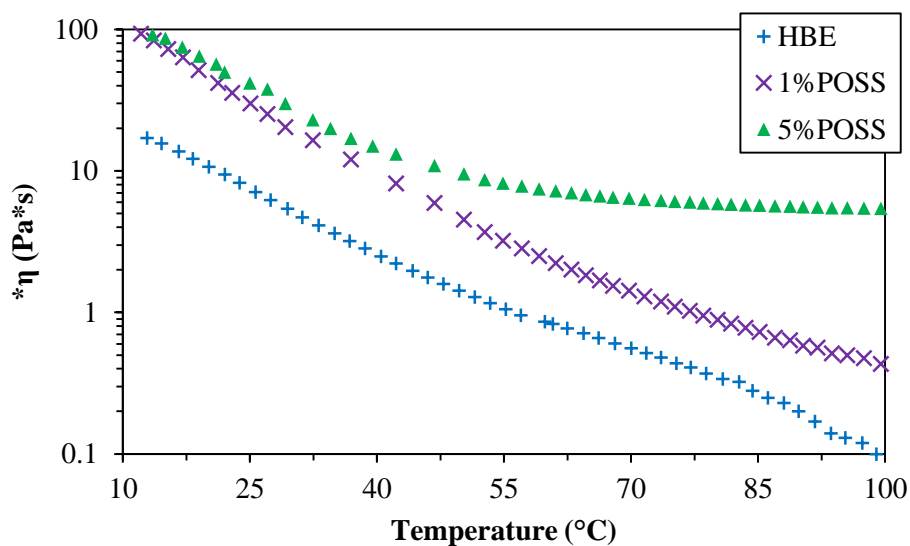
Figure 48. Log-normal dynamic viscosity vs. temperature plot for HBE and POSS-HBE pre-reaction mixtures.

Summary

Synthesis and characterization of the different materials employed throughout this

dissertation were described. Cyclic oligomers of oPEEK based upon catechol and

difluorobenzophenone were synthesized using a pseudo-high dilution technique. The

employed parameters provided good yields and purity, but the obtained macrocyclic

mixture contained a high concentration of the thermodynamically stale cyclic dimer. The

virtually unpolymerizable dimer was removed using its poor solubility and was

characterized by NMR, GPC, and DSC. The macrocylic mixtures were polymerized via

entropically-driven ring opening with CsF, and the ROP parameters were studied. It was

found that higher conversion of cyclic oligomers was obtained after the removal of dimer

and that crosslinking was prevented by using temperatures around 280 °C. Although the MCO-project was not further pursued, it spawned a new research direction with the synthesis of AEK-modifiers for epoxy networks. Three different molecular weight AEK-diamine curatives and one AEK-diepoxide were synthesized and characterized via NMR, GPC, and DSC. The diepoxide compound could not be repeated and was not discussed further in this dissertation.

An aliphatic, epoxide-functional hyperbranched polymer was synthesized through proton-transfer polymerization. It was found that the targeted molecular weight between 4000-5000 g/mol could be obtained after 12 hours of bulk polymerization. ^{1}H-NMR characterization revealed that the obtained molecular weight provided high epoxide functionality (f=10). Acid-base titration discovered that hydroxyl content stays unaffected throughout the reaction. After obtaining the HBE, it was modified with amino-functional POSS at two POSS concentrations (1 and 5 wt%). Similarly, the POSS structure and properties were characterized with NMR, GPC, and parallel plate rheology.

CHAPTER IV

MULTIFUNCTIONAL EPOXY NETWORKS BASED ON ARYL-ETHER-KETONE

DIAMINE CURATIVES

Objective

The purpose of this chapter is to discuss the formation and resulting properties of novel multifunctional epoxy networks cured by aryl-ether-ketone (AEK) diamines. TGDDM-based epoxy networks were prepared using three AEK curatives by two cure procedures, an initial, "industrial" cure protocol, and a post-cure (Chapter II). A holistic characterization of the novel networks' properties was performed to study the effects of curative chemical structure, molecular weight, and cure schedule. These effects were compared to a baseline network of TGDDM and 44DDS. DSC thermal analysis was used to describe the cure process through reaction kinetics and degree of cure. Thermal characteristics were probed with TGA and DMA, and mechanical properties were obtained from compression testing. Finally, the networks' fluid resistance was analyzed by ingress of water. The observed properties are discussed and related to differences in chemical composition and network structure. Subsequent analysis and formulation of these unique networks is described in Chapters V and VI.

Results and Discussion

DSC Results

Extent of cure, referred to here as degree of cure (α_R), and isoconversional analysis were used to gain insight into the development of AEK-cured TGDDM networks. Isoconversional analysis was performed using non-isothermal DSC data to produce plots of activation energy vs. conversion to observe changes in reaction mechanism without use of a kinetic model. Developed by Vyazovkin and Sbirrazzuoli[114,115] as an extension to the well-known Flynn-Wall-Ozawa (FWO) and Kissenger-Akira-Sunrose (KAS) methods, use of non-isothermal data to obtain E_a from DSC is a common method throughout the polymer community.[116–118] The DSC data herein was subjected to the above FWO analysis using the following equation:

$$\log(\beta) = \frac{-1.052E_a}{RT} + A'$$

where β is the heating rate in K s^{-1}, T is the temperature of the exotherm peak maximum in K, and R is the universal gas constant. Conversion is then calculated as a function of temperature through integration of the exothermic peak. For each degree of conversion (%), T in the FWO equation is the temperature at which that conversion is reached.

The isoconversional analysis process is demonstrated below for TGDDM-44DDS. The exothermic peaks of four different heating rates (Figure 49) were integrated to give the total heat of reaction, H_T, for each scan. The integral value at each temperature of the scan was then divided by H_T to find conversion (Figure 49); conversions of 10-90% were used in this analysis. At each degree of conversion, the temperature (T) at which conversion had occurred was found for each heating rate. Plots of ln(β) vs. *1/T* (Figure

50) were then used to calculate activation energy from the slopes of the best fit lines according to the FWO equation above.
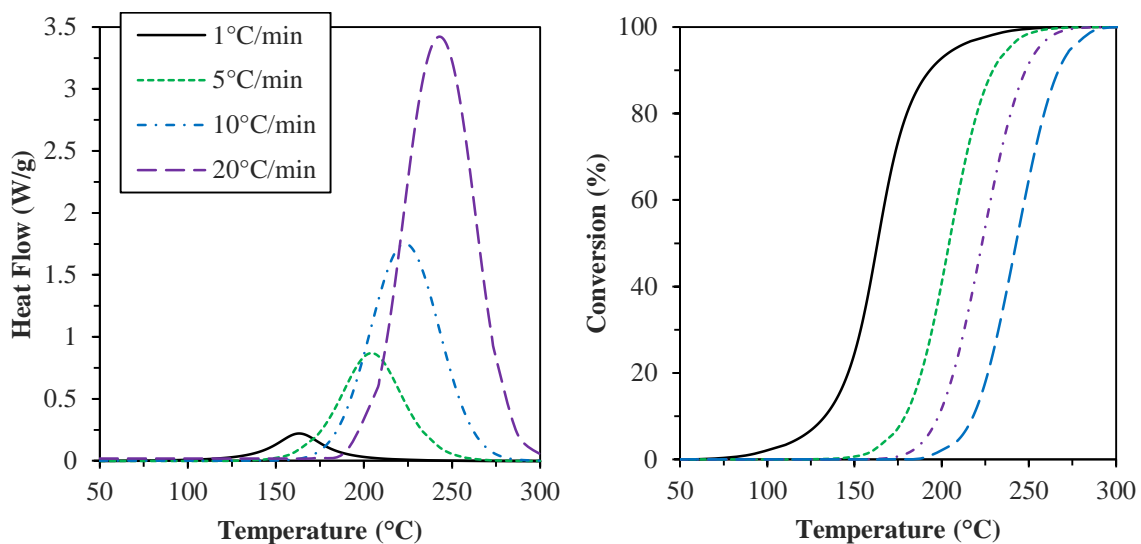
Figure 49. Heat flow vs. temperature and conversion vs. temperature at each heating rate for TGDDM-44DDS.

The product of this analysis, E_a vs. conversion, is shown in Figure 57. Activation energy increased during the cure reaction. This increase is attributed to the hindrance of reactive chain ends with the building of molecular weight until gel. After gelation (~40-50% conversion) the reaction rate stays constant over a conversion range of 40%, after which the activation energy significantly increases again. In isoconversional analysis, a change in slope of E_a vs. conversion signifies a change in reaction mechanism. TGDDM-DDS appear to have three changes in reaction mechanisms. At low times, the rapid increase in molecular weight leads to chain hindrance and an increase in E_a. The activation energy plateau-region is believed to be a characteristic of reactions occurring after gelation, where an infinite network has been formed but both primary and secondary amines are still reacting at equal rates.[119] The final increase in activation energy is

attributed to network vitrification, where in the glassy state the cure reaction becomes diffusion-controlled.[114,115,119] Furthermore, the large increase in E_a is also a result of functional group scarcity after high conversion of amino-hydrogens, which in-turn forces high activation-energy etherification to begin.
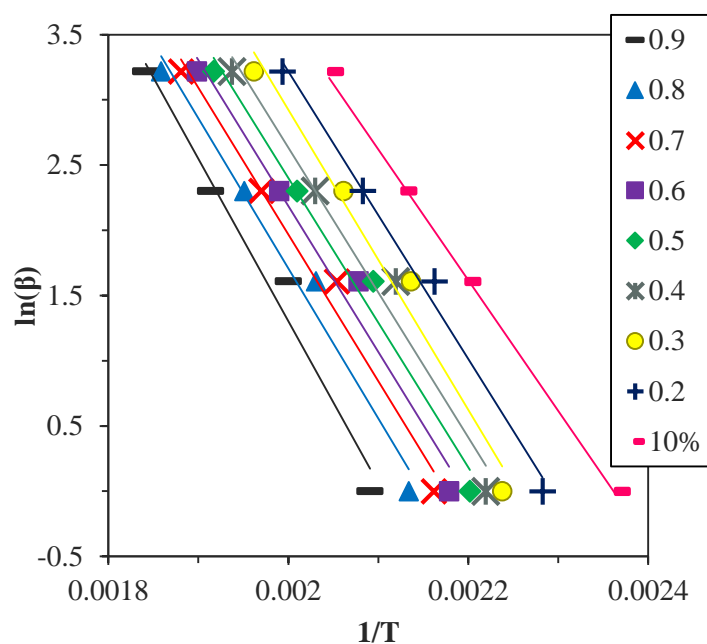
Figure 50. ln(β) vs. 1/T for TGDDM-44DDS at conversions 10-90%.

The above analysis was repeated for all AEK-cured epoxy networks. Exotherms and conversion plots for each AEK curative (4RA-, 5RA-, and 6RA-cured epoxies) are shown in Figures 51, 53, and 55, while plots of ln(β) vs. *1/T* are shown in Figures 52, 54, 56 respectively. Finally, a comparison of E_a vs. conversion for each curative is shown in Figure 57.
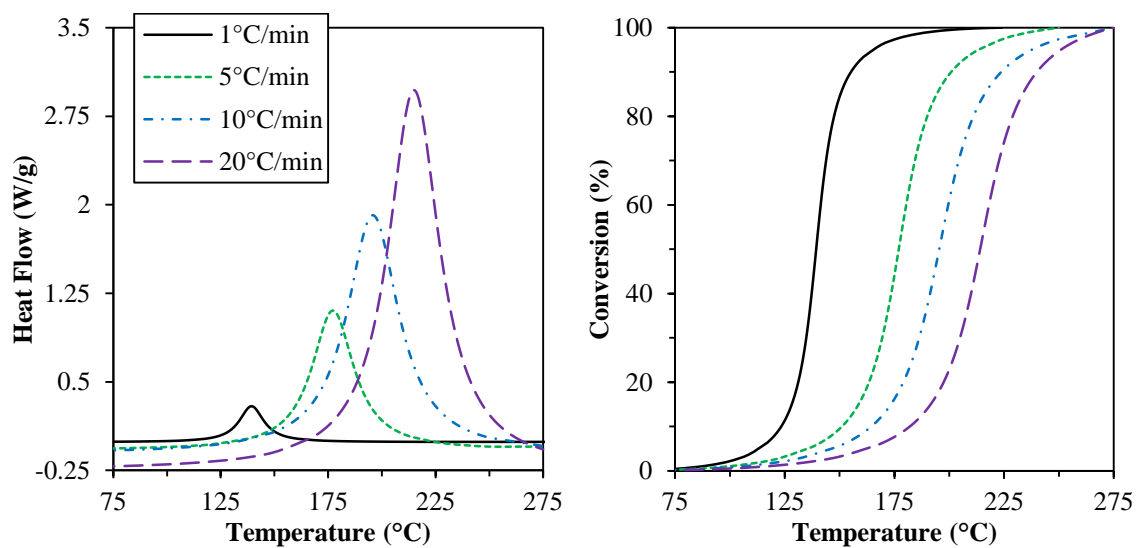
Figure 51. Heat flow vs. temperature and conversion vs. temperature at each heating rate for TGDDM-4RA.
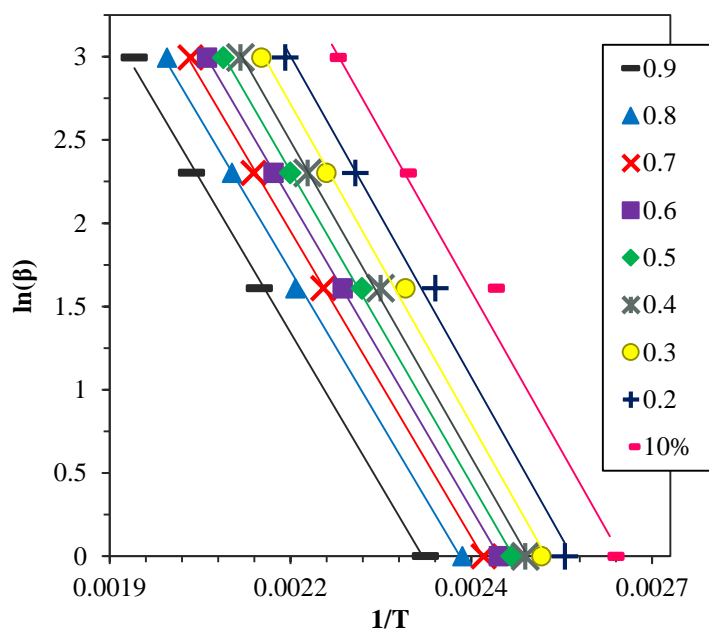
Figure 52. ln(β) vs. 1/T for TGDDM-4RA at conversions 10-90%.
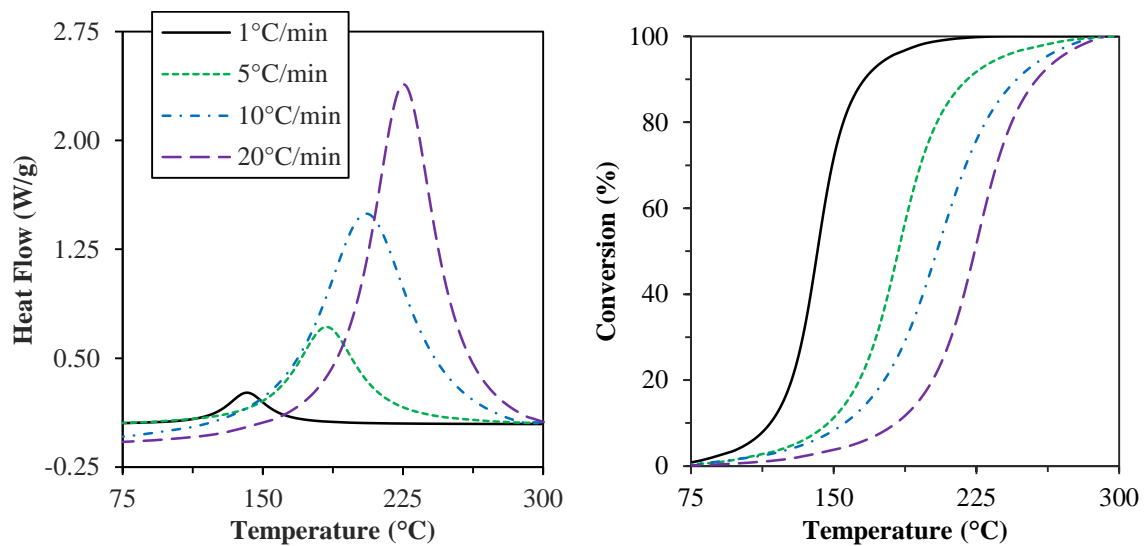
Figure 53. Heat flow vs. temperature and conversion vs. temperature for TGDDM-5RA.
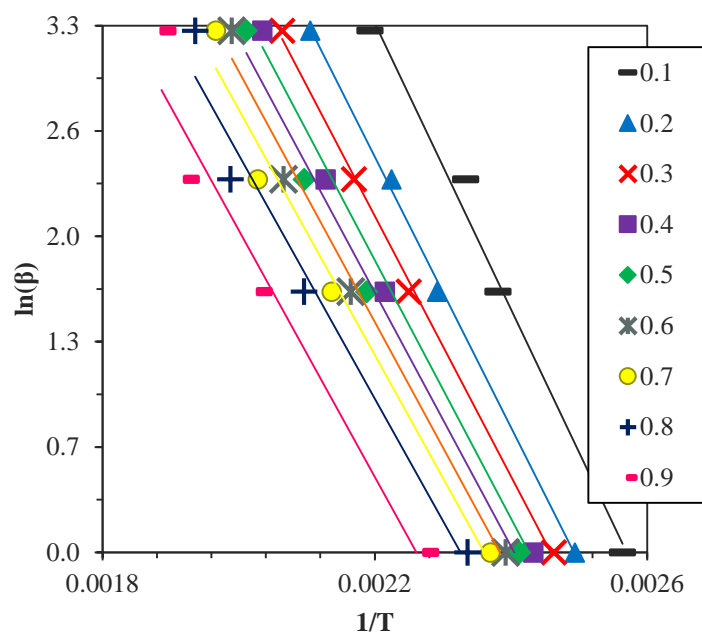
Figure 54. ln(β) vs. 1/T for TGDDM-5RA at conversions 10-90%.
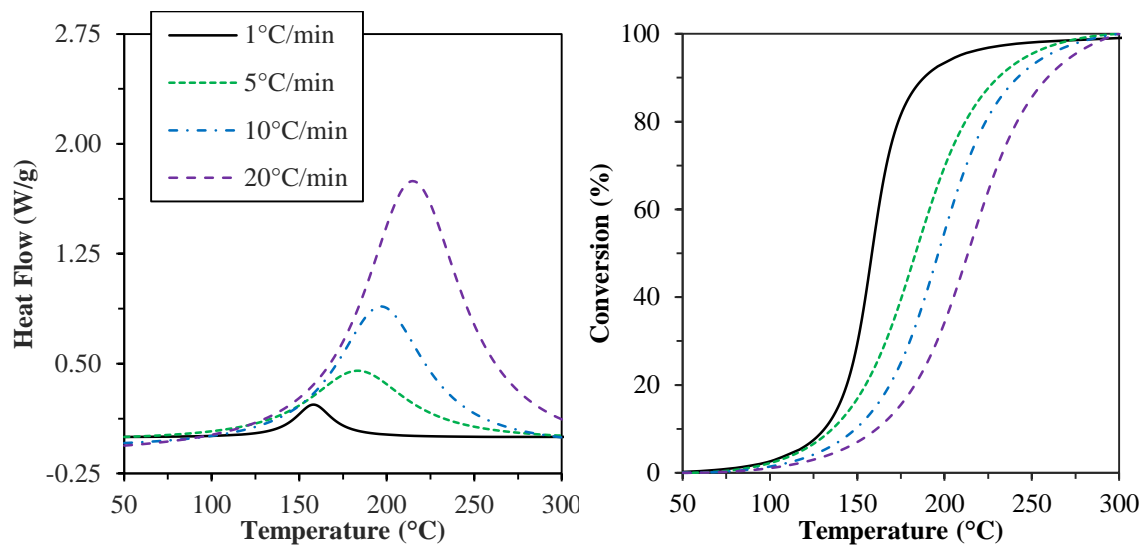
Figure 55. Heat flow vs. temperature and conversion vs. temperature for TGDDM-6RA.
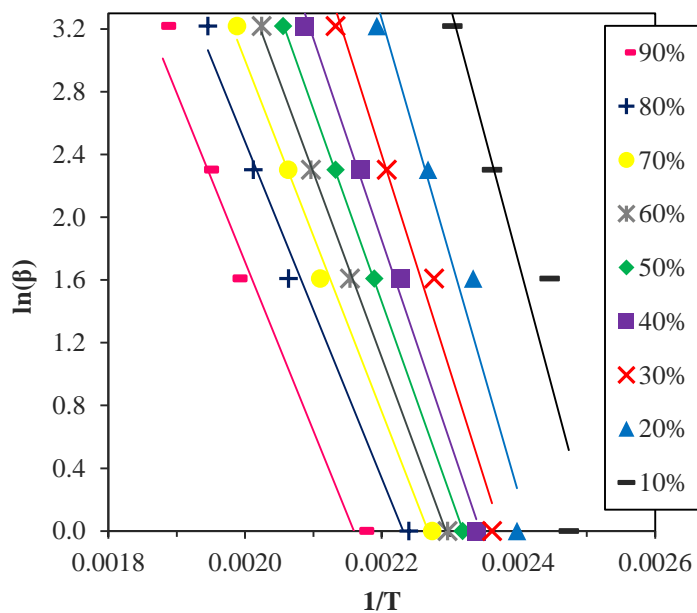
Figure 56. ln(β) vs. 1/T of TGDDM-6RA for conversions 10-90%.
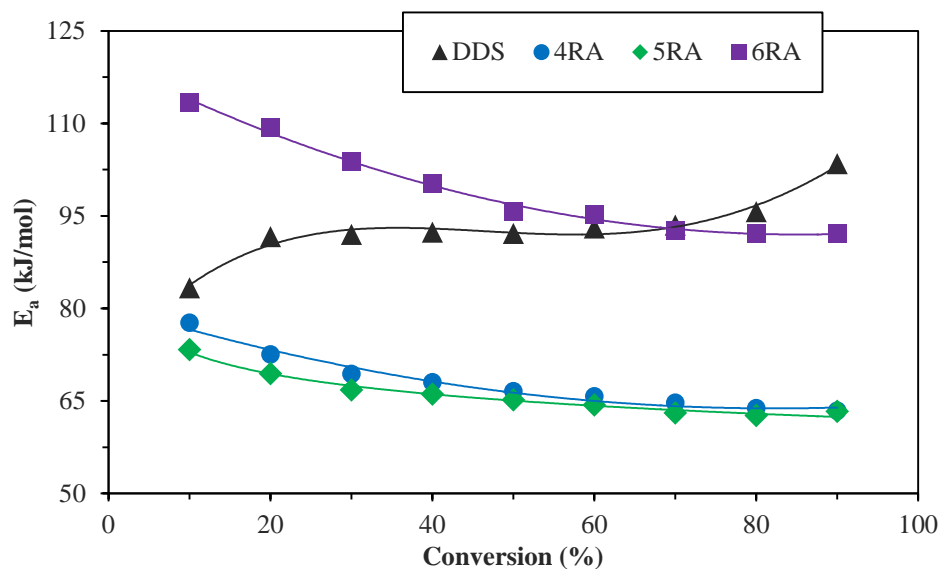
Figure 57. Activation energy vs. conversion comparison for each curative at conversions 10-90%.

Appreciable network development differences are shown by the E_a vs. conversion plot for DDS- and AEK-cured networks. While the activation energy of DDS-cured TGDDM increases with conversion, the similarly-shaped curves of AEK-cured networks showed a decrease in E_a with conversion. Typically in epoxy-amine cure reactions this decrease is attributed to autocatalysis from an increase in basicity as network formation progresses. This basicity increase can come from creation of secondary-hydroxyls and tertiary amines which are formed during the ring-opening of epoxides[120], but the theoretical molar concentration of hydroxyls and tertiary amines generated is the same for both AEK and DDS networks. Thus it is believed different chemical moieties are responsible. Small molecule, aliphatic tertiary amines have theoretical pKa values in the range of 5-11 while aromatic ketones have pKa's between 20-27.[121] Although the ketone moieties within the AEK curatives do not have extractable protons, it is hypothesized that

these groups enhance the basicity of the system and improve the catalysis efficiency of both secondary hydroxyls and tertiary amines. Similarly, group interactions are also increased with AEK-based networks due to increased free-volume from the larger AEK curatives. These enhanced interactions and mobility are also believed to contribute to autocatalysis.[122,123]

No trend in E_a magnitude with curative molecular weight was observed, but activation energy values can be described by the differences in chemical structure and reactivity. The strong electron-withdrawing sulfone group of DDS creates a lower nucleophilicity curative and therefore requires more thermal energy to overcome the initial stages of reaction. 4RA and 5RA systems have lower initial activation energies due to the higher-reactivity aminophenol end-group. Aminophenol's increased reactivity is afforded by the *para*-substitution which provides electron-donation through the ether-aryl-amine groups, creating a more nucleophilic curative compared to DDS. Due to 6RA's low-temperature-insolubility and elevated melt temperature, its activation energy magnitude is higher than those of the other three curatives and their respective networks. If 6RA was fully soluble within the TGDDM-epoxy pre-polymer, it is hypothesized that the activation energy magnitude would be similar to that of the 4- and 5-ring curatives.

Cure-reaction and α_R data for both cure prescriptions are shown by Table 15. The onset temperature, T_0, describes the initial stages of the cure reaction and was used to provide a relative reactivity of each AEK curative. DDS exhibited the highest onset temperature due to its low reactivity from the electron-withdrawing sulfone group and its low pKa. AEK-based networks started to react at temperatures ~20 °C lower than the DDS networks due to the *para*-aminophenol group. In amines used to cure epoxy, higher

pKa provides an increase in reactivity and depresses the gel-time. From an industrial standpoint, increased reaction kinetics translates to a decreased working time and out-life of the prepreg materials these are intended for. When compared between themselves, an increase in AEK curative molecular weight leads to a slight increase in T_0. This result is believed to result from the decrease in collision frequency upon increasing the physical length of the curative. From the T_0 results it was determined that the monomer stiffness and length at these relatively low molecular weights did not greatly affect the onset temperature.

Table 15

DSC data obtained from 10 °C/min ramp rates for degree of cure, α_R, calculations

Sample Name	T_0 °C	T_P °C	H_T J/g	$^aH_{C1}$ J/g	$^bH_{C2}$ J/g	$^a\alpha_{R1}$ (IC)	$^b\alpha_{R1}$ (PC)
DDS	183	227	430	31	-	0.93	>0.99
4RA	166	195	449	84	-	0.81	>0.99
5RA	168	205	404	78	-	0.81	>0.99
6RA	169	199	316	153	41	0.52	0.87

a: obtained after industrial cure

b: obtained after post cure

To limit functional-group conversion before experimentation and to obtain true reaction enthalpies, or heats of reaction (H_T), specimens were mixed without heat. Heated from room temperature to 350 °C, the measured H_T's were indicative of 100% degree of cure (according to the sensitivity of the DSC), which was confirmed upon reheating the H_T sample. No correlation between molecular weight and H_T was found, but it was

observed that 6RA-cured TGDDM had the lowest heat release upon curing. This can be attributed to the occurrence of simultaneous, opposing heat flow phenomena, where an endothermic melt transition (6RA T_m=195 °C) absorbs the heat released from the exothermic curing reaction. The additive nature of the positive and negative heat flows leads to an overall lower H_T.

After reheating an either industrially or post cured sample the observed residual exotherm (H_C) can be obtained for calculation of cure extent, α_R. It was found that α_R decreased with an increase in curative molecular weight. The low degree of cure in AEK-diamine networks is attributed to lower collision frequency and faster vitrification. First, the amine functionality of "short" DDS molecules more easily find reaction sites (ie. epoxides) compared to the "long" AEK molecules due to a higher mobility. DDS mobility is maintained past gelation and further into vitrification because of lower packing efficiency of the smaller curative, thus giving a higher cure extent. Additionally, industrial cured 6RA has a cure extent (0.54) close to the theoretical critical extent of reaction (0.5) according to the Carothers equation.[6] This low α_R is a result of the modified cure procedure required for the 6RA-TGDDM networks due to the curatives high melt temperature. Once at the cure temperature of 215 °C, the curative melts and both primary and secondary amines are quickly consumed. The fast reaction brings simultaneous gelation and vitrification which severely hinders the rate at which the network can cure. Even at the elevated cure temperature, 6RA-networks are produced with final conversions just over the gel point. A more gradual cure process occurs in other networks due to the amines' miscibilities at lower temperatures. After post curing the networks all α_R increased, with DDS, 4RA, and 5RA networks showing undetectable

residual exotherms and α_R greater than 0.99, and 6RA networks having cure extents around 87%. 6RA's lower α_R was later shown to improve to >97% by extending the post cure time to four hours.
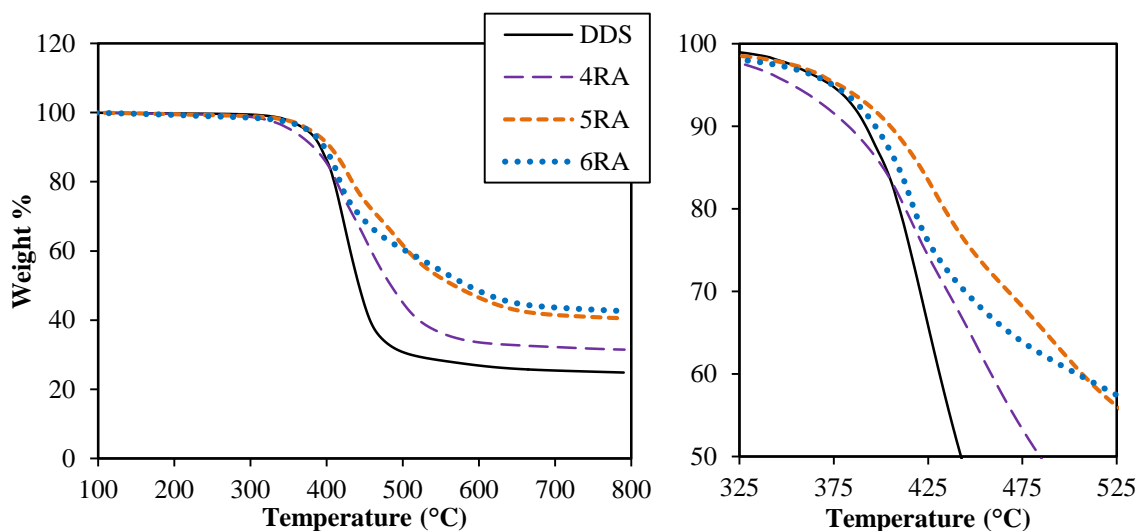
Figure 58. Thermal gravimetric temperature ramp data; cut-out shows degradation cross-over of the different networks.

TGA Characterization

Thermal gravimetric analysis was used to understand the effects of molecular weight and chemical structure on the thermal degradation of aryletherketone based networks, and representative TGA curves for post-cured samples are shown in Figure 58. The onset of degradation for all networks was above 360 °C and it was found that increasing crosslinker molecular weight does not have a significant effect on this onset temperature. However, it was shown that char yield increases with an increase in curative molecular weight. 4RA-TGDDM networks began to degrade earliest at ~364 °C but show a cross-over with DDS at around 415 °C which allowed for increased mass retention after

degradation. A similar, higher temperature cross-over occurs between 5RA and 6RA

networks, to produce the final crosslinker-molecular weight and char-yield trend.[124]

Degradation differences between cure schedule were minimal, and data for different

onset temperatures and char yields for both IC and PC samples is shown by Table 16.

Table 16

*Thermal degradation data for AEK networks after industrial cure (IC) and post cure
(PC) protocols; 5% weight loss used as degradation onset temperature*

Sample Name	5% Wt. Loss (°C)	10% Wt. Loss (°C)	Char at 600 °C (%)
DDS-IC	363.0	389.3	26.8
DDS-PC	364.4	389.7	26.9
4RA-IC	353.0	382.1	33.5
4RA-PC	357.8	384.2	34.4
5RA-IC	374.1	404.6	46.2
5RA-PC	377.5	407.0	46.5
6RA-IC	367.6	392.4	47.6
6RA-PC	375.3	396.4	48.4

Although there is an apparent trend between curative molecular weight and char-

yield, crosslinker chemical composition is believed to be a greater factor when

considering the thermal degradation properties of epoxy networks. The increase in char-

yield with increase in molecular weight is attributed less to the length of the molecule,

but to the increase in molar concentration of thermally stable aromatic-groups. 6RA-

based networks have ~2.1x the aromatic content (molar concentration) as the baseline DDS networks and therefore are provided with improved thermal stability. Furthermore, it has been previously reported that network incorporation of imide-containing structural units can significantly improve thermal stability properties, this has been attributed to crosslinking from reactions at the carbonyl-sites of the imide ring.[124,125] Similar to imide-based structural-units, the aryl-ether-ketone curatives employed herein contain high concentrations of ketone-units and it is believed that the ratio between aryl- and ketone-groups is a more important factor compared to molecular length. The 5RA-system, which has the highest ketone-to-aryl ratio of 0.4, has both the highest 5% and 10% weight loss temperatures. With a higher molar concentration of ketones, the 5RA-networks form more thermally stable degradation products compared to networks with lower concentrations and therefore create networks with higher char-yield.[55,56,125]

Cure schedule, industrial or post-cure, was found to have little effect on the thermal stability of the AEK networks. Comparison of each network showed that only minor increases in onset temperatures and char yield were found upon post curing. Although the IC networks have significantly lower degrees of cure (between 50-85%) and therefore a higher number of reactive end-groups, it was determined that the effects from aromatic content had a larger impact on the networks' thermal stability.

DMA Characterization

The effects of curative structure, crosslink molecular weight, and cure schedule on AEK-cured TGDDM thermomechanical properties were studied with DMA. Specifically, storage modulus (E') and the thermomechanical T_g from tan delta were analyzed. E' vs. temperature plots are found in Figures 59 and 60, and values at specific

temperatures are tabulated in Table 17. It should be noted that the discussion below is by no means exhaustive and that a more in-depth and comprehensive DMA analysis of the AEK networks studied herein is presented in Chapter V.
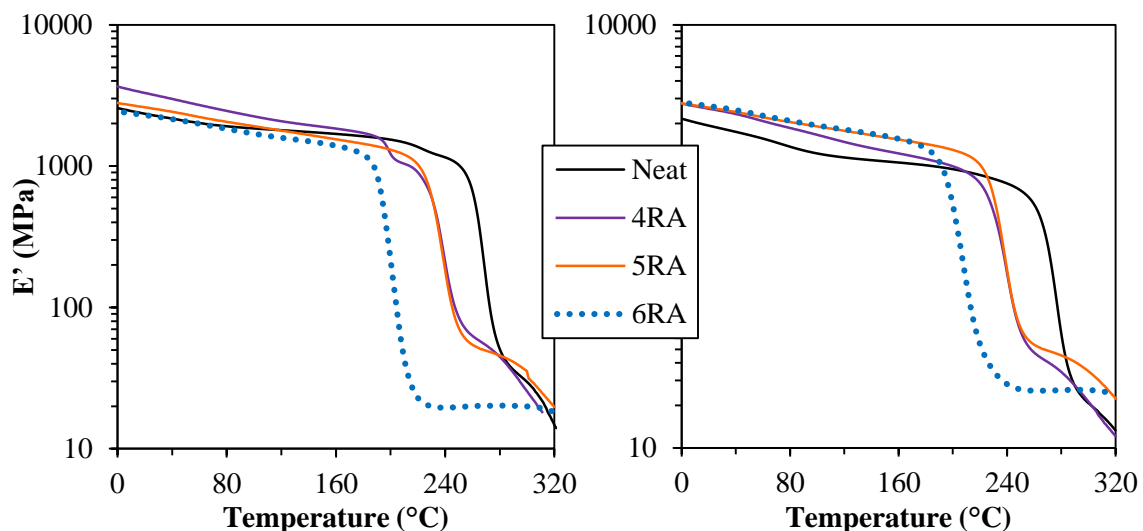
Figure 59. Storage modulus vs. temperature for IC and PC networks; obtained in tension-mode.

For IC-networks it was found that both 4-and 5-ring curatives have increased glassy-state storage moduli compared to DDS-based networks. 6RA-cured TGDDM showed slightly decreased moduli, but this is mainly attributed to the low degree of cure obtained for the first cure schedule. Except for 5-ring networks, the rubbery storage moduli (taken 30 °C above T_g) of IC-networks showed the expected trend, where an increase in curative molecular weight lead to a decrease in the observed rubbery modulus. 5RA-materials contained rubbery moduli that were higher than all other networks studied. This additional reinforcement is attributed to the *meta*-substitution within the curatives backbone, which hinders motions above T_g, resulting in antiplasticization.[126] Compared to IC-networks, PC-epoxies had lower E' for both 25 °C and 100 °C. This was

attributed to an increase in network connectivity and a decrease in the cohesive forces from secondary interactions of unconsumed functional groups.[127] PC-networks showed an increase in glassy-state moduli and a decrease in rubbery moduli (except 5RA) with an increase in curative molecular weight.
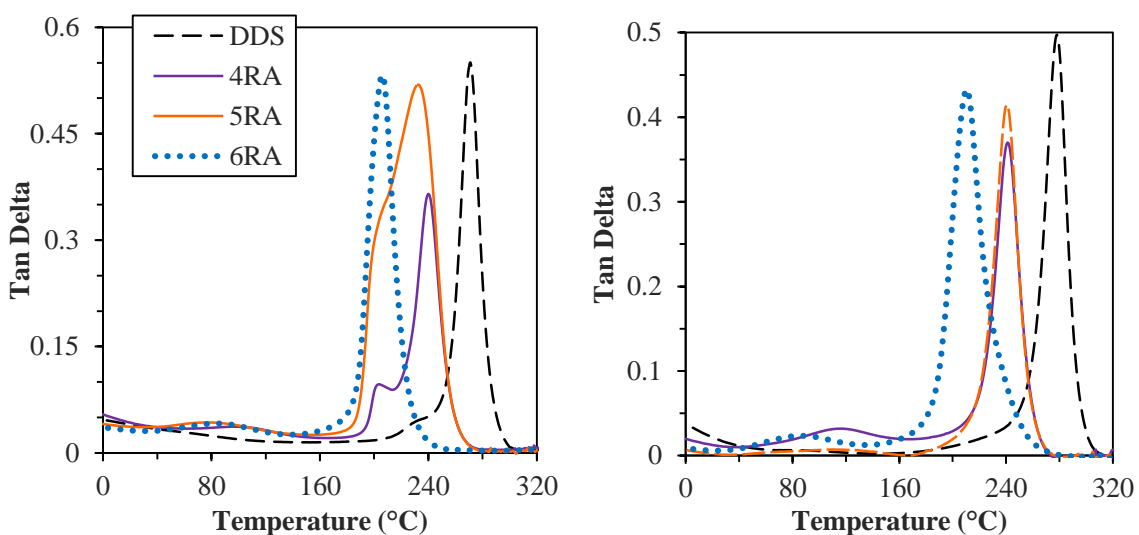
Figure 60. Tan delta vs. temperature for IC (left) and PC (right) networks.

The α-transition, related to the glass-transition, was above 200 °C for all networks. As expected, an increase in the crosslinker molecular weight led to a decrease in T_g, although it was found that 4RA- and 5RA-cured epoxies have similar T_g. The relatively stiff 4-ring curative had the second highest T_g due to its low mobility between the junction points, and it was expected that the 5-ring curative would have a decreased T_g because of its extra crosslink molecular weight. It is hypothesized that the aryl-ketone-aryl-ketone sub-structure with center meta-substitution of 5RA leads to a high stiffness structure that allows for almost zero-T_g knockdown from 4RA-cured networks. The lowest T_g was observed with the 6RA-cured networks and is attributed to the increased

molecular-level degrees of freedom that are incorporated from the relatively high molecular weight curative.

Table 17

Specific values from E' and tan delta plots for IC and PC networks

Sample Name	E', 25 °C MPa	E', 100 °C MPa	T_α (T_g) °C	E', T_g+30 °C MPa
		IC		
Neat	2300	1850	270	29
4RA	3210	2250	240	25
5RA	2570	1900	235	31
6RA	2270	1700	205	19
		PC		
Neat	1880	1250	275	37
4RA	2490	1660	241	30
5RA	2540	1850	240	32
6RA	2670	1930	210	27

It was found that industrially-cured networks contained bimodal α-transitions, whereas the post-cured samples showed discrete single peaks. These peak shoulders reveal the low degree of cure found by DSC, indicating that the networks contained regions of lower cure and crosslink density.[128,129] The multifunctionality of both the TGDDM and amine curatives leads to early network vitrification, and therefore locks the

network architecture in place at low temperatures. It is believed that lower crosslink density network contains microscale heterogeneities that have higher mobility in the T_g temperature range and therefore show a separate transition. Interestingly, 6RA-cured networks, the material with the lowest degree of cure, does not show a shoulder. It may be possible that the first cure prescription of 6RA networks allows a high degree of chain extension and little crosslinking, which would create a relatively homogeneous material, and prevent the appearance of a tan delta shoulder. Upon performing the post-cure and driving the network to full cure, the α-transition for each network was shifted to higher temperatures and the ultimate T_g was obtained. Furthermore, the α-transition's peak - width decreased after the post-cure, showing that network inhomogeneities were removed after advancing the cure state.

AEK networks contained both β- and γ-transitions which occurred around 60 – 160 °C and -120 – 40 °C respectively, while DDS networks demonstrated only a γ-transition. The strong β-transitions observed for AEK networks are attributed to larger molecular weight between crosslinks as compared to 44DDS-cured epoxy. In the glassy-state, industrially-cured networks showed relatively broad and shallow secondary-transitions due to poor mobility from enhanced non-bonded, cohesive forces.[46] It is hypothesized that the increased concentration of dangling ends in IC networks leads to improved molecular-level packing, which hinders both local and cooperative sub-T_g motions and also provides improved interactions between chains due to closer contact. These contributions lead to the lower intensity of observed transitions in industrially-cured networks. Furthermore, β- and γ-transitions of post-cured specimens were well-

defined transitions due to segmental mobility from the consumption of previously

described functional-groups and increase in network crosslinking.
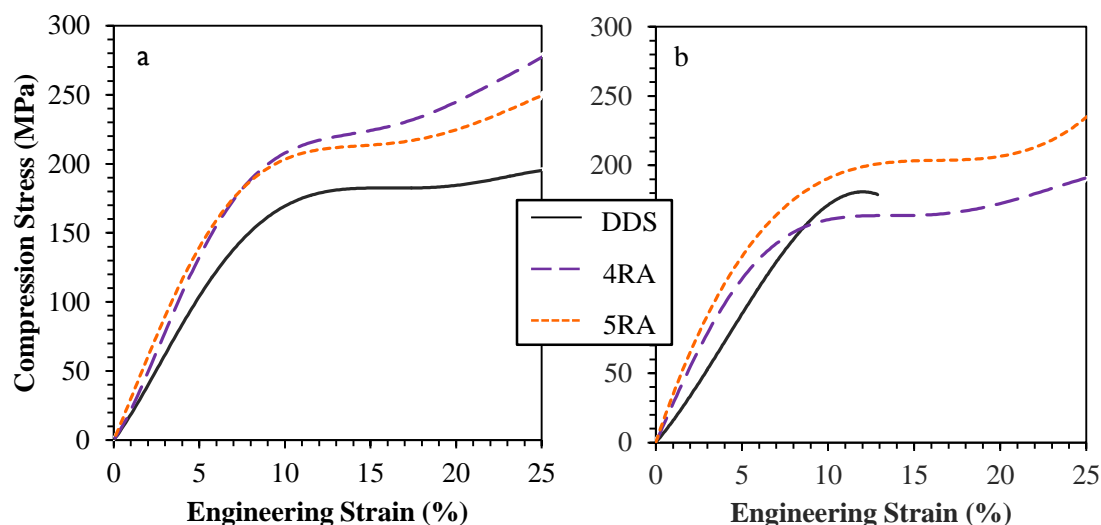
Figure 61. Uniaxial compression stress vs. strain curves for IC (a) and PC (b) networks.

Mechanical Properties

Uniaxial compression was performed on cylindrical samples to obtain mechanical

properties of the AEK networks developed. The deformations induced in compression do

not promote brittle fracture and thus the test has the ability to probe both pre- and post-

yield mechanical responses of highly crosslinked networks.[130] This information allows

for the calculation of the materials' true yield strain which is important for understanding

the distortional nature of each material. Figure 61 shows both IC and PC materials' stress

vs. strain curves and Table 18 describes the data obtained from the curves.

The compression results indicate that networks cured by AEK-amines have

significantly improved mechanical properties over DDS-cured epoxies. Compared to

DDS-networks, industrially-cured AEK compressive moduli increased by 20% and 23%

for 4- and 5-ring networks respectively. Furthermore, yield stress and yield strain for

AEK networks also increased by 19% and 18%, and 42% and 37%, respectively. Although the stress-strain plots only show strain values up to 25%, AEK networks were strained over 40% before ultimate failure, while IC-DDS networks failed catastrophically at approximately 25% strain. PC networks all show lower mechanical properties than the IC-networks, but PC-AEK materials still contain improved properties compared to PC-DDS. Furthermore, the highly crosslinked PC-DDS does not achieve high strain values before ultimate failure (~12%) whereas AEK networks do not fail until approximately 25% strain. It should be noted that because of the high melt temperature and fast cure kinetics, 6RA mechanical test specimens were not capable of being produced.

The improved mechanical properties found in AEK-based networks can be related to curative chemical structure and molecular weight. Previous molecular dynamics simulation data has shown that addition of certain chemical moieties can improve either the distortional or dilatational components of the epoxy network.[131] In terms of distortion, aryl-ether linkages allow for enhanced flexibility and local molecular mobility that provides a means of energy dissipation. 4RA-curatives have higher ether-to-aryl ratios than 5RA-curatives and thus we see improved strain-capability. Conversely, 5RA networks contain a higher concentration of aryl-ketone linkages which are comparatively stiffer than ethers and therefore has an improved linear-viscoelastic modulus. Additional stiffness is provided by the *meta*-substituted ring of 5RA which creates further hinders, or antiplasticizes, the motions of the network. Similar epoxy antiplasticization has been described for 33DDS-cured networks, which is known to have less glassy-state molecular motion from its fully *meta*-substitution.[33]

Table 18

Mechanical properties of AEK networks from uniaxial compression

Sample Name	Young's Modulus MPa	Yield Stress MPa	Yield Strain %	*Toughness MPa
IC				
DDS	2449±208	186.3±15.6	10.1±1.9	3738±212
4RA	2954±165	222.5±2.2	14.3±1.8	6100±197
5RA	3013±96	212.2±2.1	13.7±0.7	5856±163
6RA	-	-	-	-
PC				
DDS	2104±173	183.3±10.1	10.1±1.8	1448±135
4RA	2491±259	156.1±8.2	10.7±0.8	3108±216
5RA	2679±235	183.3±10.1	10.1±1.7	3986±202
6RA	-	-	-	-

*Toughness values calculated from integration of stress-strain curves between 0 and 25% strain

Molecular weight between crosslinks also appears to have an effect on the mechanical properties of the AEK-networks. Previously shown by Cook *et al*, increased molecular weight between junction points will decrease yield strength due to a decrease in the molecular units involved in the yield process.[130] In other words, yield involves both the crosslink sites and the structural units between them. Interestingly, AEK-networks demonstrated the opposite effect where an increase in curative molecular weight, and therefore the molecular weight between crosslinks, provided enhanced mechanical properties over the baseline DDS-networks. In previous epoxy research, mono-functional

chain extenders and difunctional oligomers are used to vary crosslink molecular weight

and keep a similar network chemistry. Consequently, this also varies theoretical crosslink

density.[29,40,130] AEK networks contain different molecular weights between junction

points, but because average functionality is the same, have equal theoretical crosslink

densities. It is believed that the theoretically-identical concentration of crosslink sites

leads to networks with equivalent junction-point hindrance. If the junction points are

equally hindered, than the molecular level rearrangements occur mainly between junction

points. Therefore, an increase in molecular weight between crosslinks allows for a means

of energy dissipation without yielding.

The effects of crosslink molecular weight are certainly coupled with degree of

cure for IC-networks, with DDS having the highest cure extent and lowest strength. This

connection is hypothesized to provide the enhanced strain and modulus values observed,

where a network with lower cure extent will contain less low-mobility junction points

and have improved strain. Additionally, the mobility provided by lower α_R allows for

improved secondary interactions and cohesive energy, and therefore modulus.[46]

Interestingly, before yield in IC-5RA, stress-strain curves cross over those of 4RA, which

results in 5RA's lower yield stress and strain. This increase in non-linear viscoelastic

behavior will be analyzed and described in the subsequent chapter.
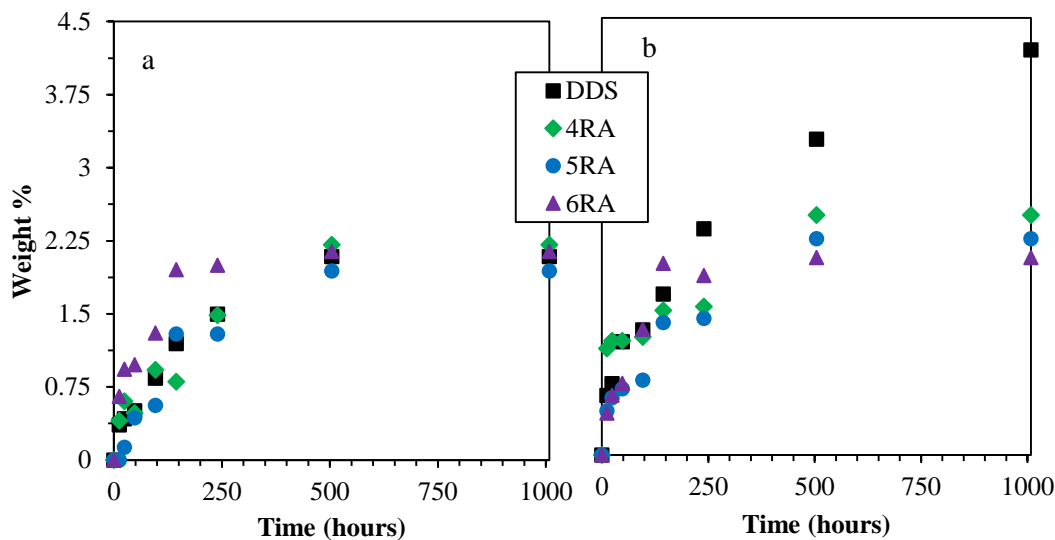
Figure 62. Water ingress as weight % uptake vs. time for IC (a) and PC (b) networks.

Moisture Ingress

Water uptake was performed for over 1000 hours at a constant temperature of 25 °C to study the effects of AEK-curative chemical structure, molecular weight, and cure prescription on the networks' fluid resistance and ingress. Figure 62 shows plots of water uptake vs. time as a weight percentage and for each cure schedule. Figure 63 displays M_t/M_{inf} vs. $t^{1/2}$ plots and subsequent analytical evaluations are summarized in Table 19. It is shown that IC networks have lower equilibrium water content than post-cured networks and no crosslink molecular weight dependence was observed. Post-cured AEK-networks show higher water uptake values as compared to industrially-cured materials, but upon driving cure, the rate and amount of water ingress in DDS-TGDDM networks greatly increases. After the allotted 1008 hours of moisture ingress testing, all networks, both IC and PC, contained less than 5 wt% water, and AEK networks had reached equilibrium values. Post-cured DDS-epoxies, although below 5 wt%, had not reached

equilibrium water content at 1008 hours, which is hypothesized to be near 6 wt% and 3000 hours according to previous reports.[12]

Table 19

Moisture ingress data combined with other network physical properties

Sample Name	Density (g/cm^3)	Equilib. Water Uptake (%)	Diffusivity $(x\ 10^{-9}\ cm^2/s)$	α_R (%)	[1]FV (%)
IC					
DDS	1.280	2.09	0.22	93	0.35
4RA	1.233	2.20	0.22	81	0.44
5RA	1.218	1.94	0.25	81	0.43
6RA	1.261	2.14	0.38	52	0.44
PC					
DDS	1.258	6.00	0.13	99	0.49
4RA	1.231	2.47	0.25	99	0.75
5RA	1.211	2.22	0.22	99	0.76
6RA	1.219	2.03	0.38	87	1.26

[1]Note: FV=free volume; simulated using different degrees of cure; IC - 80%, PC - 95%

Water uptake rate was further characterized using diffusivity data calculated from the slopes of the linear regression fit lines of M_t/M_{inf} vs. $t^{1/2}$ plots in Figure 62. At low uptake times, diffusivity, also known as the Fickian diffusion coefficient *D*, can be calculated using the following approximation:

$$\frac{M_t}{M_{inf}} = \frac{4}{L}\sqrt{\frac{Dt}{\pi}}$$

where M_t is the water absorption at time t, M_{inf} is the equilibrium water absorption, and L is half the sample thickness (accounts for diffusion from either side of the specimen). Water diffusion rate was found to increase with increasing crosslinker molecular weight for both IC and PC networks. Interestingly, moisture ingress rate in AEK networks is seemingly unaffected by increasing the degree of cure, where 4- and 5-ring networks have similar diffusivties after increasing conversion and diffusion in networks based on 6RA does not change with conversion. DDS-cured materials show a cure-state dependency with water diffusion rates in DDS networks showing a decrease with increasing degree of cure.
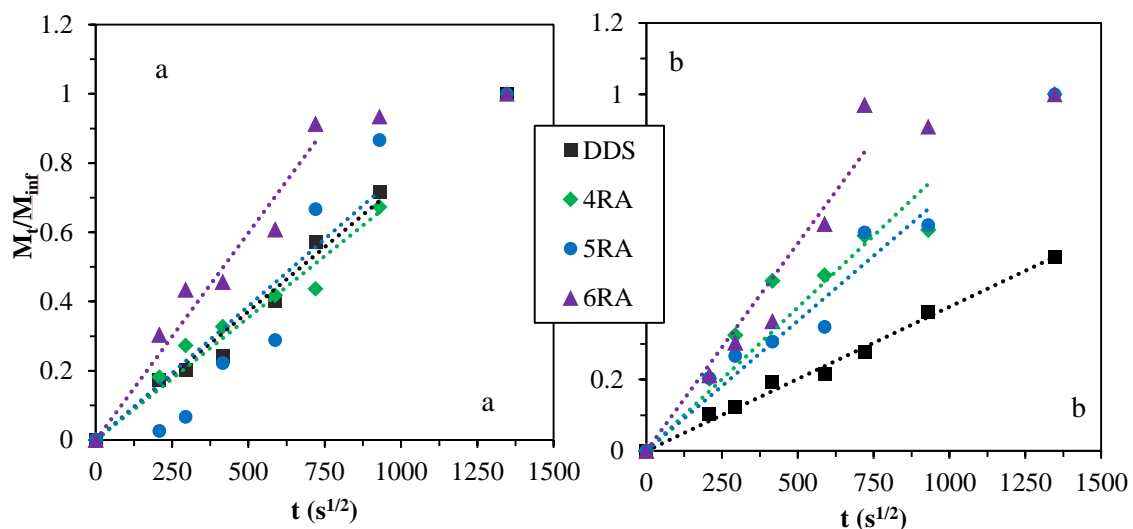
Figure 63. M_t/M_{inf} vs. $t^{1/2}$ for IC (a) and PC (b) networks.

Although they contain a lower equilibrium water content, IC networks show no clear trends regarding effects of chemical structure and molecular weight on moisture ingress. From a free-volume stand point, IC networks are assumed to have lower

fractional free volume due to chain packing of the dangling network ends; this is confirmed by the higher densities of IC-networks.[9,22] As a result of this enhanced molecular-level packing, the molecular weight contributions from each subsequently longer curative are over-come until a higher degree of cure is achieved. Upon increasing conversion with the post-cure, overall moisture content increased due to an increase in free volume.[132,133] Our group has recently supported that fractional and hole size free volumes are the key factors affecting overall moisture content and water diffusion, and that penetrant solubility plays a much smaller role.[12,134] These claims are further buttressed by the work herein. The lower cure extents in IC-networks produce materials with low FFV, high concentrations of polar groups, but low overall moisture content. However, high conversion PC-networks contained low concentrations of polar groups, increased fractional free volume and higher equilibrium water contents.

Additional support for the above claims was provided by room temperature free volume data which was calculated using molecular dynamics simulations. Free volumes of 4000 atom simulation cells were calculated for each network at two different cure states to imitate the degree of cure for both IC and PC networks (see *Chapter II* for experimental details). Through use of the Atoms, Volumes, and Surfaces tool in Materials Studio, a probe with a 1 Å radius (simulating size of positron) calculated the free volume between each molecule within each periodic cell (Table 19). Previous studies from our group have shown that the values of simulated free volume are not the same as those obtained experimentally, but the trends of are accurately predicted.[22] It was found that IC networks have lower free volume compared to PC networks and that AEK-networks have higher free volume than DDS-cured epoxy. This supports the moisture

ingress findings, where due to an increase in free volume there is an increase in equilibrium water content. Unexpectedly, it was found that DDS networks have lower free volume, but higher equilibrium water content. This was attributed to the sulfone group's affinity towards water.

While free volume may be the driving force for moisture ingress, polarity also appears to influence the networks. Increasing the molecular weight between crosslinks allows for two phenomena: firstly, the network's hydroxyl content is unchanged because average functionality is constant; secondly, the increase in crosslinker length increases polarity due to the higher concentrations of ethers and ketones, where the 6RA-network has the highest polarity. Although the hydroxyl content stays constant, the concentration of hydrogen-bonding moieties increases with ether and ketone content which is hypothesized to play a role in ingress rate and final moisture content.

Summary

This chapter examined the synthesis and characterization of multifunctional networks based on TGDDM-epoxy and aryletherketone-diamines. The effects of crosslinker molecular weight, chemical structure and cure protocol on network formation and cured network properties were assessed with DSC, TGA, DMA, mechanical testing, and water uptake. Network formation kinetics changed from noncatalytic to autocatalytic with the transition from DDS to AEK diamines. This change in mechanism is believed to play little role in final network conversion as vitrification occurs earlier in the cure protocol for AEK networks due to their higher nucleophilicity compared to DDS. AEK networks were found to be more thermally stable those based on DDS, and it was determined that thermal degradation properties improved with higher concentrations of

ketone-moieties. As expected, the glass transition decreased as crosslinker molecular weight increased, but interestingly, the elastic storage modulus showed the opposite trend. This antiplasticization was also observed in the yield strain and Young's modulus from compression testing. Finally, water uptake characteristics were found to vary depending on cure protocol, with industrially cured networks revealing similar ingress and diffusion values. The interesting properties of aryletherketone-cured epoxy networks are hypothesized to be a factor of improved secondary interactions and increased free volume, which will be discussed in the subsequent chapters.

CHAPTER V

MULTIFUNCTIONAL ARYLETHERKETONE NETWORKS: RELATING

MOLECULAR-LEVEL ATTRIBUTES TO BULK PROPERTIES

Objective

The goal of this chapter is to provide an in-depth analysis of the physical characteristics that affect AEK networks. Primarily, it is the purpose of this chapter to discuss the secondary relaxations and molecular interactions responsible for the unique properties observed in Chapter IV. Observations from dynamic mechanical analysis are correlated with molecular modeling and PALS data to relate molecular-level structures to bulk mechanical properties. Sub-T_g activation energies for γ- and β-relaxations were found to correlate with crosslink molecular weight and molecular motions for each were postulated. Molecular dynamics simulations provided insight into these motions and their origins through characterization of secondary interactions, junction-point end-to-end distances, and dihedral angles. It was found that a combination of increased cohesion, segmental folding, and broad backbone angle distributions provided the unusual property enhancements in AEK networks. Free volume measurements and simulations provided further validation of network-segment conformations. Hole size free volume was found to be similar in all networks studied, but fractional free volume was found to increase with AEK molecular weight. These two trends link the molecular motions observed in DMA to the simulated conformations. This chapter also provides additional comprehension of tetrafunctional epoxy-amine networks in terms of crosslink density, molecular weight between crosslinks, and chemical composition.

Results and Discussion

The networks studied herein were synthesized from the tetrafunctional epoxy TGDDM and one of four different tetrafunctional diamines: 44DDS, 4RA, 5RA, or 6RA. Networks were subjected to both an initial and post cure (see *Chapter II)* to drive functional group conversion to near 100%. The high cure extent allowed for study of the effects of crosslink molecular weight, M_c, by limiting the concentration of dangling ends and thus assuring constant junction point concentration. DMA was utilized to understand the relationships between M_c, secondary interactions, and chemical composition through sub-T_g relaxations. PALS and molecular simulations were performed to provide increased comprehension of the DMA data and to further probe the molecular mechanisms behind the bulk properties of AEK networks.

DMA Results

An in-depth thermomechanical characterization using DMA was performed to help understand the molecular origins of AEK-network bulk mechanical properties. Crosslink density (ν) and molecular weight between crosslinks (M_c) have been shown to play significant roles in epoxy-amine network properties[3,29,40,135] and were therefore studied here. Crosslink density and M_c were calculated from the rubbery regime of storage modulus (E_r) and are found in Table 20. DDS materials have the most densely crosslinked networks and the smallest M_c. Expectedly, AEK networks are of lower ν and higher M_c. However, the experimentally obtained values do not follow the theoretical trends of decreasing ν and increasing M_c with diamine molecular weight. It was found that 5RA has the densest crosslinking at 2.36 mol/cm^3, with 4RA and 6RA falling below at 2.21 and 2.11 mol/cm^3, respectively. The networks studied herein were driven to high

conversions and therefore it was assumed that irregularities in ν and M_c were not a factor of cure conversion. 5RA's elevated crosslink density is ascribed to the *meta*-substituted center ring which artificially stiffens the rubbery network by its lack of mobility and volume filling.[33] Crosslink density and M_c of 4RA and 6RA align well with theoretical calculations due to the higher concentration of flexible ether linkages of the fully *para*-substituted backbone. The rubbery-state stiffness of 5RA is believed to translate to less mobility in the glassy-state and is thought to reduce the number of molecular-level rearrangements these segments can endure. Analysis of the glassy state molecular mobility is presented below.

Table 20

Density, crosslink density, and molecular weight between crosslinks of networks herein

Sample Name	ρ g/cm^3	T K	E_r MPa	ν mol/cm^3	$M_{c\text{-Exp}}$ g/mol	$M_{c\text{-Th}}$ g/mol
DDS	1.258	582	37	2.55	494	670
4RA	1.231	545	30	2.21	557	820
5RA	1.211	544	32	2.36	513	922
6RA	1.219	514	27	2.11	579	1014

1: $M_{c\text{-Exp}}$ = experimentally determined crosslink molecular weight

2: $M_{c\text{-Th}}$ = theoretically calculated crosslink molecular weight

Molecular motions and relaxations above and below the glass transition are important phenomena that have implications on the engineering properties of glassy polymer networks. With the help of DMA and the thermomechanical loss tangent, it is

possible to probe these relaxations and gain insight into macroscale behavior. Tan delta vs. temperature plots containing the β- and γ-transitions at varied frequencies for DDS and AEK networks are shown in Figures 64 and 65. Firstly, it was found that DDS-based networks do not have clearly separated β- and γ-transitions, whereas all three AEK networks do. This phenomenon is attributed M_c. In epoxy-amine networks, high local crosslink density and stiff curatives prohibit segmental motions, thus reducing β-relaxations.[27] An increase in molecular weight between crosslinks relates to a decrease in local density which provides volume for molecular mobility. The volume increase is further compounded with temperature, and therefore relaxations seen between 30 and 150 °C are separated from sub-ambient relaxations with an increase in M_c. Additionally, it is hypothesized that the observed β-transitions of AEK-networks are not related to motions of TGDDM units because of the lack of such a transition in the DDS network. Finally, the dual β- and γ-transitions of AEK networks follow predicted frequency trends (discussed below), but the observed sub-T_g tan delta baselines are somewhat sporadic. Therefore the subsequent calculations and analysis were performed on baseline corrected tan delta curves using peak-fit functions from the *Origin* software package.
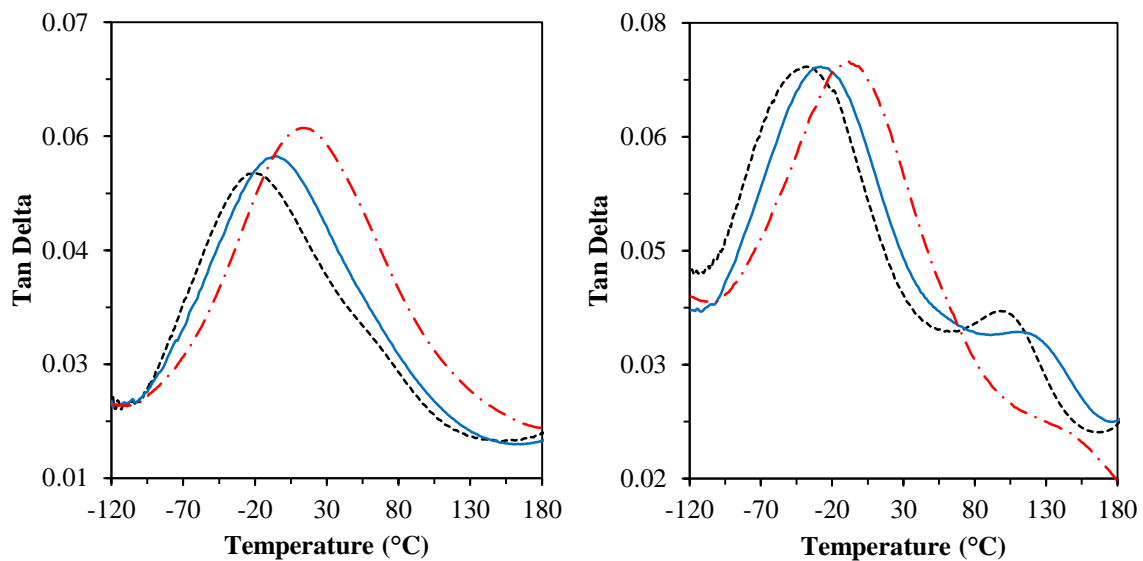
Figure 64. Uncorrected sub-Tg tan delta vs. temperature plots at 1.0 (black dot), 10.0 (blue solid line), 100.0 Hz (red dash-dot); 0.1 Hz plot removed for clarity; DDS (left), 4RA (right).
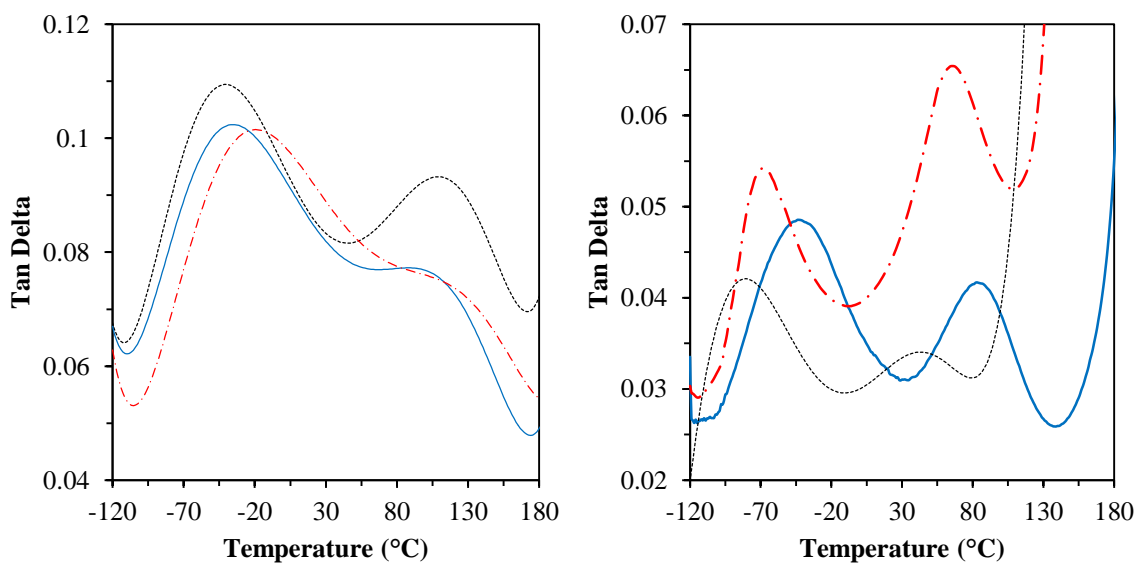
Figure 65. Uncorrected sub-Tg tan delta vs. temperature plots at 1.0 (black dot), 10.0 (blue solid line), 100.0 Hz (red dash-dot); 0.1 Hz plot removed for clarity; 5RA (left), 6RA (right).

Table 21

DMA tan delta γ-peak analysis; values from 1 Hz curve

Sample Name	Peak Maximum °C	FWHM °C	Peak Area °C
Gamma			
DDS	-23	118.8	8.8
4RA	-38	85.6	7.8
5RA	-48	79.1	4.0
6RA	-74	74.7	3.4

Specific values from peak analysis of each network's γ- and β- transitions are organized in Tables 21 and 22, respectively. Peak maxima, full widths at half maxima (FWHM), and peak areas were assessed using baseline corrected 1 Hz tan delta plots. Network γ-transition peak maxima, FHWM, and peak area were all found to be decrease with an increase in M_c. From peak analysis it is proposed sub-T_g motions of DDS have some degree of cooperativity. The high crosslink density of TGDDM-DDS severely hinders glassy state motions, requiring higher temperatures to activate such relaxations; this is manifested in the high peak maximum. Molecular-level encumbrances of tightly crosslinked networks prevent purely local motions due to segment packing, and without another mechanism for relaxation, no transition would be observed.[45,136] However, large peak breadths such as those observed in DDS-networks are associated with heterogeneous or complex motions.[35,37] Complexity can initiate other, simpler motions. Therefore, additional rearrangements of DDS segments are hypothesized to provide secondary mechanisms which initiate the observed motions in the γ-region.[38] AEK

networks follow similar trends. Peak values of AEK-γ are lower than that of DDS due to the higher mobility from decreased crosslink density. Also, the lowest crosslink density 6RA has the lowest γ-peak maximum. This agrees well with the above analysis and provides insight into the separated local and segmental motions.

Table 22

DMA tan delta β-peak analysis, values from 1 Hz curve

Sample	Maximum	FWHM	Area
Name	°C	°C	°C
Beta			
DDS	-	-	-
4RA	105	46.8	1.2
5RA	110	84.7	1.4
6RA	83	54.6	1.6

More complicated trends were observed in the β-transitions. Peak analysis revealed 5RA networks had the highest peak maximum, FWHM, and peak area; no M_c trend was observed. Similar to experimental crosslink density and M_c, the lack of correlation was attributed to the chemical structures of AEK amines. The supplementary stiffness of 5RA has been previously attributed to its *meta*-substituted backbone moiety.[137] This extra stiffness is exhibited by lower molecular mobility and therefore, similar to DDS's γ-transition, requires higher temperatures to activate the motion. Interestingly, 4RA and 5RA networks have similar β-peak temperatures but 4RA relaxations occur in a temperature range half that of 5RA. Likewise, 4RA and 6RA have

similar FWHM. This behavior is also attributed to the antiplasticization effects of 5RA's center ring. The *para*-substitution of ketones and ethers in 4RA and 6RA segments provides increased network-level conformational rearrangement compared to 5RA segments. This is hypothesized to allow motions related to the β-relaxation to occur in a similar time scale, or relaxation time, and thus a narrow peak breadth is produced. Relaxation contributions from locally-stiff *meta*-substituted rings in 5RA require longer relaxation times and higher temperatures and creates the broad β-peaks in 5RA networks. Hypothetical motions of both the γ- and β-relaxations are displayed in (Figure 68 and 69).

Sub-T_g relaxations are both temperature and frequency dependent and follow Arrhenius-type relationships.[38] This behavior allows for the calculation of relaxation activation energy, and the following form of the Arrhenius equation was applied to calculate E_a,

$$\log\frac{f}{f_o} = -\frac{2.3E_a}{R}\left[\frac{1}{T} - \frac{1}{T_o}\right],$$

where T and T_o represent the temperatures at which frequencies f and f_o are used to obtain the maximum in tan delta, and R is the gas constant. Figures 66 and 67 show typical plots for Arrhenius analysis of the β- and γ-transitions, where the slopes of each line are used to calculate activation energy, E_a (Table 23).
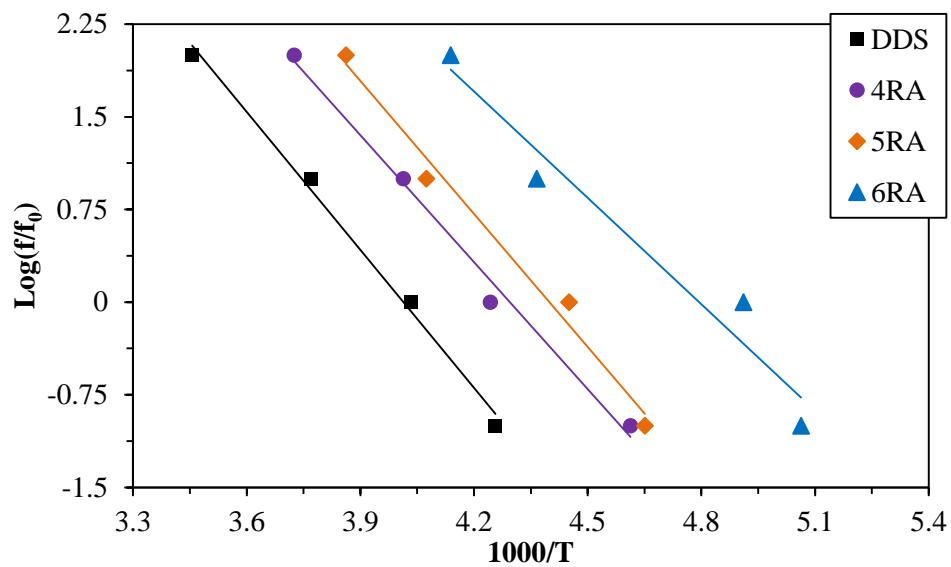
Figure 66. Log (*f/f₀*) vs. 1000/T Arrhenius plots for the γ-transition of all networks.
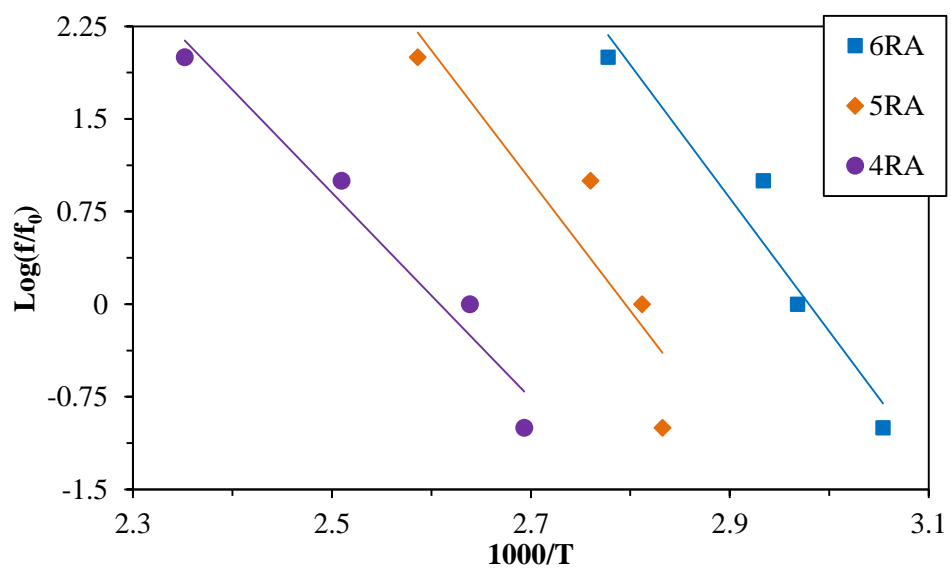
Figure 67. Log (*f/f₀*) vs. 1000/T Arrhenius plots for the β-transition of AEK networks.

Table 23

Activation energies associated with sub-Tg thermal relaxations studied herein

Sample Name	E_a, γ kJ/mol	E_a, β kJ/mol
DDS	31.0	-
4RA	28.5	69.2
5RA	27.9	87.6
6RA	23.9	89.7

E_a of the γ-transition was found to decrease when the curative was changed from DDS to AEK-diamines. This collective trend was attributed to an increase in mobility from the increase in M_c. Molecular-level hindrances are reduced with M_c to create lower energy barriers for simple motions of the γ-relaxation. On the other hand, E_a of the β-transition shows the reverse M_c trend and increases with crosslink molecular weight. E_a's obtained for the β-relaxation are also 2-3 times larger than those for the γ-transition. The difference in E_a magnitude has been previously attributed to the type of molecular motions associated with the γ- and β-relaxation, where the former is typically attributed to simple motions such as ring-flips[33,37] and the latter is attributed to cooperative, segmental motions of repeat units.[32,138] The larger size-scale motions of the β-transition require significantly more energy to overcome the thermodynamic barrier to move crosslinked segments, and are therefore twice as high. It is interesting that β-peak activation energies appear to correspond only with M_c and not with chemical composition

such as peak maxima and FWHM. This result is puzzling, additional analysis using

dielectric spectroscopy may provide more definitive E_a results.
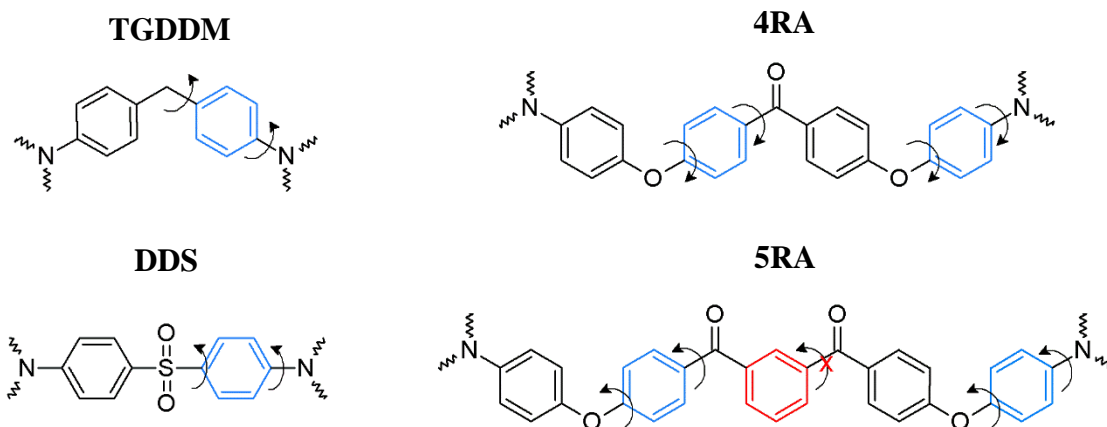
Figure 68. Molecular motions involved in simple relaxations represented by network segments studied here; red *meta*-substituted ring in 5RA represents an unlikely motion; motions of 6RA are similar to those of 4RA and not shown.

Direct determination of the units involved in sub-T_g motions is difficult without

advanced techniques such as solid state NMR or neutron scattering. Nevertheless, it was

hypothesized above that motions of AEK network γ-transitions are simple, local motions.

This is attributed to the transitions decreasing activation energies with increasing M_c. It is

then reasonable to believe that these simple motions are from 180° phenyl-ring flips from

curative and TGDDM units. However, previous reports suggest that low temperature

transitions in linear PEEK are cooperative processes and cannot result from motions of a

single moiety in a monomer unit.[139,140] These studies were performed using both

amorphous and crystalline polymers and showed that PEEK contains one broad, low

temperature transition. David *et al.* attributed PEEK's sub-T_g transition to motional

rearrangement of 5–9 phenyl-rings, describing the type of relaxation as "crank-shaft".[139]

In contrast, materials studied herein are crosslinked networks and are not capable of such large segmental rearrangements; Figure 68 shows possible molecular motions of DDS and AEK γ-motions. Therefore, as both DDS and AEK networks have γ-events with relatively low E_a, the observed transitions are suggested to occur from relatively simple motions of curative and TGDDM units.
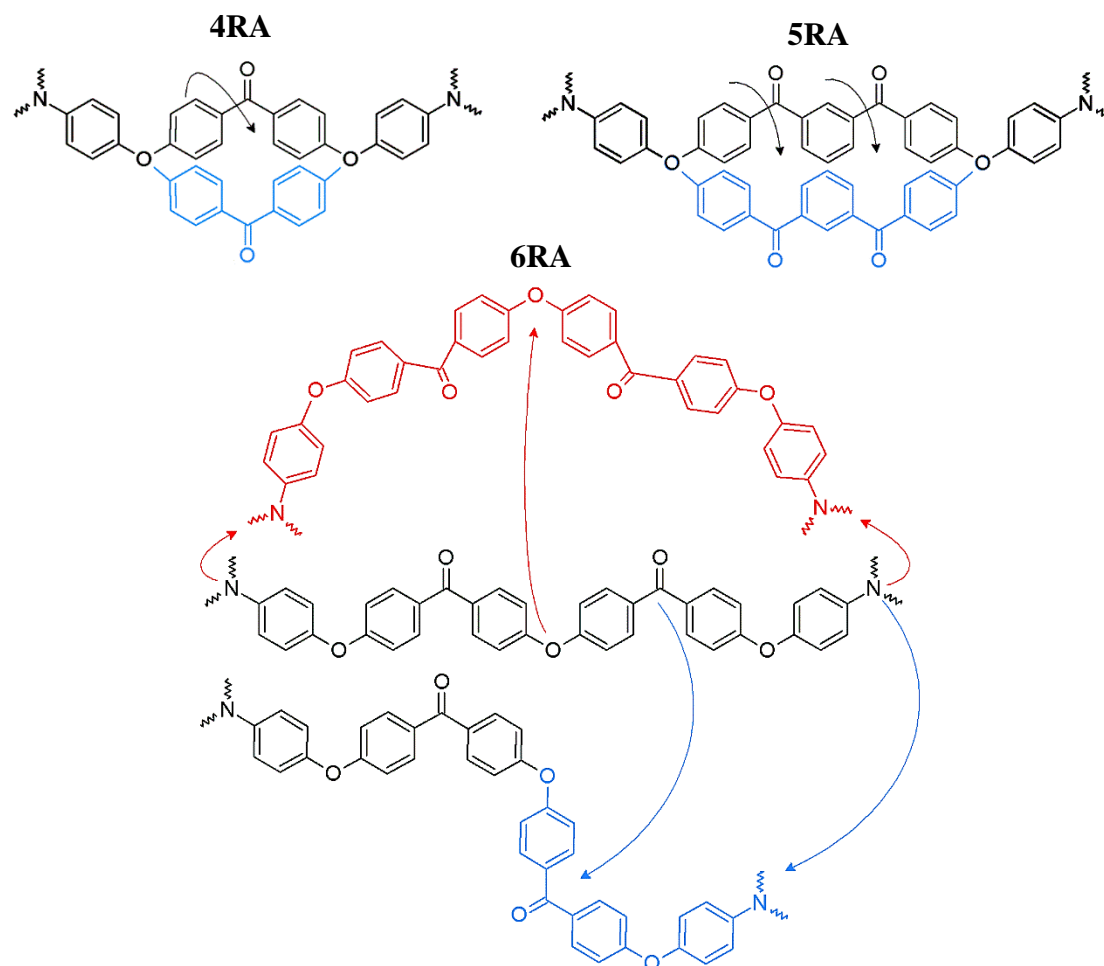
Figure 69. Hypothetical molecular motions of the β-transition in AEK networks.

Although it is believed that observed γ-transitions are composed mainly of local motions, David's hypothesis of multi-phenyl-ring processes may describe the high activation energies of the β-transitions herein. Figure 69 demonstrates motions of

segmental rearrangements in the AEK networks studied. It should be noted that the motions displayed are by no means exhaustive for each type of network. 4RA and 5RA segments likely contain the long-range cooperative motions displayed by 6RAs image but were left out for brevity. 4RA-segments have less conformations and require less space to rearrange compared to 5RA and 6RA segments, and thus, 4RA segments have the lowest β-relaxation E_a (69 kJ/mol). Additional factors contribute to the high E_a of 5RA and 6RA segments (88 and 90 kJ/mol, respectively). The energy barrier of 5RA is attributed its stiffness from the *meta*-substitution, which creates a relaxation process comprising at least three phenyl rings and likely requires significant cooperativity. On the other hand, 6RAs high activation energy is ascribed to its high molecular weight and the significant volume required to allow for the long-range motions associated with such segment length.

Modeling Results

Molecular dynamics simulations of AEK networks were performed to both visualize and further quantify the motions which occur when these polymers undergo deformation. Networks were created with the intent to emulate the materials studied experimentally, and were cured to a functional-group conversion extent of 0.9. After network "synthesis" and cell energy minimization, sets of atoms were labeled to follow specific sites while straining the simulation cell. Specifically, moieties capable of hydrogen-bonding including nitrogen, oxygen (ether, ketone, and hydroxyl), sulfur, and hydroxyl-hydrogen atoms were labeled for analysis. Also, specific functional groups and their torsion-angles, including aryl-ether, aryl-ketone, and aryl-sulfone groups, were labeled to follow angle changes during strain. Finally, the end-to-end distance between

crosslink junction points (ie. the distance between nitrogen atoms) were labeled and

followed throughout the simulations.
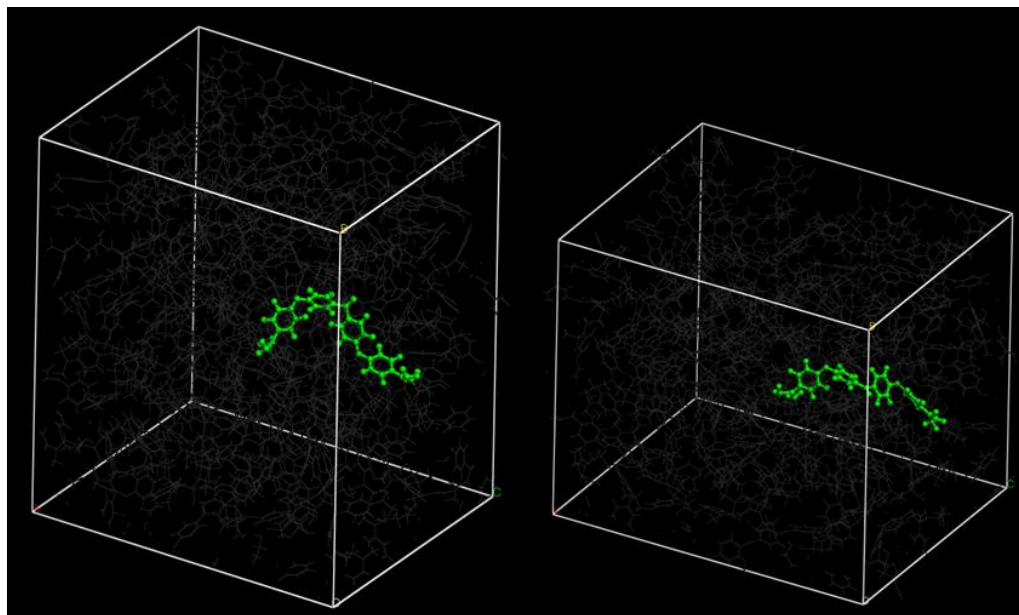
Figure 70. Example simulation cells with marked network segments to follow during
strain simulation; 0% strain (left), 25% strain (right).

Simulation cells were strained in increments of 0.1% until 25% strain. Figure 71

shows the simulated stress vs. strain curves of the studied networks. A comparison of the

simulated mechanical property values and those obtained experimentally is shown by

Table 24. Simulated compression property trends agree well with experimentally

obtained values for the AEK networks. Modeling confirmed the observed decrease in

stress and strain with increasing M_c as well as the increase in elastic moduli with M_c.

However, simulated stress and strain values for DDS networks are much higher than the

corresponding experimental values and do not agree with experimental trends; modulus

trends appear to be in agreement. This discrepancy is attributed to difficulties in energy

minimization with densely crosslink networks such as multifunctional TGDDM-DDS.

Further simulation is required to validate the DDS results.
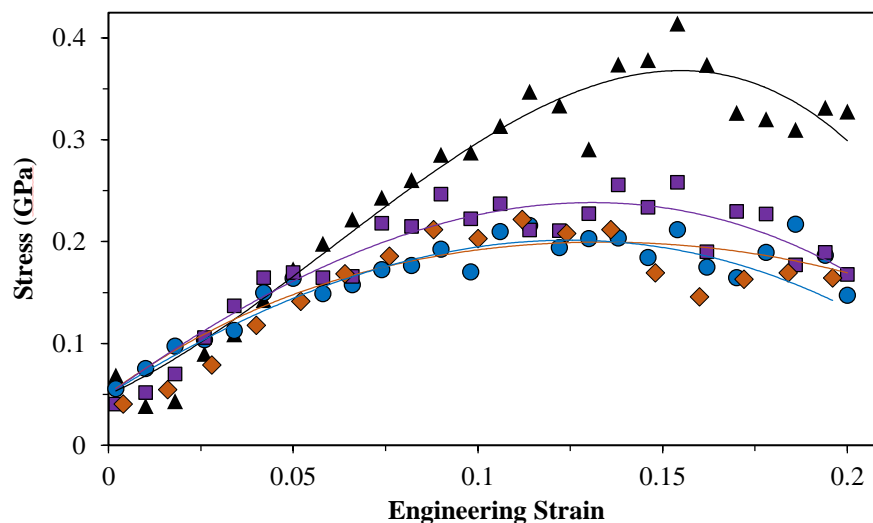
Figure 71. Simulated stress vs. strain curves, DDS (black triangles), 4RA (purple squares), 5RA (orange diamonds), 6RA (blue circles); third-order polynomial fits used to determine strain-at-yield; each curve an average of three simulations.

Table 24

Comparison of simulated and experimental mechanical properties obtained in compression

Sample	Simulated			Experimental		
Name	Stress	Strain	Modulus	Stress	Strain	Modulus
	MPa	%	MPa	MPa	%	MPa
DDS	410	15	3010	185	10	2500
4RA	260	13	3500	220	14	2900
5RA	240	12	3860	210	13	3010
6RA	220	11	4410	-	-	-

Note: Both moduli values calculated from slope of linear fit between 1% and 2% strain

The relatively good agreement between simulated and experimental mechanical properties provided confidence for more in-depth analyses of the simulation data. Secondary interactions between specific atoms were characterized to further establish the molecular origins of the improved experimental modulus, stress, and strain-capability of AEK networks. First, cohesive energies of entire simulated networks were estimated to uncover the source of improved compression moduli. It has been previously suggested that room temperature elastic modulus increases with an increase in cohesive energy, and therefore understanding the molecular contributions that effect cohesion are important.[46] In *Materials Studio* it is not possible to calculate cohesive energy of an infinite simulation cell (such as the amorphous cells used throughout this work). Consequently, cohesive energy (E_{coh}) was calculated using the following relationship[141],

$$E_{coh} \approx -E_{intermolecular} = E_{intramolecular} - E_{total}$$

where $E_{intermolecular}$ is the simulation cell energy contribution from intermolecular interactions/energy, $E_{intramolecular}$ is the energy contribution from intramolecular energy, and E_{total} is the total cell energy after minimization. The result is plotted in Figure 72 as a function of the crosslink molecular weight and then in Figure 73 against simulated and experimental compressive moduli data. These two plots show that an increase in M_c leads to an increase in cohesive energy and therefore an increase in the low strain, room temperature modulus. It is hypothesized that the observed relationships are due to improved secondary interactions from the extra volume brought about by increased M_c.[131] AEK networks have higher concentrations of hydrogen-bonding moieties allowing for increases in both quantity and strength of the secondary bonds. Furthermore, it has been shown that sulfones have poor hydrogen bonding capability due to repulsive

electrostatic forces and poor bond stability.[142,143] The combination of increased strength and concentration of interactions from larger M_c leads to the observed network cohesion.
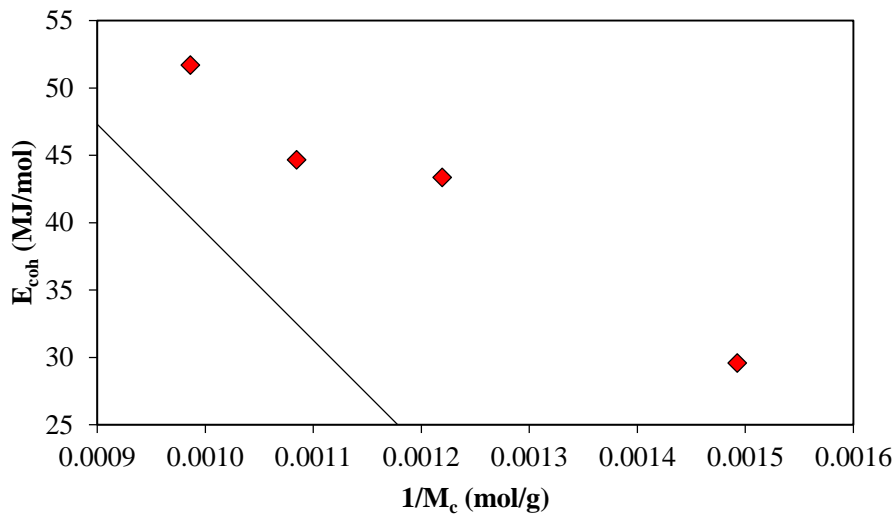
Figure 72. Cohesive energy vs. inverse molecular weight between crosslinks; best fit line $R^2 = 0.9614$.
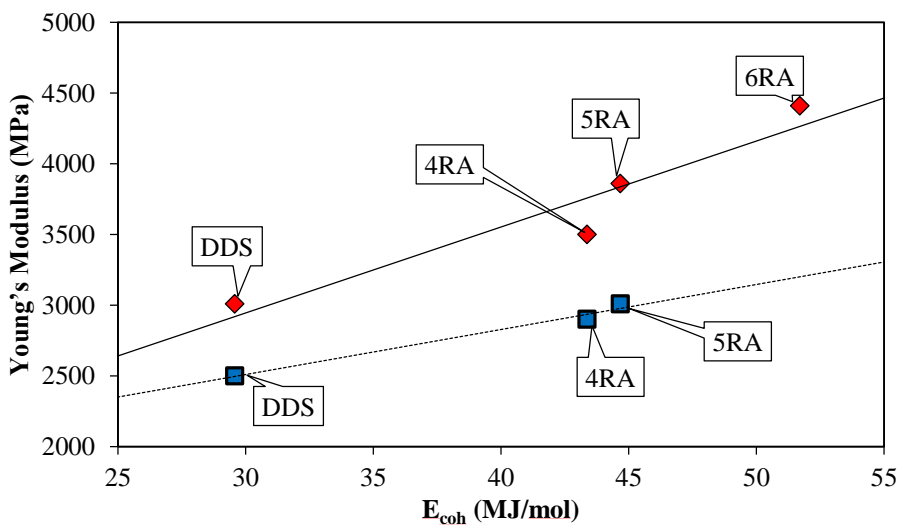
Figure 73. Simulated (red diamonds) and experimental (blue squares) Young's modulus vs. cohesive energy; simulated best fit line $R^2 = 0.9078$, experimental best fit line $R^2 = 0.9835$.

The above analysis was investigated further by use of radial distribution function (RDF) analysis in *Materials Studio.* RDFs are a type of pair correlation function that describe how atoms are packed together in a given space. RDFs are typically plotted as a function of interatomic separation radius, r, with the height of the RDF peak being related to the strength and concentration of the observed interaction. RDFs are useful in describing average structures of disordered materials such as the network glasses herein. The first pair of hydrogen-bonding atoms correlated were nitrogen and hydroxyl-hydrogen within the linear viscoelastic regime of the stress-strain curves (~0-4% strain), and are shown in Figure 74. The peaks at 2.8-3.0 Å and 3.8-4.0 Å have been previously described as regular and twist H-bonds, respectively.[144] It can been seen that both types of H-bonds are in higher concentration in AEK networks. Furthermore, because H-bonding distance specifies the strength of the bond, the narrow breadth of the AEK H-bond peaks indicates that the distribution of interactions is lower and therefore the strength of these bonds is higher.[144,145]
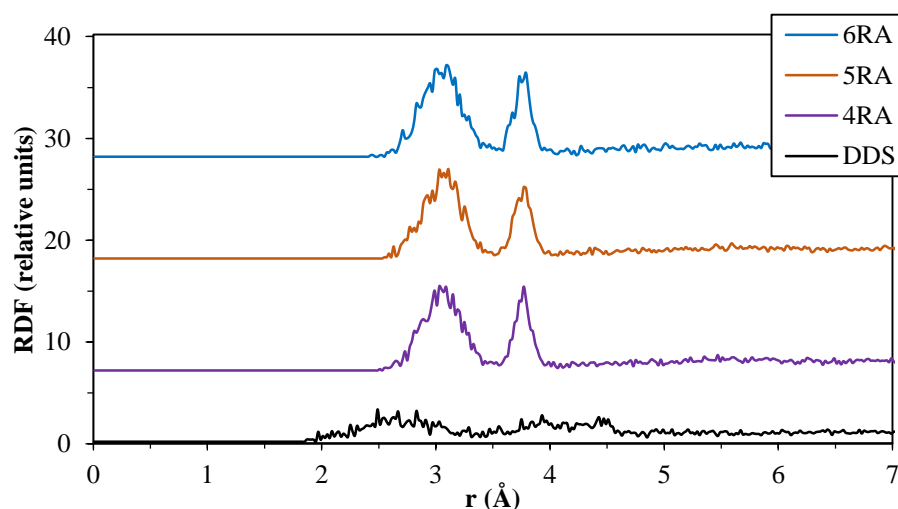
Figure 74. Radial distribution functions showing correlation between N-atoms and hydroxyl H-atoms in the linear viscoelastic regime of each network.
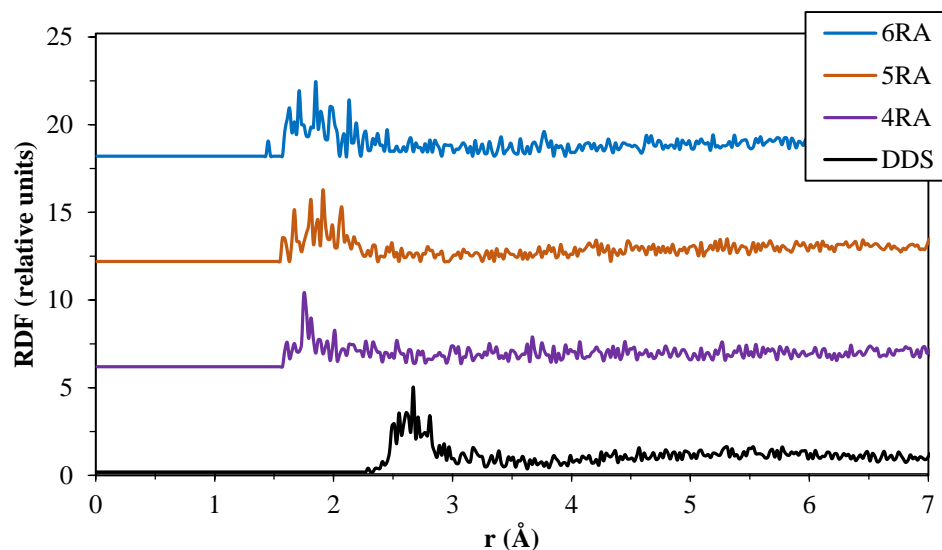
Figure 75. Radial distribution function showing correlation between ketone/sulfone O-atoms and hydroxyl H-atoms in the linear viscoelastic regime of each network.

Further RDF analysis was performed using the ketone/sulfone oxygen atoms coupled with hydroxyl-hydrogens of AEK and DDS networks. Figure 75 reveals the interactions through the numerous peaks between 1.5 and 3.2 Å. Firstly, 5RA and 6RA reveal complex interactions, but are a result of numerous ketone environments created by the multiple ketones on 5RA and 6RA curatives. Importantly, further confirmation that H-bonding in AEK networks is stronger than in DDS networks is provided by the observed interaction distances in AEKs. At 1.7 Å, the H-bonding moieties of each AEK network are considered to be at a distance where "medium-to-strong" H-bonding can occur, but in DDS networks this distance is increased to 2.8 Å where "weak" H-bonding begins to occur.[142] It is believed that the extended conformation of DDS segments increases the distance between H-bonding atoms. Due to its high stiffness at low strain, DDS remains in this conformation and reduces segmental packing, therefore decreasing the strength and concentration of cohesive interactions.
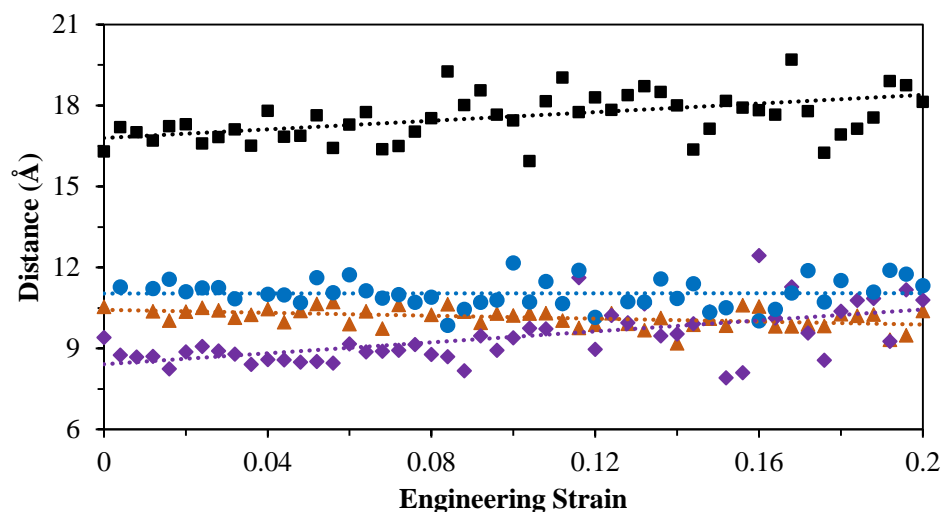
Figure 76. Simulated junction-point end-to-end distance as a function of strain for DDS (black squares), 4RA (purple diamonds), 5RA (orange triangles), and 6RA (blue circles) networks.

To gain a better understanding of the effects of glassy-state conformation on mechanical properties, crosslink junction end-to-end distance and ketone/sulfone dihedral angles were monitored during strain experiments. End-to-end distance was taken as the average distance between the two nitrogen-atoms of each diamine crosslinker within the simulation cell (Figure 76), and the dihedral angle was calculated as the average of the torsion angle between four atoms, including the respective sulfur or carbon of the sulfone and ketone groups. A schematic of the atoms used in the torsion angle calculations is shown in Figure 77.
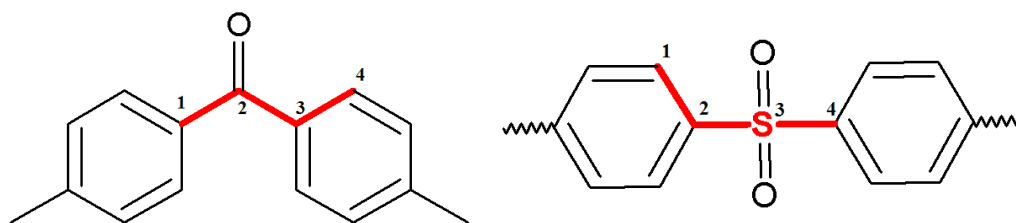
Figure 77. Segments and labeled atoms used during torsion angle calculations.

The end-to-end calculations correlated well with the RDF data, and it was found that DDS network segments have extended conformations compared to AEK diamine segments. Average end-to-end distances in the low strain, elastic regime were approximately 16.5 Å, 8.9 Å, 10.1 Å, and 11.3 Å for DDS, 4RA, 5RA, and 6RA, respectively. The flexible, multi-ring AEK-diamines appear to have compact conformations that allow for increased network level interactions, especially between nitrogen-junctions and hydroxyls. In the low strain regime these interactions increase network cohesion and provide the observed improvements in compressive modulus. As strain is increased past yield, AEK systems' end-to-end distances converge towards a similar value of approximately 10.5 Å, while DDS end-to-end increases to approximately 18.8 Å. The near constant end-to-end distances of AEK-diamines throughout the entire strain experiment indicate that these segments have increased ability to undergo torsional rearrangements, thus suggesting distortional capability.[20,21] The distributions of the ketone/sulfone torsion angles of each curative during the strain experiments are shown in Figure 78. AEK segments have broader ketone angle distributions compared to DDS sulfones, demonstrating an increased number of conformational rearrangements in AEK networks. Furthermore, AEKs contain a high concentration of ether linkages that also undergo broad torsion angle distributions. The combination of junction point proximity and broad torsion angle distributions in AEK-cured TGDDM is believed to provide improved network cohesion and increased distortional capability.
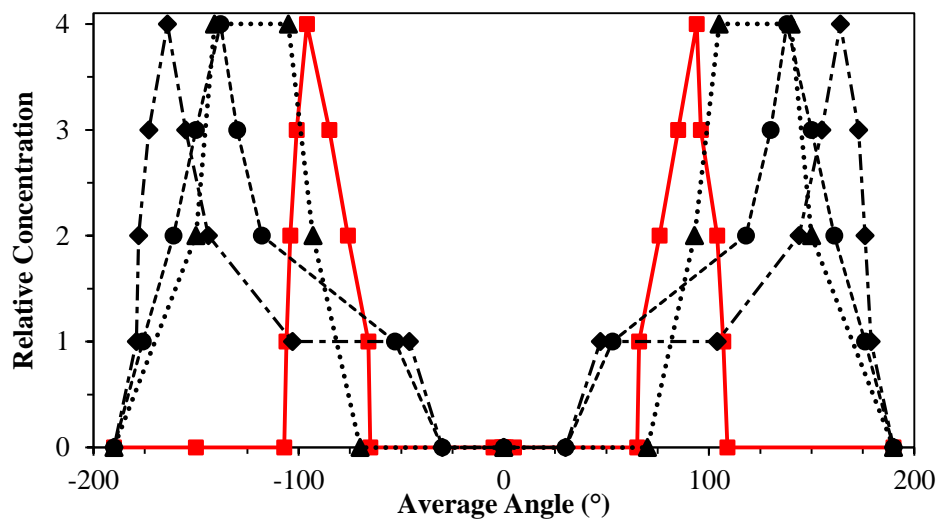
Figure 78. Torsion angle distributions corresponding to either ketone (dashed, blakc) or sulfone (solid, red) groups; 4RA (diamonds), 5RA (triangles), 6RA (circles).

Free Volume

Further explanation of the molecular motions and interactions that lead to distortional capability of multifunctional AEK networks was provided through study of free volume. Experimentally obtained hole size free volume (V_h) is plotted as a function of temperature in Figure 79. It should be noted that the V_hs measured appear to be higher than literature values and trends in V_h data were used for comparison purposes only.[146] Benchmark DDS and AEK-based networks do not show significantly different hole sizes across the observed temperature range. However, at room temperature V_h appears to decrease with increasing M_c and DDS, 4RA, 5RA, and 6RA V_hs are 105±7 Å, 99±9 Å, 92±12 Å, and 88±2 Å, respectively. This decrease in hole size is attributed to the previously shown relationship between M_c and cohesion, where an increase in curative molecular weight increased the concentration of secondary interactions.[135] At room temperature the increase in cohesion tightly holds network segments together and thus

produces the observed decrease in hole size. Hole size is known to effect solvent

diffusion through networks, therefore an increase in cohesion is hypothesized to effect

both mechanical properties and solvent ingress.[12]
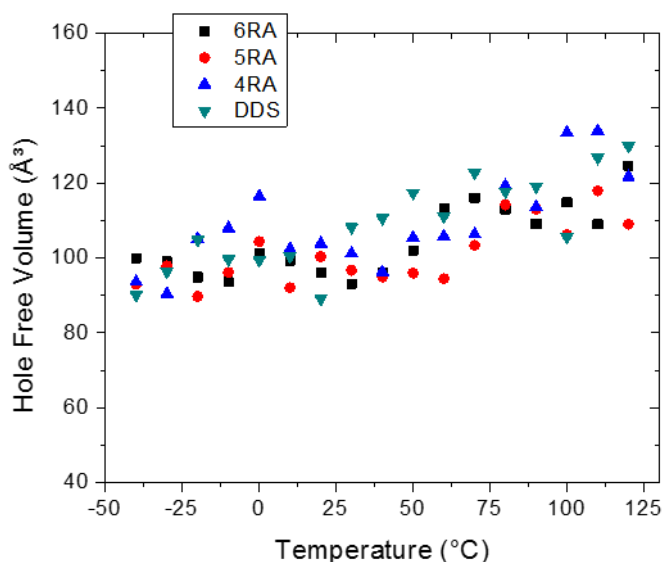
Figure 79. Hole size free volume vs. temperature; error within one standard deviation but error bars removed for clarity.

Fluctuations in V_h with temperature were ascribed to different thermally-activated

sub-T_g molecular motions. DDS-cured networks do not show the clearly separated

fluctuations of AEK-networks. This is attributed to the segmental cooperativity required

for secondary relaxations to occur in densely crosslinked DDS networks; this claim

supports the DMA data. Conversely, there are two local peaks in V_h for 4RA, 5RA, and

6RA networks. The theoretically decreased crosslink density of high M_c AEK-networks

provides increased volume which separates the relaxations into local non-cooperative and

cooperative-segmental motions. Furthermore, V_f fluctuations appear in the same

temperatures ranges as the γ- and β-transitions found in DMA. Hole sizes in the range of

the γ-transitions are larger than expected, but this correlates well with the activation

energies of γ-relaxations found from DMA. The large hole sizes allow for increased

mobility thus resulting in a lower activation energy. Hole size fluctuations which

correspond to the β-transitions are more reasonable, as segmental rearrangements require

significantly more volume than local motions.[147] The larger V_f in the β-temperature range

also correlates well with the transitions' activation energy. In an final note, the relaxation

temperatures from PALS do not directly correspond to those of the DMA data. This is

attributed to the small mechanical deformation imparted by the DMA which provides

additional energy to the system, shifting the observable temperature and frequency range

xcompared to PALS.
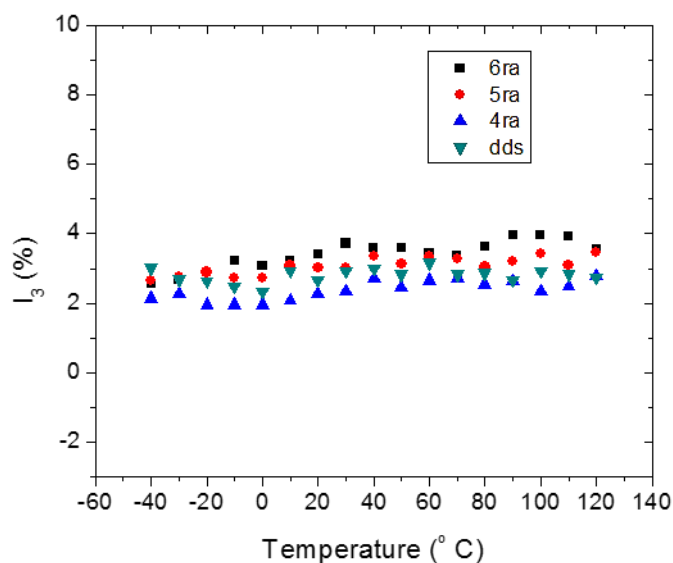
Figure 80. Hole intensity vs. temperature obtained from PALS.

At room temperature, hole size free volume agrees well with simulated junction

point end-to-end distance, which was found to be decreased as a result of increased

torsional angles of AEK networks. However, differences in hole size are statistically

insignificant across the measured temperature range. It is hypothesized that the similar

hole sizes of AEK networks are also related to segment conformation. With the end-to-end distances of increased molecular weight segments in closer proximity, the rest of the diamine segment is forced to position itself in a low-energy conformation somewhere within the surrounding network. This positioning is believed to fill local spaces, or hole free volume, and because the end-to-end distances of AEK networks are all similar, so will be V_h.
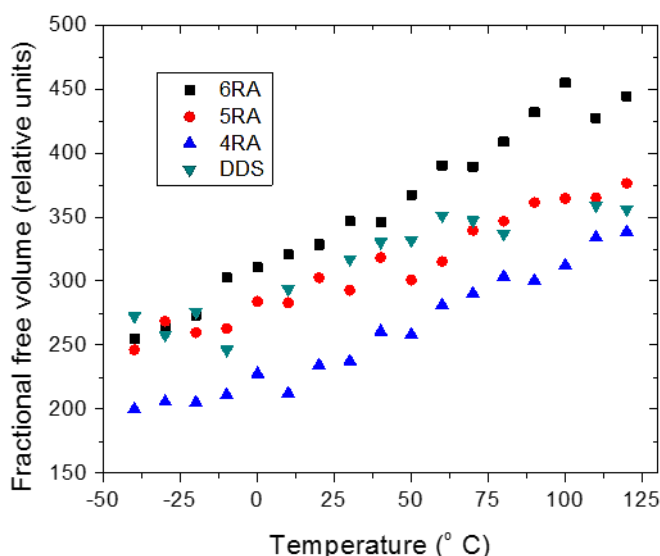
Figure 81. Fractional free volume vs. temperature calculated from hole size and hole intensity obtained from PALS.

To further understand the hole size similarity, fractional free volume (FFV) was calculated from hole size data by assuming hole size intensity, I_3, is proportional to hole concentration. I_3 and fractional free volume (FFV) plots are plotted against temperature in Figures 80 and 81. FFV was found to increase with temperature for all networks. Importantly, AEK networks' FFV increased with increasing M_c. This indicates that although V_f decreases due to local conformation, the entire free volume of the system increases as crosslink density is decreased. In terms of engineering properties, increases

in hole size and fractional free volume have been shown to increase rate and percent-uptake of moisture and organic solvents.[9,134] FFV is also believed to effect secondary molecular motions which in turn are known to contribute to the distortional capability of composite matrices.[136,147–150]

Table 25

Simulated zero-strain, room temperature fractional free volumes; average of three simulation cells

Sample Name	Cell Volume $\mathring{A}^3$	Solvent-Accessible Volume $\mathring{A}^3$	FFV %
DDS	41650±240	200±60	0.49
4RA	59000±370	445±105	0.75
5RA	65750±810	500±190	0.76
6RA	53400±425	675±125	1.26

Thermally-activated transitions such as those seen from PALS and DMA are useful for understanding distortion, but additional information on how AEK free volume evolves under during deformation was desired. Thus, FFV evolution during deformation was simulated to correlate distortional properties to free volume. Equilibrium FFVs of AEK networks are shown in Table 25. These values were found to follow the trends of experimentally determined FFV (barring DDS), which helps validate the use of PALS for FFV determination. When the simulation cell is placed under strain, the FFV of DDS and AEK networks performed very differently. Displayed in Figure 82, it was found that simulated AEK networks FFVs do not significantly change under deformations between 0 and 20% strain. On the other hand, DDS-cured networks show an increase in FFV

when placed under load. The combination of cohesive energy and torsional-angles in AEK-cured epoxies allow for negligible volume change during deformation. However, the increase in volume in DDS epoxies is attributed to the development of nano-voids due to cavitation.[148,149] In other words, AEK-based networks behave in a distortional manner while DDS-cured TGDDM behaves in a dilatational manner. The data presented herein shows promising results for prediction of distortional-capability through free-volume simulations and measurements, but additional simulation and experimental free volume data are required to determine the methods applicability.
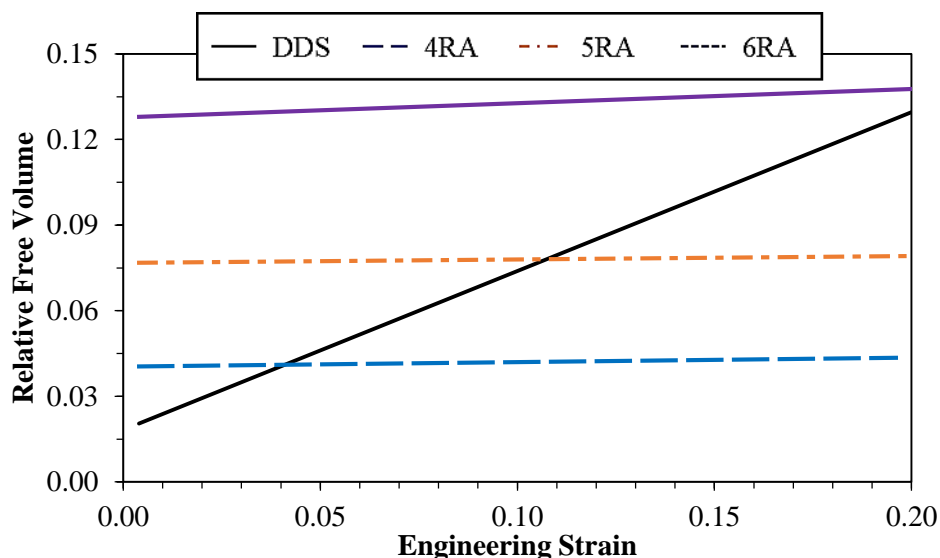
Figure 82. Simulated free volume vs. strain; DDS (solid), AEK networks (dashed).

Summary

This chapter has focused on the characterization of molecular attributes in AEK-cured TGDDM networks. DMA was used to calculate crosslink density and molecular weight between crosslinks and to quantify sub-T_g molecular motions. Experimental crosslink molecular weight in AEK-cured networks was expectedly higher than that of

DDS-cured networks, but deviated from theoretical trends due to the rigid chemical structure of 5RA. 1 Hz tan delta curves were measured to calculate γ- and β-transition peak temperatures, FWHMs, and areas. The γ-relaxation peak characteristics were all found to decrease with increasing M_c. This was ascribed to a decrease in local density from the longer curatives which provided space for the simple motions linked with γ-relaxations. Peak characteristics of the β-transition were observed only in AEK networks because of the increased number of segmental conformations from the high M_c networks. Additionally, activation energies were calculated for both observed transitions, and both were found to decrease with increasing M_c.

Network-level conformations and interactions, including hydrogen-bond distances, junction-point spatial distribution, and dihedral angles, were studied using molecular dynamics simulations. Radial distribution function analysis of hydrogen-bonding moieties showed that AEK networks have considerably stronger secondary interactions than DDS. The higher concentration and strength of these interactions leads to improved network-level cohesion and therefore mechanical properties. Interestingly, it was found that average end-to-end distance of nitrogen junction-points in AEK networks are less than those of DDS network. This was found to be related to the increased distribution of torsion angles allowed in AEK-cured networks. The combination of enhanced segment folding and greater dihedral repositioning provides the networks with greater conformational changes without the loss of cohesion, or in other words, distortional capability.

Free volume trends were estimated using PALS and molecular dynamics. Hole size volumes were found to be higher than literature values, however, it was shown that

hole sizes were similar across all networks. The similarities in DDS and AEK hole sizes was further confirmation that AEK segments tend to have folded conformations, which produces less-than-anticipated free volume. Furthermore, AEK-network hole sizes fluctuated with temperature more than DDS, showing the extra volume required for secondary relaxations observed in DMA. As γ-relaxation activation energies from DMA decrease with M_c, it is hypothesized that the apparent AEK-segment folding does not create network-level packing, but "loops" to create smaller hole sizes. This was further analyzed by fractional free volume estimations from both PALS and simulation. PALS trends for AEK networks were expected, and an increase in M_c lead to an increase in fractional free volume; DDS did not follow accordingly and fell between 5RA and 6RA. The increased fractional volume indicates that AEK-folding fills hole volume and that sub-T_g motions in these networks are related to overall free volume and less to hole size. Finally, simulated free volume provided further insight into distortional mechanisms by observing its change under strain. It was shown that distortionally capable AEK networks contain only small changes in free volume throughout the simulation (distortion), whereas DDS networks show significant increases in volume (dilation).

These studies provided a unique opportunity to study crosslink molecular weight without changing network functionality and therefore theoretical crosslink density. By understanding fundamental relationships between sub-T_g molecular motions and M_c in highly crosslinked, multifunctional epoxy networks we can begin to better control and improve mechanical properties of high performance materials. Moreover, the novel AEK-curatives herein provided insight into how secondary interactions can be used to significantly alter properties by manipulation of network-level cohesion.

CHAPTER VI

STRUCTURE-PROPERTY RELATIONSHIPS OF BLENDED HYBRID NETWORKS

BASED ON ARYLETHERKETONE DIAMINE CURATIVES

Objective

This chapter's foremost objective is to discuss the structure-property-relationships of TGDDM hybrid networks cured by blends of DDS and AEK diamines. Two chemistries were formulated and cured using stoichiometric ratios of amino-hydrogen to epoxide with 4RA or 5RA concentrations of 5, 10, and 20 mol%. Network formation was studied using Flynn-Wall-Ozawa kinetic analysis, and degree of cure calculations were performed after the industrial cure profile. Dynamic mechanical analysis and density measurements were used to relate thermal transitions, crosslink density, and crosslink molecular weight to the cure state and mechanical properties. It was hypothesized that thermal and mechanical properties could by predictably tailored by varying the molar concentration of AEK diamines, but complex relationships were discovered; degree of cure and crosslink density play important roles in these relationships. Additionally, the studied structure-property-relationships led to improved understanding of the characteristics of 100% AEK networks studied in Chapters IV and V.
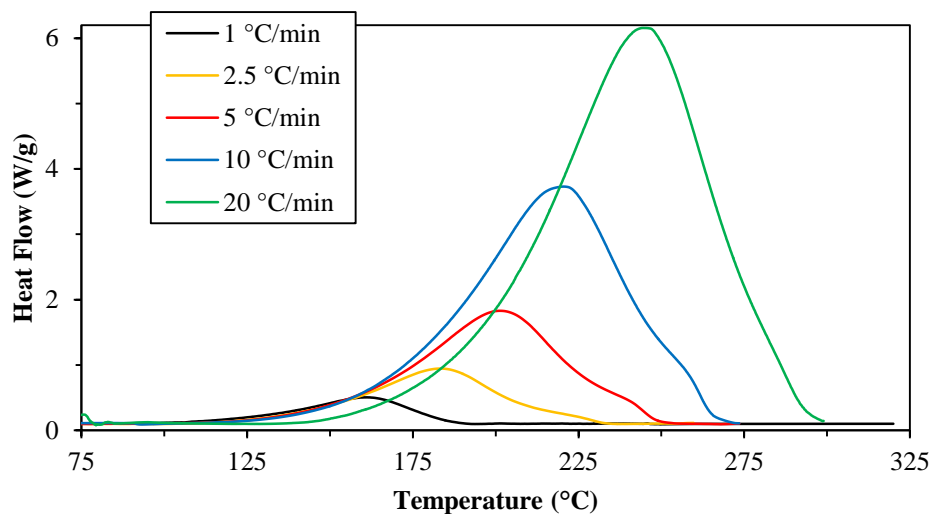
Figure 83. Example DSC reaction exotherms for 5 different heating rates from 20 mol% 4RA-hybrid network.

Results and Discussion

TGDDM-DDS networks were modified by stoichiometric incorporation of aryletherketone diamines 4RA and 5RA. Such hybrid networks are increasingly attractive due to their easily tuned processing and engineering properties, but few studies of the complexities which arise with mixed-diamine networks exist within the literature.[41,151–154] Furthermore, fewer reports exist where both diamines are aromatic. Low concentrations of each hybrid modifier were employed to ensure processability due to the low solubility of AEKs. The hybrid networks were first blended as prepolymer in a high shear mixer at room temperature to prevent premature reaction and evenly disperse the AEK diamines. Slurries were then subjected to the industrial cure profile (125-180 °C at 1 °C/min, isotherm at 180 °C, 3 hrs) to provide under-cured networks with cure extents between 80 and 95%. The resulting networks thermal and mechanical properties were characterized by DSC, DMA, and uniaxial compression. It was discovered that the engineering

properties of the hybrid networks could be significantly altered, even at low AEK

concentration.

Table 26

DSC peak exotherm data for each heating rate used in the FWO analysis of both 4RA and 5RA-based hybrid networks

Sample Name	1 °C/min	2.5 °C/min	5 °C/min	10 °C/min	20 °C/min
4RA Networks					
DDS	166.8	187.4	206.3	227.3	255.3
5%	165.0	180.7	206.1	225.4	254.8
10%	164.2	187.5	203.6	222.6	249.4
20%	161.2	183.2	201.3	220.5	245.4
4RA	131.5	147.1	168.3	187.1	209.6
5RA Networks					
DDS	166.8	187.4	206.3	227.3	255.3
5%	164.1	188.4	207.6	227.3	256.5
10%	163.5	189.6	210.0	227.2	256.2
20%	163.0	183.5	208.1	226.6	255.7
5RA	166.8	180.3	206.3	225.4	254.8

Network Formation via DSC

Cure kinetics and extent of cure for hybrid AEK networks were studied by DSC

to characterize network formation and reactivity. Flynn-Wall-Ozawa (FWO) kinetic

analysis was used to determine the apparent activation energy of cure for each network, where the apparent activation energy is an average of activation energies at each degree of conversion.[155,156] An understanding of the apparent activation energy gives insight into the reactivity of the hybrid-curative networks and allows one to extrapolate the processability of the novel blends. Similar to the kinetic analysis described in *Chapter IV,* apparent activation energies are calculated from the best fit lines of ln(β) vs. 1/T, where β is the heating rate and T is the peak temperature of a DSC cure exotherm at a given heating rate. Figure 83 shows a representative heat flow vs. temperature plot with exotherms from the five different ramp rates used in this analysis for the 20 mol% 4RA-hybrid network. A summary of the obtained DSC peak exotherm data is found in Table 26. FWO kinetic plots ln(β) vs. 1/T for both 4RA- and 5RA-based hybrids are found in Figures 84 and 85, respectively. The ultimate result for the kinetic analysis, the apparent activation energy vs. AEK-concentration plot, is found in Figure 84. Further reactivity analysis is shown by Figure 85, where cure onset temperature of the hybrids heated at 1 °C/min are plotted against AEK concentration.
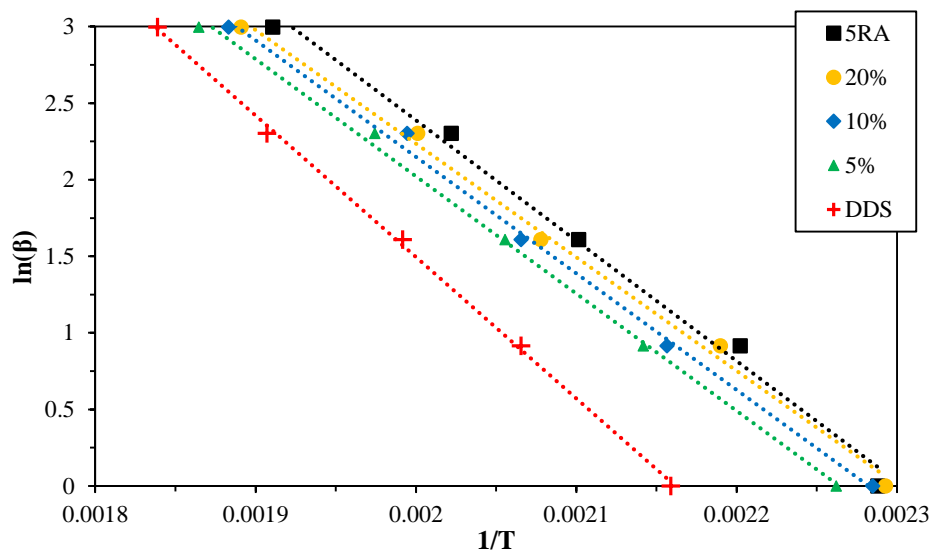
Figure 84. ln(β) vs. 1/T for 4RA-based hybrid networks; R2 values between 0.97 and 0.99.
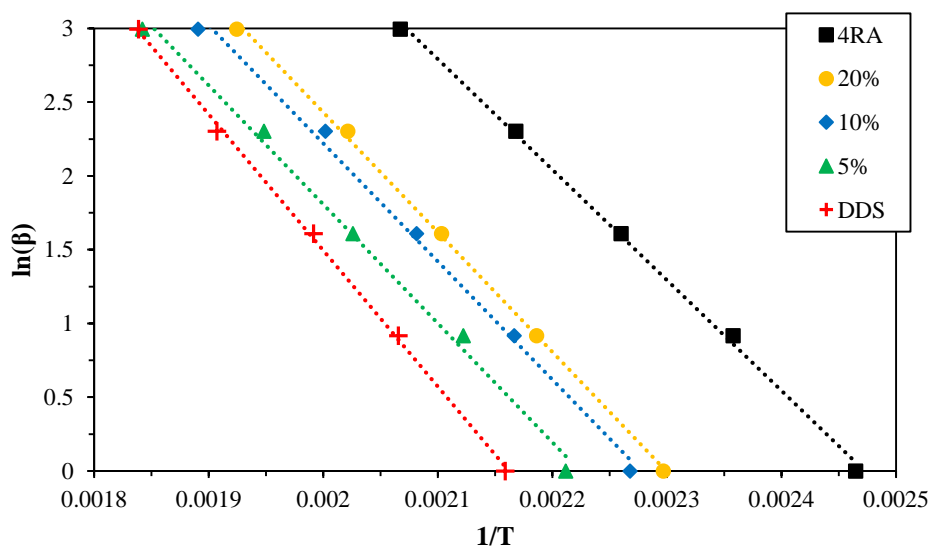
Figure 85 .ln(β) vs. 1/T for 5RA-based hybrid networks; R^2 values between 0.97 and 0.99.

The apparent activation energies plotted in Figure 86 show that an increase in

molar concentration of either hybrid modifier yields a decrease in activation energy. It

was also shown that 5RA-hybrids have lower activation energy than 4RA-hybrids. This result was expected as it was found and previously discussed in Chapter IV that 100 mol% AEK-networks showed a decrease in activation energy with conversion, which in-turn is an overall decrease in apparent activation energy. However, the more surprising result from the FWO-analysis is activation energy's trivial dependence on AEK concentration. For both 4RA- and 5RA-hybrids there is a sharp decrease in apparent activation energy between 0 and 5 mol%, where after 5 mol%, the slope flattens. Between 20 and 100% AEK, this secondary slope is between unity and zero for 5RA and 4RA networks.
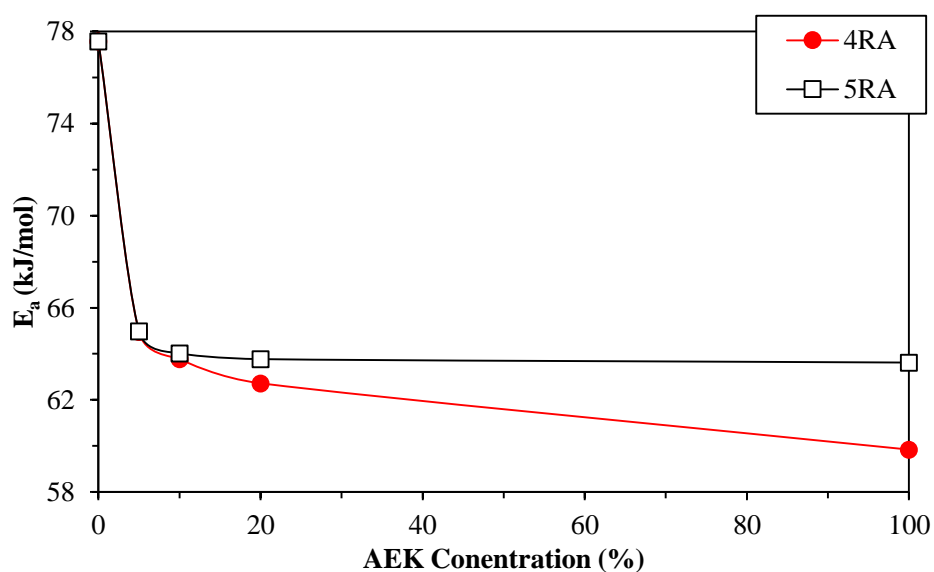
Figure 86. Apparent activation energy vs. molar concentration of AEK hybrid modifiers.

Both the magnitude and rate of decrease in activation energy with AEK concentration can be described by the nucleophilicity of the hybrid modifiers. It was hypothesized in Chapter IV that an autocatalysis mechanism was responsible for the observed decrease in activation energy with conversion of TGDDM-AEK networks due

to an increase in diamine basicity. The observations herein support this premise, where a systematic increase in AEK concentration led to a decrease in apparent activation energy. The increase in hybrid network basicity can be justified by the incorporation of basic groups such as ketones and ethers.[121] Furthermore, the nucleophilicity of both 4RA and 5RA are shown to be much higher than DDS from the theoretical pKa values in Chapter III. As the network concentration of AEK is increased, the average nucleophilicity increases, and the energy barrier required for cure is decreased. Additionally, the rapid decrease in E_a at low AEK concentration shows that the more nucleophilic AEKs drive the magnitude of the cure energy barrier.
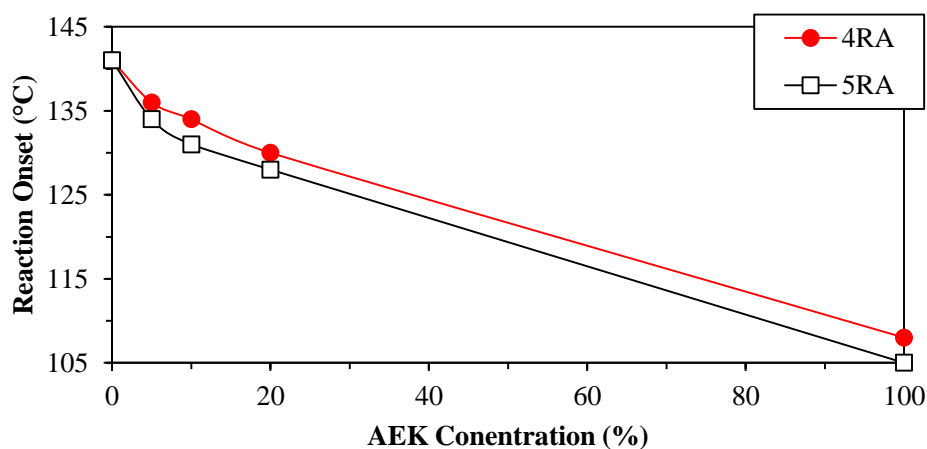
Figure 87. Cure onset temperature vs. molar concentration of AEK obtained at 1 °C/min.

Supplementary analysis of hybrid-network reactivity was shown through the cure onset temperature (Figure 87), which was obtained using the 1 °C/min heating rate employed during the cure protocol. Similar to activation energy, a decrease in reaction onset temperature with an increase in AEK concentration was observed for both hybrid networks. This anticipated result can be described by similar arguments as activation

energy, and is correspondingly attributed to the AEK nucleophilicity. The linear decrease in onset temperature, versus activation energy's rapid decrease, is ascribed to the slow ramp rate used and the fact the result is from a single point during the DSC experiment, and not an average of multiple DSCs (like E_a). This result is important in understanding and providing processability to the AEK-networks, as 100 mol% 4RA- and 5RA-based are challenging to process using traditional methods due to their low cure onset temperatures.
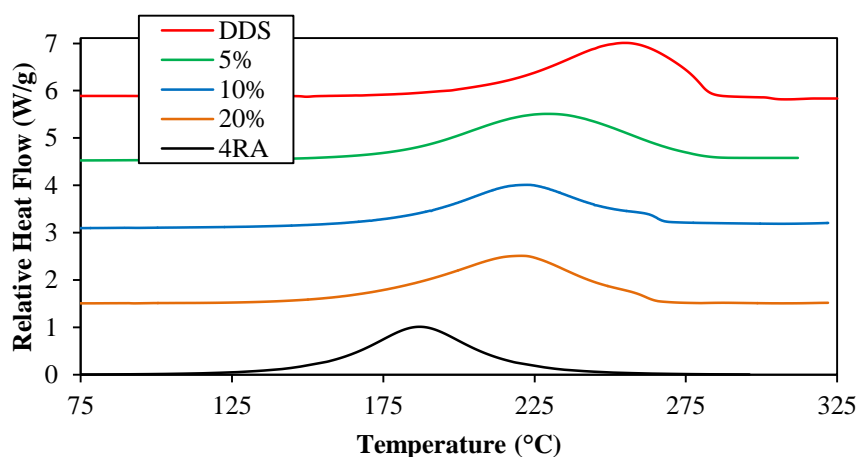
Figure 88. DSC thermograms of 4RA-hybrids; obtained at 10 °C/min.
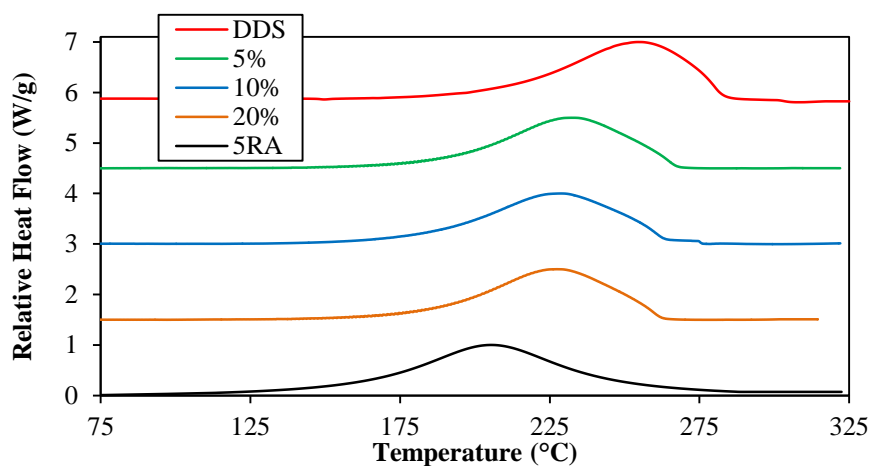
Figure 89. DSC thermograms of 5RA-hybrids; obtained at 10 °C/min.

Table 27

Degree of cure calculation parameters obtained from 10 °C/min DSC exotherms; H_T and H_C values averages of two DSC experiments

Sample	H_T	H_C	α_R
Name	J/g	J/g	%
4RA Networks			
Neat	430	31	93
5%	454	37	92
10%	467	43	91
20%	481	57	88
4RA	463	84	81
5RA Networks			
Neat	430	31	93
5%	470	37	92
10%	441	41	91
20%	300	32	89
5RA	404	78	81

Test specimens were subjected to the aforementioned Industrial cure and then reheated within the DSC to obtain extent of conversion, or relative degree of cure, α_R.[7] Figures 88 and 89 show DSC thermograms for 4RA- and 5RA-hybrids, respectively, and were obtained using a 10 °C/min ramp rate. These exothermic peaks indicate the heat released while driving the networks to 100% cure and integration of each curve yields the total heat release, H_T. Second DSC thermograms were obtained after the cure prescription to show residual heat of reaction exotherms, H_R, which were then used to calculate α_R.

Tabulated values for the integral areas of H_T and H_R, as well as the resulting α_R can be found in Table 27.

Hybrid network degree of cure was found to decrease linearly with increasing AEK-content, with α_R values between 93% and 81% for both 4RA-and 5RA hybrids. The observed decrease in α_R is attributed to earlier onset of gelation for hybrids. Due to the lower E_a and onset temperature of the AEK-diamines, it is believed that 4RA and 5RA begin to react into their respective networks before DDS. This earlier reaction will build molecular weight to further the cure extent, but more importantly, the exotherm created by early polymerization of AEK diamines provides heat to overcome the DDS energy barrier which begins the consumption of DDS at lower temperatures.[157] Assuming AEK curatives are consumed first, gelation will occur earlier with increasing concentrations of 4RA and 5RA due to the increased exotherm and subsequently earlier consumption of DDS. Once gelation occurs, the cure reaction becomes inhibited from the large viscosity of the infinite network.[158] This decrease in time to gelation ultimately leads to the decrease in the final degree of cure of the hybrid networks. As will be discussed in full below, the decrease in cure extent has consequences on the hybrids thermal and mechanical properties.

Thermomechanical Properties

The thermomechanical characteristics of cured AEK hybrid networks were investigated using dynamic mechanical analysis in tension mode. Tan delta (E''/E') was used to provide an understanding of the cure-state, network damping, and glass transition of the industrially cured networks. Figures 90 and 91 show tan delta vs. temperature curves for 4RA- and 5RA-hybrids, respectively.
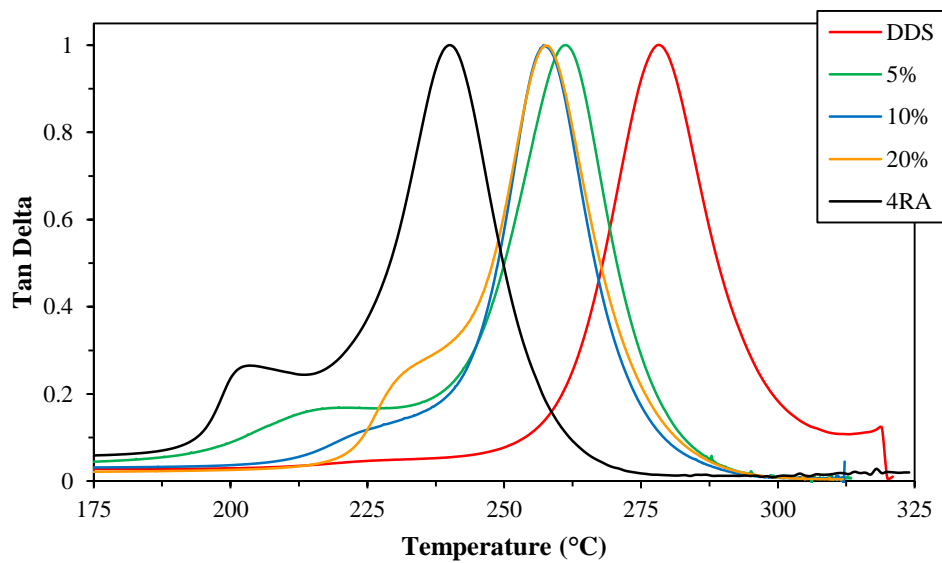
Figure 90. Thermomechanical tan delta vs. temperature for 4RA-hybrids; obtained from DMA in tension mode.
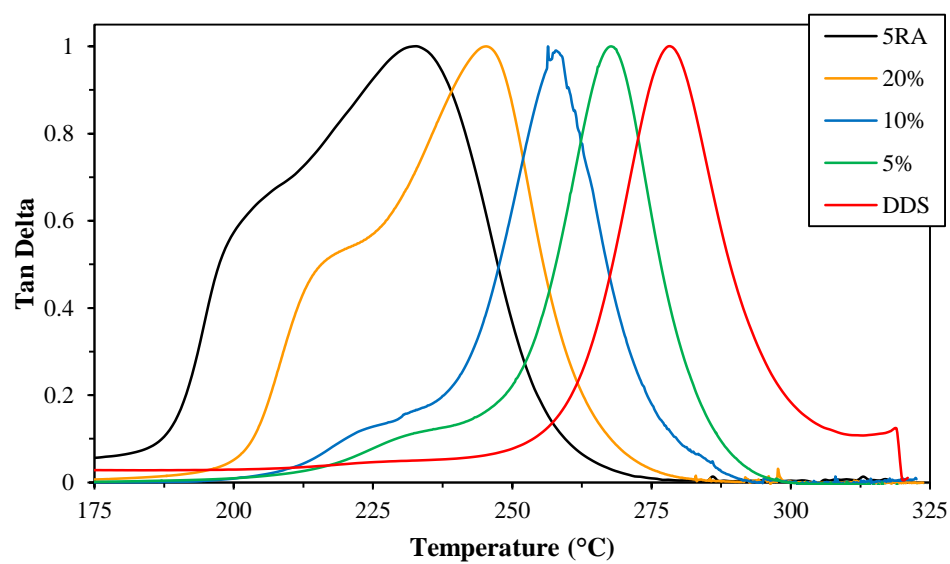
Figure 91. Thermomechanical tan delta vs. temperature for 5RA-hybrids; obtained from DMA in tension mode.

The glass transition temperature was determined from the peak of tan delta, and cured networks of pure 5RA, 4RA and DDS show T_g values of 237 °C, 240 °C, and 279 °C, respectively. As predicted, T_g decreases with the incorporation of the AEK-modifiers indicated by the shift in tan delta maxima. 5RA-based hybrids display clearly separated tan delta peaks which decrease with increasing AEK-content. However, 4RA-hybrids show a similar shift in tan delta maxima, but 10 and 20 mol% hybrids led to blended-networks with indistinguishable T_g values. Interestingly, both AEK-hybrids have relatively broad tan delta curves that possess shoulders around 200-250 °C. These attributes are indicative of heterogeneous networks which are likely a consequence of the decreasing cure extent with increasing AEK concentration.[159] Likewise, heterogeneity was further analyzed using the Fox-equation[160],

$$\frac{1}{T_g} = \frac{w_1}{T_{g1}} + \frac{w_2}{T_{g2}}$$

where, T_g, T_{g1}, and T_{g2} correspond to the glass transitions of the statistical copolymer network, pure component 1, and pure component 2, respectively, and w_1 and w_2 correspond to the weight fractions of each component. It was found that a negative deviation exists between the theoretically calculated and experimental observed T_g values for both 4RA- and 5RA-hybrids (Figure 91). Double networks characterized by the Fox treatment of T_g are well established in the literature but it has been shown that correlation with the theoretical data differs greatly with network composition.[145,154,161] Also, it has been found that conversion and network-cohesivity play significant roles in predicting T_g.[31,159,162] The deviations observed herein are therefore ascribed to the low degree of cure caused by the difference in reactivity between DDS and AEK diamines. Excitingly,

it is this low conversion and T_g deviation that are believed to provide the marked

increases in mechanical properties described below.
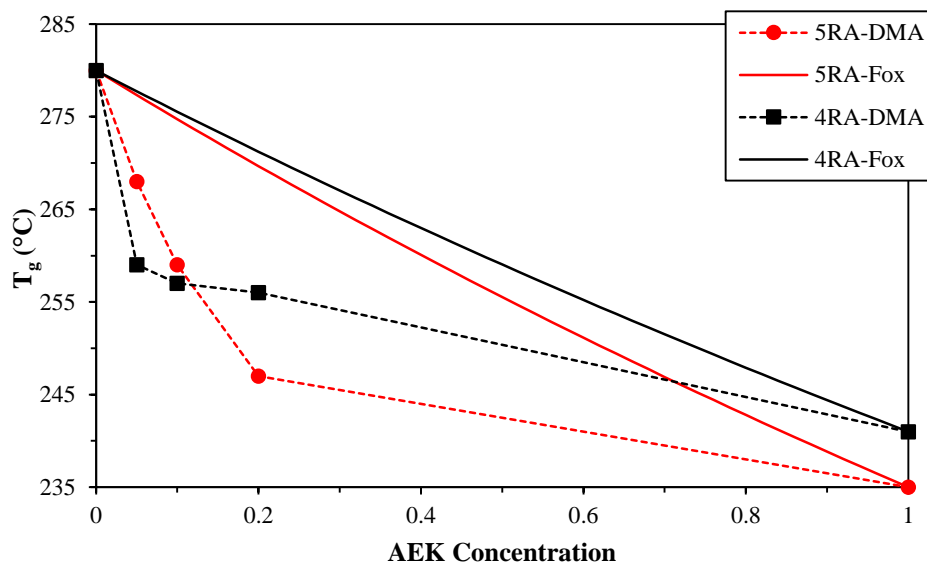
Figure 92. T_g values of hybrid networks obtained from DMA; Solid lines represent predicted T_g behavior based on Fox equation, dashed lines used only as guides.

Rubbery modulus values were taken from the post-T_g storage moduli to calculate

crosslink density and molecular weight between crosslinks values for the AEK-hybrid

networks. Bar charts in Figures 93 represent the experimentally determined rubbery

moduli and crosslink molecular weight (M_c), respectively. Crosslink density was found to

follow the expected trend of decreasing with AEK concentration. For example, calculated

values of crosslink density decrease from $3.24*10^{-3}$ mol/cm^3 for DDS cured networks to

either $2.15*10^{-3}$ mol/cm^3 or $2.45*10^{-3}$ mol/cm^3 for 4RA- and 5RA-hybrids.This decrease

is attributed to the increase in crosslink molecular weight and decreasing the segment

rigidity with incorporation of AEK content. Likewise, M_c increases with AEK content

and with the exception of 100 mol% 5RA, 4RA-networks have lower relative M_c than

5RA-networks. This occurrence is ascribed to the higher physical densities of 4RA-hybrids. The shorter 4-ring segments provide better chain-packing in the under-cured systems compared to the larger 5RA segments, thus increasing room temperature density and rubbery storage modulus. The trends deviation with 100 mol% 5RA-networks is attributed to the high concentration of *meta*-substituted moieties, stiffening the network through lower molecular mobility.
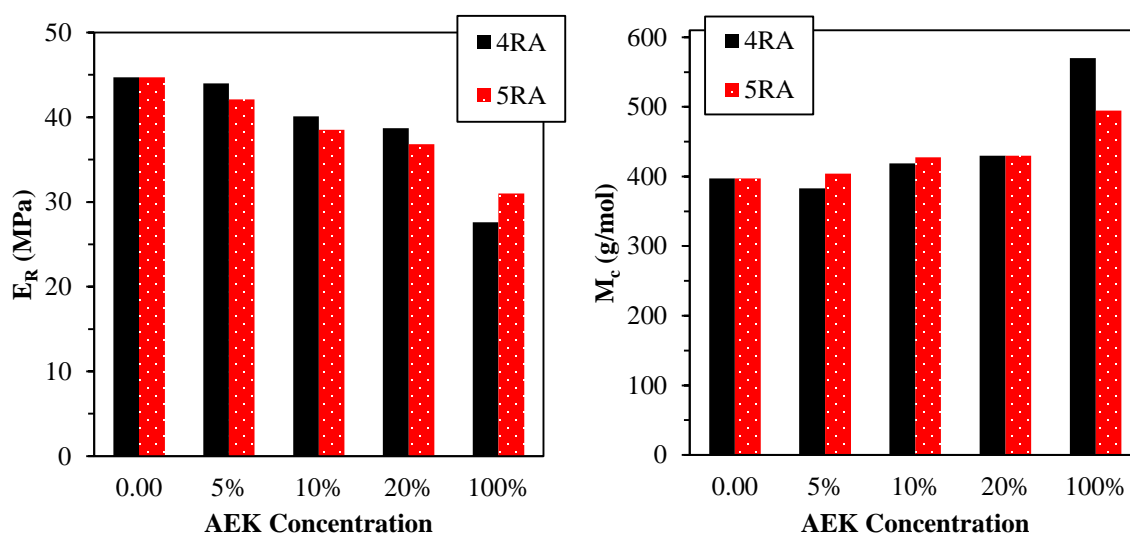
Figure 93. Rubbery moduli (E_R, left) and crosslink molecular weight (M_c, right) from DMA storage modulus.

Further examination of hybrid network thermomechanical properties was performed through analysis of the sub-T_g transitions. Glassy-state molecular motions seen as sub-T_g transitions can effect, and have previously been correlated to, bulk mechanical properties of epoxy networks both in the literature and in this body of work (*Chapter V*).[29,33,35,159] Moreover, these transitions can provide insight into the mechanical behavior of the hybrids studied herein. Shown in Figures 94 and 95 are the secondary

transitions of the tan delta curves of 4RA- and 5RA-hybrid networks, respectively. In the

5RA-hybrids, 10, 20, and 100 mol% 5RA networks show both γ- and β-transitions, where

5% and DDS-based networks contain only show the γ-transition. Similarly, 4RA-hybrids

with 20 and 100 mol% 4RA have both secondary transitions, but 5 and 10 mol% only

show a single γ-transition.
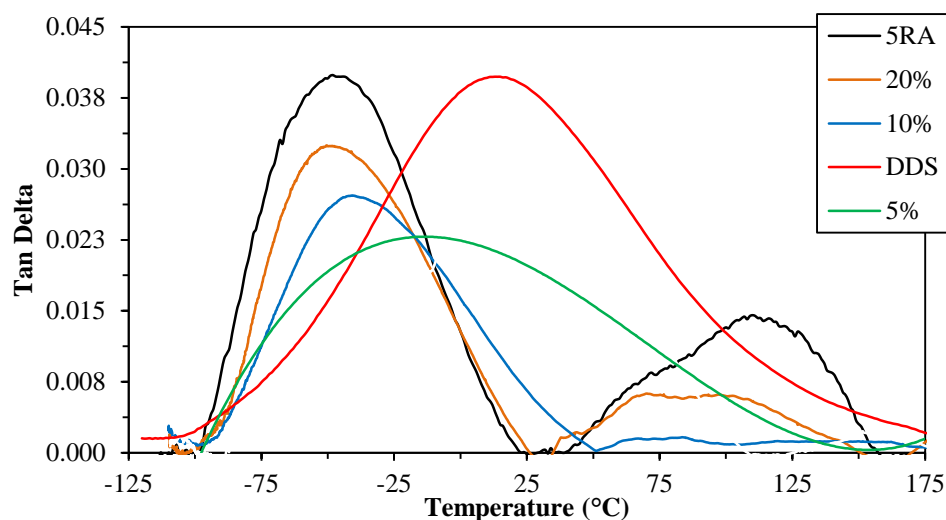
Figure 94. Tan delta secondary relaxations of 5RA-hybrid networks.
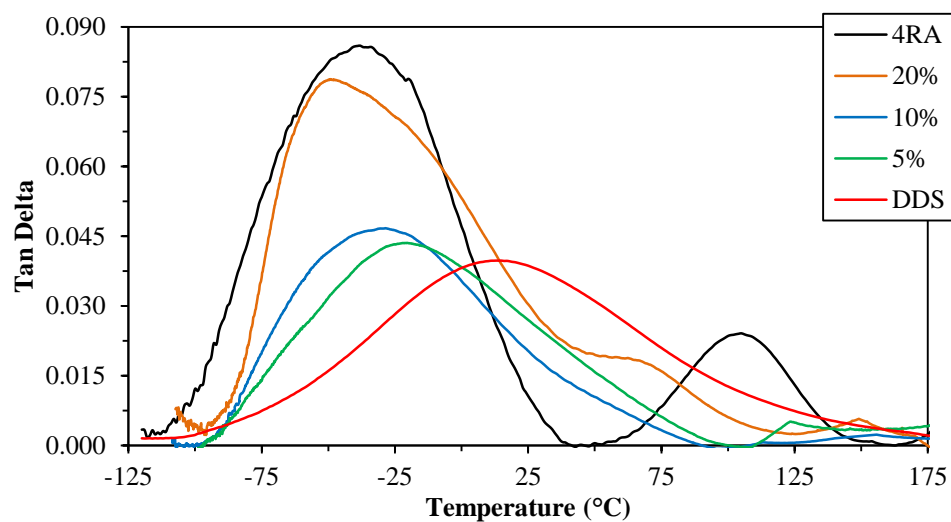
Figure 95. Tan delta secondary relaxations of 4RA-hybrid networks.

Table 28

Secondary-transition peak analysis data from 4RA- and 5RA-hybrid networks

Sample Name	γ-Peak °C	γ-FWHM °C	γ-Area °C	β-Peak °C	β-FWHM °C	β-Area °C
			4RA Networks			
4RA	-38.1	82.0	3.9	105	54.8	0.7
20%	-33.4	88.8	3.6	42.4	42.9	0.5
10%	-28.6	93.8	3.8	-	-	-
5%	-20.4	102.7	2.7	-	-	-
DDS	13	119.0	5.2	-	-	-
			5RA Networks			
5RA	-48	75.2	3.5	110	84	1.3
20%	-46	73.2	2.6	70	90	0.7
10%	-40	78.3	3.2	82.1	125	0.1
5%	2	100.5	3.2	-	-	-
DDS	13	119.0	5.2	-	-	-

Similar to the characterization performed in Chapter V, the tan delta peaks of the secondary transitions were integrated and the subsequent curve areas and FWHHs were analyzed; sub-T_g peak analysis data is summarized in Table 28. In each hybrid network, both γ-transition peak maxima and FWHH decrease to lower temperatures as the concentration of AEK-curative is increased. These decreases are indicative of less molecular-level cooperativity, suggesting that AEK-hybrids contain γ-relaxations that are

simple and from small molecular fragments.[17] This is rationalized by the hybrid networks decreased crosslink density and increased molecular weight between junction points. As average crosslink molecular weight is increased, the molecular-space required to perform localized motions such as phenylene-ring flips is also increased, freeing the local motion from contributions of segmental, cooperative movements.[34] Additionally, the observed peak shifts in hybrid networks further separate the γ- and β-relaxations indicating that these networks contain both non-cooperative (γ) and cooperative (β) motions, and they are likely separate processes.[33] The DDS-network has the largest FHWM because its secondary-motions are not separated like AEK-networks.

Further comparison shows that.4RA-hybrid networks have increased γ-peak FWHMs compared to 5RA-hybrids. This difference is ascribed to the *meta*-substituted 3-ring center of 5RA. As FWHM indicates the temperature region in which secondary motions can occur, the both stiff and volume-filling *meta*-substitution is believed to antiplasticize the network and prevent secondary relaxations from occurring in the 1 Hz frequency range which was employed.[33,44,45] Moreover, similar explanation can be used to describe the dissimilar trend of the β-transition, where an increase in AEK-content leads to an increase in 4RA-hybrid β-relaxation FWHM, but a decrease in 5RA-hybrids. As the β-relaxation is attributed to the rearrangement of molecular segments, the less stiff 4RA-strand has more mobility and therefore a larger temperature range for relaxation. 5RA-strands have stiff centers and as the concentration of those rigid segments is increased, the temperature range for relaxation decreases. The culmination of degree of cure, T_g, and secondary relaxations will be presented and related to bulk mechanical properties in the final sections of this chapter.
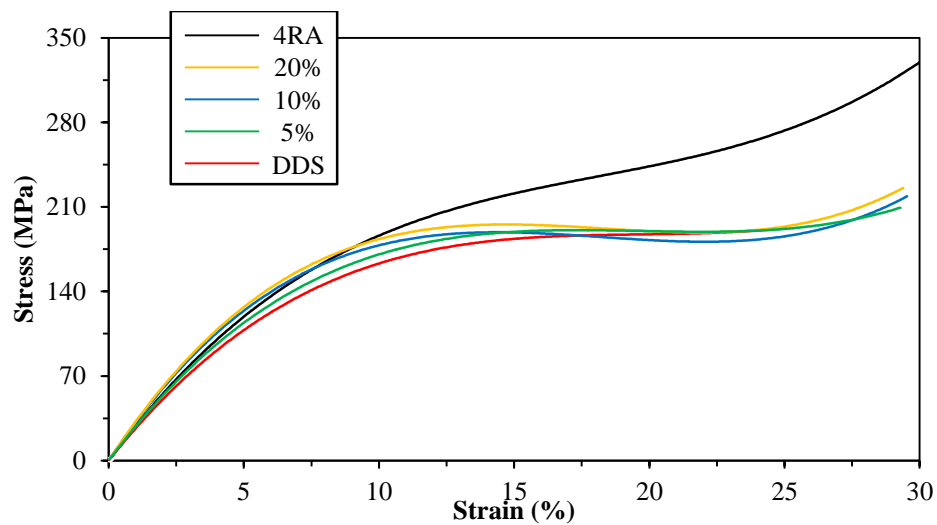
Figure 96. Stress vs. strain curves of 4RA-hybrids networks obtained from uniaxial compression.
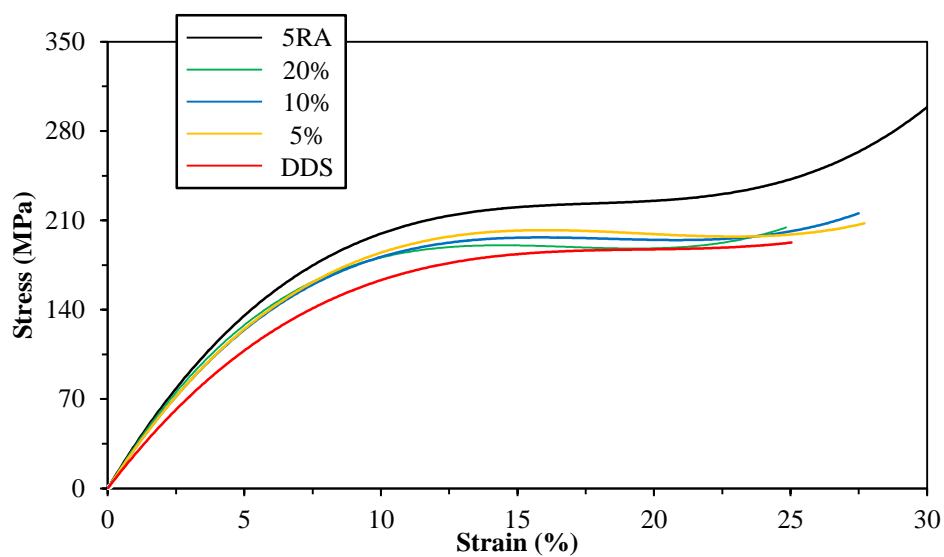
Figure 97. Stress vs. strain curves of 5RA-hybrid networks obtained from uniaxial compression.

Table 29

Mechanical properties from uniaxial compression; averages of 10 specimens

Sample Name	Young's Modulus MPa	Yield Stress MPa	Yield Strain %
4RA Networks			
DDS	2450±200	182.3±15.6	10.1±1.9
5%	2535±135	186.6±0.1	11.9±0.1
10%	3150±15	184.4±2.3	12.2±0.4
20%	3275±40	189.9±0.2	12.8±0.0
4RA	2955±165	222.5±2.2	14.3±1.8
5RA Networks			
DDS	2450±200	182.3±15.6	10.1±1.9
5%	3005±80	197.7±0.1	13.9±0.5
10%	3015±70	195.2±1.4	13.9±0.2
20%	3020±70	189.1±2.3	12.6±0.6
5RA	3015±95	212.2±2.1	13.7±0.7

Mechanical Properties

Uniaxial compression testing was performed on hybrid networks to study the effects of AEK concentration on bulk mechanical properties. One of the major objectives of this chapter was to quantify how low loading levels of 4RA- and 5RA-diamines would affect both the strain-capability and stiffness of the cured networks. Figures 96 and 97 show stress vs. strain curves for 4RA- and 5RA-hybrids, respectively, and the values

obtained from these plots are presented in Table 29. Similar to *Chapter IV,* it was found that AEK-hybrid networks have improved mechanical properties compared to those of DDS. Young's modulus obtained from compression was shown to increase with the incorporation of the AEK diamines, with maximum increases of 34% and 23% realized by 20 mol% networks of 4RA and 5RA, respectively. Yield stress and yield strain were also found to increase with AEK-content, but maxima were found in 100 mol% 4RA- and 5RA- hybrids.

The increase in mechanical properties upon AEK-incorporation is explained by combination of previously describe attributes: degree of cure, reactivity, T_g, and sub-T_g molecular motions. It has been shown maximum modulus values do not occur at full conversion, but at some cure extent between 0.75-0.9 due to increased network cohesivity.[46] As AEK concentration is increased the degree of cure decreases, and the maximum moduli occur at 20 mol% of either hybrid-diamine. The observed maxima are also hypothesized to be an effect of the type and concentration of secondary interactions; the additional polar moieties (ie. ketones and ethers) and the improved packing from increased M_c increase the networks cohesive energy and therefore its elastic modulus. Furthermore, it is believed the differences in diamine-reactivity of the play a role in the observed moduli improvements. Due to their higher reactivity, AEK-diamines, are believed to be incorporated into the network before DDS molecules. As the theoretical gel point is approximately 50% conversion, consumption of all AEK curatives, even at 20 mol%, is below the critical extent of reaction which allows the reaction rate to remained unchanged when DDS begins to react. It is hypothesized that the low AEK activation energy and its early incorporation creates AEK-rich regions of high crosslink molecular

weight that may act as ductile areas that absorb energy upon deformation, similar to a rubber toughening particle.[163,164] Moreover, because AEK-diamines are likely to be fully reacted into the network, DDS dangling-ends are likely left within the network. The DDS segments can more easily pack into, and closely interact with the network to allow for increased cohesion and the improved moduli.

The stress and strain capability of hybrid networks is related to the molecular motions found for these materials. The increased strain capability manifests itself in the increase in free volume by the addition of the long, 4- and 5-ring AEK curatives. As the average molecular weight between crosslinks increase, so do the molecular level degrees of freedom, and hence an increase in strain-capability is observed. As is the case in structure-property relationships, an increase in one property usually leads to a decrease in another, and the free volume created by the high molecular weight curatives leads to a decrease in T_g. Secondary molecular motions also appear to affect the hybrid network's mechanical properties. The AEK-hybrid networks show separated sub-T_g motions, and the segmental motions of the β-transitions reveal an extra mechanism to dissipate strain energy. During a strain event the AEK-hybrids contain molecular segments which can more easily rearrange, or distort, compared to short, stiff DDS, as evidenced by the presence of such β-transitions. This leads to an overall increase in stress and strain compared to DDS-based networks. Additionally, 4RA-hybrids show increasing stress and strain with increasing AEK-concentration, where 5RA-hybrids show a decrease until the maximum at 100 mol%. The stiff center of 5RA, in combination with increased molecular packing from low cure extent, hinders the segmental motions more than 4RA-networks which leads to this odd trend.

Summary

In this chapter two types of hybrid networks based on 4RA and 5RA were studied. Industrially-cured hybrid networks were prepared using DDS and AEK diamine concentrations of 5, 10 and 20 mol% to ensure ease of processability. DSC analysis of the networks' cure kinetics and development showed that reaction onset temperatures and activation energies were decrease upon addition of AEK diamines due to increased nucleophilicity of 4RA and 5RA. Furthermore, DSC revealed that cure conversion decreases with an increase in AEK concentration. This was attributed to the faster reaction kinetics of AEKs which led to decreased gelation and vitrification times.

Thermomechanical characteristics of the hybrid networks were studied by DMA through analysis of tan delta and storage modulus. Glass transitions of the blended systems were decreased and broadened upon AEK incorporation, and were also found to deviate from the Fox equation. These results were attributed to low degree of cure which created network-level heterogeneities and lower crosslink density. Further analysis of tan delta showed network defects similarly effect sub-T_g transitions. It was found that γ- and β-transitions are separated into different relaxations upon AEK incorporation. Furthermore, it was shown that dampening in 4RA hybrids is greater than in 5RA hybrids.

Uniaxial compression testing was performed to study the effects of AEK concentration on glassy state bulk mechanical properties. Addition of AEK diamines was found to improve mechanical properties over the baseline DDS-networks. Modulus improvements were hypothesized to be caused by nano-sized AEK-rich domains which act as ductile particles. Enhancements in moduli were also attributed to improved packing

of unreacted segments which increased network cohesion. Stress and strain improvements were ascribed to the increases in average crosslink molecular weight from the longer diamine curatives. It was shown that fully aromatic, hybrid epoxy-amine networks can provide increased distortion to composite matrices, and it is believed that further study of hybrid network tailorability will enhance the capabilities of aerospace composite matrix chemistries.

CHAPTER VII

SIMULTANEOUS REINFORCEMENT AND TOUGHNESS IMPROVEMENT IN AN

AROMATIC EPOXY NETWORK WITH AN ALIPHATIC HYPERBRANCHED

EPOXY MODIFIER

Objective

This chapter demonstrates the effects of an aliphatic, epoxide-functional hyperbranched polymer (HBE) on the thermal and mechanical properties of an aromatic epoxy-amine network. Networks based on DGEBA-33DDS were modified with 5-20 wt% HBE. DSC was used to study the cure process and, along with FTIR, provided insight into the structure-property-relationships observed. Mechanical properties including compression strength, strain, Young's modulus, and fracture toughness were studied and related to the thermal transitions observed with DMA. It was found that, although the hyperbranched structure deceased the glass transition temperature of the network, it also allowed for simultaneous enhancement in both fracture toughness and Young's modulus. These findings were attributed to relationships between chemical structure, crosslink density and non-bond interactions, and indicate the potential for further glassy network fracture toughness improvement without loss of critical mechanical properties by tailoring of the hyperbranched structure.

Results and Discussion
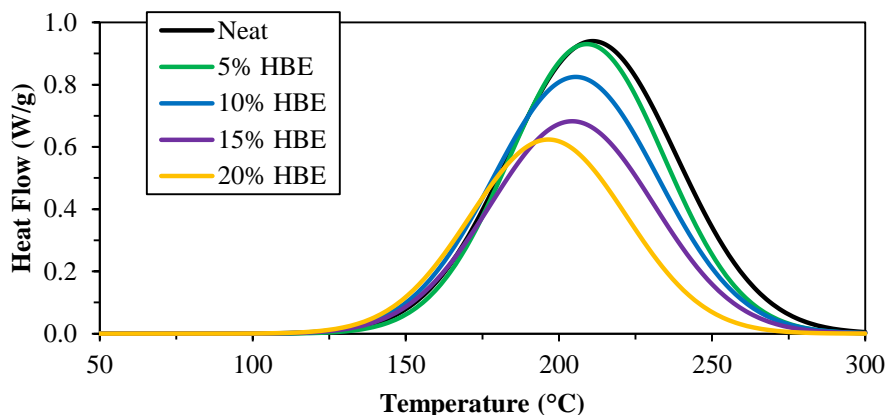
Figure 98. DSC exotherms of HBE-modified networks obtained at 10 °C/min.

Network Formation via DSC

DSC was used to characterize the formation of HBE-modified DGEBA-33DDS

networks (Figure 98 and Table 30). It was found that the onset of reaction, peak

temperature, and total exotherm all decrease with an increase in HBE content. This

indicates that incorporation of the highly mobile, aliphatic HBE increases the overall

reactivity of the epoxy blend, and we attribute this effect to a combination of chemical

functionality and molecular structure. Aliphatic functionalities such as those of HBE have

lower activation energy barriers than those of aromatic systems, which results in higher

reactivity and earlier cure onset temperatures.[5] Furthermore, it is well accepted that

hydroxyl groups, from both ring-opening of epoxides and additional chemical

incorporation, catalyze epoxy-amine reactions.[115,165,166] HBE's high concentration of

hydroxyl units is believed to enhance the catalytic effect and hasten the onset of reaction

between epoxide and amine. Secondly, the globular molecular structure of the

hyperbranched polymer provides a reduction in room temperature viscosity when it is

added to the epoxy blends. Thus at low temperatures at the start of the reaction, the reduced viscosity allows higher mobility of the functional groups and a concomitant increase in reactivity. The increased reactivity, however, results in a more rapid onset of gelation, and viscosity increases more quickly at elevated temperatures as the reaction progresses.
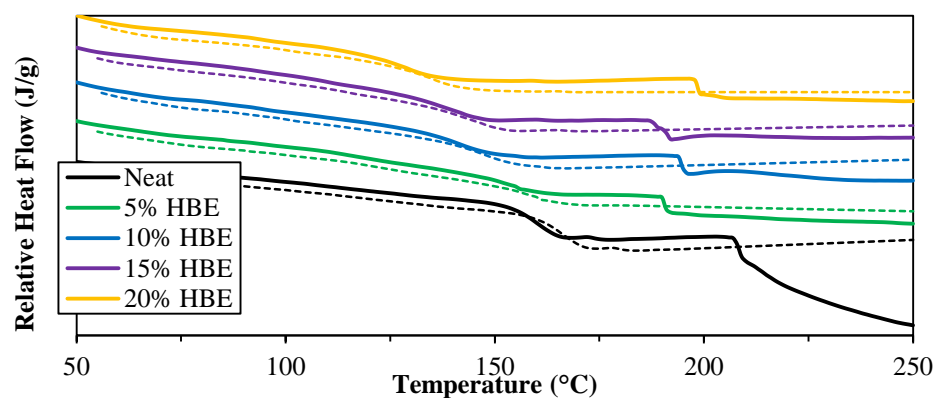
Figure 99. Residual exotherm (solid) and second reheat (dashed) after cure profile for HBE-modified networks; notice slight increase in T_g after second reheat due to full conversion.

Table 30

DSC exotherm peak data for 10 °C/min curves found

Sample Name	Onset °C	Peak °C	Total J/g	Residual J/g	DOC %
Neat	163.5	210.9	432.4	11.8	97.3
5% HBE	162.1	209.5	383.0	13.5	96.5
10% HBE	155.4	206.8	343.5	17.6	94.9
15% HBE	149.6	205.0	312.3	18.9	93.9
20% HBE	149.6	200.7	285.5	22.1	92.3

Using the total observed exotherm, degree of cure (DOC) was calculated for samples prepared using the standard cure profile described in *Sample Preparation.* Figure 99 shows the residual exotherms integrated, as well as the second reheat. DOC is of paramount importance when studying the physical properties of glassy epoxy-amine networks due to its effects on crosslink density, T_g, and mechanical properties.[132,167] Final cure extent was above 90% for all networks herein, but it was found that an increase in HBE content led to a decrease in the final DOC (97–92%). This result is hypothesized to be a consequence of the reactivity and multifunctionality of HBE. An increase in HBE content was shown to decrease the cure reaction's onset temperature, but an increase in modifier concentration also increases the average functionality of the blend. According to the Caruthers equation[6],

$$p_c = \frac{2}{f_{avg}}$$

where p_c is the critical extent of reaction at gel and f_{avg} is the average functionality of a mixture of monomers, an increase in f_{avg} leads to a decrease in the critical extent of reaction at gel. Due to the stoichiometric epoxide-amine ratio and because phase separation does not occur, this treatment can be applied to approximate the relationship between p_c and DOC. Theoretical calculations were performed for each network and are found in Table 31. It is hypothesized that an increase in HBE content decreases p_c and therefore DOC. As gelation occurs, HBE-modified networks become locked into place due to increases in viscosity, and because of their higher reactivity, the aliphatic epoxides of HBE are consumed earlier than DGEBA-epoxides. The constrained infinite-gel structure provides a decrease in reaction rate leaving behind a higher concentration of unreacted epoxides. As average functionality increases with HBE content the extent of

reaction at gel is further depressed and there is an increase in unconsumed functional

groups, which in-turn leads to the observed decrease in DOC.

Table 31

Theoretically calculated average functionality and critical extent of reaction for HBE-modified network

Sample	f_{avg}	p_c
Neat	2.688	0.744
5% HBE	2.730	0.733
10% HBE	2.776	0.720
15% HBE	2.826	0.708
20% HBE	2.880	0.695
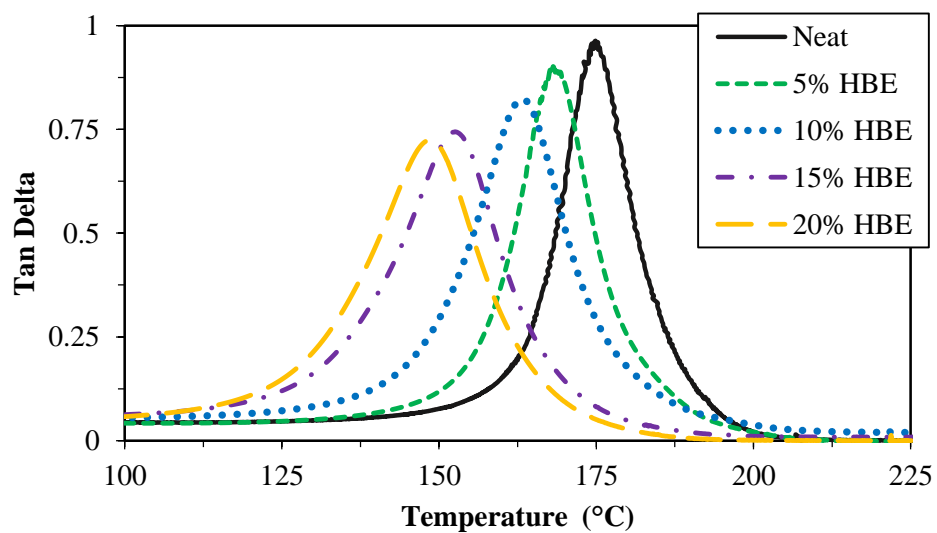
Figure 100. Tan delta α-transitions representative of T_g of HBE-modified networks.
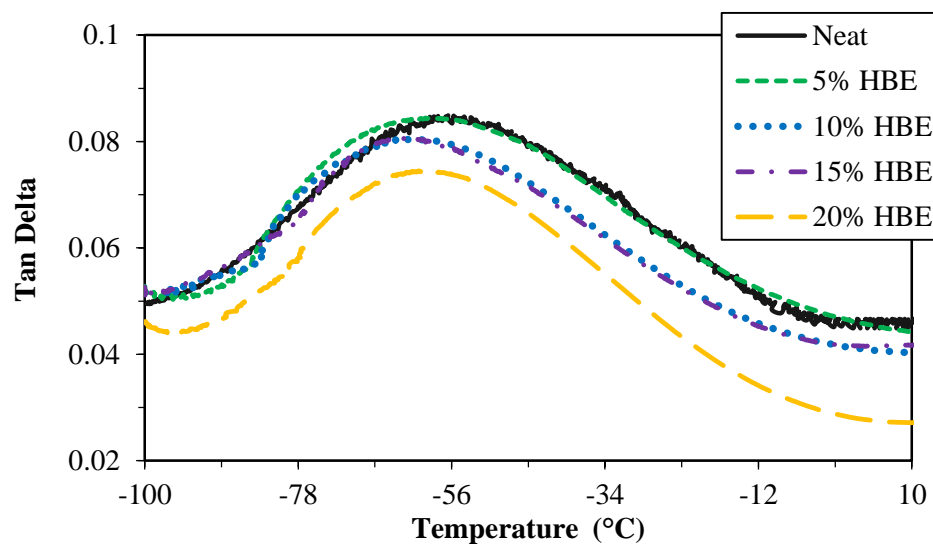
Figure 101. Tan delta β-transitions of HBE-modified networks.

DMA Thermomechanical Properties

The thermomechanical characteristics of the cured HBE-modified networks were studied by DMA in order to evaluate HBE miscibility and influence on network structure. Plots of the loss tangent as a function of temperature are displayed in Figures 100 and 101, and the peak features are tabulated in Table 32. Two characteristic peaks are observed in the temperature range evaluated, the *β*-transition (-100–10 °C) and the *α*-transition (125–200 °C). The *α*-transition (Figure 100), attributed to the glass transition, appears as a single tan delta peak for each blend. The peaks broaden on incorporation of HBE, but there is no detectable peak splitting, indicating that the HBE is well-dispersed in the network without phase separation after cure. The temperature at maximum peak height (T_g) decreases with increasing HBE content, explained by the greater chain mobility resulting from incorporation of the highly branched and flexible aliphatic HBE. The *β*-transition (Figure 101), attributed to glassy-state cooperative segmental motions of the network hydroxyl-groups[38], also appears as a monomodal peak for each of the blends.

As observed for the α-transition, the β-transition temperature at maximum peak height is decreased on incorporation of HBE.
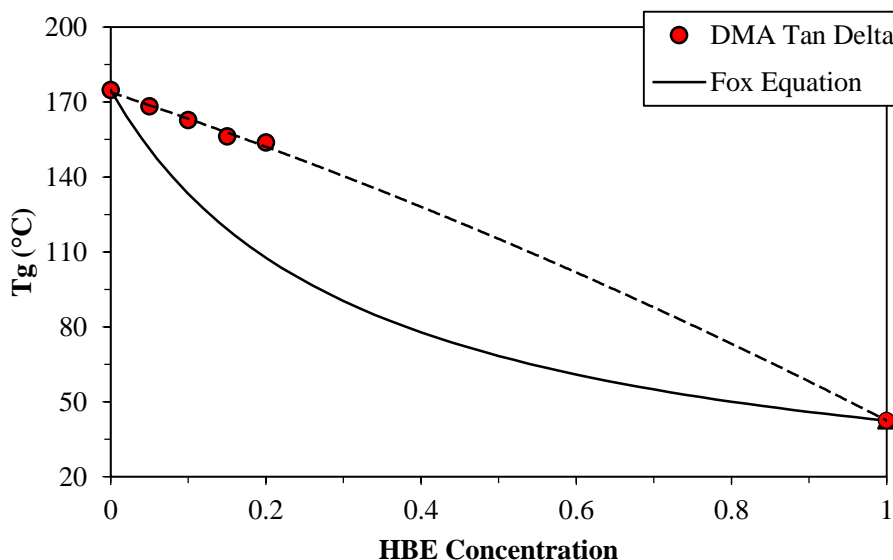
Figure 102. Experimental glass transition from DMA tan delta and Fox prediction as a function of HBE (mass concentration).

Further analysis of T_g and miscibility was performed using a rule of mixtures consideration. Treating cured networks as statistical copolymers by ignoring crosslinks, T_g vs. composition can be described by the Fox equation.[160] The applicability of the Fox equation in hyperbranched-modified epoxies was shown previously by Mezzenga *et al.* with their systems showing good agreement between the computed and experimental values. However, the HBE-modified systems herein reveal a positive deviation from the predicted T_g values (Figure 102). Positive deviations have been shown to be a result of strongly interacting mixtures, where polymers with strong secondary interactions can order at different length-scales.[162,168] As HBE content is increased there is an increasing concentration of hydroxyl-functionalities left within the network which is hypothesized to

enhance secondary interactions such as hydrogen bonding and other non-bond forces and cause the increase in T_g over the predicted values. Although miscible at length-scales greater than 10^{-6} m (shown by SEM), some phase separation of the HBE may occur at smaller scales thus causing this slight deviation. Likewise, T_g's dependence on cohesive energy density has been shown to affect these deviations and also the breadth of the T_g region (ie. tan delta width) [31]. The additional hydroxyls from HBE are believed to increase cohesive energy and thus the predicted T_gs digress from the experimental T_gs. The effects of hydroxyl-moieties on network property enhancement will be discussed further in *Network Mechanical Behavior*.

Table 32

Tan delta peak analysis data; FWHM: full width at half maximum

Sample Name	β-Peak Max °C	β-Peak FWHM °C	α-Peak Max °C	α-Peak FWHM °C
Neat	-56.5	47.9	174.9	13.0
5% HBE	-57.6	49.1	168.2	14.0
10% HBE	-59.9	51.7	163.4	17.6
15% HBE	-61.4	42.0	155.8	16.9
20% HBE	-57.1	38.2	152.1	16.3

The breadth of the loss tangent peak indicates the network's ability to dissipate energy and network homogeneity. Full width at half maximum (FWHM) for the α- and β-transitions are displayed in Table 32. The maximum value of FWHM is observed for the 10 wt% HBE network for both the α- and β-transition, indicating that this blend has the

greatest damping capability, which is better understood by comparison with crosslink density. Apparent crosslink density, ν_e, was determined from the classical theory of rubber elasticity.[92] The parameters used to calculate crosslink density, the experimentally determined crosslink density, and the network's physical density are presented in Table 33. The apparent crosslink density displays a minimum at 10 wt% HBE loading, following an inverse trend to that observed in the α- and β-transition FWHMs. This is attributed to the relationship between aliphatic content and average functionality, which both increase with increasing HBE content. Addition of aliphatic structures into an aromatic network decreases storage modulus, which lowers apparent crosslink density.[164] Increasing average functionality (through addition of the f=10 HBE) increases the number of theoretical junction points, yielding a network structure that is exceedingly hindered with higher rubbery modulus and apparent crosslink density.[169] In the 10 wt% HBE network, the effect of the increased aliphatic content is greater than that of the increased average functionality, resulting in a lower modulus network with lower apparent crosslink density. In the 15 and 20 wt% HBE composites, the average functionality effect becomes more prominent and apparent crosslink density increases.

The apparent crosslink density displays a minimum at 10 wt% HBE loading, following an inverse trend to that observed in the α- and β-transition FWHMs. This is attributed to the relationship between aliphatic content and average functionality, which both increase with increasing HBE content. Addition of aliphatic structures into an aromatic network decreases storage modulus, which lowers apparent crosslink density.[164] Increasing average functionality (through addition of the f=10 HBE) increases the number of theoretical junction points, yielding a network structure that is exceedingly

hindered with higher rubbery modulus and apparent crosslink density.[169] In the 10 wt% HBE network, the effect of the increased aliphatic content is greater than that of the increased average functionality, resulting in a lower modulus network with lower apparent crosslink density. In the 15 and 20 wt% HBE composites, the average functionality effect becomes more prominent and apparent crosslink density increases.

Table 33

Physical density and crosslink density calculations from rubbery E'

Sample Name	ρ g/cm^3	T K	E_r MPa	$v_e *10^{-3}$ mol/cm^3
Neat	1.28	478	31.5	2.64
5% HBE	1.23	471	22.2	1.89
10% HBE	1.23	465	17.6	1.52
15% HBE	1.22	456	27.0	2.37
20% HBE	1.22	453	27.4	2.43

DMA also afforded preliminary insight into the mechanical behavior of the HBE-modified blends through storage modulus (E') vs. temperature plots Figure 103. Surprisingly, it was found that addition of the hyperbranched modifier improved E' below T_g and E' increased with HBE content. As observed in tan delta, the onset of the glass transition region of E' for HBE-networks occurs earlier and more gradually compared to the Neat network. Materials that contain opposing glassy-state E' and T_g values are said to be antiplasticized, where below temperatures required for long-range segmental mobility an additive can restrict short-range molecular motions and thus stiffen

the material. These hindrances can come from the filling of free volume and/or an

increase in secondary molecular interactions and are well reported for epoxy

networks.[33,42,46] The E' trend herein is believed to be from the network-level

incorporation of HBE which provides additional functionality to enhance the network's

cohesive forces. Further confirmation of the increases in E' and antiplasticization were

found with bulk mechanical testing.
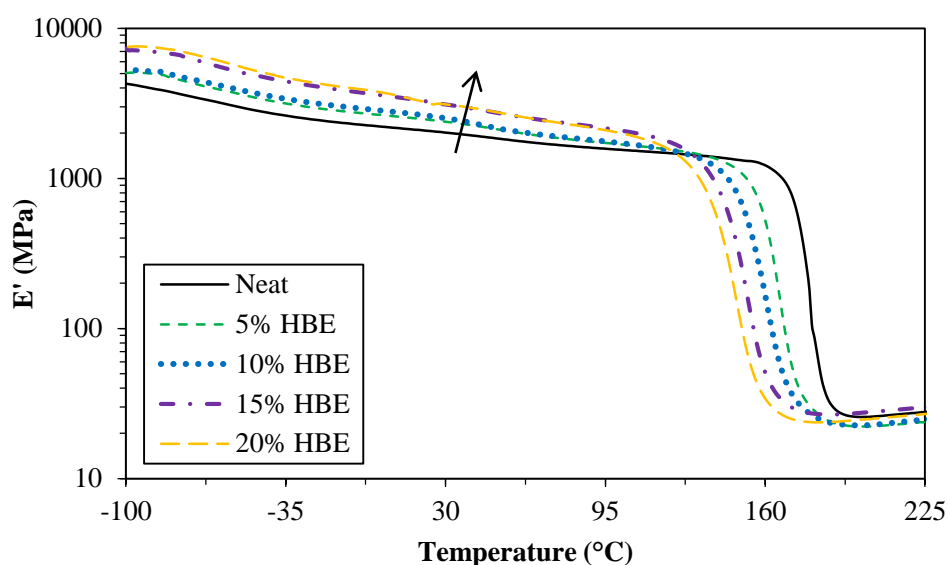
Figure 103. Storage modulus (E') obtained from DMA temperature sweep; arrow
indicates increase in HBE concentration.

Network Mechanical Behavior

The room temperature mechanical properties of the modified networks were

studied as a function of HBE loading and are shown in Table 34. Yield strength, yield

strain, and Young's modulus were measured under uniaxial compression (Figure 104).

Average compression yield strength of the modified networks was found to decrease with

an increase in HBE content, with the highest loading level of HBE giving the greatest

decrease of approximately 9.5% below that of the neat network (significant to p<0.05 for the neat sample in comparison to all samples with HBE, 5% HBE significantly different from15% and 20% samples to p<0.05). This diminution of strength is attributed to the increase in aliphatic content within the network, as well as the general decrease in crosslink density.
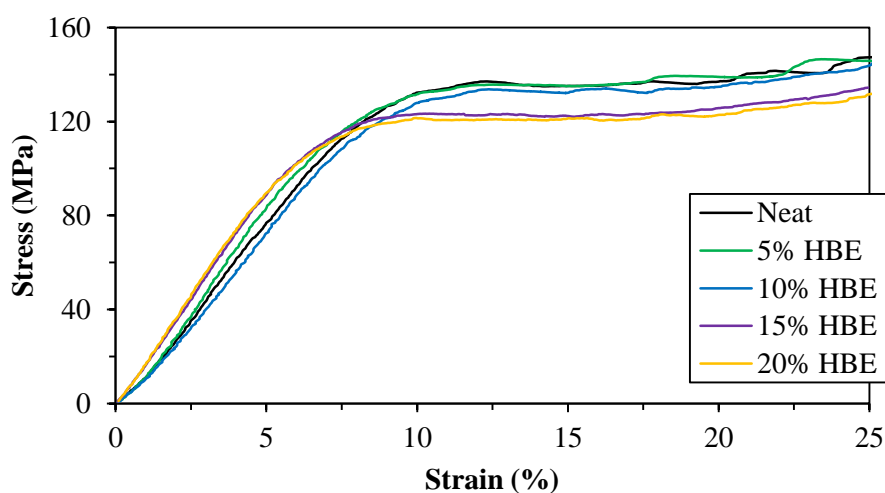
Figure 104. Uniaxial compression stress vs. strain curves of HBE-modified networks.

Compressive yield strain which describes a material's macro-scale energy absorbing capability, was found to follow a similar trend as the α- and β-peaks FWHM's, where the 10 wt% HBE material possesses a maximum average strain value approximately 7% higher than that of the neat network (significant to p<0.05 for neat compared to 10% HBE). This maximum in strain is credited to the network's lower crosslink density. The loosely bound network-segments have greater ability to rearrange and change molecular-level conformation during mechanical loading. These rearrangements are related to the glassy state motions of the β-transition, and indicate that the 10 wt% material can absorb more energy before failure than the neat network. The

improved distortional capability is also attributed to the homogeneous nature of the cured material, which provides a more even dissipation of energy throughout the network compared to phase separated systems. As the concentration of HBE is increased to 20 wt%, the networks' average yield strain decreases to below that of the neat material (significant to $p<0.07$ for neat compared to 20% HBE). This is also attributed to crosslink density, where the increased average functionality leads to more highly crosslinked systems that possess fewer possibilities for molecular rearrangements, and in turn are less elastic materials.

Table 34

Bulk mechanical properties obtained from uniaxial compression and tension testing

Sample Name	Yield Stress MPa	Yield Strain %	Young's Modulus GPa	Tensile Modulus GPa
Neat	137.1 ± 0.4	10.3 ± 0.3	1.8 ± 0.08	1.5 ± 0.35
5% HBE	133.1 ± 2.0	10.8 ± 0.3	2.1 ± 0.14	1.7 ± 0.61
10% HBE	130.6 ± 3.5	10.9 ± 0.2	2.2 ± 0.05	1.8 ± 0.44
15% HBE	127.9 ± 0.8	9.5 ± 0.6	2.3 ± 0.09	2.0 ± 0.36
20% HBE	124.1 ± 3.4	8.8 ± 0.4	2.6 ± 0.14	2.1 ± 0.41

Note: values are averages of 10 specimens and error represents one standard deviation

The most interesting observation from the uniaxial compression testing is the improvement in compressive modulus with increasing HBE content. The 20 wt% HBE modulus is 45% higher than that of the neat network (significant to $p<0.05$ for neat compared to all HBE samples). Interestingly, this trend occurs while incorporating a

flexible aliphatic structure into the network, which both decreases the glass transition and increases mechanical dampening. This promising development was further characterized by tensile testing (Figure 105), and shows a similar trend, although stress and strain values are lower, as is typical when tensile testing of brittle materials. To the authors' knowledge the observed manifestation of an enhanced Young's modulus in hyperbranched-modified epoxy networks has not been previously reported, and we believe that this remarkable finding is due to the inherent structure of the HBE studied herein.
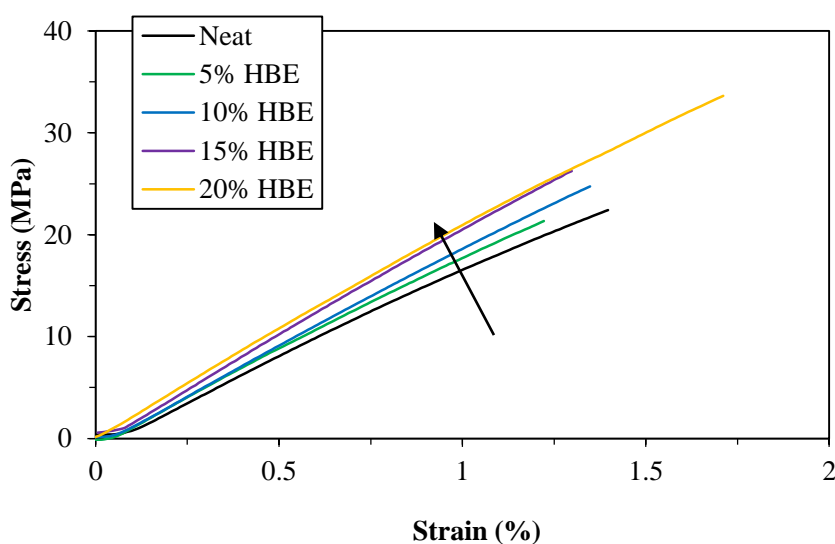
Figure 105. Uniaxial tensile stress vs. strain curves of HBE-modified networks; arrow indicates increase in HBE content.

During the synthesis of HBE, the hydroxyl content stays constant due to the ring-opening polymerization which consumes trifunctional B3-hydroxyls and generates HBE backbone hydroxyls. Although the hydroxyl-moieties have potential to react, the majority remain preserved as pendant units on the HBE backbone, and inclusion of this hydroxyl-

rich material into the network allows for an increase in secondary bonding and

interaction. The increase in non-bond interactions is understood to enhance the network's

cohesive energy density, which has been previously shown to improve room temperature

modulus.[46] FTIR spectra were taken to confirm that the additional hydroxyl-functionality

remains after the HBE-modifier is cured into the network (Figure 106). Integration of the

peak between 3710 cm^{-1} and 3096 cm^{-1} was performed assuming that primary and

secondary amino-hydrogens have been consumed and NH-stretching does not contribute

to the peak area.[170] It was confirmed that there was a steady increase in hydroxyl content

above that measured for the neat network. Non-bond interactions typically decrease while

driving conversion of functional groups, but because the HBE-hydroxyls remain

unreacted within the HBE's core, an increase in the modifier content allows an

exceptional increase in the room temperature compressive modulus. Likewise, the

decrease in degree of cure with increasing HBE content further supports the hypothesis

that an increase in intermolecular interactions is driving an increase in stiffness.
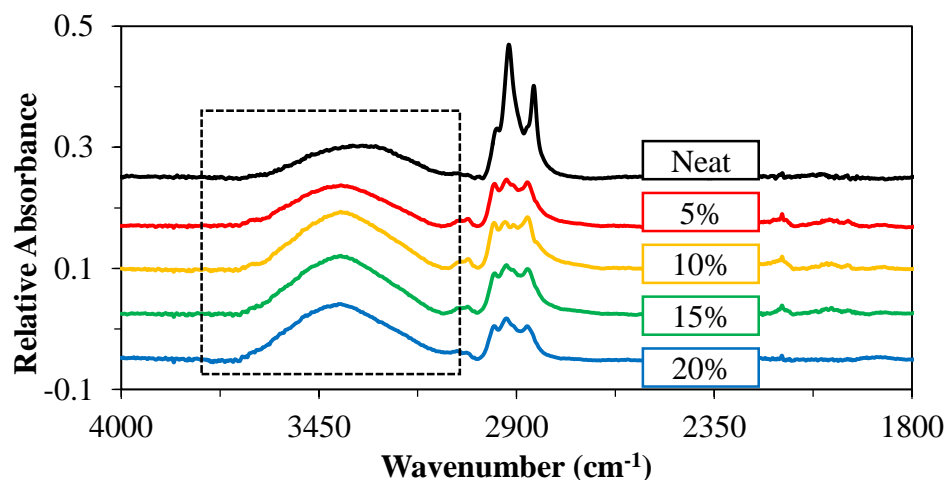
Figure 106. Mid-IR spectra of HBE-modified networks showing increase in –OH concentration after cure.

Fracture Toughness

The fracture toughness of a material in mode-1 fracture is determined by the stress intensity factor, K_{1C}, which was calculated for each HBE-modified network from SENB experiments using Equation 2 and are presented in Figure 107. K_{1C} shows substantial improvements from the addition of HBE. Fracture toughness values for K_{1C} approach a maximum at 10 wt% HBE incorporation, representing an increase of over 175% in comparison to that of the neat sample. For networks with concentrations higher than 10 wt% HBE, the average values decrease slightly and standard deviations increase. The maxima correlate with both the apparent crosslink density and the compressive strain data, where the 10 wt% network's crosslink density is at its lowest and strain-energy dissipation is at its highest.
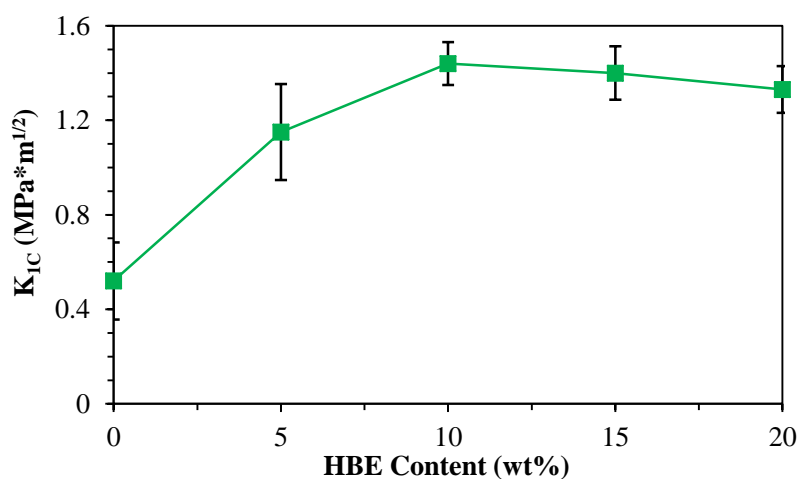
Figure 107. Stress intensity factor (K_{1C}) of HBE-modified networks; error bars represent one standard deviation.

This overall improvement in fracture toughness is attributed to the hyperbranched material's network architecture and its morphology. The epoxide moieties of the HBE provide miscibility during cure and allow reaction with other network functional groups,

which in turn produces greater adhesion to the matrix, as observed by Miao et al.[66] This

relatively homogenous architecture offers advantages in epoxy toughening over

unreactive tougheners because it provides greater flexibility between crosslinks and an

increased number of conformational rearrangement modes during a fracture event.
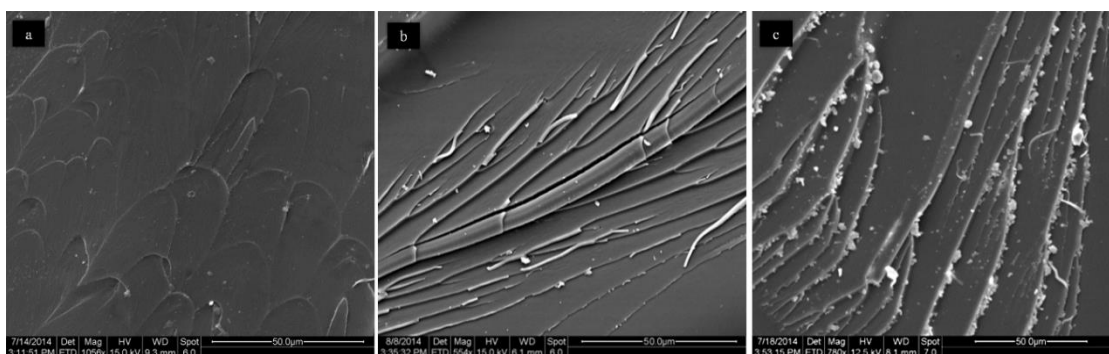
Figure 108. SEM images of fracture surfaces from fracture toughness specimens; (7a)
Neat, (7b) 10% HBE, (7c) 20% HBE.

Fracture Surface Morphology

The SEM images displayed in Figure 108 are of the fracture surfaces from the

SENB fracture toughness specimens for the neat, 10 wt%, and 20 wt% HBE samples.

The neat specimens exhibit characteristic epoxy fracture-surface morphology, with

minimal deformation observed from the smooth surface pattern, indicative of poor

fracture toughness. The addition of HBE to the networks allows improved energy

dissipation and toughening through the formation of fibrils proceeding from the surface

during the fracture event; this type of morphological enhancement is an indication of

yielding before failure and has been described as *in situ* toughening.[71] Typical

hyperbranched-toughened systems show dimple-like structures on their fracture surfaces

which are indicative of phase separation, but the materials described here are without

depressions and of a single-phase. The homogeneous nature of the fracture surface morphology is a visible, qualitative confirmation that the HBE is fully miscible within the cured network. The 10 wt% specimen has the largest and highest concentration of these fibrillar fracture structures, consistent with the DMA, yield strain, and K_{1C} data, showing the greatest energy dissipation for this concentration of HBE.

Summary

A fully miscible, aliphatic hyperbranched epoxy was studied as a glassy epoxy network toughness modifier at concentrations of 5, 10, 15 and 20 wt%. The synthesized HBE's low molecular weight (~4000 g/mol) and high epoxide content ($f \approx 10$) were targeted to obtain a homogenous network upon cure, which allowed for the observed *in situ* property improvements. Network thermomechanical characteristics were studied using DMA, and through peak analysis of the *α*- and *β*-relaxation it was revealed that the 10 wt% HBE network provided the greatest energy dampening. This was attributed to the synergy between the network's low crosslink density and its increase in aliphatic content.

Uniaxial compression testing was performed to study the network's glassy-state mechanical properties to compare different length scales of energy dissipation. A decrease in yield strength was ascribed to an increase in aliphatic content on incorporation of HBE into the mostly aromatic network. A maximum in yield strain was found for the 10 wt% network, attributed to its low apparent crosslink density which allowed enhanced molecular rearrangement. The most interesting finding was the improvement in Young's modulus over the range of HBE concentrations. This unique enhancement was explained by the high concentration of –OH groups that provided an increase in the network's non-bond interactions. These secondary interactions were

confirmed by FTIR, which revealed a steady increase in –OH groups with HBE content, even after cure.

SENB tests showed that K_{IC} fracture toughness increases with HBE content, and a maximum increase of 175% was found for the 10 wt% network. To our knowledge, this is the first report that demonstrated improvement in both fracture toughness and modulus by incorporation of a hyperbranched material. This simultaneous increase in multiple mechanical properties was attributed to the HBE's highly branched, functional, and miscible structure. We believe that the enhancement in modulus and toughness results from the HBE modified network's synergistic combination of high cohesive energy and glassy-state conformational mobility, which was elucidated on multiple length scales.

CHAPTER VIII

POSS-FUNCTIONALIZED HYPERBRANCHED EPOXY NANOCOMPOSITES:

MULTISCALE DISPERSION AND THERMOMECHANICAL PROPERTIES

Objective

The incorporation of POSS into epoxy-amine networks provides the opportunity to improve engineering properties of composite matrices. The goal of this chapter is to describe multiscale structure-property-relationships of novel POSS-modified hyperbranched epoxy nanocomposites. In this chapter amino-functional POSS and HBE were pre-reacted to provide a multifunctional handle to drive POSS dispersion within the aromatic DGEBA-33DDS network. The employed concentrations of HBE (10 wt%) and POSS (1 and 5 wt%) were selected based on studies in *Chapter VII* and from previous work.[87] Multiscale dispersion, thermomechanical characteristics, mechanical properties, and fracture toughness of cured materials were examined. Network architectural-formation was studied by DSC. The morphology of the hybrid nanocomposites was studied by SEM, TEM, and AFM. Finally the thermal, mechanical and fracture properties were evaluated by DMA, uniaxial compression, and notched 3-point bend, respectively. It was found that further improvements in both modulus and fracture toughness were obtained by POSS-incorporation, all without significant alteration of other mechanical or thermal properties. The concurrent increase in both thermomechanical and fracture properties was attributed to differences in multiscale dispersion states and interactions between POSS, HBE, and the epoxy-amine matrix.

Results and Discussion

Network Formation: DSC Kinetics

It is well known that the final properties of epoxy networks depend on its

chemical structure[171], cure conditions (such as time and temperature)[9], and extent of

functional group conversion.[159] The first step in understanding the relationships between

POSS, HBE, and the resulting nanocomposite properties, was through study of network

development with DSC isoconversional analysis (description of technique in *Chapter IV*).

The exotherm and conversion vs. temperature curves at each ramp rate (1, 5, 10, 20

°C/min) are shown by Figures 109, 111, 113, and 115, while the kinetics plots, ln(β) vs.

1/T, are shown by Figures 110, 112, 114, and 116 respectively.
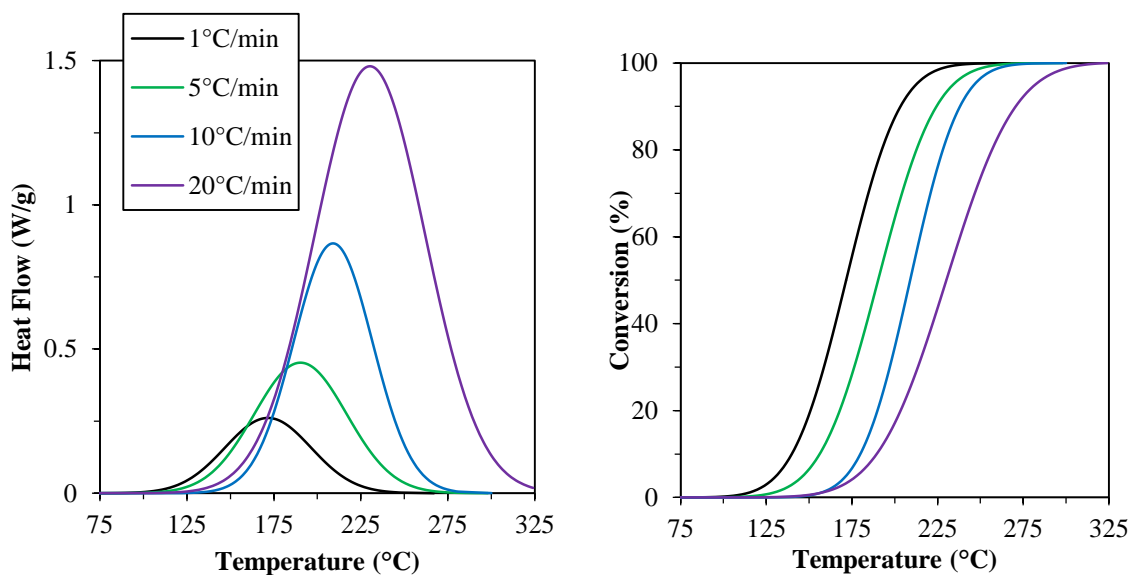
Figure 109. Heat flow vs. temperature (left) and conversion vs. temperature (right) for
DGEBA-33DDS, neat network.
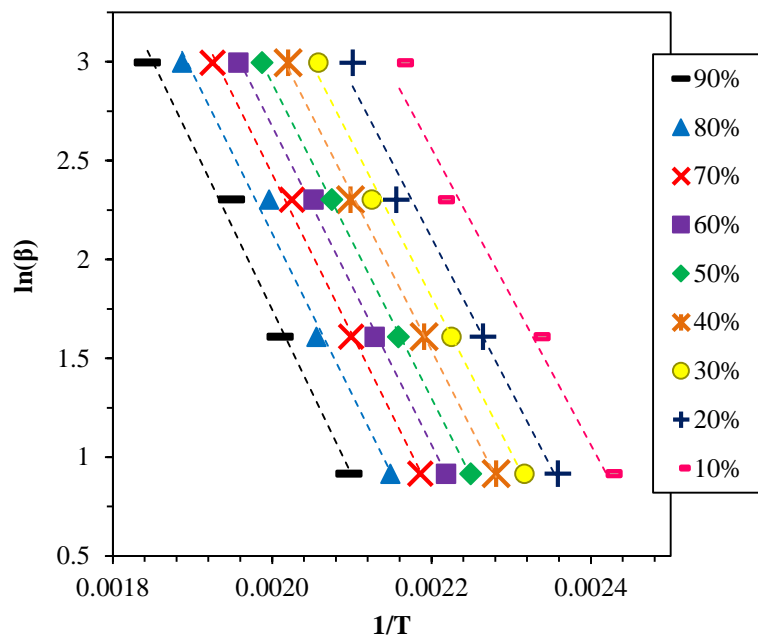
Figure 110. ln(β) vs. 1/T kinetic plot for neat DGEBA-33DDS at conversion 10-90%.
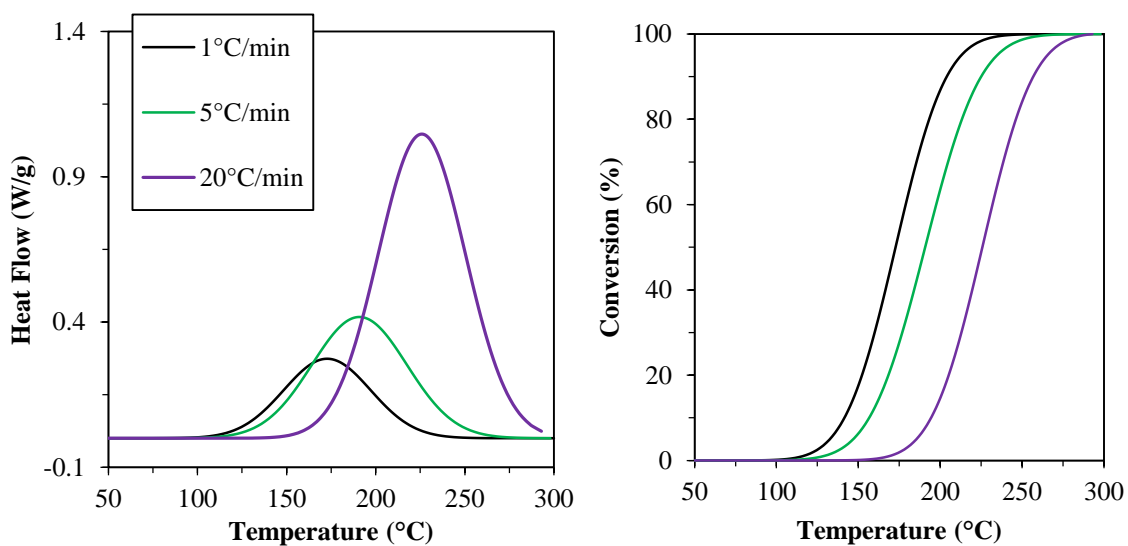
Figure 111. Heat flow vs. temperature (left) and conversion vs. temperature (right) for 10H networks.
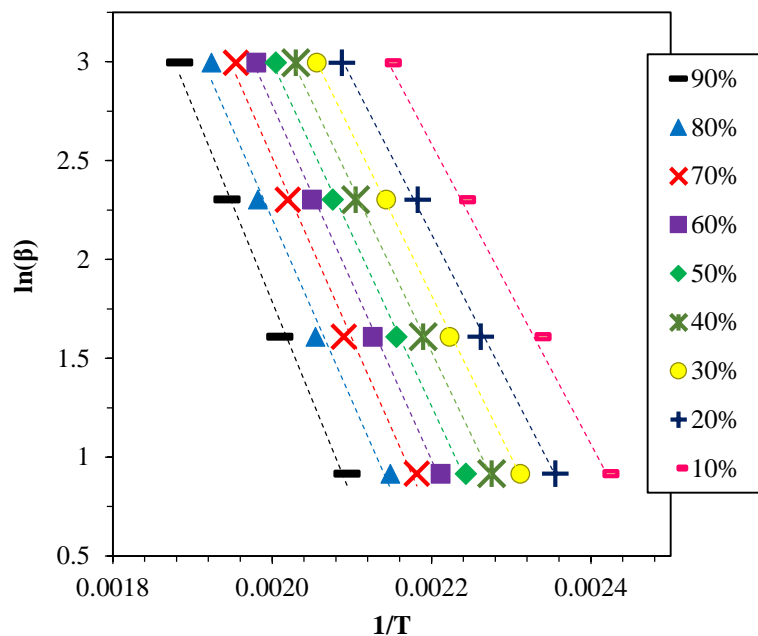
Figure 112. ln(β) vs. 1/T kinetic plot for the 10H network at conversions 10-90%.
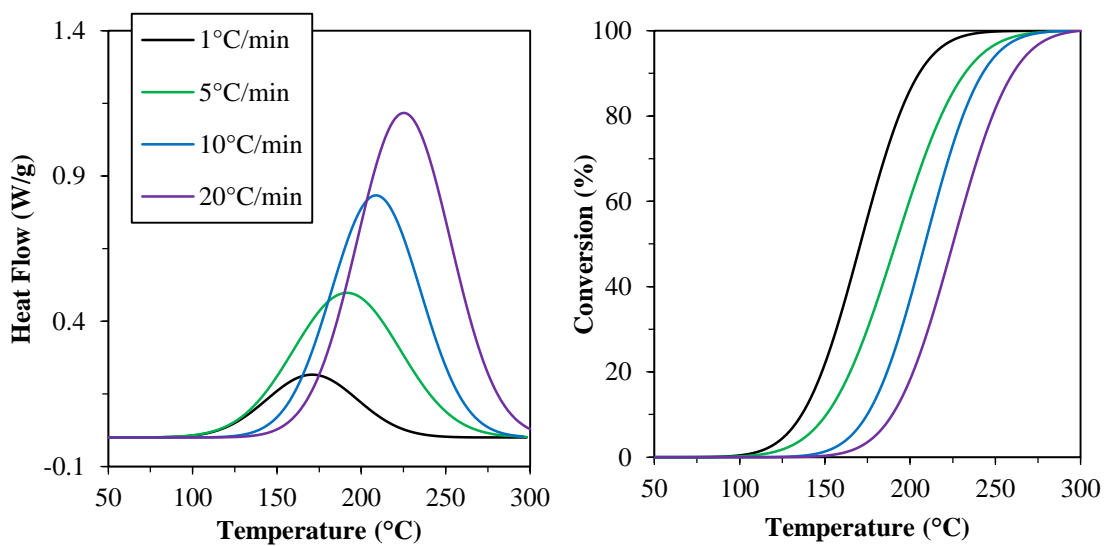
Figure 113. Heat flow vs. temperature (left) and conversion vs. temperature (right) for the 1P-10H network.
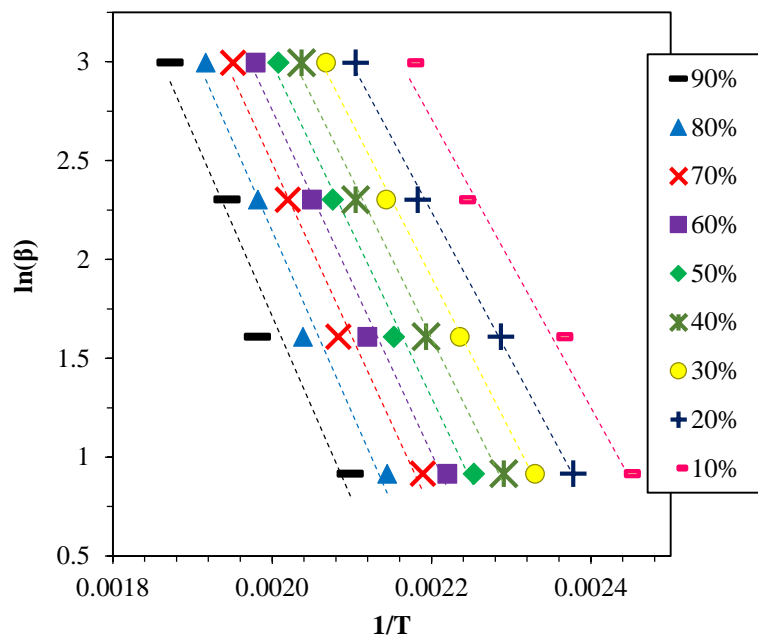
Figure 114. ln(β) vs. 1/T kinetic plot for the 1P-10H network at conversions 10-90%.
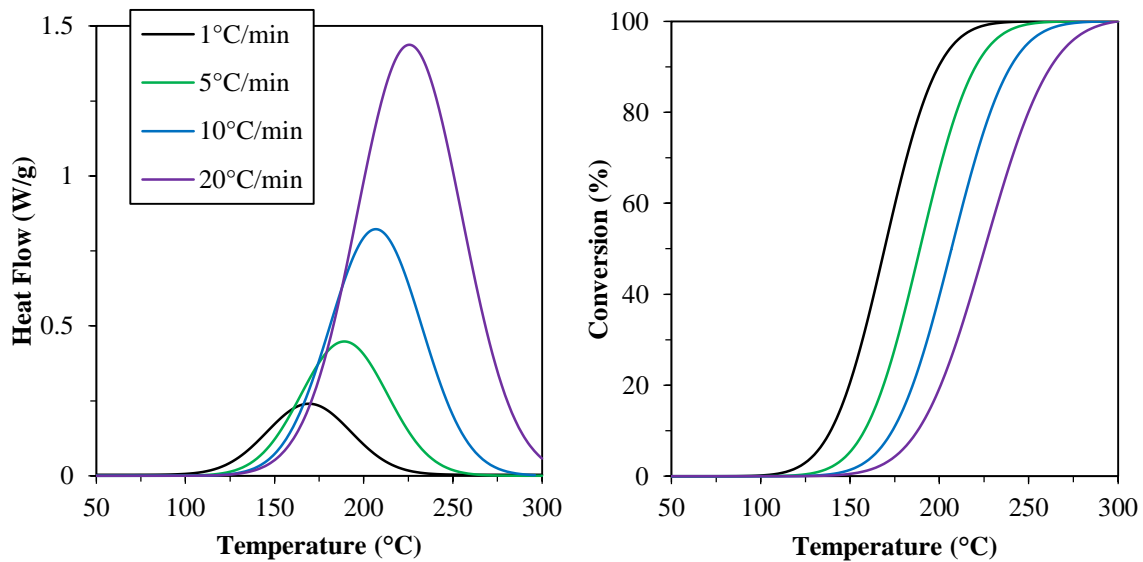
Figure 115. Heat flow vs. temperature (left) and conversion vs. temperature (right) for the 5P-10H network.
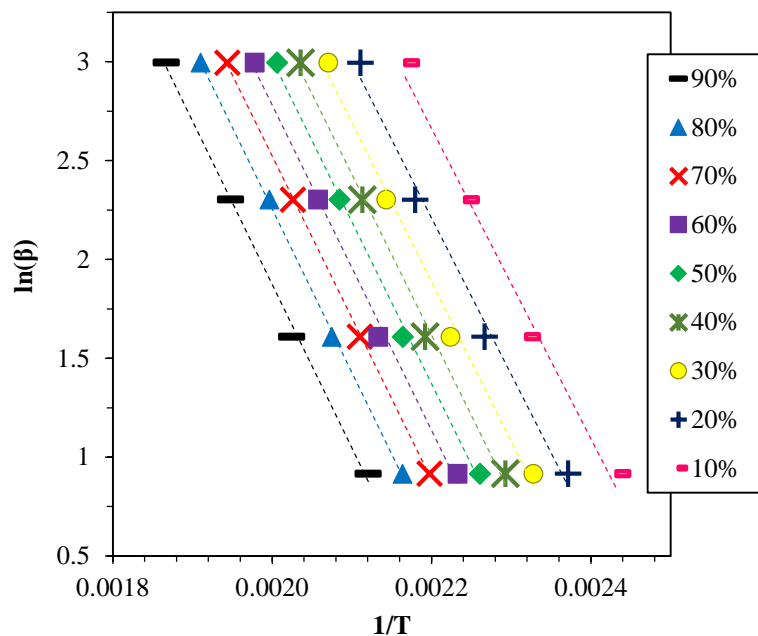
Figure 116. ln(β) vs. 1/T kinetic plot for the 5P-10H network at conversions 10-90%.
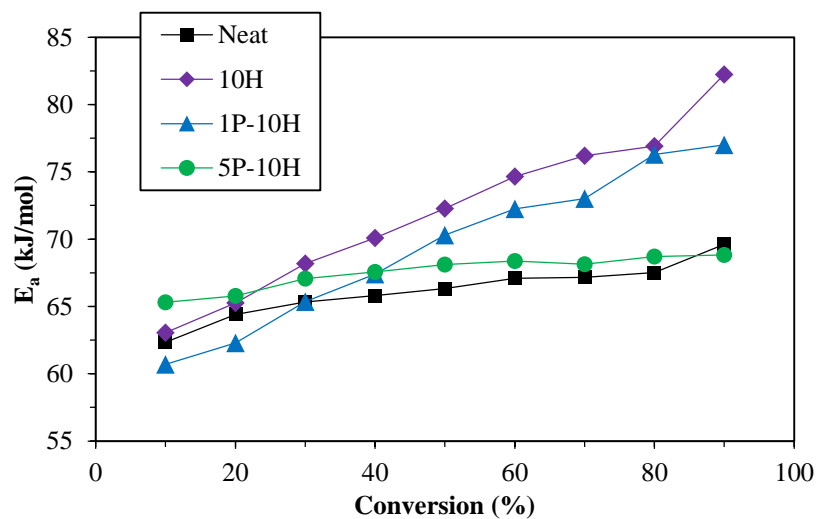
Figure 117. Activation energy, Ea, vs. conversion during network formation for conversions 10-90%.

Displayed in Figure 117 is the final result of the isothermal analysis. Each

material, be it epoxy or nanocomposite, displays gradually increases in E_a with

conversion. As epoxy and amine functional groups are consumed and a gel formed, further conversion of functional groups becomes more difficult due to lower accessibility and decreasing concentration of reactive groups. This behavior is typical for the stiff aromatic network and represents a constant reaction mechanism during crosslinking.[7,114] The studied networks are grouped into two different E_a trends, with 10H and 1P-10H networks having accelerated E_a increases over 5P-10H and neat networks. Additionally, the apparent activation energy follows the same grouping, where 10H and 1P-10H networks have higher apparent E_a (72.1 and 69.4 kJ/mol, respectively) than neat and 5P-10H networks (66.2 and 67.5 kJ/mol, respectively). This behavior is attributed to the concomitant effects of higher reactivity and faster viscosity increase in the two networks containing the higher concentration of aliphatic-HBE. Because of low POSS concentration and high HBE-reactivity, 1P-10H activation energy and network development are driven by HBE. As the POSS concentration increases to 5 wt% in 5P-10H, the reaction mechanism and kinetics appear to revert back to those of the neat network. It is hypothesized that POSS-particles may begin to aggregate with the higher concentration of 5P-10H. This aggregation potentially drives POSS-HBE molecules to phase separate on various size-scales, which prevents the kinetic increases observed in 1P-10H.[123] Furthermore, aggregation creates less miscible components and therefore DGEBA-33DDS acts as the kinetic driving force in 5P-10H network development. These results coincide with similar POSS-concentration cure-dependency reports in literature.[80,81]

Test specimens were cured using the industrial cure protocol (1 °C/min from 100-180 °C, isotherm at 180 °C for 3 hours) and then cure extent was measured by DSC from

the residual exotherm. Curing produced networks with high degrees of conversion (all above 97%), and it was found that incorporation of HBE and POSS increased the cure extent. Although POSS-epoxides and -amines are reported to have lower reactivity than their monomer analouges[81,89], it is hypothesized that HBE's higher reactivity leads to the early consumption of HBE and POSS. Since the cure temperature is above the final network T_g, early-onset vitrification is prevented and the remaining functionalities (both aliphatic and aromatic) are less hindered to react and provide the observed conversions.

Table 35

Data used to calculate cure extent from 10 °C/min DSC experiments; values averaged from two runs

Sample Name	Onset °C	Peak °C	^aH_T J/g	^bH_C J/g	α_R %
Neat	163.6	210.6	410.6	11.3	97.3
10H	155.0	207.8	480.2	7.3	98.5
1P-10H	154.6	205.2	405.3	2.8	99.3
5P-10H	154.3	205.1	390.8	1.5	99.6

a: exotherm of uncured specimens

b: obtained after 3 hour industrial cure at 180 °C

Bulk Morphology Characterization – SEM

Microscale phase separation and POSS dispersion were assessed via SEM analysis of cured specimen fracture surfaces (Figure 118). Differences in fracture surface morphology from the incorporation of HBE and POSS-HBE were observed. The relatively smooth surfaces of neat specimens is typical of fully-cured aromatic epoxy

fracture, and is indicative of its brittle nature.[172,173] Upon incorporation of 10 wt% HBE, the fracture morphology displays a change from brittle to ductile with the observation of material-pullout in the form of matrix strands. These fibrillar-structures are indicative of good energy dissipation and have been previously reported as an *in situ* network toughening mechanism.[64,174] This type of toughening is due to network-level incorporation and minimal phase-separation after cure. Based on these results, it was hypothesized that the highly soluble HBE would provide pre-reacted POSS-HBE enhanced miscibility and improve POSS dispersion to provide increased distortional-capability.
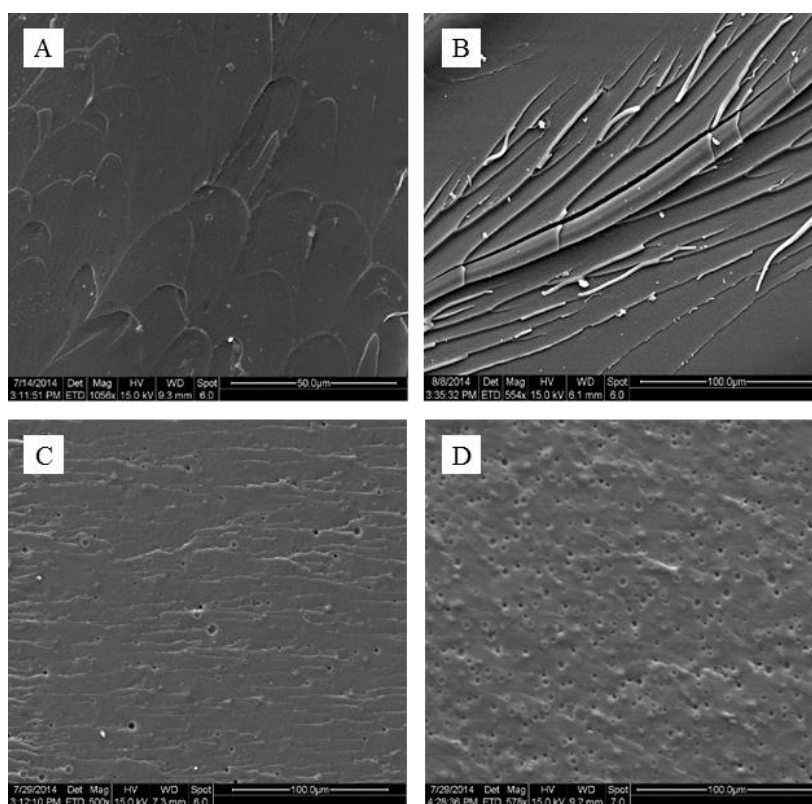
Figure 118. SEM images of POSS-HBE nanocomposite fracture surfaces; (A) Neat, (B) 10H, (C) 1P-10H, (D) 5P-10H.
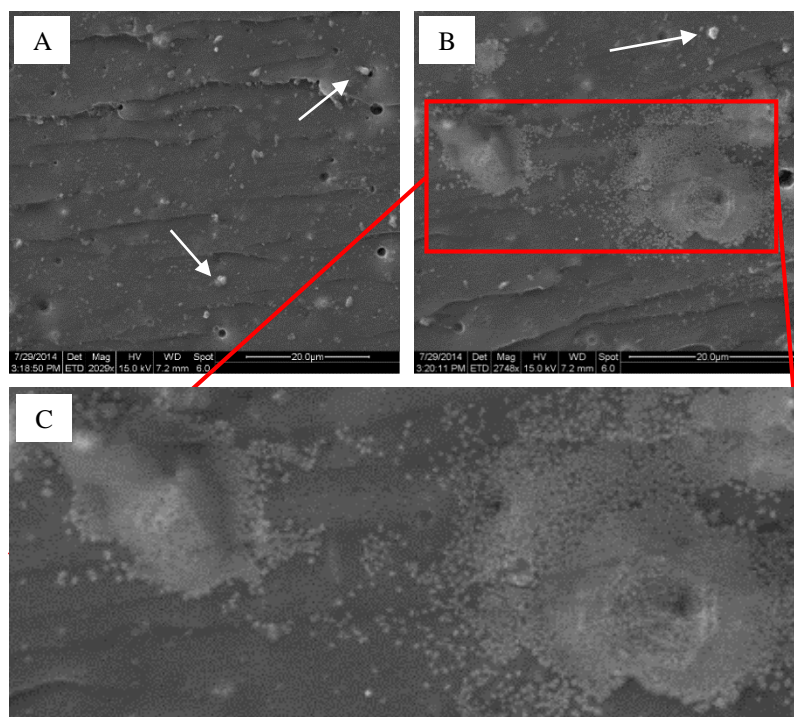
Figure 119. SEM micrographs of POSS agglomerates and clusters; 1P-10H (A), 5P-10H (B); arrows show largest observable agglomerates; cutout (C) shows finely separated POSS clusters.

Figures 118C (1P-10H) and 118D (5P-10H) show an abrupt transition from 10H's

in situ toughness behavior to signs of POSS-driven morphology. The fracture surfaces of

1 wt% POSS networks exhibits very few surface features and are indicative of

macroscale POSS dispersion. The few POSS aggregates that existed at the fracture

surface were confirmed via EDX and were between 1.0–2.0 μm in diameter. These

aggregates were attributed to unreacted POSS. 5 wt% POSS samples contain dispersed

indentations that form a dual-phase similar to island-sea morphologies. Further imaging

found that, upon fracture, pull-out of POSS clusters (1–20 μm) from the matrix led to the

detected morphology. Observed only within 5P-10H (Figure 119), these clusters are

composed of individual POSS crystallites (0.01–0.1 μm), many of which are finely

separated by matrix material. Further investigation of the POSS clusters and their phase-separated morphology was performed with TEM and AFM.
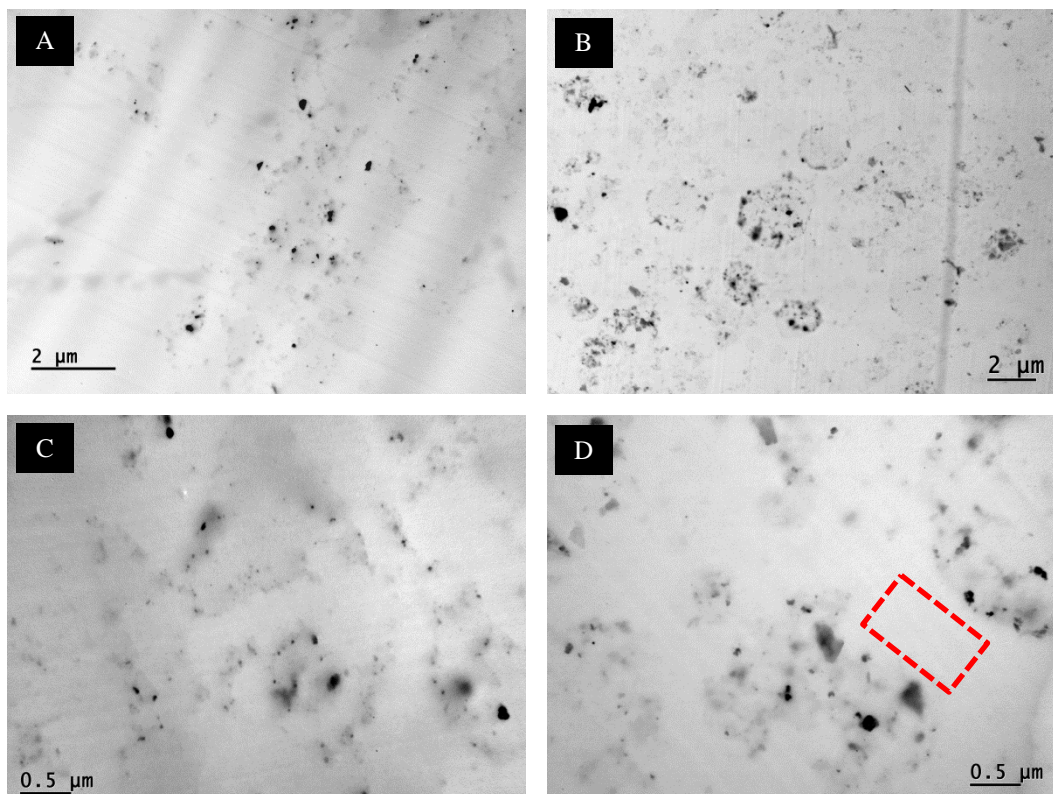
Figure 120. TEM micrographs of POSS-HBE nanocomposites at two magnifications; 1P-10 (left, A, C), 5P-10H (right, B, D); dashed-rectangle represents areas scanned by AFM.

Microscale Morphology Characterization - TEM

TEM micrographs were obtained to study POSS agglomerates observed in SEM of 1 and 5 wt% POSS-HBE nanocomposites, and are shown in Figure 120. It was found that the two POSS-containing materials have varying degrees of agglomeration and dispersion due to pre-reaction. Molecularly disperse POSS was difficult to observe with the relatively thick sections obtained from microtoming, however, discernable POSS aggregates were visible and found to be between 10–500 nm. 1P-10H (Figure 120A)

shows very good dispersion with an average nanocrystallite size less than 200 nm. Micrographs of 5P-10H shown in Figures 118B and 118D help describe the clusters of discretely separated POSS aggregates observed in 5 wt% POSS SEM micrographs. It is shown that the individual POSS aggregates are of similar size as observed within 1 wt% POSS (10–500 nm), but tend to segregate to form POSS-rich domains. These POSS-rich clusters are believed to develop from 5P-10H's higher concentration of unreacted POSS which can aggregate with itself and with pre-reacted pendant-POSS. It should be noted that 1P-10H specimens did show signs of this clustering, but in much lower concentration. Due to this POSS-drive clustering, it is hypothesized that the interiors of the phase separated domains contain higher concentrations of HBE; this was investigated and supported by AFM and DMA.

Nanoscale Morphology Characterization - AFM

Nanomechanical mapping using AFM was performed to obtain information on the nanoscale morphology and to provide further insight into the toughening mechanisms of POSS-HBE. Using a calibrated probe with known physical parameters, relative stiffness images from the calculated DMT-modulus can be obtained to probe phase separation. Figure 121 shows both micro- and nano-scale images of the samples studied; micro-scale height images (column A) are shown as reference for the DMT-modulus images (columns B and C). Due to the inherent surface roughness of the POSS nanocomposites, large, high resolution scan sizes (> 5x5 µm) were obtained with difficulty. However, the nanoscale areas separating the POSS clusters, represented by the rectangle in TEM Figure 120D, were imaged via AFM to directly probe the effects of molecularly-disperse POSS-cages on network phase behavior.

Neat specimens, Figure 121 row 1, display no apparent phase separation on the micro or nanoscale and show typical epoxy-amine morphology.[129] Similar to what was observed with SEM, the 10H sample demonstrates a homogeneous micro-scale morphology with HBE evenly dispersed throughout the network. Scan sizes of 500 x 500 nm show disordered, oblong regions which are of low modulus (1–1.5 GPa) and between 100–300 nm in size. These flexible regions are believed to be DGEBA-deficient (ie HBE-rich) and their formation is attributed to HBE's higher reactivity. The onset of reaction for epoxides of HBE with the primary amines of DDS is 10 °C lower than that of DGEBA and DDS. Because the cure temperature is ramped to 180 °C, the initial HBE-DDS reaction occurs for a short time before DGEBA-DDS begin to aid in network-formation. Although DGEBA and HBE are relatively miscible before reaction occurs, this initial HBE-DDS reaction allows for step-wise network formation and creates the observed nanoscale domains. However, 10H DMT-modulus images also reveal a higher concentration of increased-stiffness regions compared to the Neat network. This is credited to increased cohesive forces from the hydroxyl-moieties of highly-dispersed HBE molecules interacting with DGEBA's hydroxyproyplether segments.[26,46]
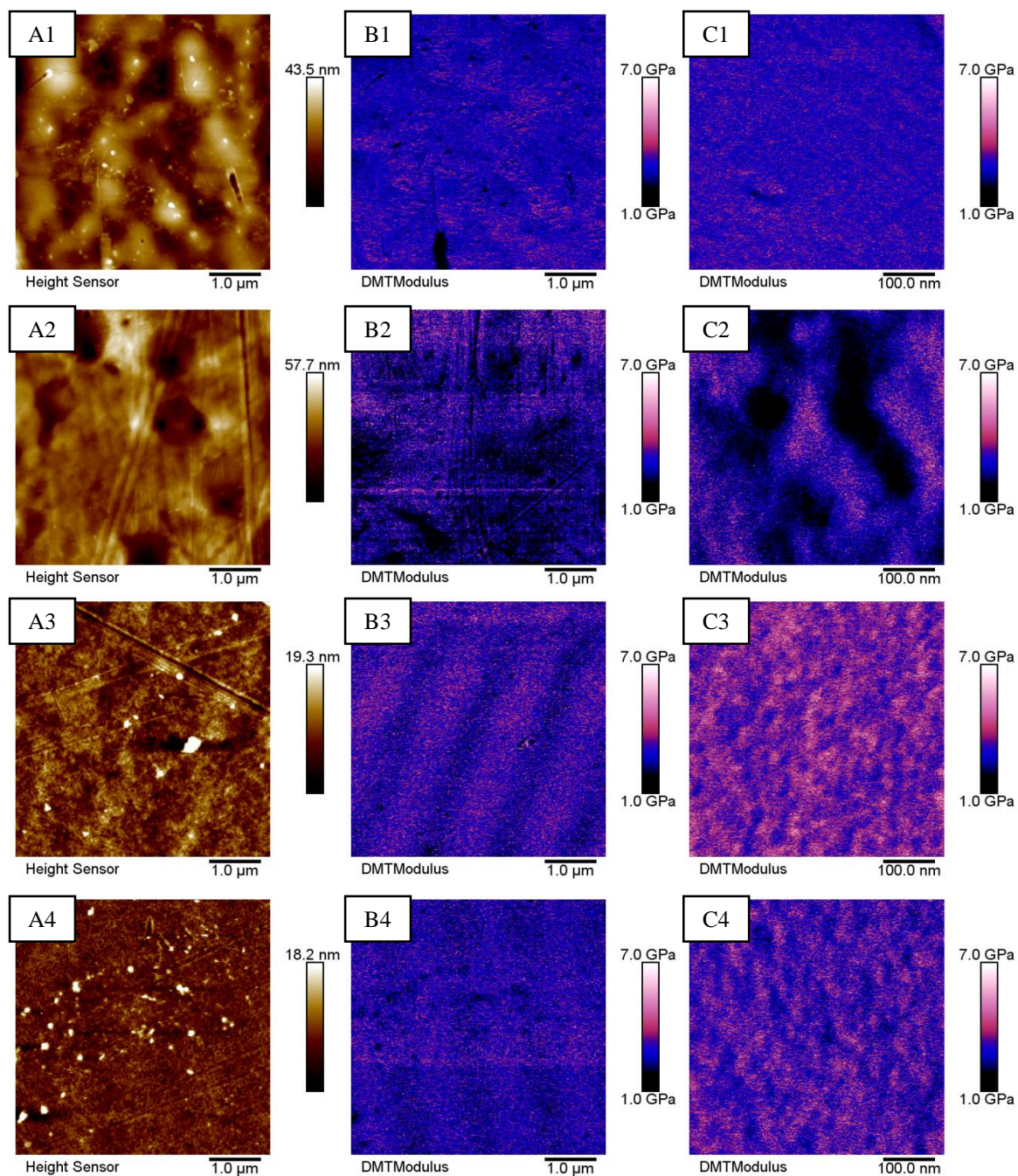
Figure 121. AFM images of modified networks; (Column A) 5 μm height images, (Column B) 5 μm DMT-modulus images, (Column C) 500 nm DMT-modulus images; (Row 1) Neat, (Row 2) 10H, (Row 3) 1P-10H, (Row 4), 5P-10H.

The effects of pre-reacted POSS-HBE on nanoscale morphology are shown by the

500 x 500 nm scans in Figure 119 A3-C3 and A4-C4 for 1P-H10 and 5P-10H,

respectively. Displayed are small, evenly dispersed nanodomains between 10-20 nm (1P-10H) and 5-10 nm (5P-10H). It is also shown that POSS-modified systems have higher DMT-moduli values than the Neat network. Both the reduction in domain-size and increase in modulus are attributed to the generation of strong particle-polymer interactions through the pre-reaction. It is well known that POSS tends to aggregate, but it has also been shown that pre-reaction helps to reduce aggregation and increase dispersion.[87,88] Furthermore, POSS dispersion and its effects on mechanical properties have been shown to be a result of its interactions with the surrounding epoxy matrix.[82,83,89] It is hypothesized that pre-reaction of POSS and HBE both tethers POSS and forms a favorable interphase between the nanoparticle and modifier. The generation of an interphase is due to intimate interaction of POSS's iso-octyl pendants and HBE's aliphatic backbone. This interaction limits aggregation and hinders HBE molecular motion to create the observed high modulus nanodomains. Additionally, 1P-10H shows the highest DMT-modulus values (5.5-6.5 GPa). This is ascribed to the low POSS concentration and a high degree of molecular-level dispersion. The detected nanoscale phase behavior and its role in improved modulus and fracture toughness properties of the nanocomposites will described in the subsequent sections.

Dynamic Mechanical Behavior

DMA was used to investigate the prepared materials' viscoelastic properties as well as gain further insight into POSS dispersion. Figure 122 shows storage modulus vs. temperature (E'), Figure 123 and Figure 124 shows tan delta vs. temperature for two temperature regions, and Table 36 has specific values from the curves. Glassy state storage moduli increase with an increase in formulation complexity, with 5P-10H having

the highest E' and the baseline network showing the lowest. However, 10H and 1P-10H networks have very similar E' below T_g. Above T_g a completely different trend is observed. Neat networks show the highest rubbery moduli, 10 wt% HBE networks have the lowest, and POSS-containing networks fall in between.
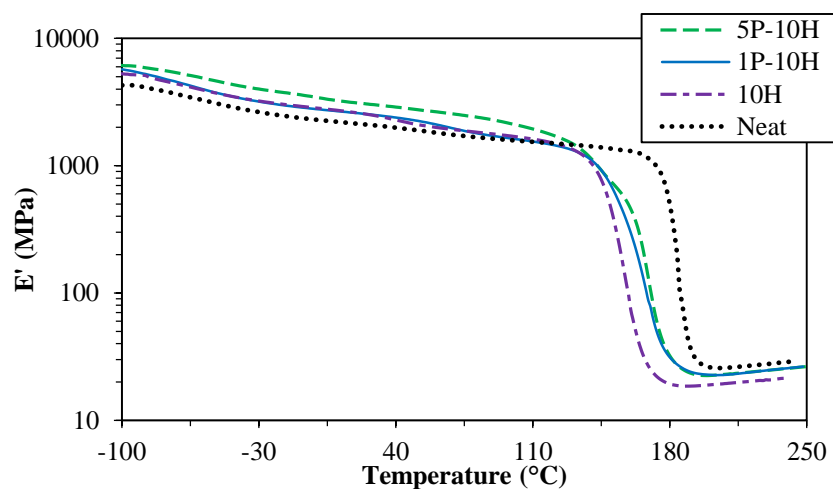
Figure 122. Storage modulus of POSS-HBE nanocomposites obtained from DMA in tension-mode.

Table 36

Thermomechanical data of POSS-HBE nanocomposites obtained from DMA

Sample	E', 25 °C	E', 225 °C	T_β	T_α
Name	MPa	MPa	°C	°C
Neat	2105	27.2	-56.5	174.9
H10	2540	19.7	-62.8	163.6
P1-H10	2675	24.2	-55.4	167.7
P5-H10	3055	24.7	-54.5 (3.1)	(142.1) 170.8

As observed in Chapter VII, the initial increase in E' from the incorporation of HBE is attributed to the enhancement of network-level cohesive forces and interactions. The high level of miscibility and additional hydroxyl-moieties allow for increased hydrogen bonding with the neat network, thus restricting previous motions. Addition of POSS-HBE allows for similar increases in cohesion from the pre-reacted modifier, but further hindrance of molecular motion is provided by the nanoreinforcement effects of the molecularly disperse POSS.[78] This reinforcement is attributed to restriction of individual and cooperative motions from the POSS-cage. With less volume for segmental rearrangement and an increase in the spatial extent required for these rearrangements, molecular-level motion is suppressed and E' is increased. Likewise, 1P-10H and 5P-10H nanocomposites negate the viscous effects observed in the rubbery modulus from HBEs aliphatic backbone through strong POSS-POSS and POSS-polymer interactions. POSS-POSS interactions form strong physical networks which hinder motion of the matrix constituents within the different size-scale domains, and have been previously described to enhance both glassy- and rubbery-state storage moduli.[89] 5P-10H shows further fortification across the examined temperature range because of the higher concentration of POSS agglomerates and therefore additional physical crosslinks
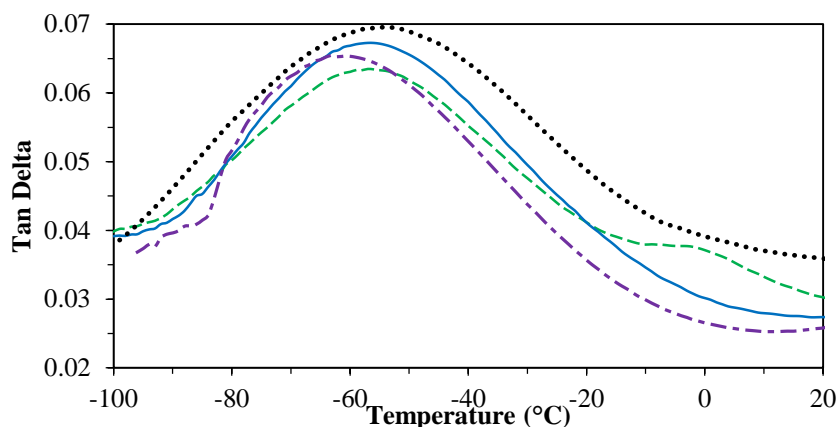
Figure 123. β-transition of thermomechannical tan delta vs. temperature curves for POSS-HBE nanocomposites obtained by DMA.

Tan delta was studied to gain further insight into micro-scale heterogeneities of POSS-HBE nanocomposites. Deep within the glassy state the low temperature peak referred to here as the *β*-transition provides information on the extent of local motion [33,35,147] and can be related to ductility.[28,175] The *β*-peak temperature first decreases with incorporation of HBE from -57 °C to -63 °C. Added free volume from the flexible HBE backbone provides the numerous hydroxyl/ hydroxypropylether moieties additional space for local motions which increases the timescale of relaxation, and therefore is observable at a lower temperature. Upon addition of POSS, the *β*-transition peak increases from -63 °C to -55 °C (both POSS concentrations), or back towards the Neat network value. This is attributed to molecularly disperse-POSS hindering the local motion of HBE segments by restricting aliphatic chain mobility and filling free volume created by the hyperbranched polymer.[89] It is also believed that the POSS-HBE pre-reaction and the isooctyl R-groups of the POSS-cage provide increased matrix solubility which creates an intimate and rigid POSS-HBE interface.[176,177] This sterically hindered interfacial region intensifies cooperativity of local motions and thus reinforces the network (also observed

in E'). Additionally, POSS-crystallites which have aggregated into micro-domains likely play a different role in the network's glassy state motions. 5P-10H shows a shoulder at ~0 °C. This small peak is indicative of the previously observed micro-scale phase separation due to POSS-HBE and free-POSS aggregation into POSS-rich domains (TEM, Figure 120). The peak temperature suggests that network segments within the clusters have increased cooperativity, and it is believed that the POSS-crystallites constrain the encapsulated segments and slow local motions; this allows observation of the POSS-rich domains local motions at higher temperatures.
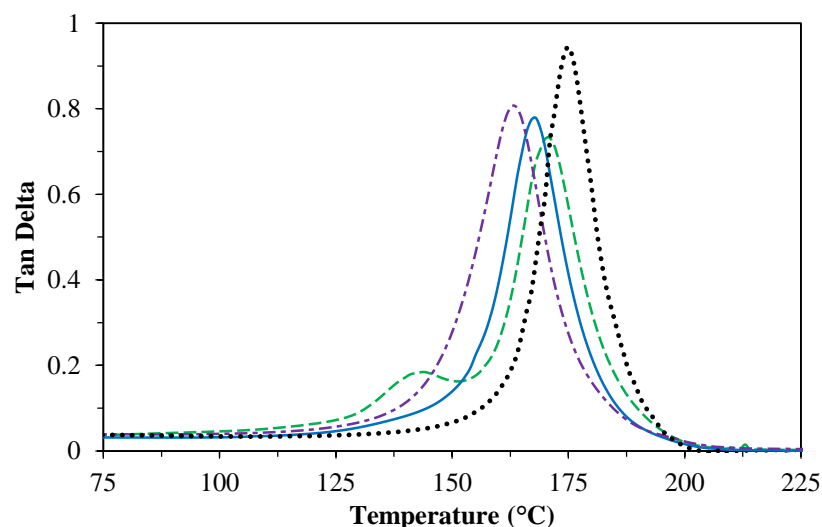
Figure 124. Tan delta α-transitions for POSS-HBE nanocomposites.

The elevated temperature transition observed between 125 °C and 200 °C corresponds to the glass transition, referred to here as the α-transition, and was studied to further understand microstructural homogeneity. The peak of the α-transition is decreased from 175 °C to 163 °C upon addition of HBE, and incorporation of 1 and 5 wt% POSS leads to the subsequent T_g increases of 168 °C and 171 °C respectively. Interestingly, 5P-

10H's α-transition displays a shoulder at 142 °C. A second T_g is related to microscale phase-separation of immiscible or partly miscible polymer blends[123] and, in this case, is attributed to the POSS-rich domains previously discussed. It was hypothesized that these domains contain a higher concentration of HBE than the bulk due to strong interactions between free-POSS and pre-reacted POSS-HBE molecules. These interactions are proposed to drive POSS-HBE to aggregate with other POSS-crystallites, "dragging-along" the attached HBE molecule.
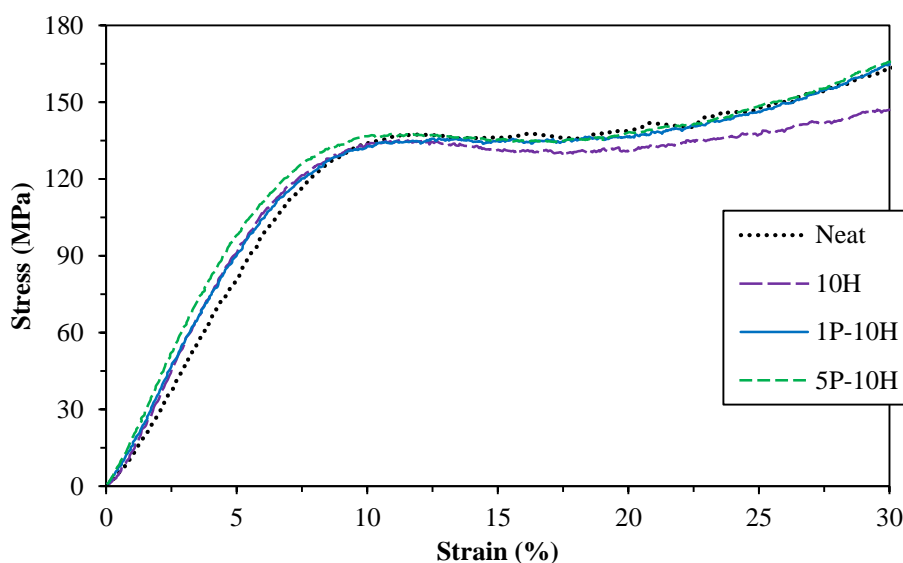
Figure 125. Uniaxial compression stress vs. strain curves of POSS-HBE nanocomposites.

Mechanical Properties and Fracture Toughness

As a result of the interesting dispersion states found from microscopy and thermomechanical analysis, the bulk mechanical behavior of POSS-HBE modified systems was studied. Figure 125 shows representative uniaxial compression stress-strain curves, and Table 37 summarizes the mechanical properties of the studied networks. The compression results indicate that incorporation of both HBE and POSS-HBE modifiers

into an epoxy matrix do not lead to statistically significant changes in either yield stress or strain. On the other hand, each of the modified networks provided increases in Young's modulus. The compressive moduli increased by 17, 19, and 28% for networks 10H, 1P-10H, and 5P-10H respectively. Similar to the results of the AFM and DMA studies, an increase in bulk modulus is attributed to the increase in cohesive forces from incorporation of HBE, as well as the reinforcing effects of molecularly disperse POSS.

Table 37

Uniaxial compression data for POSS-HBE nanocomposites

Sample Name	Yield Stress (MPa)	Yield Strain (%)	Young's Modulus (GPa)
Neat	137±0.3	10.3±0.3	1.77±0.1
H10	135±3.5	11.5±0.7	2.15±0.1
P1-H10	137±1.3	11.5±0.2	2.22±0.1
P5-H10	135±3.4	12.2±0.9	2.26±0.1

The inherently brittle nature of highly aromatic, glassy epoxy networks impedes the materials' further utilization in high performance composite laminates. SENB tests were performed to study fracture toughness and are presented in Figure 126. These measurements indicate that K_{IC}, related to the energy absorbed prior to failure, is considerably improved upon network modification with both HBE and POSS-HBE. Neat matrix fracture toughness is improved by 177%, 229%, and 223% with addition of 10H, 1P-10H, and 5P-10H respectively. It should be noted that the brittle DGEBA-33DDS networks have a higher margin of error within the tested population (10 SENB

specimens), but network modification leads to an increase in ductility and also reduces the error attached to the test method; this further indicates the effectiveness of POSS-HBE toughening. Furthermore, the systems herein show atypical fracture resistance vs. T_g behavior, where the greatest improvement in toughness is obtained by a material with only a moderate decrease in T_g.
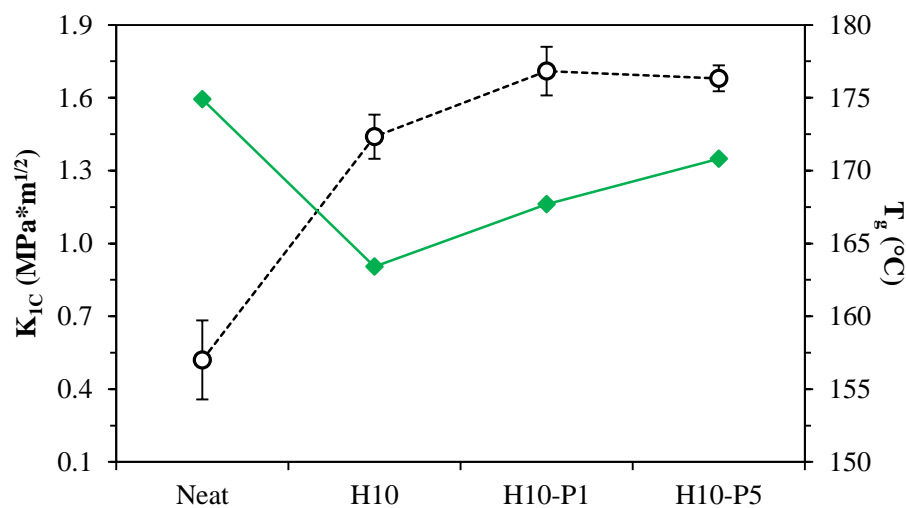
Figure 126. Fracture toughness of each POSS-HBE material compared to T_g; error bars indicated one standard deviation.

The observed improvements in fracture toughness are attributed to two the multiscale structures of both HBE and POSS. First, incorporation of HBE leads to modification of the network's molecular-level architecture as well as its nano-scale morphology. The highly branched and aliphatic chemical structure of HBE allows for higher free volume and therefore increases the modes of conformational rearrangement in which the network can undergo during a strain event.[21,178] These rearrangements, or distortions, produce molecular-level mechanisms for energy dissipation which preserve other mechanical properties, as confirmed by compression testing. Also, compared to the

Neat material, the HBE nanodomains are large and disordered. These domains act as covalently bonded soft particles that further enhance energy dissipation at the crack front, similar to rubber-toughening.[163,179,180] Continuing the dichotomy, further enhancement is realized by addition of POSS, which plays an entirely different role in toughening. The chemical structure of the POSS used herein comprises a rigid, inorganic core; seven flexible, organic pendant groups; and a single difunctional, reactive pendant moiety. The inorganic core provides a stiff site for stress and energy transfer from the comparatively ductile matrix. The isooctyl pendants and amino-functionalities (both primary and secondary amine) allow for POSS dissolution into HBE-nanodomains and DGEBA matrix, creating a strongly-interacting interphase which promotes energy absorption. Furthermore, pre-reaction of POSS and HBE creates a nanocomposite with good dispersion which improves the molecular-level interactions of POSS and the matrix. These mechanisms are reminiscent of those described by Bates *et al.* who used reactive block copolymer micelles and vesicles to enhance toughness through nanomorphology and matrix adhesion.[181,182] Similarly, POSS-HBE microstructural features such as those observed in 5P-10H (TEM), are hypothesized to act like core-shell microparticles, where the core is composed mostly of ductile HBE and the shell mostly of POSS-aggregates. During a deformation event, generated stresses at the crack front are hypothesized to translate from the "stiff" components (DGEBA matrix and POSS) to the "soft" components (HBE). As a result, segmental rearrangement of core-HBE fosters energy dissipation and toughness while POSS and its multiscale structures enhance modulus.

Summary

POSS-HBE nanocomposites were studied as glassy epoxy toughness modifiers. Four networks were compared: Neat, 10 wt% HBE, 1% POSS-10 wt% HBE, and 5 wt% POSS-10 wt% HBE. Network formation and cure state were studied with DSC and cure kinetics were found to vary depending on POSS concentration. 10 H and 1H-10P networks had similar reaction mechanisms while 5P-10H networks revealed a mechanism similar to that of the neat network. This was attributed to the differences in phase separation size-scales. Multi-scale dispersion and the differences in phase separation were revealed through SEM, TEM, and AFM. It was discovered that HBE-modified systems are miscible through the micro-scale, but separate into HBE-rich nano-domains upon cure. Addition of POSS led to entirely different type of multiscale morphologies, with 1 wt% POSS systems containing high levels of particle dispersion on each size scale examined. 5 wt% POSS nanocomposites showed heightened microscale phase separation. An interesting morphology was discovered where clusters of POSS were finely separated into nano-sized agglomerates. Nanoscale analysis using AFM showed high modulus regions between these clusters which was attributed to molecularly disperse POSS-pendants and constrained network segments.

Thermal transitions from DMA were used to further characterize the dispersion states of HBE and POSS. 5% POSS nanocomposites were the only materials to show signs of phase separation, but decreases and broadening in HBE and POSS-HBE peaks revealed energy dissipation capability of the modified networks. The addition of HBE decreased the T_g, but subsequent addition of POSS provided a shift in T_g back towards that of the neat network. Sub-T_g transitions were assessed to correlate mechanical

properties to glassy-state molecular motions. It was speculated that HBE increased free volume and enhanced molecular mobility, but addition of POSS was found to hinder the motions of HBE and reinforce the network. These observations were further confirmed with the thermomechanical storage modulus. Similar to observations in *Chapter VII* all modified networks had improved storage modulus, attributed to increased secondary interactions as well as nanoreinforcement.

Bulk mechanical properties were tested using uniaxial compression and SENB 3-point bend. Appreciable increases in both the stress and strain capability were not observed. However, linear viscoelastic compressive modulus and fracture toughness showed significant increases for all modified networks. The synergistic ductility and reinforcing effects of HBE and POSS were ascribed to the strong interactions between the aliphatic chain segments of HBE and the iso-octyl pendants of POSS, as well as the multiscale dispersion states of POSS. The modifiers' good miscibility allows the "hard" POSS component and the "soft" HBE component to more efficiently dissipate strain energy while maintaining stiffness.

CHAPTER IX

POSS-HBE MATRICES FOR CARBON-FIBER REINFORCED COMPOSITES

Objective

The purpose of this chapter is to report the preliminary evaluation of HBE and

POSS-HBE as distortional matrix modifiers in carbon-fiber composites. It was proposed

that the improved mechanical and fracture resistance properties of the bulk networks

observed in *Chapters VII* and *VIII* would translate to composite properties. Therefore

carbon-fiber composites composed of either DGEBA-33DDS, 10H, or 1P-10H matrices

were manufactured and then mechanically tested. The manufacturability of both the

initial prepreg and final laminates were characterized by the resin's viscosity and the

fiber/matrix content, respectively. Distortional and interlaminar fracture toughness

properties were studied by use of the 10° off-axis tension and dual cantilever beam

experiments. Mechanical tests were performed using digital image correlation to obtain

high accuracy results of the critical mechanical properties, strain and G_{1C}.

Results and Discussion

Prepreg and Laminate Manufacturability

To manufacture 100 ft of six inch wide prepreg tape with a fiber:matrix ratio of

approximately 0.65:0.35, 500 grams of epoxy-prepolymer is required. Each of the three

formulations was B-staged in a batch reactor until the prepolymer solutions became

transparent. In the past our group has found that the B-staged epoxy formulations used in

the manufacture of prepreg require an apparent viscosity at 70 °C of 50 Pa*s. Therefore,

after B-staging each formulation, the reactor was cooled to 70 °C and viscosity was

advanced and measured over one hour's time. The viscosity vs. time curves for each

formulation are shown in Figure 127. Similar to what was previously described in *Chapters VII* and *VIII*, viscosity increases more quickly with the addition of HBE due to its more reactive aliphatic structure. Therefore, the processing window of HBE and POSS-HBE modified composites is shortened, and, to reduce excessive chain extension and curing, lower temperatures were required during prepregging.
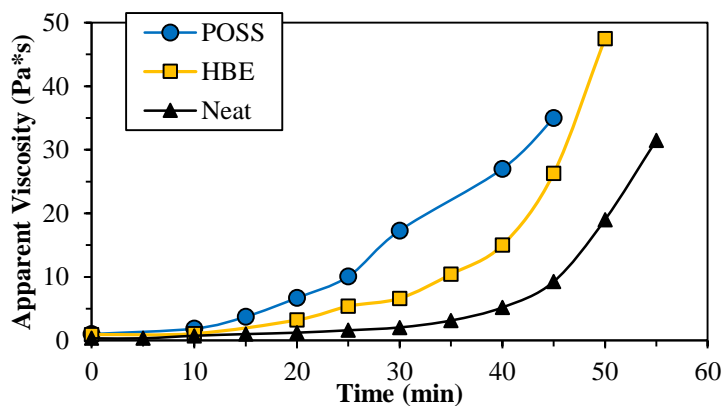
Figure 127. Apparent viscosity vs. time at 70 °C obtained by Brookfield Viscometer.
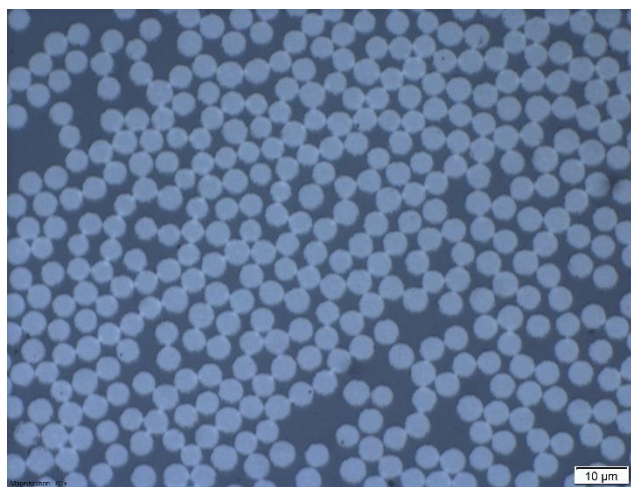
Figure 128. Representative optical microscopy image of laminate cross-section used to calculate fiber:matrix ratio; 70x magnification, scale bar 10 μm.

After the laminates were autoclave-cured, test coupons were cut to specific dimensions and orientations using a diamond saw. Pieces of the laminates and coupons

were then polished to a Class A finish and imaged by optical microscopy to determine fiber and resin content. An example optical image of an HBE specimen cross-section at 70x magnification is shown in Figure 128. Fiber and matrix volumes were extracted from optical images by calculating the area of regions of interest (ROIs) by the RGB color difference between the fibers (light) and the surrounding matrix (dark). Table 38 summarizes the calculated volume fraction data. Image-calculated fiber and matrix volume fractions were found to correlate well with targeted mass fraction values. Using a fiber density of 1.6 g/cm^3 and an average matrix density of 1.2 g/cm^3, fiber mass fraction was calculated from the images and found to be 0.63±0.02, 0.65±0.05, and 0.62±0.04 for Neat, HBE, and POSS composites, respectively. In addition, optical images were used as a qualitative measure of void content, although none were visible at this size scale. The high fiber mass fractions signify the cured laminates' high quality and ease of manufacturing. Moreover, these aerospace-grade materials provide the first level of confidence required to obtain the subsequent mechanical testing data.

Table 38

Fiber and matrix volume fractions calculated from optical images; 2 different locations on 3 specimens were used in the averaging of fiber volume

Sample Name	Fiber Volume Fraction %	Matrix Volume Fraction %
Neat	55.6	44.4
HBE	58.0	42.0
POSS	55.2	44.8

Laminate Distortional Properties

Intralaminar mechanical properties of the novel CFRPs were examined using the 10° off-axis tension test. Off-axis tension testing of composites, such as 10° tension tests herein, are used to study the distortional capability of composites. As the fiber angle increases from 0° to 90° the composite is forced to fail due to cavitation, and therefore the failure mechanism transitions from distortional to dilatational. As a result, a 10° fiber angle allows for a matrix-dominated failure-event and provides the best indication to if the matrix deforms, and ultimately fails, in distortion. Off-axis tensile properties were measured using both the linear variable differential transformer (LVDT) and digital image correlation (DIC) to ensure accurate calculation of matrix strain capability.[126] Representative surface strain visualizations from DIC are shown in Figure 129 to indicate the uniformity of the specimens tested and the strain development about the fiber axis.
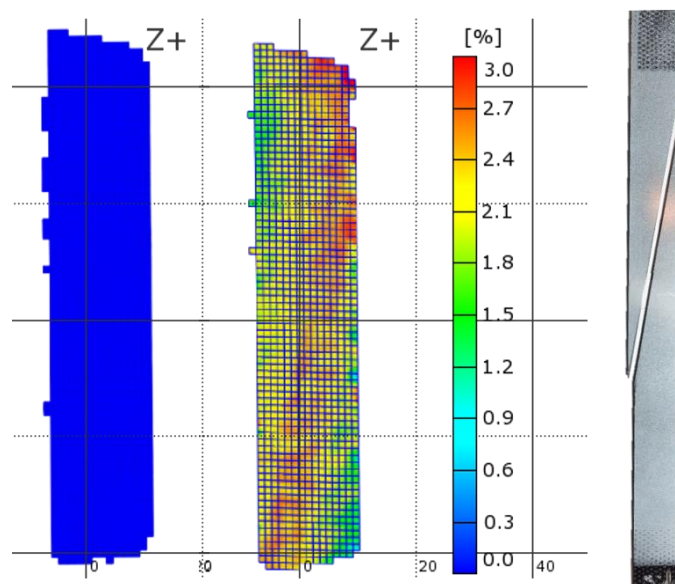
Figure 129. Example images of major surface strain maps before loading (left) and before break (center) obtained by DIC with corresponding broken coupon for 10H composites.

Figure 130 shows stress vs. strain plots generated for the 10° tests while Table 39 contains the specific values obtained from the curves. It was found that both HBE and POSS-HBE matrices provide improved composite mechanical properties over the neat network. Modulus calculated from LVDT increased for HBE and POSS systems by 37% and 28%, respectively. However, HBE and POSS composites modulus values are within experimental error of one another and both will be considered a general increase. The percentage increase in moduli for bulk matrix materials are lower than those in the respective composites. Improvements in modulus for bulk HBE and POSS-HBE networks were previously related to increased cohesive interactions brought on from HBE's high concentration of hydroxyls and POSS's nanoreinforcement effect (*Chapter VII and VIII*). It appears that the matrix structure-property relationships are amplified by incorporation and constraint from carbon fibers. Additionally, incorporation of hyperbranched polymers has been previously shown to decrease modulus values, but the network-level incorporation of HBE provides enhanced matrix-matrix interactions and therefore increase composite modulus.[183,184] It should be noted that fiber-orientation greatly affects elastic modulus and values found herein are similar to other 10° data reported in literature.[185]
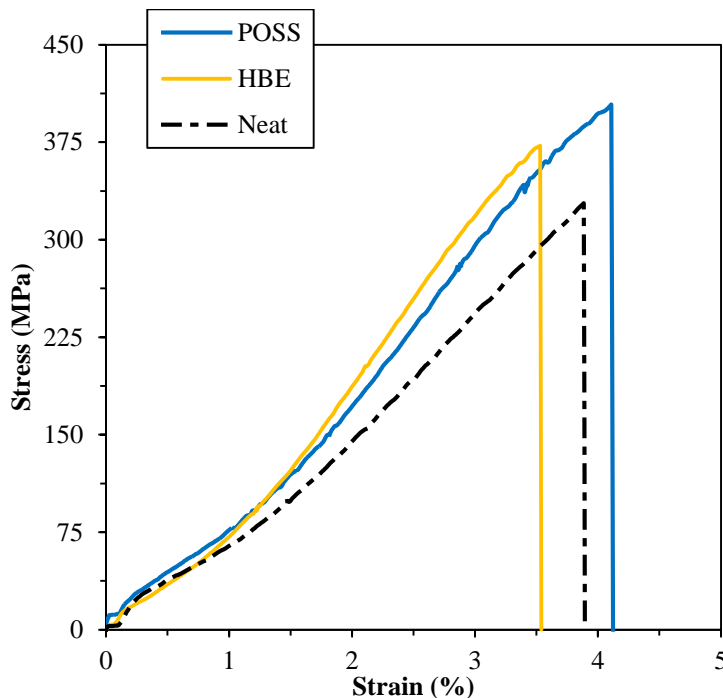
Figure 130. Stress vs. strain curves for 10° off-axis composite specimens.

Both stress- and strain-capability of composite materials have been predicted to increase through use of a distortional-matrix.[4,178] Such hypothesis are supported by the data herein where both critical properties for HBE and POSS-composites were increased in the 10° tensile test. It is shown that the strength of HBE- and POSS-composites was improved by 13% and 17% and the strain (from DIC) was increased by 54% and 59%, respectively. These property increases can be described by the distortional-capability of the bulk matrices. Strain of the bulk networks was shown to increase for both HBE and POSS and was related to network level HBE incorporation and improved secondary interactions (*Chapter VII and VIII*).[174] The increase in strain in the bulk networks translates to distortional-capability of a composite matrix provides, and as strain energy transfer from matrix to fiber is improved, so is composite performance. In a final note, surface strain from DIC was used in the composite analysis. This is because of the odd

trends in LVDT modulus and strain, which are attributed to machine compliance. As DIC

is a surface-strain mapping technique, machine variability does not affect strain data and

is assumed to be more accurate.[126]

Table 39

Composite mechanical properties; averages of 5 specimens, error within one standard deviation

Sample	Modulus	Stress	Strain	[1]Surface Strain
Name	GPa	MPa	%	%
Neat	9.8±0.6	327.4±7.6	3.75±0.09	2.24±0.22
HBE	13.4±0.2	371.0±29.3	3.53±0.07	2.60±0.15
POSS	12.5±1.3	382.1±7.9	4.10±0.34	3.28±0.19

1: surface strain obtained from ARAMIS

Interlaminar Fracture Toughness

Mode 1 fracture toughness, or G_{1C}, is the critical value for delamination growth as

a result of an opening load.[186] It is commonly measured using dual cantilever beam

(DCB) specimen geometries with unidirectional composite coupons. During composite

manufacturing a 76 mm non-adhesive insert, or "crack-starter", was placed at the mid-

plane of the laminate to create an initiation site for delamination. After curing, the DCB

specimens were cut to the correct dimensions and piano hinges were adhesively bonded

to both sides of the specimen. In this work G_{1C} was calculated using the modified beam

theory expression for fracture toughness,

$$G_{1C} = \frac{3P\delta}{2ba}$$

where, P is the opening load, δ is DCB displacement, b is specimen width, and a is

specimen delamination length.[186] Figure 131 shows a schematic of a typical DCB

specimen and the experimental testing set-up.
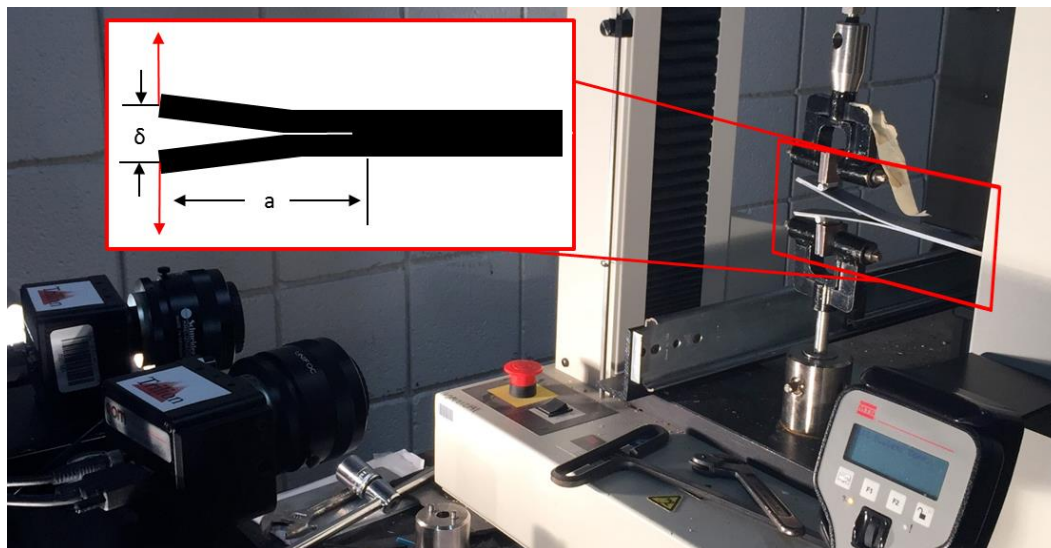
Figure 131. Experimental set-up and schematic of DCB test with G_{1C} parameters labeled.
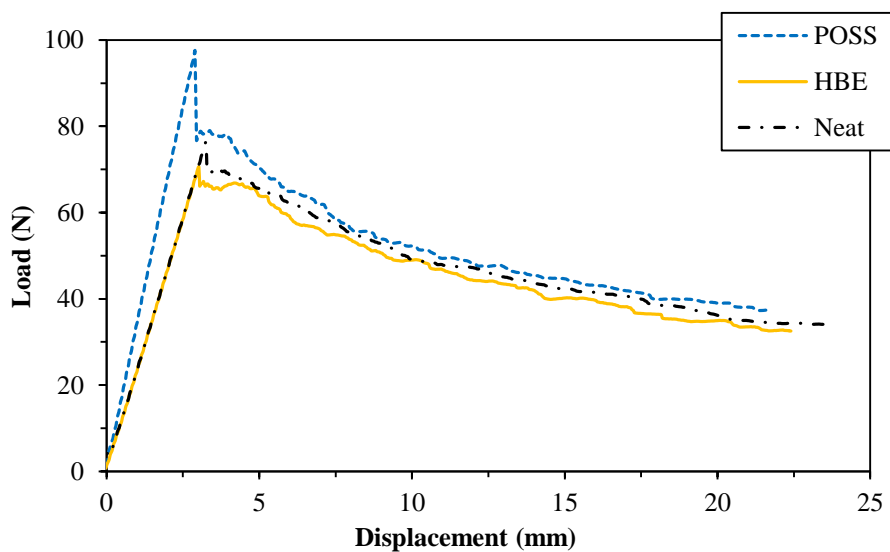
Figure 132. Load vs. displacement curves obtained from DCB mode 1 fracture toughness specimens.
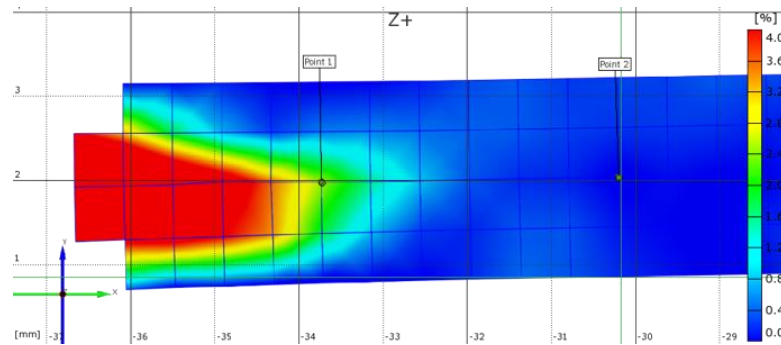
Figure 133. Representative DIC strain-field image of DCB specimen used to measure crack length and crack tip strain; Point 1 and Point 2 represent the beginning of the pre-crack and the failure point, respectively.

Load vs. displacement curves were obtained to abstract G_{1C} parameters *P* and δ using the LVDT of the test-frame and are shown in Figure 132. Delamination length was obtained using DIC by observation of major strain at the crack front. Strain increases during deformation of the DCB specimen until the crack begins to propagate, at which strain is released. The crack length can be measured by the ARAMIS software from the difference of the initial pre-crack and observation of crack tip strain release. A representative image of the points used to calculate crack delamination length, *a* are shown in Figure 133. The final results of the G_{1C} analysis are summarized in Table 40.

It was found that HBE- and POSS-matrix composites had improved mode 1 fracture toughness over the neat-matrix materials. HBE composites showed a G_{1C} increase of 53% while POSS composites had an increase of over 60%. Unlike many literature reports[187,188], the fracture behavior of the bulk matrix material transferred well to corresponding CFRP composites to give improved interlaminar fracture energies. This is likely due to the inherent energy dissipation mechanisms afforded from *in situ* toughening with HBE. Hunston has suggested that fibers constrain the size of the crack

deformation zone, thus limiting the amount of energy that can be dissipated.[189] The

HBE-matrix was shown in *Chapter VII and VIII* to separate into nano-sized domains that

were likely higher in free volume and acted similar to a rubber nanoparticle. These

domains are hypothesized to help reduce the fiber-constraints placed on the deformation

zone through their higher flexibility. The high interlaminar fracture toughness of POSS-

matrix composites is hypothesized to be a combination of HBE's flexibility as well as

improved fiber-matrix interactions brought about by the POSS nano-particles. Previous

research has shown that chemically grafting POSS to the surface of carbon fibers greatly

enhances the energy transfer from the matrix to the fiber by creation of large interphase

region.[190–192] Although is not chemically grafted, it is believed that pendant POSS

provides increased interactions with the fiber, allowing for a larger interphase region to

be developed. Further analysis of the composites are required to understand the

translation of network toughness to composite toughness.

Table 40

*Mode 1 fracture toughness and DCB crack-tip strain results; values averaged from 5
test-coupons*

Sample	Load	δ	a	[1]G_{1C}	[2]Crack-Tip Strain
Name	N	mm	mm	J/m^2	%
Neat	76.20	2.97	5.95	577	2.70
HBE	73.35	3.37	4.00	650	3.05
POSS	97.55	3.23	3.55	870	4.05

1: Obtained from crack initiation values

2: Obtained from DIC

Another less common method of describing the energy release upon crack propagation is through study of crack-tip surface-strain energies with DIC. The values of crack-tip strain directly before delamination agreed well with G_{1C} values. It was found that HBE and POSS matrix composites showed the same percent increases in both crack-tip strain and G_{1C}, approximately 53% and 60%, respectively. The increased strain capability is related to the matrix material's ability to transfer energy to the fiber, which was shown in the 10° off-axis tension tests to be due to a distortional mechanism. In DCB specimens, the energy dissipated by molecular-level shape-changes of the distortional matrix prolongs the initiation of cracking and delamination. This distortion increases strain energy dissipation and improves the fracture resistance of HBE and POSS composites. Additionally, agreement between the G_{1C} and crack-tip strain indicates the quality and confidence in G_{1C} tests herein. Furthermore, it also suggests that an easier, more straightforward method of determining fracture toughness can be developed through use of DIC.

Summary

The efficacies of carbon-fiber composites with hyperbranched-epoxy and POSS matrices were evaluated in terms of distortional and fracture-resistance capability. The manufacturability of the modified composite prepregs and laminates was found to be unchanged from the baseline material, and it was shown that high quality test specimens could be fabricated. 10° off-axis tension tests revealed increased modulus, stress, and strain for modified networks, POSS-HBE laminates having the highest distortional performance. This was attributed to bulk matrix improvements observed in previous chapters as well as increased fiber interactions from POSS cages. Likewise, it was found

that POSS-HBE composites had the highest fracture toughness values. This was shown

by both G_{1C} and DIC crack-tip strain. The observed improvements indicate that bulk

network properties can be used to help predict composite performance.

REFERENCES

(1)   Strong, B. *Fundamentals of Composites Manufacturing: Materials, Methods, and Applications*, Second.; Society of Manufacturing Engineers: Dearborn, **2008**.

(2)   Malandro, D. L.; Lacks, D. J. *J. Chem. Phys.* **1999**, *110* (9), 4593.

(3)   Sindt, O.; Perez, J.; Gerard, J. F. *Polymer* **1996**, *37* (14), 2989–2997.

(4)   Gosse, J.; Christensen, S. *Am. Inst. Aeronaut. Astronaut.* **2001**.

(5)   May, C. A. *Epoxy Resins: Chemistry and Technology,* Second Edition; Marcel Dekker, **1988**.

(6)   Odian, G. *Principles of Polymerization*; John Wiley & Sons, **2004**.

(7)   Yousefi, a; Lafleur, P. G.; Gauvin, R. *Polym. Compos.* **1997**, *18* (2), 157–168.

(8)   Meyer, F.; Sanz, G.; Eceiza, A.; Mondragon, I.; Mijović, J. *Polymer* **1995**, *36* (7), 1407–1414.

(9)   Frank, K.; Wiggins, J. *J. Appl. Polym. Sci.* **2013**, *130* (1), 264–276.

(10)   Hiemenz, P. C.; Lodge, T. P. *Polymer Chemistry*, Second Edition; CRC Press, **2007**.

(11)   Halary, J. L. *High Perform. Polym.* **2000**, *12*, 141–153.

(12)   Frank, K.; Childers, C.; Dutta, D.; Gidley, D.; Jackson, M.; Ward, S.; Maskell, R.; Wiggins, J. *Polymer* **2013**, *54* (1), 403–410.

(13)   Matějka, L. *Macromolecules* **2000**, *33* (10), 3611–3619.

(14)   Girard-Reydet, E.; Riccardi, C. C.; Sautereau, H.; Pascault, J. P. *Macromolecules* **1995**, *28* (23), 7599–7607.

(15)   Blanco, M.; Ramos, J. A.; Goyanes, S.; Rubiolo, G.; Salgueiro, W.; Somoza, A.; Mondragón, I. *J. Polym. Sci. Part B Polym. Phys.* **2009**, *47*, 1240–1252.

(16)   Bellenger, V.; Verdu, J.; Francillette, J.; Hoarau, P.; Morel, E. *Polymer* **1987**, *28* (7), 1079–1086.

(17)   Tran, T.; Simkins, D.; Lim, S. H.; Kelly, D.; Pearce, G.; Prusty, B. G.; Gosse, J.; Christensen, S. *28th International Congress Of The Aeronautical Sciences* **2012**. Conference Proceedings.

(18) Svaneborg, C.; Everaers, R.; Grest, G. S.; Curro, J. G. *Macromolecules* **2008**, *41* (13), 4920–4928.

(19) Lorenz, C. D.; Stevens, M. J. *Phys. Rev. E. Stat. Nonlin. Soft Matter Phys.* **2003**, *68*.

(20) Argon, A. S.; Cohen, R. E. *Polymer* **2003**, *44* (19), 6013–6032.

(21) Chui, C.; Boyce, M. C. *Macromolecules* **1999**, *32* (11), 3795–3808.

(22) Jackson, M. B. Effects of Molecular Architecture on Fluid Ingress Behavior of Glassy Polymer Networks, Dissertation. **2011**.

(23) Capaldi, F. M.; Boyce, M. C.; Rutledge, G. C. *Phys. Rev. Lett.* **2002**, *89* (17), 175505.

(24) Tucker, S. J. Study of 3,3' vs. 4,4' DDS Isomer Curatives on Physical Properties and Phenyl Ring Motions of DGEBA Epoxy via Molecular Dynamics, Deuterium NMR and Dielectric Spectroscopy, Dissertation. **2010**.

(25) Atkins, P.; Atkins, J. *Physical Chemistry*, 8th ed.; Company, W. H. F. and, Ed.; 2006.

(26) Pellice, S. a.; Fasce, D. P.; Williams, R. J. J. *J. Polym. Sci. Part B Polym. Phys.* **2003**, *41* (13), 1451–1461.

(27) Monnerie, L.; Lauprêtre, F.; Halary, J. L. *Adv. Polym. Sci.* **2005**, *187*, 35–213.

(28) Chen, L. P.; Yee, A. F.; Moskala, E. J. *Macromolecules* **1999**, *32* (18), 5944–5955.

(29) Urbaczewski-Espuche, E.; Galy, J.; Gerard, J. F.; Pascault, J. P.; Sautereau, H. *Polym. Eng. Sci.* **1991**, *31* (22), 1572–1580.

(30) Liu, J.; Yee, A. F. *Macromolecules* **1998**, *31* (22), 7865–7870.

(31) Boyer, R. F. *Macromolecules* **1992**, *25*, 5326–5330.

(32) Alegría, A.; Mitxelena, O.; Colmenero, J. *Macromolecules* **2006**, *39* (7), 2691–2699.

(33) Tu, J.; Tucker, S. J.; Christensen, S.; Sayed, A. R.; Jarrett, W. L.; Wiggins, J. S. *Macromolecules* **2015**, *48* (6), 1748–1758.

(34) Perchak, D.; Skolnick, J.; Yaris, R. *Macromolecules* **1987**, *20*, 121–129.

(35)   Bartolotta, A.; Cerini, G.; Carini, G.; Di Marco, G.; Tripodo, G. *Macromolecules* **2010**, *43* (10), 4798–4804.

(36)   Wan, J.; Li, B. G.; Fan, H.; Bu, Z. Y.; Xu, C. J. *Thermochim. Acta* **2010**, *511* (1-2), 51–58.

(37)   Starkweather, H. W. *Macromolecules* **1981**, *14* (5), 1277–1281.

(38)   Cukierman, S.; Halary, J.-L.; Monnerie, L. *Polym. Eng. Sci.* **1991**, *31* (20), 1476–1482.

(39)   Bandyopadhyay, A.; Valavala, P. K.; Clancy, T. C.; Wise, K. E.; Odegard, G. M. *Polymer* **2011**, *52* (11), 2445–2452.

(40)   Levita, G.; Petris, S.; Marchetti, A.; Lazzeri, A. *J. Mater. Sci.* **1991**, *26* (9), 2348–2352.

(41)   Yang, G.; Fu, S.-Y.; Yang, J.-P. *Polymer* **2007**, *48* (1), 302–310.

(42)   Laiarinandrasana, L.; Fu, Y.; Halary, J. L. **2011**.

(43)   Sauvant, V.; Halary, J. L. *J. Appl. Polym. Sci.* **2001**, *82* (3), 759–774.

(44)   Zerda, A. S.; Lesser, A. J. *Polym. Eng. Sci.* **2004**, *44* (11), 2125–2133.

(45)   Heux, L.; Lauprêtre, F.; Halary, J. L.; Monnerie, L. *Polymer* **1998**, *39* (6-7), 1269–1278.

(46)   Marks, M. J.; Snelgrove, R. V. *ACS Appl. Mater. Interfaces* **2009**, *1* (4), 921–926.

(47)   Gómez-del Río, T.; Rodríguez, J. *Mater. Des.* **2012**, *35*, 369–373.

(48)   Hoffmann, U.; Mallen, K. *Macromolecules* **1994,** *27*, 3515-3579.

(49)   Fink, J. K. In *High Performance Polymers*; **2008**.

(50)   Cai, M.; Zhu, M.; Sun, Y.; Qian, J. *React. Funct. Polym.* **2010**, *70* (3), 182–188.

(51)   Yonezawa, N.; Ikezaki, T.; Nakamura, H.; Maeyama, K. *Macromolecules* **2000**, *33* (22), 8125–8129.

(52)   Ben-Haida, A.; Colquhoun, H. M.; Hodge, P.; Williams, D. J. *Macromolecules* **2006**, 6467–6472.

(53)   Díez-Pascual, A. M.; Naffakh, M.; Marco, C.; Ellis, G.; Gómez-Fatou, M. A. *Prog. Mater. Sci.* **2012**, *57* (7), 1106–1190.

(54)   Strong, B. *Plastics: Materials and Processing*, 3rd ed.; Prentice Hall, 2005.

(55)   Hwang, S.; Lee, G.; Lee, K.; Jung, J. *Polym. Adv. Technol.* **2001**, *12*, 441–444.

(56)   Gupta, N.; Varma, I. K. *J. Appl. Polym. Sci.* **1997**, *68,* 1759–1766.

(57)   Flory, P. J. *J. Am. Chem. Soc.* **1952**, *74* (11), 2718–2723.

(58)   Kim, Y. H.; Webster, O. W. *J. Am. Chem. Soc.* **1990**, *112* (11), 4592–4593.

(59)   Žagar, E.; Žigon, M. *Macromolecules* **2002**, *35* (27), 9913–9925.

(60)   Žagar, E.; Žigon, M. *Prog. Polym. Sci.* **2011**, *36* (1), 53–88.

(61)   Gao, C.; Yan, D. *Prog. Polym. Sci.* **2004**, *29* (3), 183–275.

(62)   Jikei, M.; Kakimoto, M. *Prog. Polym. Sci.* **2001**, *26* (8), 1233–1285.

(63)   Emrick, T.; Chang, H.; Frechet, J. M. J. *J. Polym. Sci. Part A Polym. Chem.* **2000**, *38*, 4850–4869.

(64)   Tang, B.; Liu, X.; Zhao, X.; Zhang, J. *J. Appl. Polym. Sci.* **2014**, *131*, 1–9.

(65)   Miao, X.; Meng, Y.; Li, X. *Polymer* **2015**, *60*, 88–95.

(66)   Miao, X.; Meng, Y.; Li, X. *J. Appl. Polym. Sci.* **2015**, *132*.

(67)   Chang, H.; Fre, J. M. J. **1999**, *3* (10), 2313–2314.

(68)   Mezzenga, R.; Boogh, L.; Ma, J. E. **2001**, *61*, 787–795.

(69)   Zhang, D.; Jia, D. *J. Appl. Polym. Sci.* **2006**, *101* (4), 2504–2511.

(70)   Morell, M.; Ramis, X.; Ferrando, F.; Yu, Y.; Serra, A. *Polymer* **2009**, *50*, 5374–5383.

(71)   Tomuta, A.; Ferrando, F.; Serra, À.; Ramis, X. *React. Funct. Polym.* **2012**, *72*, 556–563.

(72)   Cicala, G.; Recca, a.; Restuccia, C. *Polym. Eng. Sci.* **2005**, *45* (2), 225–237.

(73)   Varley, R. J. *Polym. Int.* **2004**, *53* (1), 78–84.

(74)   Ratna, D.; Simon, G. . *Polymer* **2001**, *42* (21), 8833–8839.

(75)   Wu, H.; Xu, J.; Liu, Y.; Heiden, P. *J. Appl. Polym. Sci.* **1999**, *72* (2), 151–163.

(76)   Ratna, D.; Varley, R.; Simon, G. P. *J. Appl. Polym. Sci.* **2003**.

(77)   Mezzenga, R. **2001**, *6*, 4883–4891.

(78)   Kuo, S. W.; Chang, F. C. *Prog. Polym. Sci.* **2011**, *36* (12), 1649–1696.

(79)   Musto, P.; Abbate, M.; Pannico, M.; Scarinzi, G.; Ragosta, G. *Polymer* **2012**, *53* (22), 5016–5036.

(80)   Florea, N. M.; Lungu, A.; Badica, P.; Craciun, L.; Enculescu, M.; Ghita, D. G.; Ionescu, C.; Zgirian, R. G.; Iovu, H. *Composites Part B* **2015**, *75*, 226–234.

(81)   Strachota, A.; Whelan, P.; Kříž, J.; Brus, J.; Urbanová, M.; Šlouf, M.; Matějka, L. *Polymer* **2007**, *48* (11), 3041–3058.

(82)   Boček, J.; Matějka, L.; Mentlík, V.; Trnka, P.; Šlouf, M. *Eur. Polym. J.* **2011**, *47* (5), 861–872.

(83)   Strachota, A.; Kroutilová, I.; Kovářová, J.; Matějka, L. *Macromolecules* **2004**, *37* (25), 9457–9464.

(84)   Kim, G. M.; Qin, H.; Fang, X.; Sun, F. C.; Mather, P. T. *J. Polym. Sci. Part B Polym. Phys.* **2003**, *41* (24), 3299–3313.

(85)   Matějka, L.; Amici Kroutilová, I.; Lichtenhan, J. D.; Haddad, T. S. *Eur. Polym. J.* **2014**, *52*, 117–126.

(86)   Strachota, A.; Ples, J.; Whelan, P. *Macromolecules* **2004**, 9449–9456.

(87)   Frank, K. L.; Exley, S. E.; Thornell, T. L.; Morgan, S. E.; Wiggins, J. S. *Polymer* **2012**, *53* (21), 4643–4651.

(88)   Zucchi, I. a.; Galante, M. J.; Williams, R. J. J.; Franchini, E.; Galy, J.; Gérard, J. F. *Macromolecules* **2007**, *40* (4), 1274–1282.

(89)   Matějka, L.; Murias, P.; Pleštil, J. *Eur. Polym. J.* **2012**, *48* (2), 260–274.

(90)   Pistor, V.; Ornaghi, F. G.; Ornaghi, H. L.; Zattera, A. J. *Mater. Sci. Eng. A* **2012**, *532*, 339–345.

(91)   ASTM International. *ASTM D1652-11e1, Standard Test Method for Epoxy Content of Epoxy Resins.* **2011**.

(92)   Flory, P. J. *Polymer* **1979**, *20* (11), 1317–1320.

(93)   GOM. *ARAMIS User Manual*; Braunshweig, Germany, **2007**.

(94)   Godara, A.; Rabbe, D. *Compos. Sci. Technol.* **2007**, *67*, 2417–2427.

(95)   Sachs, C.; Fabritius, H.; Raabe, D. *J. Struct. Biol.* **2006**, *155*, 409–425.

(96)   Godara, A.; Raabe, D.; Bergmann, I.; Putz, R.; Muller, U. *Compos. Sci. Technol.* **2009**, *69*, 139–146.

(97)   Parson, E.; Boyce, M.; Parks, D.; Weinberg, M. *Polymer* **2005**, *46*, 2257–2265.

(98)   Li, C.; Strachan, A. *Polymer* **2010**, *51* (25), 6058–6070.

(99)   Brunelle, D. J. *J. Polym. Sci. Part A Polym. Chem.* **2008**, *46* (4), 1151–1164.

(100)   Chen, M. Macrocyclic Monomers: Synthesis, Characterization and Ring-Opening Polymerization, Dissertation. **1997**.

(101)   Strandman, S.; Gautrot, J. E.; Zhu, X. X. *Polym. Chem.* **2011**, *2* (4), 791.

(102)   Ding, Y.; Hay, A. S. *Macromolecules* **1996**, *29* (9), 3090–3095.

(103)   Zolotukhin, M. G.; Fomine, S.; Colquhoun, H. M.; Zhu, Z.; Drew, M. G. B.; Olley, R. H.; Fairman, R. a.; Williams, D. J. *Macromolecules* **2004**, *37* (6), 2041–2053.

(104)   Xie, D.; Ji, Q.; Gibson, H. W. **1997**, *9297* (97), 4814–4827.

(105)   Ben-Haida, A.; Colquhoun, H. M.; Hodge, P.; Williams, D. J. *Macromolecules* **2006**, *39* (19), 6467–6472.

(106)   Ben-Haida, A.; Colquhoun, H. M.; Hodge, P.; Williams, D. J. *J. Mater. Chem.* **2000**, *10* (9), 2011–2016.

(107)   Chan, K. P.; Wang, Y.; Hay, A. S. **1996**, *10*, 6705–6717.

(108)   Feng-Chih Chang, Michael I. Heather, Robert P. Shirtum, I. H. J. Process for the preparation of epoxy resins. Patent. 4,582,892, **1986**.

(109)   John F. Arnett, G. A. D. Preparation of Glycidyl Ethers. Patent. 4,284,573, **1981**.

(110)   Raha, S.; Majumdar, S.; Mitra, K. *Macromol. Theory Simulations* **2004**, *13* (2), 152–161.

(111)   Boogh, L.; Pettersson, B.; Ma, J. E. *Polymer* **1999**, *40*, 2249–2261.

(112)   Cicala, G., G. R. *J. Appl. Polym. Sci.* **2009**, *115*, 1395–1406.

(113) ASTM International. *ASTM E222-10, Standard Test Method for Hydroxyl Groups Using Acetic Anhydride Acetylation*; **2010**.

(114) Sbirrazzuoli, N.; Vyazovkin, S. *Thermochim. Acta* **2002**, *388* (1-2), 289–298.

(115) Vyazovkin, S.; Sbirrazzuoli, N. *Macromolecules* **1996**, *29* (6), 1867–1873.

(116) Ghumara, R. Y.; Adroja, P. P.; Parsania, P. H. *J. Therm. Anal. Calorim.* **2013**, *114* (2), 873–881.

(117) Tripathi, G.; Srivastava, D. *J. Appl. Polym. Sci.* **2009**, *112* (5), 3119–3126.

(118) Roşu, D.; Mititelu, a.; Caşcaval, C. N. *Polym. Test.* **2004**, *23* (2), 209–215.

(119) Deng, Y.; Martin, G. C. *Macromolecules* **1994**, *27* (18), 5141–5146.

(120) Wan, J.; Li, B.-G.; Fan, H.; Bu, Z.-Y.; Xu, C.-J. *Thermochim. Acta* **2010**, *510* (1-2), 46–52.

(121) Smith, M. B.; March, J. *March's Advanced Organic Chemistry: Reactions, Mechanisms, and Structure*; John Wiley & Sons, **2007**.

(122) Mezzenga, R.; Boogh, L.; Månson, J.-A. E.; Pettersson, B. *Macromolecules* **2000**, *33* (12), 4373–4379.

(123) Su, Chean C, Woo, E. M. *Polymer (Guildf).* **1995**, *36* (15), 2883–2894.

(124) Levchik, S. V; Weil, E. D. *Polym. Int.* **2004**, *53* (12), 1901–1929.

(125) Sharma, P.; Choudhary, V.; Narula, A. K. *J. Appl. Polym. Sci.* **2008**, *107*, 1946–1953.

(126) Heinz, S. R.; Wiggins, J. S. *Polym. Test.* **2010**, *29* (8), 925–932.

(127) Pascault, J.-P.; Sautereau, H.; Verdu, J.; Williams, R. J. J. *Thermosetting Polymers*; CRC Press, **2002**.

(128) Foster, S. F.; Hoff, E. A.; Curtzwiler, G. W.; Williams, E. B.; Davis, K. B.; Patton, D. L.; Rawlins, J. W. *J. Polym. Sci. Part B Polym. Phys.* **2015,** *53.*

(129) Sahagun, C. M.; Morgan, S. E. *ACS Appl. Mater. Interfaces* **2012**, *4* (2), 564–572.

(130) Mayr, A. E.; Cook, W. D.; Edward, G. H. *Polymer* **1998**, *39* (16), 3719–3724.

(131) Christensen, S.; D'Oyen, R. *Scr. Mater.* **2014**, *70*, 18–24.

(132) Enns, J. B.; Gillham, J. K. *J. Appl. Polym. Sci.* **1983**, *28* (9), 2831–2846.

(133) Mijovic, J.; Zhang, H. **2003**, 1279–1288.

(134) Jackson, M.; Kaushik, M.; Nazarenko, S.; Ward, S.; Maskell, R.; Wiggins, J. *Polymer* **2011**, *52* (20), 4528–4535.

(135) Lesser, A. J.; Calzia, K. J. *J. Polym. Sci. Part B Polym. Phys.* **2004**, *42*, 2050–2056.

(136) Kins, C. F.; Dudenko, D.; Sebastiani, D.; Brunklaus, G. *Macromolecules* **2010**, *43* (17), 7200–7211.

(137) Yee, A. F.; Smith, S. A. *Macromolecules* **1981**, *14* (1), 54–64.

(138) Matsuoka, S.; Hale, A. *J. Appl. Polym. Sci.* **1997**, *64* (1), 77–93.

(139) David, L.; Etienne, S. *Macromolecules* **1992**, *25*, 4302–4308.

(140) Jonas, A.; Legras, R. *Macromolecules* **1993**, *26* (4), 813–824.

(141) Biovia Materials Studio 7.0 Help - Cohesive Energy, **2015**.

(142) Kwan, E. E. An Introduction to Hydrogen Bonding, **2009**.

(143) Kingsbury, C. A. Why are the Nitro and Sulfone Groups Poor Hydrogen Bonders?, Thesis. **2015**.

(144) Wu, C.; Xu, W. *Polymer* **2007**, *48* (19), 5802–5812.

(145) Yang, S.; Qu, J. *Polymer* **2012**, *53* (21), 4806–4817.

(146) Ravindrachary, V.; Ramani, R.; Ranganathaiah, C.; Gopal, S. *Int. J. Mod. Phys. B* **1994**, *8* (13), 1699–1711.

(147) Liu, J.; Yee, A. F. *Macromolecules* **2000**, *33* (4), 1338–1344.

(148) Goyanes, S.; Salgueiro, W.; Somoza, a.; Ramos, J. a.; Mondragon, I. *Polymer* **2004**, *45* (19), 6691–6697.

(149) Goyanes, S.; Rubiolo, G.; Salgueiro, W.; Somoza, a. *Polymer* **2005**, *46* (21), 9081–9087.

(150) Craword, E. D.; Lesser, A. J. *Polym. Eng. Sci.* **1999**, *39* (2), 385–392.

(151) F. Fdez de Nograro, R. Llano-Ponte, I. M. *Polymer* **2004**, *6774* (9), 1589–1600.

(152) Cai, H.; Li, P.; Sui, G.; Yu, Y.; Li, G.; Yang, X.; Ryu, S. *Thermochim. Acta* **2008**, *473* (1-2), 101–105.

(153) Detwiler, A. T.; Lesser, A. J. *J. Mater. Sci.* **2012**, *47* (8), 3493–3503.

(154) Sirk, T. W.; Karim, M.; Khare, K. S.; Lenhart, J. L.; Andzelm, J. W.; Khare, R. **2015**, *58*, 199–208.

(155) Flynn, J. H. *Thermochim. Acta* **1997**, *300* (1-2), 83–92.

(156) Ozawa, T. *J. Therm. Anal. Calorim.* **1970**, *2* (301).

(157) Childers, C. H. Computational and Experimenta Invesitgation into Yield Behavior and Cure Rate Dependence of Thermoset Polymers, Dissertation. **2014**.

(158) Halley, P. J.; Mackay, M. E. *Polym. Eng. Sci.* **1996**, *36* (5).

(159) Enns, J. B.; Gillham, J. K. *J. Appl. Polym. Sci.* **1983**, *28* (9), 2831–2846.

(160) Fox, T. *Bull Am Phys Soc* **1956**, *123* (1).

(161) Detwiler, A. T. Aspects of Network Formation and Property Evolution in Glassy Polymer Networks, Dissertation. **2011**.

(162) Painter, P. C.; Graf, J. F.; Coleman, M. M. *Macromolecules* **1991**, *24* (20), 5630–5638.

(163) Ruiz-Pérez, L.; Royston, G. J.; Fairclough, J. P. a; Ryan, A. J. *Polymer* **2008**, *49* (21), 4475–4488.

(164) Downey, M. A.; Drzal, L. T. *Polymer* **2014**, *55* (26), 6658–6663.

(165) Wang, X.; Gillham, J. K. *J. Appl. Polym. Sci.* **1991**, *43* (12), 2267–2277.

(166) Resins, T.; Development, M.; Cole, K. C. **1991**, 3093–3097.

(167) Enns, J. B.; Gillham, J. K. *J. Appl. Polym. Sci.* **1983**, *28* (8), 2567–2591.

(168) Pinal, R. *Entropy* **2008**, *10* (3), 207–223.

(169) Pierre, A.; Sindt, O.; Thorne, N.; Perez, J.; Gérard, J. F. *Macromol. Symp.* **1999**, *147*, 103–112.

(170) Nikolic, G.; Zlatkovic, S.; Cakic, M.; Cakic, S.; Lacnjevac, C.; Rajic, Z. *Sensors* **2010**, *10*, 684–696.

(171) Jackson, M.; Kaushik, M.; Nazarenko, S.; Ward, S.; Maskell, R.; Wiggins, J. *Polymer* **2011**, *52* (20), 4528–4535.

(172) Pritchard, G.; Rhoades, G. V. *Mater. Sci. Eng.* **1976**, *26* (1), 1–11.

(173) Robertson, R. E.; Mindroiu, V. E.; Cheung, M.-F. *Compos. Sci. Technol.* **1985**, *22* (3), 197–207.

(174) Wu, J.; Xiao, C.; Yee, A. F.; Klug, C. a.; Schaefer, J. *J. Polym. Sci. Part B Polym. Phys.* **2001**, *39* (15), 1730–1740.

(175) Yoonessi, M.; Lebro, M.; Scheiman, D.; Meador, M. A. *ACS Appl. Mater. Interfaces* **2014**, *6,* 16621-16630.

(176) Martinez-Rubi, Y.; Ashrafi, B.; Guan, J.; Kingston, C.; Johnston, A.; Simard, B.; Mirjalili, V.; Hubert, P.; Deng, L.; Young, R. J. *ACS Appl. Mater. Interfaces* **2011**, *3* (7), 2309–2317.

(177) Christensen, S.; D'Oyen, R. *Scr. Mater.* **2014**, *70* (1), 18–24.

(178) Yee, A. F.; Pearson, R. A. *J. Mater. Sci.* **1986**, *21* (7), 2462–2474.

(179) Tang, L. C.; Wang, X.; Wan, Y. J.; Wu, L. Bin; Jiang, J. X.; Lai, G. Q. *Mater. Chem. Phys.* **2013**, *141* (1), 333–342.

(180) Dean, J. M.; Grubbs, R. B.; Saad, W.; Cook, R. F.; Bates, F. S. *J. Polym. Sci. Part B Polym. Phys.* **2003**, *41* (20), 2444–2456.

(181) Dean, J. M.; Lipic, P. M.; Grubbs, R. B.; Cook, R. F.; Bates, F. S. *J. Polym. Sci. Part B Polym. Phys.* **2001**, *39* (23), 2996–3010.

(182) DeCarli, M.; Kozielski, K.; Tian, W.; Varley, R. *Compos. Sci. Technol.* **2005**, *65* (14), 2156–2166.

(183) Verrey, J.; Winkler, Y.; Michaud, V.; Månson, J. A. E. *Compos. Sci. Technol.* **2005**, *65* (10), 1527–1536.

(184) Chamis, C.; Sinclair, J. *10-Degree Off-Axis Tensile Test for Intralaminar Shear Characterization of Fiber Composites*; **1976**.

(185) Jin, Q.; Misasi, J. M.; Wiggins, J. S.; Morgan, S. E. *Polymer.* **2015**.

(186) ASTM International. *ASTM D5528-01 - Standard Test Method for Mode I Interlaminar Fracture Toughness of Unidirectional Fiber-Reinforced Polymer Matrix Composites*, **2007**.

(187) Kinloch, a. J.; Masania, K.; Taylor, a. C.; Sprenger, S.; Egan, D. *J. Mater. Sci.* **2008**, *43* (3), 1151–1154.

(188) Hunstson, D.; Moulton, R.; Johnston, N. *Toughened Composites*, **1985**.

(189) Kinloch, A. J.; Shaw, S. J.; Tod, D. A.; Hunston, D. L. *Polymer* **1983**, *24* (10), 1341–1354.

(190) Zhao, F.; Huang, Y. *Mater. Lett.* **2010**, *64* (24), 2742–2744.

(191) Zhao, F.; Huang, Y.; Liu, L.; Bai, Y.; Xu, L. *Carbon.* **2011**, *49* (8), 2624–2632.

(192) Jiang, D.; Liu, L.; Long, J.; Xing, L.; Huang, Y.; Wu, Z.; Yan, X.; Guo, Z. *Compos. Sci. Technol.* **2014**, *100*, 158–165.

(193) Roberts, G. D. Shantaram; St. Martin's Griffin, 2005.